CRANFIELD UNIVERSITY

ARYEH MARKS

A FAULT HIDING APPROACH FOR FAULT TOLERANT CONTROL OF A CLASS OF VTOL VEHICLES

SCHOOL OF ENGINEERING

CRANFIELD UNIVERSITY

SCHOOL OF ENGINEERING

Ph.D. THESIS

ARYEH MARKS

A fault Hiding Approach for Fault Tolerant Control of a Class of VTOL Vehicles

Supervisor: Dr James F Whidborne

February 2015

Abstract

The octorotor is an unmanned VTOL capable vehicle with eight motors with fixed pitch rotors. It is controlled by varying the speeds of its eight motors which are placed around the vehicle. There is no need for a complex swashplate system, making the vehicle low cost and dynamically simple. The increase in the number of effectors over the quadrotor allows for inbuilt hardware redundancy. It is this redundancy which is of particular interest as the capabilities and applications of VTOL capable UAVs increases and the payloads become more expensive and sensitive. It would be unacceptable for a hardware failure to result in the loss of the vehicle and payload, especially if operating in close proximity to people.

An operational requirement is that the operator must be able to control the vehicle's position and yaw angle. Position reference commands are generated in an inertial frame and these must be related to the vehicle-fixed frame through a rotation matrix. The downfall of this method is that trigonometric singularities exist for large body angles where gimbal lock can occur. For this reason the unit quaternion attitude representation is used. The octorotor is not open-loop stable so a PD controller is used to provide for singularity-free, almost global asymptotic stability which is capable of following flightpaths as well as recovering from an initial inverted attitude. The output of the controller is called the virtual control since this demand is passed to the control allocation subsystem where the overall forces and moments are generated.

A suitable control allocation method is needed since there are more effectors than actuated degrees of freedom. The effectors are assumed to be linear and various methods are used to provide constrained control allocation. If the virtual control is constrained then the allocation problem is always the unconstrained allocation problem and is guaranteed to be successful. By applying the constraints directly to the effectors it is not necessary to use complex face searching algorithms to calculate the constrained virtual control.

An objective of this thesis is to ensure that effector failures do not affect the vehicle's flight performance. This is integral to the aim of demonstrating that the hardware redundancy is sufficient to allow flights over populated areas. Effector failures are modelled as an instantaneous loss of thrust from an effector. This causes an adverse roll, pitch, and yaw disturbance as well as a drop in altitude. The recovery is based on the fault hiding method where the virtual control remains invariant from

the nominal case and the fault is hidden in the plant. If none of the remaining effectors are saturated then the failure-free performance is maintained and the operator should not notice any change to the vehicle handling. Kalman controllability analysis is done to determine the combinations of effector failures which result in a controllable vehicle.

Flight testing has demonstrated the suitability of the controller to the task of stabilising the vehicle. The failure scenarios are initialised before the flight and the performance is invariant to the health of the effectors. The reasons for differences between the simulation data and flight data are explained. Future work will implement an online fault detection scheme.

Acknowledgements

First and foremost I would like to acknowledge that even though my name is on the front of this thesis it would not have been possible to achieve this work without the help and guidance of so many people.

I would like to begin by thanking the staff and my colleagues at Cranfield University, especially my supervisor James Whidborne who has put up with my Tuesday afternoon rant sessions for 3 years. His knowledge and patience has been invaluable and I would not have been able to complete this thesis without him. Further appreciation is shown to Alastair Cook who took the time to explain helicopter principles and shared supervisor responsibilities during my first year.

My housemates Mikael and Jérémie were always available when I needed to be distracted and were helpful in troubleshooting problems with code, and Chris came in extremely useful for his knowledge of RC components. Furthermore, Mudassir, Arturo, and the entire Dynamics, Simulation, and Control group are also responsible for making sure that I always had questions to answer and the 5 minute presentation challenge really lived up to its name!

I would also like to thank the staff and my colleagues at The University of Kitakyushu, especially Ikuo Yamamoto, Naohiro Inagawa, Makoto Isoda, and Ito Shin. You all made me feel so welcome in Japan and I thoroughly enjoyed the experience of conducting research in a new environment as well as being given the opportunity to demonstrate the research through outreach to the students in Taragi. The weekend spent demonstrating robotic fish in Kumamoto prefecture really opened my eyes to the importance of making research accessible to the public - even through the language barrier.

My family have been a constant source of encouragement throughout my life and I would not have been able to realise my dream of developing aerospace products without their love and support. Thanks to my dad for always sending me articles of interest about UAVs, and to my mum for coming up with the pizza delivery robot idea. My sisters have always found ways to cheer me up whenever I suffered a setback and genuinely appear interested in what I'm up to.

Finally, I would like to thank my fiancée Kate who has been a constant source of encouragement, support, and love. Thank you for putting up with my rotor

blade demonstrations (with accompanying hand gestures), obsession with looking at robots, and for having the patience and belief in me over the course of this research.

Contents

List of Figures

List of Tables

Nomenclature

A	State matrix
$\mathcal{A}$	Set of control constraints
B	Control effectiveness matrix
$\hat{B}$	Input matrix
b	Relationship between squared rotor speed and thrust
C	Output matrix
$C(\mathbf{x})$	Skew symmetric cross product maxtrix function
c	Offset vector
c_θ	$\cos\theta$
D	Feedfordward matrix
d	Relationship between squared rotor speed and gyroscopic drag
E	Map from Euler angle vector to Euler rates matrix
$\hat{e}$	Unit vector
F	Reliability of a system
F'	Unreliability of a system
f	Reference frame
$\mathcal{F}$	Set of effector constraints
g	Acceleration due to gravity
H	Rotation matrix relating body fixed frame to inertial frame
I	Identity matrix
J	Inertia matrix
K	Controller
k	Euler angle vector
l	Vehicle arm length
M	Vector of applied torques
m	Vehicle mass
P, Q, R	Roll, pitch, yaw rate
$\dot{P}, \dot{Q}, \dot{R}$	Roll, pitch, yaw acceleration
p	Number of Effectors on VTOL vehicle
$Q(\bar{q})$	Quaternion matrix function
q	Vector portion of quaternion attitude
$\bar{q}$	Attitude Quaternion
R	Rotation matrix
$\mathbb{R}$	Real number
r	Reference input to linear system
s_θ	$\sin\theta$
t	Time
t_0	Initial time
t_θ	$\tan\theta$

U	Force and moment output of effectors
U_f	Force and moment output of effectors after failure
U_n	Nominal force and moment output of effectors
u, v, w	Longitudinal, lateral, vertical velocity
$\dot{u}, \dot{v}, \dot{w}$	Longitudinal, lateral, vertical acceleration
$\mathbf{u}$	Vector of squared rotor speeds
$\mathbf{V}$	Vector of linear velocities
v_x, v_y, v_z	Inertial frame velocities
W	Controls weighting matrix
x_b, y_b, z_b	Body axis frame
x_w, y_w, z_w	Position in inertial frame
$\dot{x}, \dot{y}, \dot{z}$	Velocity in inertial frame
$\mathbf{x}$	State vector of linear system
$\mathbf{y}$	Output vector of linear system
$\mathbb{Z}$	Integer

Greek Letters

α	Attitude magnitude
β	Roll and pitch saturation function
γ	Angle subtended by a vehicle arm and the x_b axis
Δ	Vector of effector health
δ	Health of an effector
θ	Pitch angle [rad]
Λ	Failure rate of a system
λ	Ratio of unconstrained to constrained control demand
σ	Saturation function
τ	Virtual control
τ_c	Constrained virtual control
τ_u	Unconstrained virtual control
ϕ	Roll angle [rad]
ψ	Yaw angle [rad]
Ω	Effector speed [rad/s]
ω'	Vector of angular velocities

Abbreviations

ESC	Electronic Speed Controller
GPS	Global Positioning System
IMU	Inertial Measurement Unit
LOE	Loss of Effectiveness
RPI	Redistributed Pseudo Inverse
UAV	Unmanned Air Vehicle
VTOL	Vertical Takeoff and Landing

Chapter 1

Introduction

1.1 Overview

VTOL capable UAVs offer a number of advantages over their fixed wing and manned counterparts. They are capable of vertical flight and thus do not require a large infrastructure when deploying from a forward operating point. They can hover so that target lock can be maintained, and are able to perform agile and aggressive manoeuvres such as vertical drops, flips [Lupashin et al., 2010], and pass through narrow gaps [Mellinger and Kumar, 2011]. Their unmanned aspect allows for operations in hostile environments where it is too risky to endanger a pilot, either because of atmospheric conditions such as volcanic ash and toxic fumes, or because of enemy air defences when flying in a contested airspace.

In this thesis the p-rotor is the generic name given to a class of VTOL capable rotorcraft with p effectors, which are generally formed of a motor-rotor combination. The quadrotor (sometimes referred to as a quadcopter or quadrocopter) is a popular platform with four independently controlled motors spaced evenly around the vehicle body in either a 'plus' shape (Figure 1.1a) or a 'cross' shape (Figure 1.1b). The difference between the two vehicle layouts is that for the 'plus' shaped vehicle the effectors lie on the body axis lines. This means that only some of the effectors are used for a manoeuvre, whilst with the 'cross' shaped vehicle all of the effectors are used in combination to perform a manoeuvre. The quadrotor is underactuated in the sense that the effectors can directly alter four of the six degrees of freedom. [1] For this reason only four control demands can be performed and are chosen as the 3 inertial positions and the yaw angle. This enables the description of the vehicle position in space as well as the pointing direction.

[1] This is not to be confused with the opposite of 'overactuated' used later in this thesis which means that there are more effectors than actuated degrees of freedom.

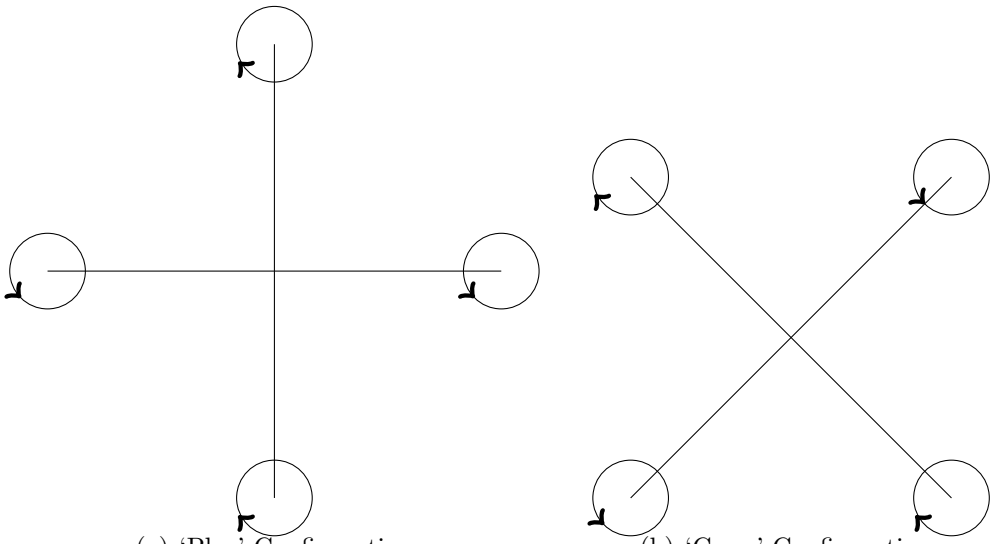

(a) 'Plus' Configuration (b) 'Cross' Configuration

Figure 1.1: Examples of Quadrotor Layout

Definition 1. *For the purposes of VTOL rotorcraft the motor-rotor combination is termed the effector.*

The number of p-rotor vehicles has increased greatly over the last few years, both in the hobbyist/toy market, and in the commercial market as a platform for cameras and other sensors. Many research projects are either utilising proprietary models or 'off-the-shelf' solutions such as the Quanser Qball-X4 [qba] and Draganflyer X4-P [X4-P]. The materials used to build these robots include metal, plastic, wood, and carbon fibre. Most of the current generation of quadrotors are small (typically under 3kg with a payload capacity of under 1kg) but there are a number of larger models. Indeed, the first recorded quadrotor [Leishman, 2002] had a diameter of 8.1m, and the AeroVelo human powered quadrotor won the Igor I. Sikorsky Human Powered Helicopter Competition in 2013 with a diameter of 47m [Aer]!

The vehicle variety has similarly increased to include bicopters [Papachristos et al., 2011], trirotors [Salazar-Cruz and Lozano, 2005], hexarotors [Voyles and Jiang, 2012], octorotors [Marks et al., 2012, Alwi and Edwards, 2013a,b, Yamamoto et al., 2014], variations on these themes such as Y4 [Driessens and Pounds, 2013], coaxial octorotor [Raharja et al., 2011], tilt rotors [Ryll et al., 2012, Senkul and Altug, 2013, Elfeky et al., 2013] and hybrid VTOL capable flying wings [Guerrero et al., 2009, Sinha et al., 2012, Ferrell et al., 2013]. There are a number of advantages to be gained as the number of effectors is increased:

- The useful payload generally increases if the motors and rotors are similarly scaled, or
- the motors and rotors can be made smaller and have a lower inertia so that the control bandwidth is increased. This also reduces the chance of damage during a rotor strike, and

- there is inbuilt redundancy in case of effector failures.

1.2 Hardware Redundancy

This thesis concentrates on the advantage of the inbuilt hardware redundancy. This is required because the vehicle is underactuated. An effector failure in an octorotor does not impact in the controllability. However, when there are fewer effectors (such as a quadrotor) an effector failure means that control is lost on one or more degrees of freedom. When this occurs it might be impossible to hover or follow a flight path. The outcome of this is likely to be a loss of the vehicle which could damage the payload and also damage wherever it collides with the ground, endangering people in the process. Flights in close proximity to obstacles are realiseable because of the miniaturisation of sensors and flight controllers which allows for a small vehicle which are less noticeable to people and they can be used for surveillance in close proximity to targets where a larger platform (such as a manned helicopter) would cause disruption. The vehicle can also be used to survey structures that are in use by the general public without having to impose large exclusion zones [Metni and Hamel, 2007]. In such cases it is unacceptable to allow a single failure to cause a loss of control since the vehicle can be used to operate in close proximity to bystanders. This thesis shows that with inbuilt hardware redundancy it is possible to retain full control of all of the vehicle states even after a number of failures. It is hoped that this improvement in the safety of the vehicle which should ease restrictions on flight locations and allow for integration of VTOL UAVs into the commercial airspace. However, at the time of publishing this work, the UK CAA references a restriction that small UAVs (irrespective of their mass) that are being used for surveillance purposes are subject to tight restrictions with regards to minimum distances that they can be flown near people or proerties. The full text of this regulation can be found in Article 166 of the ANO 2009 [CAA].

Definition 2. *A fault is a partial loss of effectiveness (LOE) and a failure is a complete loss of effectiveness in an effector.*

1.3 Controller

The p-rotor vehicle is not open-loop stable and so a suitable control scheme is implemented. Many methods have been successfully implemented including PID control [Bouabdallah et al., 2004b, Salih et al., 2010, Raharja et al., 2011, Marks et al., 2012], backstepping [Bouabdallah and Siegwart, 2005, 2007, Bouchoucha et al., 2008b, Madani and Benallegue, 2006b, de Vries and Subbarao, 2010, Huang et al., 2010], integral backstepping [Bouabdallah and Siegwart, 2007, Bouchoucha et al., 2008a, Hoffmann et al., 2010, Tan et al., 2012], adaptive integral backstepping [Fang and Gao, 2011], H_∞ [Raffo et al., 2008, Araar and Aouf, 2014], and sliding mode control [Bouabdallah and Siegwart, 2005, Madani and Benallegue, 2006a, Waslander

et al., 2005, Xu and Ozguner, 2006]. In order to avoid chattering due to the inherent switching logic of sliding mode control the control input is adapted [Xu and Ozguner, 2006, Fang et al., 2008, Zhang et al., 2011, Diao et al., 2012, González et al., 2014] to smooth the discontinuous control law into a thin boundary layer next to the switching surface to achieve an optimal tradeoff between control bandwidth and tracking precision. Another approach is to use an integral sliding mode control scheme [Ramirez-Rodriguez et al., 2013].

The robustness to external disturbances and insensitivities to model errors and parametric uncertainties has allowed for passive fault tolerant control of quadrotors [Xu and Ozguner, 2006, Sharifi et al., 2010, Besnard et al., 2012, Runcharoon and Srichatrapimuk, 2013] and octorotors [Alwi and Edwards, 2013b]. When used for passive fault tolerant control it is possible to view effector faults as external disturbances.

1.4 Reference Frames

The attitude control problem has attracted considerable research interest as it is applicable to many fields such as dynamic control of aircraft [Tayebi and McGilvray, 2004, 2006, Guerrero-Castellanos et al., 2007, Stingu and Lewis, 2009, Fresk and Nikolakopoulos, 2013], spacecraft [Wie and Barba, 1985, Joshi et al., 1995, Ma et al., 2014], missiles [Chatterji and Tahk, 1989, Yeh et al., 2001, 2004], underwater vehicles [Fjellstad and Fossen, 1994, Antonelli and Chiaverini, 1998], and robot manipulators [Yuan, 1988, Caccavale et al., 1999, Marins et al., 2001]. The simplest and most intuitive attitude representation involves the use of a body angle parameterisation as well as a rotation matrix so that angles in one reference frame are related to their corresponding angles in another reference frame [Wen and Kreutz, 1988]. For aerospace applications the Euler angles are commonly used [Diebel, 2006].

This representation could be considered ideal for non-aerobatic flight since it is easy to visualise and the controller can be easily designed. However there is a limitation on the Euler representation for large attitude manoeuvres due to gimbal lock. This occurs when two of the rotational senses of the vehicle become 'locked' to each other causing a trigonometric singularity and full attitude control is not attainable. Large attitude manoeuvres are often carried out by spacecraft and can be experienced by aircraft during aerobatic manoeuvres and so a different attitude representation is implemented.

The unit quaternion is used to remove the possibility of the singularity and provides for a global solution to the attitude control problem. However they have an ambiguity in representing an attitude as the three-sphere S^3 double covers SO(3) so each physical attitude has two representations and the controller designed to provide global asymptotic stability could command a large rotation for convergence to either of the two disconnected, antipodal points on S^3 [Chaturvedi et al., 2011, Lee, 2013]. This unwinding phenomenon can be eradicated by implementing a non-continuous control strategy [Bhat and Bernstein, 2000, Mayhew et al., 2011] or by

implementing an interim attitude representation [Song and Cai, 2012]. This introduces a unique solution in that the shortest rotation is chosen to achieve a desired attitude. Heuristic methods can be used to account for initial rotation rates as well as to avoid chattering about an equilibrium position [Mayhew et al., 2011]. The control used for this thesis is based on model independent PD control and is almost globally asymptotically stable due to its non-continuous design. Effector saturation is considered meaning that the virtual controls are bounded, ensuring that that control allocation is perfect when considering the attitude control only (i.e. ignoring the effects of gravity). The control is applied for position control of the octorotor and also demonstrates suitability to return the vehicle to a level hover even when initialised with an inverted attitude and after suffering effector failures.

1.5 Vehicle Layout

In this thesis an octorotor is chosen as the main test vehicle but many of the results can be generalised to p-rotor vehicles. The octorotor is chosen because it has a large number of effectors giving a suitable scale of redundancy (it can experience more than one failure) as well as being capable of lifting a large payload. Kalman controllability analysis is used to show that this vehicle remains controllable even after a number of effector failures. In general, the higher the number of effectors the more resilient the vehicle is to individual failures, i.e. it can still be controlled with a large number of individual effector failures. However, there is a hardware cost that must be considered and this is explained further in Section 3.2.

For this reason a payoff between the number of effectors and the expected failure scenarios must be considered, especially when carrying a sensitive or expensive payload. A greater number of effectors also requires a larger amount of power and this is limited by current battery technology.

As the number of effectors increases the possible ways in which these are placed on the vehicle also increases. For the octorotor the following layouts are commonly found:

- Effectors aligned vertically but stacked in pairs so as to resemble a quadrotor as in Figure 1.2.
- Four effectors aligned vertically to provide vertical lift and four effectors aligned horizontally to provide translational forces [Romero et al., 2007, 2009] - see figure 1.3.
- Effectors aligned vertically and equally spaced around the vehicle as in Figure 1.4.

Figure 1.2: 3D Robotics X8 [3dr]

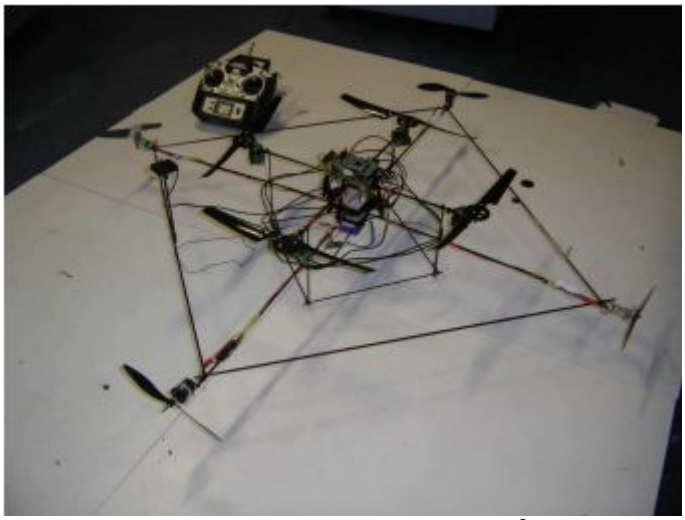

Figure 1.3: VTOL Aircraft with Eight Rotors [Romero et al., 2007]

The vehicle setup was chosen as in Figure 1.4 and shows axisymmetric properties which are exploited when tracking position demands. This means that the position of the vehicle can be changed without having to change the yaw angle (i.e. it is just as capable of flying forwards/backwards as flying sideways), a property which is utilised when pointing direction is important and when performing stall turns [Huang et al., 2009]. There is also less concern when hovering in a crosswind/tailwind than for a traditional helicopter since there is no tail rotor.

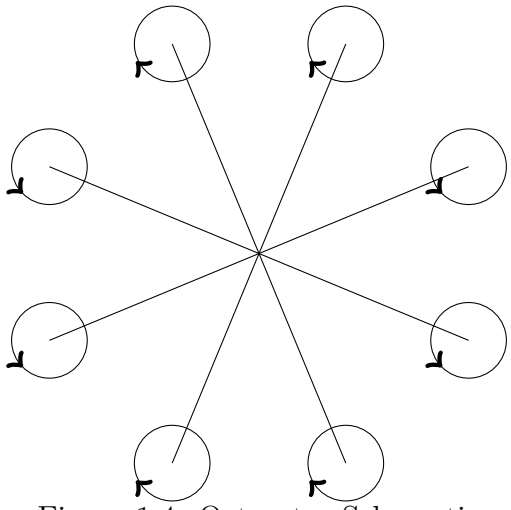

Figure 1.4: Octorotor Schematic

In this configuration the position of the vehicle and the yaw angle are the four state variables which are controlled. The velocity of the vehicle is coupled with the body attitude and this leads to a 'nested' controller where the outer loop controls the position and outputs body demands, and the inner loop controls the vehicle attitude to track the outputs of the outer loop. This controller design is analysed in Section 4.2. The reference demands are given by a reference signal, which can be generated by a pilot-in-the-loop or by a path planning algorithm.

1.6 Manoeuvre Methods[2]

There are three popular methods to change the direction of the thrust vector of a VTOL capable vehicle. The first (and mechanically simplest) way is to use fixed pitch propellers mounted to rigid arms. These are then spaced as desired around the vehicle. Each motor-rotor combination can produce thrust independently of the others (while keeping the direction of the thrust vectors aligned) and so the required combination of roll, pitch, and yaw moments can be allocated to the effectors with a suitable control allocation scheme. The thrust contribution of each effector is changed by varying the voltage to the motor which reduces or increases the rotational speed. By using a fixed pitch rotor blade the thrust can be considered to vary linearly with the motor speed. This mechanism for changing the thrust by changing the motor speed is contrasted to the method for a larger manned helicopter where the thrust is changed by changing the rotor blade pitch angle and keeping the motor speed constant. This requires a mechanically complex swashplate assembly. The swashplate is susceptible to wear-and-tear, especially when operating in dusty environments. It is used for large rotor blades due to the inertia properties of the blades and the limitations imposed by the natural frequencies in helicopter structures which would be excited by a variable-speed motor.

[2]The English spelling 'manoeuvre' is used throughout this thesis, but the American spelling 'maneuvre' is commonly found in the literature.

The fixed-pitch rotor method is applied to the octorotor as shown in Figure 1.5 where the relative thrusts of the effectors are represented by the thickness of the arrow showing the rotation of the motor with a thicker arrow representing a larger thrust value than a thin arrow.

- Level hover is achieved by allocating the thrust equally between all 8 effectors (Figure 1.5a).
- By increasing (decreasing) the four left side effectors and decreasing (increasing) the four right side effectors the vehicle will roll to the right (left) (Figure 1.5b).
- Similarly, increasing (decreasing) the four front effectors and decreasing (increasing) the four rear effectors will pitch the vehicle backwards (forwards) (Figure 1.5c).
- Yaw control is accomplished by increasing the speed of the counter-clockwise effectors and decreasing the speed of the clockwise effectors whilst ensuring that the total thrust remains constant. The imbalance in gyroscopic drag caused by the rotation of the rotors causes the vehicle to rotate about the z_b axis (Figure 1.5d).

Because the motors are rigidly fixed to the vehicle body the translational motion is coupled with the change of the vehicle attitude.

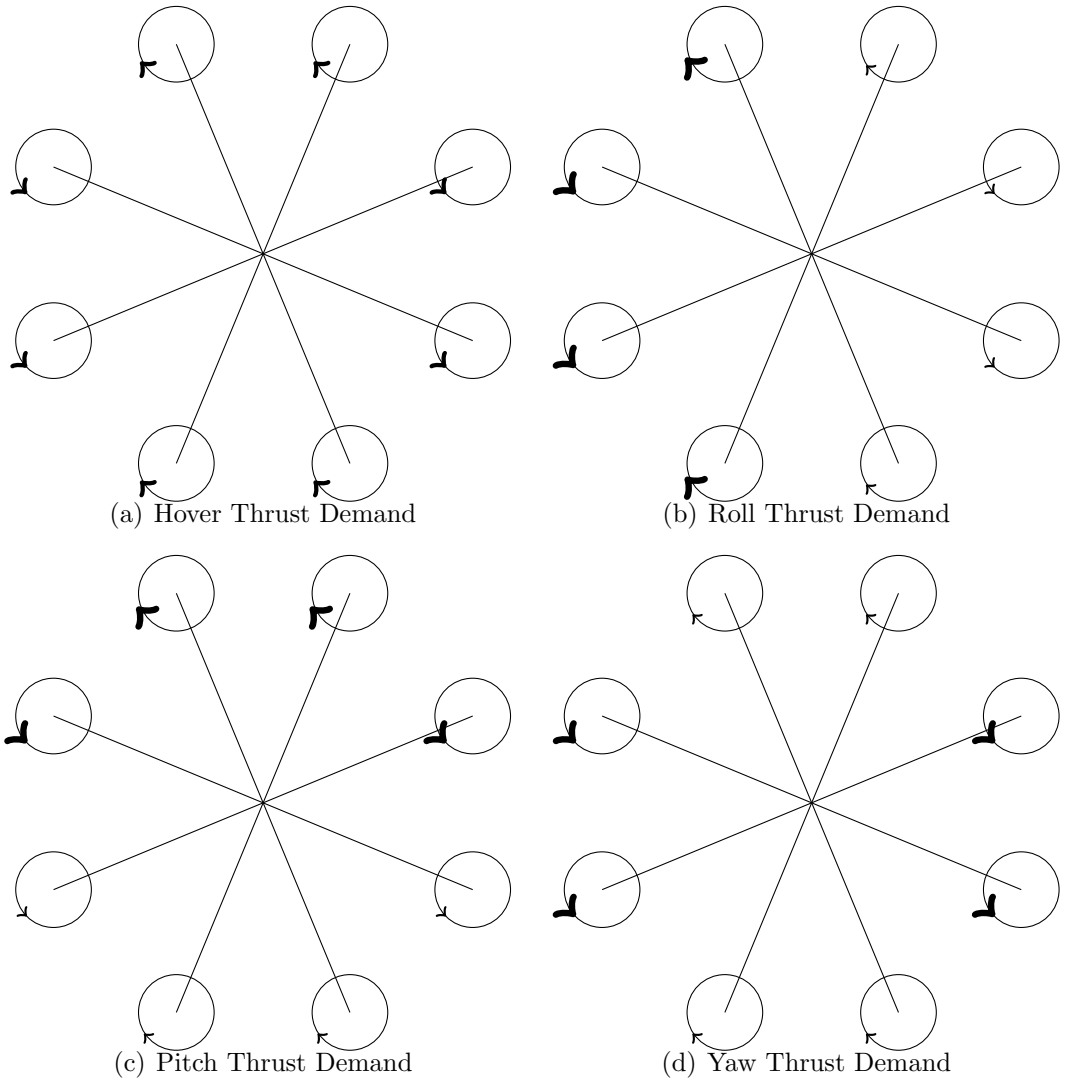

(a) Hover Thrust Demand (b) Roll Thrust Demand

(c) Pitch Thrust Demand (d) Yaw Thrust Demand

Figure 1.5: Thrust Demands

The second manoeuvre method involves using constant pitch rotors on movable mounts where the thrust of each motor-rotor combination can be individually controlled, and the direction of the thrust vector can be rotated independently. This increase in degrees of freedom allows for hover attitudes which are not accomplishable by a standard platform, since it is possible to control the position and orientation of the vehicle independently [Ryll et al., 2012]. By increasing the degrees of freedom of effector rotation so that they can be controlled in roll and pitch with respect to the airframe, the need to tilt the airframe for manoeuvring is eliminated. This has advantages when using sensors which are sensitive to their pointing direction [Senkul and Altug, 2013, Elfeky et al., 2013]. However this layout increases the mechanical complexity of the vehicle and so is generally reserved for marine applications where the large increase in manoeuvrability afforded by swivelling the thrusters is worth the potential mechanical complications [Spjtvold and Johansen, 2009, Shi et al., 2011]. A similar, but mechanically simpler effect can be achieved by separating the attitude and position effectors such as rigidly mounting some effectors vertically and

some horizontally [Romero et al., 2007, 2009] or by implementing moveable surfaces in the rotor wash in order to control the direction of the thrust vector [Cetinsoy, 2013]. This allows the vehicle to traverse like a blimp and allows translation without having to change attitude.

The third method is a hybrid of the first two where the motors are rigidly fixed to the vehicle body but it is possible to change the pitch of the rotor blades. The advantage of such a vehicle is that in general as the size of the vehicle increases the size and inertia of the rotors increases as well. The variable pitch rotors allow for an increase in the control bandwidth while at the same time providing for the ability to hover with an inverted attitude [Michini et al., 2011]. Further advantages include an optimisation of power consumption and an increase in maneouvrability at the expense of some mechanical complexity.

1.7 Control Allocation

1.7.1 Over-Actuated Systems

Effectors are used to generate forces and moments on a mechanical system. For an aircraft the effectors are generally broken into groups controlling the pitch (elevators, canards, thrust vectoring), the roll (ailerons, canards, all moving tailplane, thrust vectoring), and yaw angle (rudder, differential thrust, thrust vectoring). For the p-rotor vehicle each effector (or combination of effectors) can be used to provide thrust and roll, pitch, and yaw moments. By design it is possible that there are more effectors than needed to provide motion control. This can be for a number of reasons:

- There is effector redundancy so that control can be maintained after a failure.
- There is flexibility in choice of which effector or combination of effectors to use so that an optimal problem can be solved which minimises a secondary cost function such as energy, time, or radar cross section.
- Certain effectors can be shared by different control objectives such as a fully moving tailplane on an agile aircraft. In this instance the primary purpose of the tailplane is to provide pitch control by moving both halves equal amounts and in the same direction. However, if the surfaces deflect equal amounts in the opposite directions it can be used to augment roll control [Johansen and Fossen, 2013].

Of these, only the first is of concern for the control of the octorotor since the effectors are identical and spaced evenly around the vehicle body.

We consider the controller output $\tau \in \mathbb{R}^m$ and the effectors $\mathbf{u} \in \mathbb{R}^p$. The control effectiveness matrix is the linear mapping $B : \mathbb{R}^p \to \mathbb{R}^m$. For the overactuated

system such as the octorotor, $p > m$. If the control allocation is successful then the forces and moments generated by the effectors will be equal to the overall forces and moments demanded by the controller.

Note that the over-actuated control allocation problem can be viewed as the dual of the sensor fusion problem where there are more sensors than measurements.

1.7.2 Linear Control Allocation

Consider the linear state space model

$$\dot{\mathbf{x}} = A\mathbf{x} + \hat{B}\mathbf{u} \tag{1.1}$$
$$\mathbf{y} = C\mathbf{x} \tag{1.2}$$

where $\mathbf{x}, \mathbf{u}$, and $\mathbf{y}$ are vectors. For a rotorcraft the state vector $\mathbf{x}$ may contain the GPS coordinates, altitude, heading, Euler angles, and air speed. The input vector $\mathbf{u}$ contains the square rotor speeds. The system including closed loop feedback control and control allocation is shown in Figure 1.6.

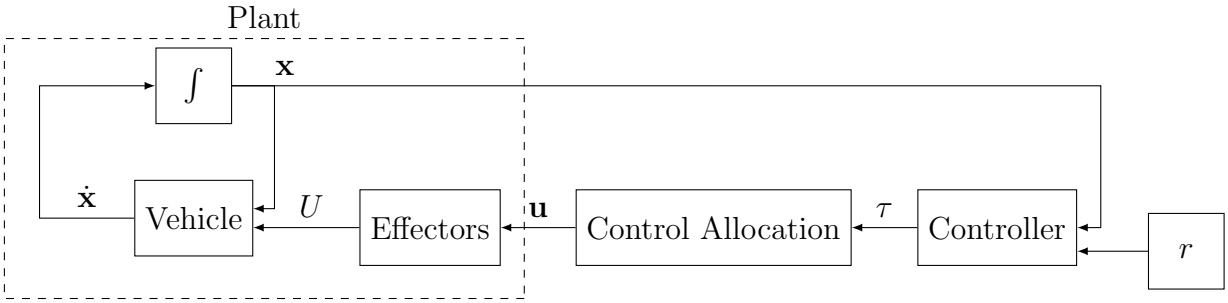

Figure 1.6: Closed Loop Feedback System

The controller output is τ. This is termed a 'virtual' control since this command is not sent directly to the effectors, rather it is passed to the control allocation subsystem where the forces and moments are allocated to the individual effectors. When considering the fault tolerant case the control allocation subsystem has fault diagnosis and active fault detection mechanisms. The effector outputs $\mathbf{u}$ are the squared rotor speeds that are mapped through the control allocation matrix to provide the inputs to the vehicle dynamics. The reference signal r can be generated by a pilot in the loop or via path planning software.

Definition 3. *Perfect allocation is the term used when the allocated forces and moments achieved from the effector outputs are equal to the virtual control, i.e.* $U = \tau$.

The control allocation problem is to map the virtual controls τ to the effector outputs $\mathbf{u}$ through the linear control effectiveness matrix B:

$$\tau = B\mathbf{u} \tag{1.3}$$

to give the allocated forces and moments, U. If perfect allocation is not achievable then the direction of τ is maintained whilst the magnitude is scaled so that the effector constraints are not exceeded.

Various methods are used to solve (1.3) for constrained and unconstrained sets of $\mathbf{u}$. When constrained the limits on $\mathbf{u}$ generally are of the form $\mathbf{u}_{\min} \leq \mathbf{u}_i \leq \mathbf{u}_{\max}$ with rate constraints $\dot{\mathbf{u}}_i \leq \dot{\mathbf{u}}_{\max}$. There may not be a feasible solution within the limits, and there is no guarantee that a found solution is unique. The problem of finding a vector $\mathbf{u}$ that is the "best" solution of (1.3) within the constraints is known as the control allocation problem [Bodson, 2002].

It is possible that B will depend on the system state and time-varying parameters or inputs. An example of this is the change in aerodynamic loading at various flight speeds and angles of attack. Interactions between the effectors (such as deploying an upstream control surface) can change the forces and moments produced by a downstream surface compared to when it is not deployed. It is possible to view the control allocation problem as a static problem and disregard how B can change with time, states, and inputs [Johansen and Fossen, 2013]. The matrix is updated at each time step and so does not exclude time-varying, parameter-varying, and linearized models.

1.7.3 Explicit Ganging

The main challenge of inverting the control allocation matrix in (1.3) is that B is not necessarily a square matrix. Indeed, when the matrix B is square and invertible (the number of effectors equals the number of controlled variables and the mapping is $B : \mathbb{R}^m \to \mathbb{R}^m$) a matrix inverse is performed to find $\mathbf{u}$ such that

$$\mathbf{u} = B^{-1}\tau \tag{1.4}$$

For the over-actuated system B is not square. An explicit ganging method can be used where effectors are combined in order to reduce the effective control devices. The goal is to find a matrix $G \in \mathbb{R}^{p\times m}$ where $m \leq p$ that relates a set of pseudo controls $\mathbf{u}_{\text{pseudo}} \in \mathbb{R}^m$ to the actual controls $\mathbf{u} \in \mathbb{R}^p$ such that

$$\mathbf{u} = G\mathbf{u}_{\text{pseudo}} \tag{1.5}$$

This method does not take effector saturation into account and so is not utilised for the octorotor.

1.7.4 Pseudo Inverse

The pseudo inverse method is an optimisation technique that requires a pseudo inverse of the (generally) non-square B matrix. It is the minimum 2-norm solution

to the control allocation problem and can be formulated as follows [Oppenheimer et al., 2006]:

$$\min_{\mathbf{u}} J = \min_{\mathbf{u}} \frac{1}{2}(\mathbf{u}+c)^T W(\mathbf{u}+c) \tag{1.6}$$

subject to $\tau = B\mathbf{u}$ where $W \in \mathbb{R}^{p\times p}$ is a weighting matrix and $c \in \mathbb{R}^p$ is an offset vector used to represent an off-nominal condition with one of more effectors. Forming the Hamiltonian and taking partial derivatives and setting them to zero yields the result [Oppenheimer et al., 2006]

$$\mathbf{u} = -c + W^{-1}B^T(BW^{-1}B^T)^{-1}[\tau + Bc] = -c + B^{\#}[\tau + Bc] \tag{1.7}$$

where $B^{\#}$ is the weighted pseudo inverse of B. It should be noted that if an effector is offset (locked and unable to move) two items must be taken into account, position offset $(-c)$ and the moments generated by the offset (Bc). For the position offset, the negative of the locked position is placed in the corresponding entry of the c vector. For a fixed wing aircraft example consider that there are four controls and that the third control effector is locked at 5 degrees due to a failure. Then $c = [0\ 0\ -5\ 0]^T$. This is exploited further for the constrained control allocation method utilising a cascade generalised inverse. For the VTOL vehicle considered in this thesis the considered case is a failure of the effector and so this generates no practical disturbing moment. The failed effector is therefore removed from the control allocation matrix and no adverse input compensation is required.

The weighting matrix W can be selected to incorporate the position limits of the control effectors. For example, a diagonal element of W can be selected to be a function of the corresponding component of $\mathbf{u}$ so that the weighting function approaches infinity as the control approaches a physical limit. An example of this approach is

$$W \propto \frac{\mathbf{u}_{\max} - \mathbf{u}}{\mathbf{u}_{\max}} \tag{1.8}$$

As $\mathbf{u} \to \mathbf{u}_{\max}$, $W \to 0$ and the effector will no be used for the control allocation. There are no guarantees that commands to the control effectors will not exceed the position limits; however, in practice the method is effective in constraining the positions of the controls [Oppenheimer et al., 2006]. This method can be useful in generating preference vectors for more complex optimisation based methods for the purpose of robustness analysis. For the special case $W = I$, there are no effector offsets $(c = 0)$, the solution to (1.7) $\mathbf{u} = B^{\dagger}\tau$ is defined by the Moore-Penrose pseudo inverse.

1.7.5 Redistributed Pseudo Inverse

The redistributed pseudo inverse method is used when considering constrained control allocation. In constrained control allocation the goal is to find $\mathbf{u}$ such that $\tau = B\mathbf{u}$ subject to $\mathbf{u}_{\min} \le \mathbf{u}_i \le \mathbf{u}_{\max}, |\dot{\mathbf{u}}_i| \le \dot{\mathbf{u}}_{\max}$.

The redistributed pseudo inverse method accounts for these saturations by first solving for the unconstrained problem. If the solution satisfies the constraints then

no further steps are needed. However, if the solution does not satisfy the constraints then the effectors exceeding the constraints are set to the constraint value and their input to the overall forces and moments is removed from the desired forces and moments and the control allocation is performed again. This continues until either

- a feasible solution is found, or
- no feasible solution exists.

Numerous control allocation algorithms have been developed for both the unconstrained and the constrained sets of $\mathbf{u}$ and survey papers have been written that point out the strengths and weaknesses of the approaches [Durham, 1993, Enns, 1998, Bodson, 2002, Fossen and Johansen, 2006, Johansen and Fossen, 2013]. Most of the algorithms assume that the forces and moments are linearly related to the effector outputs. This assumption is generally true for p-rotor VTOL vehicles and is applicable locally to aircraft except when considering a control surface's non-linear force contribution (such as adverse yaw generated by parasitic drag). Research has focused on linearising the control effectiveness matrix so that a mix of linear and non-linear controls can be implemented with the same control allocation scheme [Bolender and Doman, 2004, Johansen, 2004, Bolender and Doman, 2005].

1.7.6 Applying Constraints in the Controller

It is possible to constrain the controller demands so that τ is always feasible and the allocation problem is the unconstrained allocation problem [Durham, 1994, de Lamberterie et al., 2011]. For this method, the controller is informed about the effector limits and failure values. To constrain τ, a set $\mathcal{A}$ is constructed such that

$$\mathbf{u} \in \mathcal{F} \Leftrightarrow \tau \in \mathcal{A} \tag{1.9}$$

where the set $\mathcal{F}$ is defined by the constraints on the effectors.

$$\mathcal{F} \subset \mathbb{R}^p \Leftrightarrow \mathcal{A} \subset \mathbb{R}^m \tag{1.10}$$

From (1.9)

$$\mathbf{u} \subset \mathbb{R}^p, \quad \tau \subset \mathbb{R}^m \tag{1.11}$$

Firstly we compute the unconstrained control τ_u and then scale it if the allocated demands on the effectors lie outside the constrained set $\mathcal{F}$ so that it stays on the boundary of the set, i.e.

$$\tau = \begin{cases} \tau_u & \text{if } B^\dagger \mathbf{u} \in \mathcal{F} \\ \lambda \tau_u & \text{if } B^\dagger \mathbf{u} \notin \mathcal{F} \end{cases} \tag{1.12}$$

where $\lambda < 1$ is determined such that

$$B^\dagger \lambda \tau_u \in \partial \mathcal{F} \tag{1.13}$$

where $\partial \mathcal{F}$ is the boundary of $\mathcal{F}$ and the direction of τ_u is preserved.

Definition 4. *Successful allocation is the term used when $\tau_c = \lambda\tau_u$, i.e. the allocated forces and moments are scaled from the virtual control input without rotation. The allocation is perfect when $\lambda = 1$.*

An algorithm is set such that

1. Compute the unconstrained control allocation and obtain τ_u.
2. Set $\lambda = 1$.
3. If $\tau_{u,i} > \mathcal{A}_i$ and $\mathcal{A}_i/\tau_{u,i} < \lambda$, then reset $\lambda = \mathcal{A}_i/\tau_{u,i}$. Repeat for all i of $\tau_{u,i}$.

Once the scaling factor λ is computed it is updated at every time sample period and the constrained control τ_c is implemented such that

$$\tau_c = \lambda\tau_u \tag{1.14}$$

In such a case the nominal performance will not be attained but the control allocation is guaranteed to be successful. This method can become complex when there are a large number of effectors and a novel method for performing this algorithm is introduced in Section 3.5.3.

1.8 Effector Faults

Simulations have shown that it is possible to control a quadrotor after an effector fault. A number of scenarios are presented ranging from 25% - 50% loss of effectiveness in one [Ranjbaran and Khorasani, 2010, Merheb et al., 2013], two [Rotondo et al., 2013], or all effectors [Sharifi et al., 2010, Sadeghzadeh et al., 2012, Yu et al., 2013]. The simulations show that the vehicle is controllable after the fault and until the effectors saturate the nominal performance is maintained - the fault scenario is comparable to a gain increase in the controller output to the faulty effector. For example, if the hover thrust required is 10N and all four effectors suffer a 50% loss of effectiveness, the controller output (τ) will be 20N which is achieved through an increase in the gains and the effectors (U) will output 10N providing hover thrust.

In practice it is not easy to conceive of a scenario in which an effector will become faulty and not fail. The most likely failure scenario is after contact with an obstacle and this would likely lead to rotor separation from the motor spindle. It is possible that a partial fracture leaves a portion of the rotor still attached (thereby reducing the thrust available from the effector) but the vibration introduced with this scenario would make it difficult to process any IMU data. With redundant effectors it would be possible to selectively shut down faulty effectors so that they do not introduce disturbances to the vehicle dynamics, i.e. to deliberately turn the faults into failures and reconfigure the virtual controls to the functioning effectors.

Research focusing on effector failures in a quadrotor has shown through simulations that even though a degree of freedom in the controls is lost the vehicle maintains a steady yaw rate and is able to follow a path [Freddi et al., 2011, Akhtar et al., 2013, Lanzon et al., 2014]. The rotational rate will depend on the thrust demand and the subsequent adverse yaw generated by the functional effectors. Provided that the vehicle rotates sufficiently quickly it is possible to synchronise the yaw angle with the demands sent to the effector diametrically opposite the failure in order to provide roll and pitch control.

Figure 1.7 demonstrates the challenge of providing sufficient thrust after the failure. Figure 1.7a demonstrates that when all effectors are functional the control allocation divides the hover thrust equally. However, after a failure in an effector (Figure 1.7b) it is not possible to achieve the same linear hover state as before since an adverse yaw is generated by allocating the controls to the counter-clockwise rotating motors.

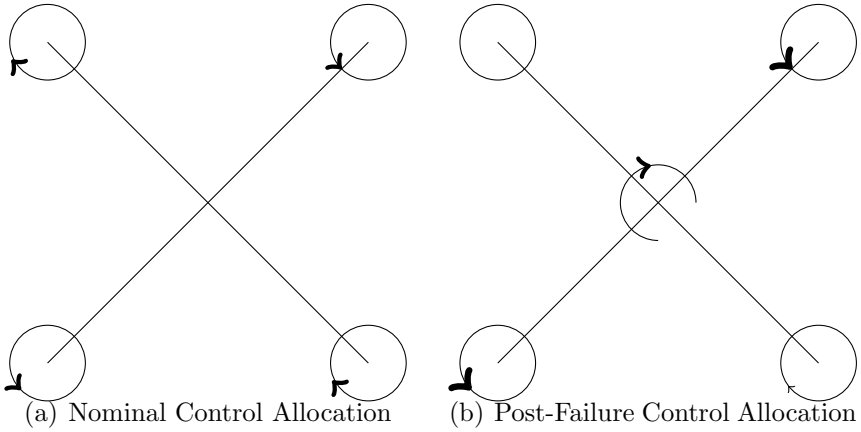

(a) Nominal Control Allocation (b) Post-Failure Control Allocation

Figure 1.7: Thrust Demands

Kalman controllability analysis shows that the vehicles are not controllable (which is expected since the control method relies on yaw rotation) and there are no successful flight testing results to support the theoretical results. It is worthwhile noting that the two papers providing vehicle details consider a vehicle with inertia terms that are either an order of magnitude higher, or an order of magnitude lower than provided for a commercial vehicle such an the Qball-X4. Table 1.1 gives the vehicle parameters from Akhtar et al. [2013] and Lanzon et al. [2014] and these are compared to the values obtained for the Qball-X4. Vehicle parameter data are not avilable from Freddi et al. [2011].

	Akhtar et al. [2013]	Lanzon et al. [2014]	Qball-X4
Mass [kg]	4.493	0.5	1.54
I_x	0.177	0.0059	0.03
I_y	0.177	0.0059	0.03
I_z	0.344	0.0016	0.04
l	0.1	0.255	0.2

Table 1.1: Quadrotor Parameters

It is not clear how such a small vehicle as suggested by Akhtar et al. [2013] is capable of producing sufficient hover thrust with its short arms since the rotors are effectively constrained by this dimension to avoid colliding with each other and the body centre. Their vehicle also has an exceptionally high mass. Moreover the residual yaw rate in Akhtar et al. [2013] is 15 rad/s, for Lanzon et al. [2014] it is 3 rad/s, whilst for Freddi et al. [2011] the residual yaw rate is between 0.1 and 0.15 rad/s suggesting that there is a large aerodynamic drag term that is introduced to retard the yaw rate. This research looks promising but to increase confidence that this method is suitable, it should be applied to using sufficiently representative vehicle parameters.

Studies using an octorotor [Adîr et al., 2011, Marks et al., 2012, Alwi and Edwards, 2013a] have shown resilience to multiple failures where controllability is maintained after failures and faults.

1.9 Fault Hiding

The concept of fault hiding makes it possible to keep the nominal controller in the reconfigured closed-loop system. This has the advantage that the controller needs to only be designed once and can be applied to the nominal and post-failure systems whilst the closed loop response of the vehicle remains the same. Furthermore, the operator does not need to be trained to counter every failure scenario. Finally, if the failure affects only a small subsystem in the plant it is not necessary to redesign the entire controller. Consider the faulty plant shown in Figure 1.8 which is part of a closed loop control system.

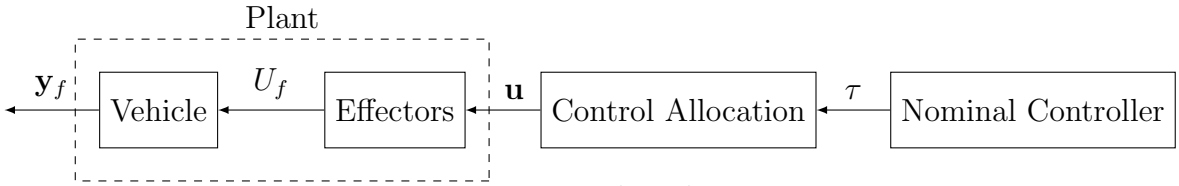

Figure 1.8: Faulty Plant

The fault hiding approach is to insert a reconfiguration block between the nominal controller and the faulty plant as shown in Figure 1.9 which is part of a closed loop feedback system. The control reconfiguration block performs the nominal control allocation as well as the re-allocation after a failure.

Definition 5. *For the fault hiding method the 'plant' contains the vehicle dynamics, effector model and the control allocation subsystem.*

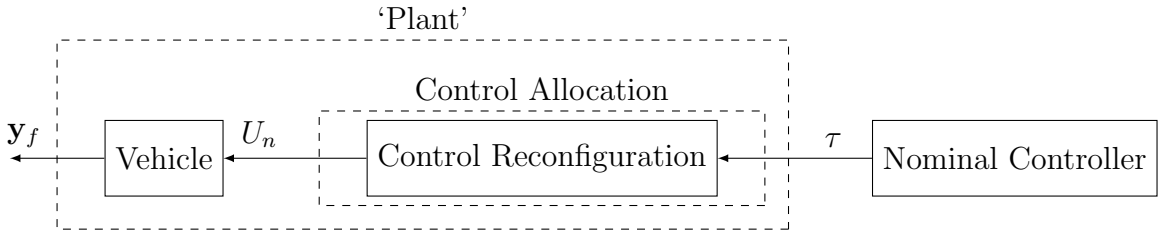

Figure 1.9: Fault Hiding Method

In this approach the virtual control τ is the same as for the nominal case and from the perspective of the controller the reconfiguration block is remodelling the plant to make it behave like the nominal case. If this is successfully performed within the new saturation limits (as set by the reconfiguration block which has a model of the effectors) then $\mathbf{y}_f = \mathbf{y}$ and the nominal performance is maintained. This is achieved by changing the control effectiveness matrix B to reflect the failed effector control effectiveness matrix B_f to reflect the post-failure vehicle. Fault hiding is considered to be successful if $\mathbf{y}_f = \mathbf{y}$ as shown in Figure 1.10. The method relies on an active fault detection system in order to determine B_f and throughout this thesis it is assumed that such a system which is sensitive to failures and does not produce false alarms is in place. This point is raised by Maciejowski [2008] who also criticises the supposition that the post-failure performance be the same as the nominal performance. It is the opinion of this author that by using a p-rotor vehicle with sufficient hardware redundancy the operator should not necessarily be aware that an effector failure has occurred and that nominal performance can realistically be maintained for the post-failure vehicle. This will allow for fully predictable flight charateristics and should mean that operator training is reduced.

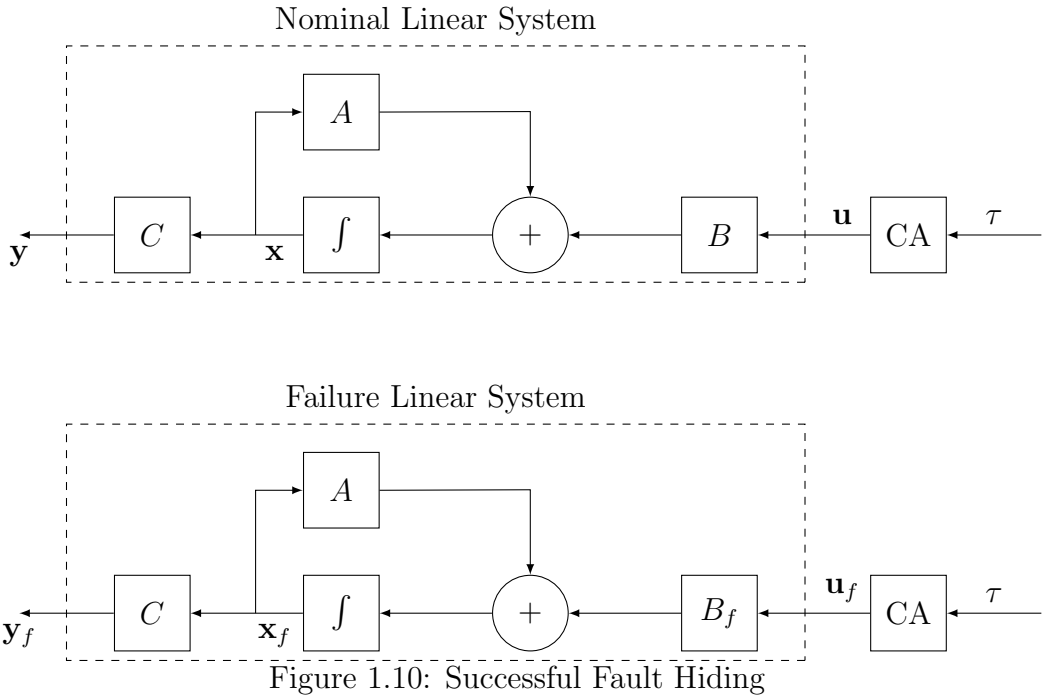

Figure 1.10: Successful Fault Hiding

1.10 Outline and Contributions

The work in this thesis makes the following contributions to knowledge:

- Construction of the linear effector model and the application to the octorotor. This allows for a number of control allocation schemes.
- Implementing the attainable force set based on the effectors instead of the set of the overall forces and moments. This means that the constraints are observed and the resultant thrust vector does not rotate.
- Simulation results demonstrate the quaternion attitude representation control is successful even for large initial perturbations away from hover. This controller accounts for gravity and generates a vertical force command to achieve altitude tracking. When the vehicle attitude is far from level hover the altitude tracking is sacrificed in order to reduce the amount of lateral position divergence.
- Simulation results are included showing the disturbance attributed to the delay in failure detection. The controls are reallocated to the functional effectors and the vehicle is returned to its initial position.
- Flight testing of an octorotor demonstrates the suitability of the control scheme to the real-world application.

1.11 Document Structure

The rest of this thesis contains a more in-depth analysis of the following topics

- Chapter 2
  - Derivation of the equations of motion. The effect of gimbal lock is explained and the quaternion attitude representation is introduced.
  - The general linear effector model is introduced as well as the control allocation matrix which is applied to the octorotor.
- Chapter 3
  - Linear control allocation is introduced and the difference between constrained and unconstrained allocation is discussed.
  - Two methods for constrained control allocation are compared for a number of scenarios where the virtual control is not attainable due to effector saturation. A suitable constrained allocation is implemented.
- Chapter 4

  - A quaternion-based position controller is developed.
  - Attitude saturation limits are imposed to prevent aerobatic virtual control demands and ensure that the controller is able to generate virtual controls to right an inverted initial attitude.

- Chapter 5
  - Results for 7 missions are given where the controller is tasked to attain step changes in inertial position from a number of initial attitudes.

- Chapter 6
  - The method for failure modelling is described.
  - Linear controllability analysis is performed for all combinations of failures.
  - The fault hiding concept is introduced which allows the controller to remain invariant and provide nominal performance after a failure.
  - Recovery after failures is demonstrated through simulation.

- Chapter 7
  - The flight test vehicle is described and flight test results are presented.

- Chapter 8
  - Concluding remarks include analysis of the contribution to knowledge as well as providing a framework for future work.

1.12 Publications

The following publications resulted from the work in this thesis.

- V.G.Adîr, A.M. Stoica, A. Marks, and J.F. Whidborne. 'Modelling, Stabilization, and Single Motor Failure Recovery of a 4Y Octorotor'. In Proc. 13th IASTED International Conference on Intelligent Systems and Control (ISC 2011), pp 82-87, Cambridge, U.K. July 2011

- A. Marks, J.F. Whidborne, and I. Yamamoto. 'Fault Tolerant Control of a VTOL Octorotor UAV using Control Allocation'. In UKACC International Conference on Control 2012, Cardiff, U.K. September 2012

- I. Yamamoto, R. Zhu, J.F. Whidborne, A. Marks. 'Research and Design on a Control System for a Disk-Type Flying Robot with Multiple Rotors'. In UKACC International Conference on Control 2104, July 2014

Chapter 2

Attitude Representation

2.1 Introduction

This chapter outlines the dynamics of the octorotor and how the motion of the vehicle is described in related reference frames. The chapter starts by deriving the equations of motion using the Newton Euler method. At large angles of attack (such as when performing aerobatic manoeuvres) the Euler angles are undefined. This is termed gimbal lock. The unit quaternion attitude representation is implemented since it does not suffer gimbal lock, and provides a global solution to the attitude control problem. Finally, this chapter concludes with the linear effector model and applies it to derive the control allocation matrix for the octorotor.

2.2 Body Angles

The motion of the vehicle is defined in terms of its body-fixed axes set. This is defined as a right hand orthogonal set with the origin at the vehicle's centre of gravity (cg). The x-axis, x_b points forwards along the logitudinal axis of the vehicle frame. The y-axis y_b points to starboard. The axis z_b is positive downwards. Positive rotations around these axes are in common with the right hand convention.

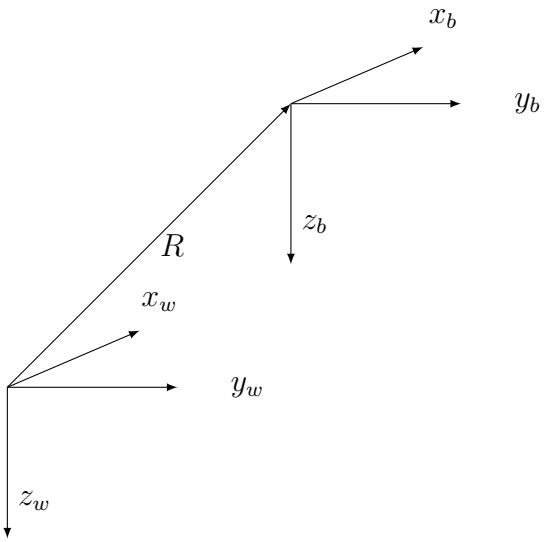

Figure 2.1: Rotation Matrix $R \to SO(3)$

2.3 Rotation Matrices

A rotation matrix desribes the orientation of one coordiante system with respect to another. A vector in one system can be transformed into the other system by multiplying it by the rotation matrix. The transformation in the reverse direction can be accomplished by using the inverse (or, since it is orthogonal, the transpose) of the rotation matrix as shown in (2.1)

$$\begin{aligned} \eta' &= R\eta \\ \eta &= R^T\eta \end{aligned} \tag{2.1}$$

where $\eta \in \mathbb{R}^3$ is a vector expressed in one coordinate system and $\eta' \in \mathbb{R}^3$ is the same vector expressed in the rotated frame.

Coordinate transformations of the x, y, and z axes (numbered 1,2,3) in a counter-clockwise direction when looking towards the origin give the matrices in $\mathbb{R}^3$ give $R_i : \mathbb{R} \to SO(3)$ for $i \in \{1, 2, 3\}$

$$R_1(\phi) = \begin{bmatrix} 1 & 0 & 0 \\ 0 & \cos\phi & \sin\phi \\ 0 & -\sin\phi & \cos\phi \end{bmatrix} \tag{2.2}$$

$$R_2(\theta) = \begin{bmatrix} \cos\theta & 0 & -\sin\theta \\ 0 & 1 & 0 \\ \sin\theta & 0 & \cos\theta \end{bmatrix} \tag{2.3}$$

$$R_3(\psi) = \begin{bmatrix} \cos\psi & \sin\psi & 0 \\ -\sin\psi & \cos\psi & 0 \\ 0 & 0 & 1 \end{bmatrix} \tag{2.4}$$

According to Euler's rotation theorem, any rotation may be described using three angles. If the rotations are written in terms of rotation matrices R_1, R_2, R_3 then a

rotation matrix R can be written as

$$R = R_1 R_2 R_3 \tag{2.5}$$

The order in which the individual rotation matrices are multiplied will affect the final rotation matrix R. There are three axes and the rotations can take place in any order provided that the same rotation is not performed twice in a row. This leaves the following 12 rotation orders [Diebel, 2006]

$$\begin{aligned}(i,j,k) \in \{ \quad & (1,2,1)\ (1,2,3)\ (1,3,1)\ (1,3,2)\ (2,1,2)\ (2,1,3) \\ & (2,3,1)\ (2,3,2)\ (3,1,2)\ (3,1,3)\ (3,2,1)\ (3,2,3)\}\end{aligned} \tag{2.6}$$

The most common rotation order choice for aerospace applications is (1,2,3). The angles associated with this rotation sequence are known as the Euler angles and are roll angle ϕ, pitch angle θ, and yaw angle ψ. The rotation matrix is

$$\begin{aligned}&R_{123}(\phi,\theta,\psi) = R_1(\phi)R_2(\theta)R_3(\psi) = \\ &\begin{bmatrix} \cos\theta\cos\psi & \cos\theta\sin\psi & -\sin\theta \\ \sin\phi\sin\theta\cos\psi - \cos\phi\sin\psi & \sin\phi\sin\theta\sin\psi + \cos\phi\cos\psi & \cos\theta\sin\phi \\ \cos\phi\sin\theta\cos\psi + \sin\phi\sin\psi & \cos\phi\sin\theta\sin\psi - \sin\phi\cos\psi & \cos\theta\cos\phi \end{bmatrix}\end{aligned} \tag{2.7}$$

This rotation matrix is used to convert between a body-fixed coordinate system with x_b, y_b, z_b axes originating at the centre of mass of the vehicle and an inertial coordinate system with conventional North-East-Down arrangement with the assumptions that

- the Earth is flat and stationary and
- the centre of gravity lies at the origin of the body axis frame.

The time derivative of this Euler angle vector is the vector of Euler angle rates [Diebel, 2006]. This matrix is used to relate the Euler angle rates and the angular velocity of the body. If the Euler angle rates matrix is multiplied with the vector of Euler angle rates it gives the angular velocity in the global coordinates. Consider $\hat{e}_i$ the ith unit vector used for the function that maps an Euler angle vector to its corresponding Euler angle rates matrix $E : \mathbb{R}^3 \to \mathbb{R}^{3\times3}$ is

$$E_{ijk}(\phi,\theta,\psi) := [R_k(\psi)^T R_j(\theta)^T \hat{e}_i,\ R_k(\psi)^T \hat{e}_j,\ \hat{e}_k] \tag{2.8}$$

whose conjugate matrix function $E' : \mathbb{R}^3 \to \mathbb{R}^{3\times3}$ is

$$E'_{ijk}(\phi,\theta,\psi) := [\hat{e}_i,\ R_i(\phi)\hat{e}_j,\ R_i(\phi)R_j(\theta)\hat{e}_k] \tag{2.9}$$

Using the notation

$$k := [\phi\ \theta\ \psi]^T \tag{2.10}$$

to represent the Euler angle vector and the same notation as (2.1) gives

$$\begin{aligned}\omega &= E_{ijk}(k)(\dot{k}) \\ \omega' &= E'_{ijk}(k)(\dot{k})\end{aligned} \tag{2.11}$$

The angular velocity in the body fixed coordinates can be related to the angular velocity in the inertial frame by

$$\begin{aligned} \omega' &= R_{ijk}(k)\omega \\ \omega &= R_{ijk}(k)^T\omega' \end{aligned} \tag{2.12}$$

2.4 Dynamic Modelling

2.4.1 Assumptions

A number of assumptions are used when modelling a p-rotor vehicle when deriving the equations for the control system design:

- the structure is rigid,
- the propellers are rigid,
- the centre of gravity lies at the origin of the body axis reference frame,
- the Earth is flat and stationary,
- the thrust and drag are proportional to the square of the speed of the rotor (for a constant pitch rotor blade),
- the rotor axes are parallel and lie in the z_b direction,
- ground effect is neglected,
- the inertia matrix is diagonal,
- the rotor Coriolis force and wind forces are not included,
- and the motor inertia is small therefore motor lag is ignored.

Equations of Motion - Newton Euler Method

The dynamics of small VTOL UAVs are well developed. Here, the Newton-Euler approach is used [Bouabdallah et al., 2004a, Mian and Daobo, 2008, Yali et al., 2010]. The state variables used in this analysis are:

$$X = [u\ v\ w\ P\ Q\ R\ x_w\ y_w\ z_w\ \phi\ \theta\ \psi]^T \tag{2.13}$$

where u, v, w are the body-centric velocities of the vehicle, P, Q, R are the rotation rates, x_w, y_w, z_w describe the position of the vehicle in the inertial frame and ϕ, θ, ψ

are the Euler angles. The total forces and moments in the body axis are given by

$$F_{net} = \frac{d}{dt}\left[m\mathbf{V}\right] + \omega' \times \left[m\mathbf{V}\right] \tag{2.14}$$

$$M_{net} = \frac{d}{dt}\left[J\omega'\right] + \omega' \times \left[J\omega'\right] \tag{2.15}$$

where $\mathbf{V}$ is the vector of linear velocities, ω' is the vector of angular velocities, J is the inertia matrix and m is the mass of the vehicle. The gravitational force F_g is

$$F_g = m\ R \begin{bmatrix} 0 \\ 0 \\ g \end{bmatrix} = mg \begin{bmatrix} -\sin\theta \\ \cos\theta\sin\phi \\ \cos\theta\cos\phi \end{bmatrix} \tag{2.16}$$

where g is the acceleration due to gravity. The total force F_{net} is the force of gravity and the forces generated through the rotors, F_p,

$$F_{net} = F_g + F_p, \tag{2.17}$$

which from (2.14) gives

$$\begin{bmatrix} \dot{u} \\ \dot{v} \\ \dot{w} \end{bmatrix} = -\frac{1}{m} \begin{bmatrix} F_{px} \\ F_{py} \\ F_{pz} \end{bmatrix} + g \begin{bmatrix} -\sin\theta \\ \cos\theta\sin\phi \\ \cos\theta\cos\phi \end{bmatrix} - \begin{bmatrix} Qw - Rv \\ Ru - Pw \\ Pv - Qu \end{bmatrix} \tag{2.18}$$

The effectors are aligned vertically and so $F_{px} = F_{py} = 0$ and so from (2.16), (2.17)

$$F_{net} = m\ R \begin{bmatrix} 0 \\ 0 \\ g \end{bmatrix} + \begin{bmatrix} 0 \\ 0 \\ F_{pz} \end{bmatrix} = mg \begin{bmatrix} -\sin\theta \\ \cos\theta\sin\phi \\ \cos\theta\cos\phi \end{bmatrix} + \begin{bmatrix} 0 \\ 0 \\ F_{pz} \end{bmatrix} \tag{2.19}$$

with F_{pz} acting positively upwards.

From (2.15), the total moments M_{net} acting on the vehicle are

$$M_{net} = \begin{bmatrix} M_x \\ M_y \\ M_z \end{bmatrix} = \begin{bmatrix} J_x & 0 & 0 \\ 0 & J_y & 0 \\ 0 & 0 & J_z \end{bmatrix} \begin{bmatrix} \dot{P} \\ \dot{Q} \\ \dot{R} \end{bmatrix} + \begin{bmatrix} P \\ Q \\ R \end{bmatrix} \times \begin{bmatrix} J_x & 0 & 0 \\ 0 & J_y & 0 \\ 0 & 0 & J_z \end{bmatrix} \begin{bmatrix} P \\ Q \\ R \end{bmatrix} \tag{2.20}$$

Rearranging in terms of the state variable derivatives gives

$$\begin{bmatrix} \dot{P} \\ \dot{Q} \\ \dot{R} \end{bmatrix} = \begin{bmatrix} \frac{M_x}{J_x} \\ \frac{M_y}{J_y} \\ \frac{M_z}{J_z} \end{bmatrix} - \begin{bmatrix} \frac{J_z - J_y}{J_x} QR \\ \frac{J_x - J_z}{J_y} RP \\ \frac{J_y - J_x}{J_z} PQ \end{bmatrix} \tag{2.21}$$

The rotation matrix, R, from (2.7) is used to express the movement of the vehicle in the global axes once the body-centric velocities are known:

$$\begin{bmatrix} \dot{x} \\ \dot{y} \\ \dot{z} \end{bmatrix} = R^T \begin{bmatrix} u \\ v \\ w \end{bmatrix}$$

$$= \begin{bmatrix} c_\theta c_\psi & s_\phi s_\theta c_\psi - c_\phi s_\psi & c_\phi s_\theta c_\psi + s_\phi s_\psi \\ c_\theta s_\psi & s_\phi s_\theta s_\psi + c_\phi c_\psi & c_\phi s_\theta s_\psi - s_\phi c_\psi \\ -s_\theta & s_\phi c_\theta & c_\phi c_\theta \end{bmatrix} \begin{bmatrix} u \\ v \\ w \end{bmatrix} \tag{2.22}$$

The flight path is found by integrating (2.22). It contains the body-centric Euler angles and these are related to the global body angles through

$$\begin{bmatrix} P \\ Q \\ R \end{bmatrix} = \begin{bmatrix} 1 & 0 & -\sin\theta \\ 0 & \cos\phi & \sin\phi\cos\theta \\ 0 & -\sin\phi & \cos\theta\cos\phi \end{bmatrix} \begin{bmatrix} \dot{\phi} \\ \dot{\theta} \\ \dot{\psi} \end{bmatrix}$$
$$= E'_{123} \begin{bmatrix} \dot{\phi} \\ \dot{\theta} \\ \dot{\psi} \end{bmatrix} \tag{2.23}$$

giving

$$\begin{bmatrix} \dot{\phi} \\ \dot{\theta} \\ \dot{\psi} \end{bmatrix} = {E'_{123}}^{-1} \begin{bmatrix} P \\ Q \\ R \end{bmatrix} \tag{2.24}$$

where

$${E'_{123}}^{-1} = \frac{1}{\cos\theta} \begin{bmatrix} \cos\theta & \sin\phi\sin\theta & \cos\phi\sin\theta \\ 0 & \cos\phi\cos\theta & -\sin\phi\cos\theta \\ 0 & \sin\phi & \cos\phi \end{bmatrix} \tag{2.25}$$

2.5 State Space Model

The general state space model $\dot{X} = f(X, \tau)$ is obtained from (2.18), (2.21), (2.22), (2.24) and (1.3) with state variables given by (2.13) and control given by

$$\tau = \begin{bmatrix} F_{pz} \\ M_p \end{bmatrix} \tag{2.26}$$

where $M_p = M_{net}$. This gives the state equation

$$\frac{d}{dt} \begin{bmatrix} u \\ v \\ w \\ P \\ Q \\ R \\ x_w \\ y_w \\ z_w \\ \phi \\ \theta \\ \psi \end{bmatrix} = \begin{bmatrix} -g\ s_\theta - (Qw - Rv) \\ g\ c_\theta s_\phi - (Ru - Pw) \\ \left(\frac{-F_{pz}}{m}\right) + g c_\theta c_\phi - (Pv - Qu) \\ \frac{M_x}{J_x} - \left(\frac{J_z - J_y}{J_x}\right) QR \\ \frac{M_y}{J_y} - \left(\frac{J_x - J_z}{J_y}\right) RP \\ \frac{M_z}{J_z} - \left(\frac{J_y - J_x}{J_z}\right) PQ \\ (c_\psi c_\theta)u + (c_\psi s_\theta s_\phi - s_\psi c_\phi)v + (c_\psi s_\theta c_\phi + s_\psi s_\phi)w \\ (s_\psi c_\theta)u + (s_\psi s_\theta s_\phi + c_\psi c_\phi)v + (s_\psi s_\theta c_\phi - c_\psi s_\phi)w \\ -s_\theta u + (c_\theta s_\phi)v + (c_\theta c_\phi)w \\ P + (t_\theta s_\phi)Q + (t_\theta c_\phi)R \\ c_\phi Q - s_\phi R \\ \left(\frac{s_\phi}{c_\theta}\right) Q + \left(\frac{c_\phi}{c_\theta}\right) R \end{bmatrix} \tag{2.27}$$

2.6 General Linear Effector Model

For a p-rotor VTOL aircraft, for each rotor $i \in 0, 1, \ldots, p-1$ let $b_i : \mathbb{R} \to \mathbb{R}$ represent the mapping from the independent effector control inputs σ_i to the effector vertical thrust F_{iz} and let $d_i : \mathbb{R} \to \mathbb{R}$ represent the mapping from the effector control inputs to the effector vertical torque M_{iz}. Consider the planar p-rotor system configuration shown in Figure 2.2.

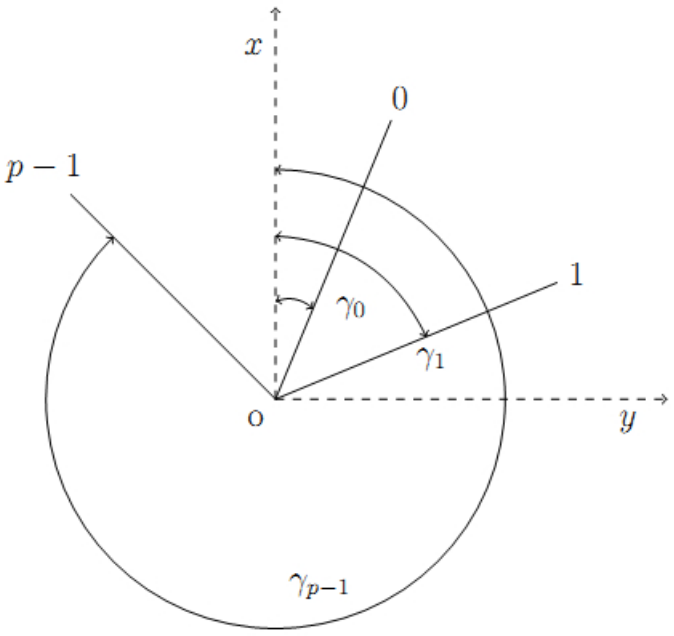

Figure 2.2: General Quad-Plus Vehicle

The rotor axes are assumed to be parallel and aligned with the z-axis, the resulting total forces and moment components of τ can be given by

$$F_z = \sum_{i=0}^{p-1} F_{iz} = \sum_{i=0}^{p-1} b_i\ (\sigma_i) \tag{2.28}$$

$$M_x = \sum_{i=0}^{p-1} M_{ix} = -\frac{1}{I_x} \sum_{i=0}^{p-1} l_i b_i(\sigma_i) \sin\gamma_i \tag{2.29}$$

$$M_y = \sum_{i=0}^{p-1} M_{iy} = \frac{1}{I_y} \sum_{i=0}^{p-1} l_i b_i(\sigma_i) \cos\gamma_i \tag{2.30}$$

$$M_z = \sum_{i=0}^{p-1} M_{iz} = \frac{1}{I_z} \sum_{i=0}^{p-1} d_i(\sigma_i) \tag{2.31}$$

Assuming that the mappings b_i and d_i are linear (this is a reasonable assumption if the independent control signals are taken to be the rotor rotation speed squared $\sigma_i = \Omega|\Omega|$), then

$$\tau = B\mathbf{u} \tag{2.32}$$

where $\tau \in \mathbb{R}^4$, $B \in \mathbb{R}^{4\times p}$, $\mathbf{u} \in \mathbb{R}^p$, and where

$$\tau = [F_z \quad M_x \quad M_y \quad M_z]^T, \tag{2.33}$$

$$B = \begin{bmatrix} b_0 & b_1 & \dots & b_{p-1} \\ -l_0 b_0 s_{\gamma_0} & -l_1 b_1 s_{\gamma_1} & \dots & -l_{p-1} b_{p-1} s_{\gamma_{p-1}} \\ l_0 b_0 c_{\gamma_0} & l_1 b_1 c_{\gamma_1} & \dots & l_{p-1} b_{p-1} c_{\gamma_{p-1}} \\ d_0 & d_1 & \dots & d_{p-1} \end{bmatrix}, \tag{2.34}$$

$$\mathbf{u} = [\sigma_0 \quad \sigma_1 \quad \dots \sigma_{p-1}]^T, \tag{2.35}$$

where the sign of d_i depends on the direction of rotor rotation, l_i is the length of the ith arm, γ_i is the angle subtended by the ith arm with the x-axis, and $s_{\gamma_i} = \sin\gamma_i$, $c_{\gamma_i} = \cos\gamma_i$.

2.6.1 Application to the Octorotor

A schematic for a 'cross' type octorotor is shown in Figure 2.3 with specifications shown in Table 2.1. The motor specifications are commonly found in literature (for example in Tayebi and McGilvray [2006]), and the other data were measured from the test vehicle. These parameters are used throughout this thesis.

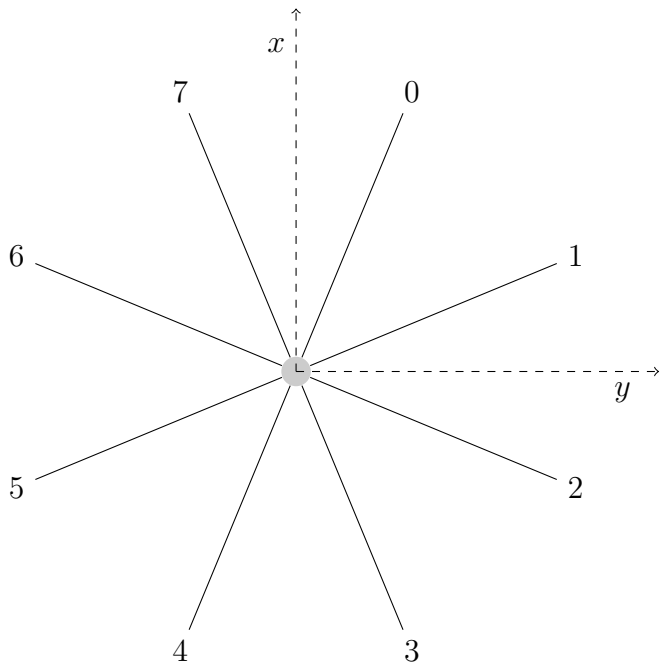

Figure 2.3: Octorotor Schematic

For this vehicle $l_i = l$, and the effectors are identical so $b_i = b$ and $d_i = d$. The control effectiveness matrix (2.34) becomes (2.36)

$$B = \begin{bmatrix} b & b & b & b & b & b & b & b \\ -bls_{\gamma_0} & -bls_{\gamma_1} & -bls_{\gamma_2} & -bls_{\gamma_3} & -bls_{\gamma_4} & -bls_{\gamma_5} & -bls_{\gamma_6} & -bls_{\gamma_7} \\ blc_{\gamma_0} & blc_{\gamma_1} & blc_{\gamma_2} & blc_{\gamma_3} & blc_{\gamma_4} & blc_{\gamma_5} & blc_{\gamma_6} & blc_{\gamma_7} \\ d & -d & -d & d & d & -d & -d & d \end{bmatrix} \tag{2.36}$$

Table 2.1: Octorotor Specifications

Thrust factor, b	3.13×10^{-5}
Drag factor, d	7.5×10^{-7}
Inertia J_x, J_y	7.5×10^{-3} kg m^2
Inertia J_z	1.3×10^{-2} kg m^2
Rotor inertia, $\hat{J}$	6×10^{-5} kg m^2
Arm length, l	0.4m
Mass	1.2kg
γ_n	$22.5° + 45° \times n$

where s_γ and c_γ are $\sin(\gamma)$ and $\cos(\gamma)$ respectively.

Another layout for the vehicle where the arms are aligned with the body axes as shown in Figure 2.4. The control effectiveness matrix is similarly constructed using (2.34) with different values of γ_i where $\gamma_n = 45° \times n$ giving the control effectiveness matrix (2.37).

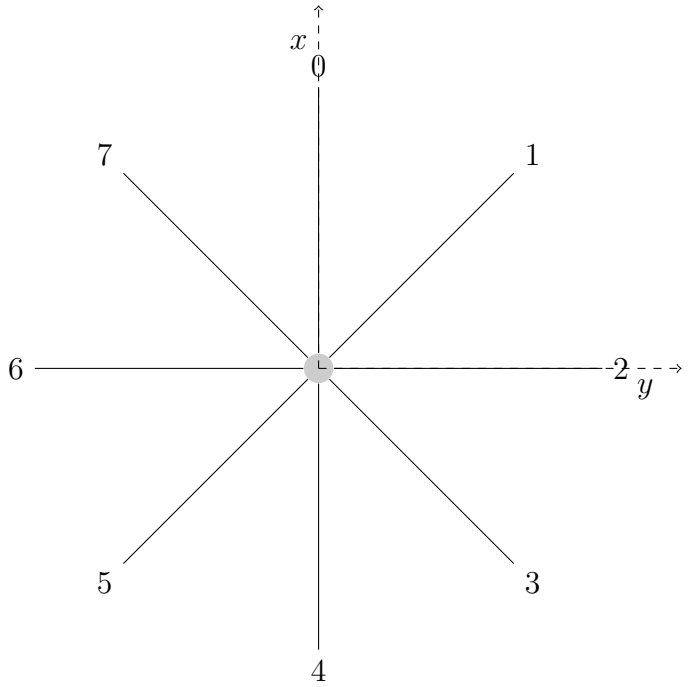

Figure 2.4: Octorotor Schematic, Aligned Configuration

$$B = \begin{bmatrix} b & b & b & b & b & b & b & b \\ 0 & -bls_{\gamma_1} & -bl & -bls_{\gamma_3} & 0 & -bls_{\gamma_5} & bl & -bls_{\gamma_7} \\ bl & blc_{\gamma_1} & 0 & blc_{\gamma_3} & -bl & blc_{\gamma_5} & 0 & blc_{\gamma_7} \\ d & -d & -d & d & d & -d & -d & d \end{bmatrix} \tag{2.37}$$

Note how due to the vehicle effector layout not all of the effectors are used for a single manoeuvre.

2.7 Linear Analysis

2.7.1 Linear State Space Model

The controllability of the octorotor is investigated using the well-known Kalman controllability test. The small perturbation linear model about hover is

$$\dot{\mathbf{x}} = A\mathbf{x} + \hat{B}\mathbf{u}, \quad t \in [t_0, \infty) \tag{2.38a}$$

$$\mathbf{y} = C\mathbf{x} \tag{2.38b}$$

where $\mathbf{x} \in \mathbb{R}^n$ is the state vector, $\mathbf{u} \in \mathbb{R}^p$ is the input vector, $A \in \mathbb{R}^{n\times n}$ is the state matrix, $\hat{B} \in \mathbb{R}^{n\times p}$ is the input matrix, $\mathbf{y} \in \mathbb{R}^n$ is the output vector, $C \in \mathbb{R}^{n\times n}$ is the output matrix, and t_0 is the initial time.

The octorotor vehicle dynamics given by (2.27) are linearized about the hover condition to obtain (2.38). The vehicle is trimmed at hover by setting $\dot{X} = 0$ and solving (2.27) giving $\tau_1 = \hat{\tau}_1 = mg$ and $\tau_i = 0$ for $i = 2, 3, 4$. A suitable allocation method is then applied to obtain the trimmed inputs, $\hat{\sigma}_i$ for the operational effectors. The hover condition is chosen since this is one of the major advantages of the VTOL-capable vehicle during surveillance missions. There is no need to maintain forward airspeed and targets may not be lost as could happen when flying 'racetrack' patterns in fixed wing aircraft. It should be noted that this analysis is equally valid for remotely operated underwater vehicles where the desired orientation of the vehicle is set by connecting ports and can be with a level attitude and no translational velocity. As the body angles are low the Euler angle attitude representation is suitable. The state matrix of (2.38) is given by

$$A = \begin{bmatrix} 0_{1\times6} & 0_{1\times3} & 0 & -\hat{\tau}_1 & 0 \\ 0_{1\times6} & 0_{1\times3} & \hat{\tau}_1 & 0 & 0 \\ 0_{1\times6} & 0_{1\times3} & 0 & 0 & 0 \\ 0_{3\times6} & 0_{3\times3} & 0_{3\times1} & 0_{3\times1} & 0_{3\times1} \\ I_{6\times6} & 0_{6\times3} & 0_{6\times1} & 0_{6\times1} & 0_{6\times1} \end{bmatrix} \tag{2.39}$$

For linear analysis of a general p rotor vehicle with control allocation matrix $B \in \mathbb{R}^{4\times p}$, the input matrix $\hat{B} \in \mathbb{R}^{12\times p}$ is

$$\hat{B} = \begin{bmatrix} 0_{2\times p} \\ B \\ 0_{6\times p} \end{bmatrix} \tag{2.40}$$

For the fully operational rotor set on the octorotor in Figure 2.3, the input matrix of (2.38) is given by

$$\hat{B} = \begin{bmatrix} 0_{2\times1} & 0_{2\times1} & 0_{2\times1} & 0_{2\times1} & 0_{2\times1} & 0_{2\times1} & 0_{2\times1} & 0_{2\times1} \\ b_1\hat{\sigma}_0 & b_1\hat{\sigma}_1 & b_1\hat{\sigma}_2 & b_1\hat{\sigma}_3 & b_1\hat{\sigma}_4 & b_1\hat{\sigma}_5 & b_1\hat{\sigma}_6 & b_1\hat{\sigma}_7 \\ -b_2\hat{\sigma}_0 & -b_2\hat{\sigma}_1 & -b_2\hat{\sigma}_2 & -b_2\hat{\sigma}_3 & -b_2\hat{\sigma}_4 & -b_2\hat{\sigma}_5 & -b_2\hat{\sigma}_6 & -b_2\hat{\sigma}_7 \\ b_3\hat{\sigma}_0 & b_3\hat{\sigma}_1 & b_3\hat{\sigma}_2 & b_3\hat{\sigma}_3 & b_3\hat{\sigma}_4 & b_3\hat{\sigma}_5 & b_3\hat{\sigma}_6 & b_3\hat{\sigma}_7 \\ b_4\hat{\sigma}_0 & -b_4\hat{\sigma}_1 & -b_4\hat{\sigma}_2 & b_4\hat{\sigma}_3 & b_4\hat{\sigma}_4 & -b_4\hat{\sigma}_5 & -b_4\hat{\sigma}_6 & b_4\hat{\sigma}_7 \\ 0_{6\times1} & 0_{6\times1} & 0_{6\times1} & 0_{6\times1} & 0_{6\times1} & 0_{6\times1} & 0_{6\times1} & 0_{6\times1} \end{bmatrix} \tag{2.41}$$

where $b_1 = b_i g/m$, $b_2 = l_i b_i \sin\gamma_i / I_x$, $b_3 = l_i b_i \cos\gamma_i / I_y$, $b_4 = d_i / I_z$

2.7.2 Kalman Controllability

The $n \times nm$ controllability matrix is

$$R = \begin{bmatrix} \hat{B} & A\hat{B} & A^2\hat{B} & \dots & A^{n-1}\hat{B} \end{bmatrix} \tag{2.42}$$

The system is controllable if and only if the controllability matrix has full rank, i.e. $\text{rank}(R) = n$. Using (2.39), (2.41) the Kalman controllability analysis is performed. The controllability matrix R (2.42) has full rank when the linearized model is linearized with a control input $\tau_1 > 0$. This represents a linearized point where the vehicle is not in free-fall.

2.8 Gimbal Lock

The R_{123} Euler angle parametrisation breaks down when $\theta = \frac{\pi}{2} + n\pi$ for $n \in \mathbb{Z}$ and therefore is only suitable to represent the attitude of a vehicle that does not perform highly aerobatic manoeuvres. When the Euler angles are close to 90° (for example, during aerobatic flight) $\cos\theta \approx 0, \sin\theta \approx 1$ and the rotation matrix becomes

$$\begin{aligned} R_{123}(\phi, \frac{\pi}{2}, \psi) &= R_1(\phi) R_2(\frac{\pi}{2}) R_3(\psi) \\ &= \begin{bmatrix} 1 & 0 & 0 \\ 0 & \cos\phi & \sin\phi \\ 0 & -\sin\phi & \cos\phi \end{bmatrix} \begin{bmatrix} 0 & 0 & -1 \\ 0 & 1 & 0 \\ 1 & 0 & 0 \end{bmatrix} \begin{bmatrix} \cos\psi & \sin\psi & 0 \\ -\sin\psi & \cos\psi & 0 \\ 0 & 0 & 1 \end{bmatrix} \\ &= \begin{bmatrix} 0 & 0 & -1 \\ \sin\phi\cos\psi - \cos\phi\sin\psi & \sin\phi\sin\psi + \cos\phi\cos\psi & 0 \\ \cos\phi\cos\psi + \sin\phi\sin\psi & \cos\phi\sin\psi - \sin\phi\cos\psi & 0 \end{bmatrix} \end{aligned} \tag{2.43}$$

Changing the values of ϕ or ψ in (2.43) changes the rotation angle, but the axis remains in the z direction (the last column of (2.43) remains the same). This is shown in Figures 2.5 and 2.6. The three gimbals are roll (green), pitch (blue), and yaw (red).

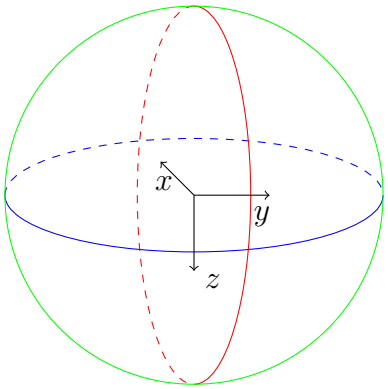

Figure 2.5: Gimbal System

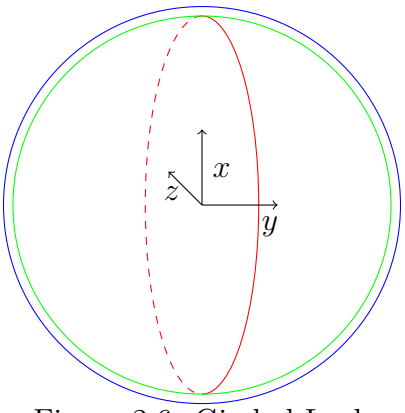

Figure 2.6: Gimbal Lock

It can be seen from Figure 2.6 that when the pitch gimbal (blue) angle reaches 90 degrees the yaw (red) and roll (green) apply the same rotation to the vehicle. This is because of the order of the rotations as specified in (2.7). The rotation about x_b is independant, rotating about y_b moves the pitch gimbal as well as the roll gimbal, and rotation about z_b moves all three.

This is further seen in the mathematics of the rotation matrices describing the Euler angular rates where from (2.8) the relationship is

$$E_{123}(\phi,\theta,\psi) = \begin{bmatrix} \cos\theta\cos\psi & -\sin\psi & 0 \\ \cos\theta\sin\psi & \cos\psi & 0 \\ -\sin\theta & 0 & 1 \end{bmatrix} \tag{2.44}$$

The inverse of (2.44) is

$$E_{123}^{-1} = \frac{1}{\cos\theta}\begin{bmatrix} \cos\psi & \sin\psi & 0 \\ -\cos\theta\sin\psi & \cos\theta\cos\psi & 0 \\ \cos\psi\sin\theta & \sin\psi\sin\theta & \cos\theta \end{bmatrix} \tag{2.45}$$

and from the leading term it is clear that there is a singularity when $\theta = \frac{\pi}{2} + n\pi$ for $n \in \mathbb{Z}$.

One suggestion when encountering this singularity with the (1,2,3) representation might be to change to another rotation sequence from (2.6). Let us introduce the

rotation sequence (3,1,3) and define the R_{313} rotation matrix

$$R_{313}(\phi,\theta,\psi) = R_3(\phi)R_1(\theta)R_3(\psi) = \begin{bmatrix} \cos\phi\cos\psi - \sin\phi\cos\theta\sin\psi & \cos\phi\sin\psi + \sin\phi\cos\theta\cos\psi & \sin\phi\sin\theta \\ -\sin\phi\cos\psi - \cos\phi\cos\theta\sin\psi & -\sin\phi\sin\psi + \cos\phi\cos\theta\cos\psi & \cos\phi\sin\theta \\ \sin\theta\sin\psi & -\sin\theta\cos\psi & \cos\theta \end{bmatrix} \quad (2.46)$$

The Euler angle rates matrix as a function of the Euler angles is

$$E_{313}(\phi,\theta,\psi) = \begin{bmatrix} \sin\theta\sin\psi & \cos\psi & 0 \\ -\sin\theta\cos\psi & \sin\psi & 0 \\ \cos\theta & 0 & 1 \end{bmatrix} \quad (2.47)$$

The inverse of this matrix is

$$[E_{313}(\phi,\theta,\psi)]^{-1} = \frac{1}{\sin\theta}\begin{bmatrix} \sin\psi & -\cos\psi & 0 \\ \sin\theta\cos\psi & \sin\theta\sin\psi & 0 \\ -\sin\psi\cos\theta & \cos\psi\cos\theta & \sin\theta \end{bmatrix} \quad (2.48)$$

Now when $\theta = \frac{\pi}{2} + n\pi$ there is no singularity. However, there exists a singularity at $\theta = n\pi$ for $n \in \mathbb{Z}$. The strategy of changing the rotation matrix representation as a function of the Euler angles means that switching must take place in order to change between attitude representations and therefore the unit quaternion attitude representation is preferred.

2.9 Quaternion Attitude Representation

In order to avoid the singularities which can occur when using the Euler angle attitude description, it is possible to represent the attitude of a rigid body by a quaternion $\bar{q} \in \mathbb{H}$ where $\mathbb{H} = \left\{\bar{q} = [q_0\ q]^T,\ q_0 \in \mathbb{R},\ q \in \mathbb{R}^3\right\}$. $Here q = [q_1\ q_2\ q_3]^T$ and q_0 are the vector and scalar parts of the quaternions respectively.

The function that maps the Euler angles to their corresponding unit quaternion is [Diebel, 2006]:

$$\bar{q}(\phi,\theta,\psi) = \begin{bmatrix} \cos\frac{\phi}{2}\cos\frac{\theta}{2}\cos\frac{\psi}{2} + \sin\frac{\phi}{2}\sin\frac{\theta}{2}\sin\frac{\psi}{2} \\ -\cos\frac{\phi}{2}\sin\frac{\theta}{2}\sin\frac{\psi}{2} + \cos\frac{\theta}{2}\cos\frac{\psi}{2}\sin\frac{\phi}{2} \\ \cos\frac{\phi}{2}\cos\frac{\psi}{2}\sin\frac{\theta}{2} + \sin\frac{\phi}{2}\cos\frac{\theta}{2}\sin\frac{\psi}{2} \\ \cos\frac{\phi}{2}\cos\frac{\theta}{2}\sin\frac{\psi}{2} - \sin\frac{\phi}{2}\cos\frac{\psi}{2}\sin\frac{\theta}{2} \end{bmatrix} \quad (2.49)$$

The adjoint, norm and inverse of a quaternion are

$$\bar{q}^* = \begin{bmatrix} q_0 \\ -q \end{bmatrix} \quad (2.50)$$

$$||\bar{q}|| = \sqrt{q_0^2 + q^T q} \quad (2.51)$$

$$\bar{q}^{-1} = \frac{\bar{q}^*}{||\bar{q}||} \quad (2.52)$$

Quaternion multiplication is non-commutative. Quaternion multiplication between two quaternions $\bar{q}$ and $\bar{p}$ is defined by

$$\begin{aligned} \bar{q} \otimes \bar{p} &= \bar{q}_m(\bar{q}, \bar{p}) && (2.53) \\ &= \begin{bmatrix} q_0 p_0 - q^T p \\ q_0 p + p_0 q - q \times p \end{bmatrix} && (2.54) \\ &= \begin{bmatrix} q_0 & -q^T \\ q & q_0 I_3 + C(q) \end{bmatrix} \begin{bmatrix} p_0 \\ p \end{bmatrix} && (2.55) \end{aligned}$$

where I_3 is the identity matrix and the skew-symmetric cross product matrix function $C : \mathbb{R}^3 \to \mathbb{R}^{3\times3}$ is defined by

$$C(\mathbf{x}) = \begin{bmatrix} 0 & -x_3 & x_2 \\ x_3 & 0 & -x_1 \\ -x_2 & x_1 & 0 \end{bmatrix} \tag{2.56}$$

Quaternion multiplication may also be written as the second quaternion multiplied by a matrix-valued function of the first quaternion:

$$\bar{q} \otimes \bar{p} = \bar{q}_m(\bar{q}, \bar{p}) = Q(\bar{q})\bar{p} = Q^*(\bar{p})\bar{q} \tag{2.57}$$

where $Q : \mathbb{H} \to \mathbb{R}^{4\times4}$ is the quaternion matrix function and defined as

$$\begin{aligned} Q(\bar{q}) &= \begin{bmatrix} q_0 & -q^T \\ q & q_0 I_3 + C(q) \end{bmatrix} && (2.58) \\ &= \begin{bmatrix} q_0 & -q_1 & -q_2 & -q_3 \\ q_1 & q_0 & -q_3 & q_2 \\ q_2 & q_3 & q_0 & -q_1 \\ q_3 & -q_2 & q_1 & q_0 \end{bmatrix} && (2.59) \end{aligned}$$

The time derivative of the quaternion (quaternion rates) $\dot{\bar{q}}_\omega : \mathbb{H} \in \mathbb{R}^4 \to \mathbb{R}^4$ can be represented as

$$\dot{\bar{q}}_\omega(\bar{q}, \vec{\omega}) = \frac{1}{2}\bar{q} \otimes \begin{bmatrix} 0 \\ \vec{\omega} \end{bmatrix} = \frac{1}{2} Q(\bar{q}) \begin{bmatrix} 0 \\ \vec{\omega} \end{bmatrix} \tag{2.60}$$

where $\vec{\omega} = [\omega_x, \omega_y, \omega_z]^T \in \mathbb{R}^3$ is the angular velocity of the body with respect to an inertial frame.

The rotation of a vector by a quaternion involves the multiplication of a quaternion and the vector. We consider a vector v as a pure quaternion in which the scalar part is zero and vector part is v, i.e. $\bar{v} = [0\ v]^T$. From (2.54) the multiplication of a vector and a quaternion is defined as

$$\bar{q} \otimes v = [q_0\ q]^T \otimes [0\ v]^T = -q \cdot v + q_0 v + q \times v \tag{2.61}$$

The quaternion operator should provide us with another pure vector or a pure quaternion. Evaluation shows that neither $w = \bar{q} \otimes v$ nor $w = v \otimes \bar{q}$ is necessarily a pure vector. However, using (2.61) gives the rotation matrix relating the body fixed frame to the inertial frame [Guerrero-Castellanos et al., 2007, Yang, 2012].

$$H = [(q_0^2 - q^T q) I_3 + 2qq^T - 2q_0 C(q)] \tag{2.62}$$

2.9.1 Quaternion Equations of Motion - State Equation

The Newton Euler equations of motion describing the dynamic motion of the vehicle are given by

$$\begin{bmatrix} 0 \\ \ddot{r}_i \end{bmatrix} = \frac{1}{m}\bar{q} \otimes \begin{bmatrix} 0 \\ F_b \end{bmatrix} \otimes \bar{q} - \begin{bmatrix} 0 \\ g_i \end{bmatrix} \tag{2.63}$$

$$J\dot{\vec{\omega}} = -\vec{\omega} \times J\vec{\omega} + M \tag{2.64}$$

where $\ddot{r}_i \in \mathbb{R}^3$ is the acceleration of the origin of the body frame with respect to the inertial frame, m is the mass of the vehicle, $F_b \in \mathbb{R}^3$ is the total thrust expressed in the body frame, g_i is the vector of gravity acceleration, $J \in \mathbb{R}^{3\times3}$ is the symmetric positive definite constant inertia matrix of the rigid body expressed in the body frame, and $M \in \mathbb{R}^3$ is the vector of applied torques. The state variables used for this analysis are:

$$X = [x_w \ y_w \ z_w \ v_x \ v_y \ v_z \ q_0 \ q_1 \ q_2 \ q_3 \ \omega_x \ \omega_y \ \omega_z]^T \tag{2.65}$$

where x_w, y_w, z_w describe the position of the vehicle in the inertial frame, v_x, v_y, v_z are the inertial frame velocities of the vehicle, q_0, q_1, q_2, q_3 is the unit quaternion attitude representation of the vehicle, and $\omega_x, \omega_y, \omega_z$ are the rotation rates.

For a normalized quaternion satisfying $||\bar{q}(t)|| = 1$ for all (t) we have

$$q_0 = \sqrt{1 - q_1^2 - q_2^2 - q_3^2} \tag{2.66}$$

With reference to (2.60) the reduced kinematics equation becomes

$$\begin{bmatrix} \dot{q}_1 \\ \dot{q}_2 \\ \dot{q}_3 \end{bmatrix} = \frac{1}{2}\begin{bmatrix} q_0 & -q_3 & q_2 \\ q_3 & q_0 & -q_1 \\ -q_2 & q_1 & q_0 \end{bmatrix}\begin{bmatrix} \omega_x \\ \omega_y \\ \omega_z \end{bmatrix} \tag{2.67}$$

$$= \frac{1}{2}Q(q_1, q_2, q_3)\omega \tag{2.68}$$

$$= g(q_1, q_2, q_3, \omega) \tag{2.69}$$

For pure attitude tracking and ignoring the effects of gravity the Newton Euler equations of motion are simplified to

$$\dot{\bar{q}} = \frac{1}{2}Q(\bar{q})\begin{bmatrix} 0 \\ \vec{\omega} \end{bmatrix} \tag{2.70}$$

$$\dot{\vec{\omega}} = J^{-1}(M - \vec{\omega} \times J\vec{\omega}) \tag{2.71}$$

2.9.2 Conclusion

- This section has explained how reference frames are rotated so that vectors in one frame can be described as a vector in another. The equations of motion for the octorotor are derived using the well-developed Newton Euler method and the state model is given.

- The linear model of the octorotor is developed and linear analysis is performed using Kalman controllability criteria.
- The problem of gimbal lock is demonstrated and the alternative attitude representation of the unit quaternion is implemented to avoid the singularities.
- The control effectiveness matrix is constructed for the proposed octorotor platform.

Chapter 3

Control Allocation

3.1 Introduction

Control allocation is used to distribute the virtual controls (τ) among a redundant set of effectors. For flight control of a p-rotor vehicle the total control effort corresponds to the total lift and aerodynamic moments to be produced. A general block diagram of a system with control allocation is shown in Figure 3.1.

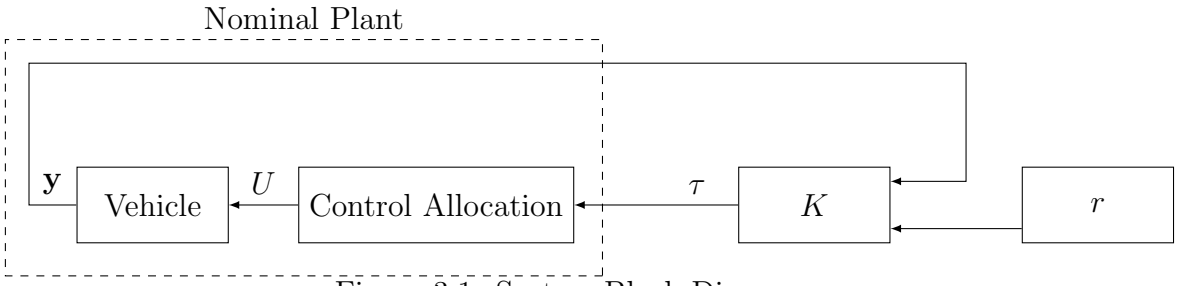

Figure 3.1: System Block Diagram

The control allocation is chosen to take place in the plant

$$\tau = B\mathbf{u} \tag{3.1}$$

With perfect control allocation

$$U = B\mathbf{u} \tag{3.2}$$

$$U = \tau \tag{3.3}$$

3.2 Reliability of a System

A common method to predict the reliability of a system is to use a "bottom-up" approach whereby the failure rate for each element is estimated and then combined for the entire assembly. A simple demonstration is shown in Figure 3.2.

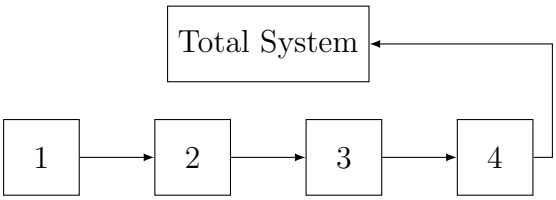

Figure 3.2: "Bottom-up" Serial System Reliability Block Diagram

Here the failure rate of the system is the sum of the individual failure rates of the subsystems 1, 2, 3, and 4. As these subsystems are in series, any failure in one subsystem results in the failure of the total system. Reliability predictions are generally made for steady-state operation and usually the exponential distribution is assumed. The reliability function for the exponential distribution

$$F(t) = e^{-\Lambda t} \tag{3.4}$$

is the probability of a component surviving to time t. For a system of p components, where any component failure causes a system failure, the probability of survival for the whole system is

$$F_{\text{system}} = F_1 F_2 F_3 \dots F_p \tag{3.5}$$

or

$$e^{-\Lambda_{\text{system}} t} = e^{\Lambda_1 t} e^{\Lambda_2 t} e^{\Lambda_3 t} \dots e^{\Lambda_p t} = e^{-(\Lambda_1 + \Lambda_2 + \Lambda_3 + \dots + \Lambda_p)t} \tag{3.6}$$

Example 1 Consider the case of a quadrotor with no effector failure redundancy. This can be modelled as in Figure 3.2 where the subsystems represent the propulsion group of each motor-rotor combination. The failure rates of all of the subsystems 1, 2, 3, and 4 are identical and for this example are arbitrarily set at 0.1/hour. Since the total failure rate of the system is the sum of the individual rates, the failure rate of the quadrotor system is 0.4/hour.

We now introduce the concept of parallel systems which indicate redundancy. The simplest example of redundancy is a situation in which two elements are both required to fail before the system fails. This is demonstrated in figure 3.3.

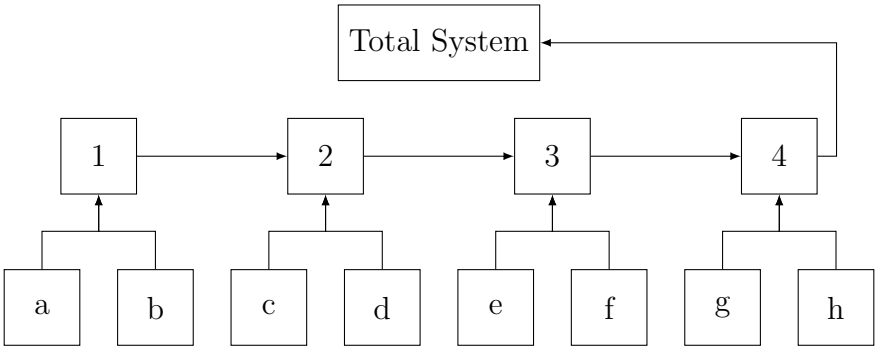

Figure 3.3: "Bottom-up" Parallel System Reliability Block Diagram

When determining the reliability of subsystem 1, 2, 3, or 4 it is more convenient to work with failure probabilities $F' = (1 - F)$. The probability of a system failing

when composed of two parallel elements is

$$F'_{\text{system}} = F'_a F'_b \tag{3.7}$$

or

$$1 - F_{\text{system}} = (1 - F_a)(1 - F_b) \tag{3.8}$$

Expanding this gives

$$F_{\text{system}} = F_a + F_b - F_a F_b \tag{3.9}$$

Substituting into the reliability function for the expontential distribution gives

$$F_{\text{system}} = e^{-\Lambda_a t} + e^{-\Lambda_b t} - e^{-(\Lambda_a + \Lambda_b)t} \tag{3.10}$$

The effective failure rate of the system is therefore

$$\frac{1}{\Lambda_{\text{effective}}} = \frac{1}{\Lambda_a} + \frac{1}{\Lambda_b} - \frac{1}{\Lambda_a + \Lambda_b} \tag{3.11}$$

The following example demonstrates the reduction in the failure rate of the overall system by implementation of parallel system reliability. With the octorotor this is achieved by increasing the number of motors/rotors so that the subsystems 1, 2, 3, and 4 are made up of parallel systems of effectors a&b etc.

Example 2 The failure rates of parts a and b in subsystem 1 are 0.1 as in Example 1. The failure rate for subsystem 1 is

$$\frac{1}{\Lambda_{\text{effective 1}}} = \frac{1}{0.1} + \frac{1}{0.1} - \frac{1}{0.1 + 0.1} = \frac{1}{15} \tag{3.12}$$

Subsystems 2, 3, and 4 are identical and so have the same effective failure rate. This means that the failure rate of the total system is now calculated as the sum of the failure rates of the subsystems 1, 2, 3, and 4 and is 0.268/hour. This is an improvement of 33% over the vehicle in Example 1.

It is possible to study the number of effectors in parallel in a thrust subsystem. The quadrotor has one (it has one effector per subsystem), the octorotor has two, etc. The failure rate of the subsystem is determined as in Example 2. The failure rates of the subsystems are combined in series to find the failure rate of the system. It is now possible to determine the change in the system reliability as more effectors are added in parallel. The relative (normalised) cost of each subsystem is found such a quadrotor = 1, octorotor =2 etc. The cost per percentage increase in system safety is then calculated and compared as in Table 3.1. This calculation shows that the octorotor offers the lowest cost for the increase in system reliability.

Table 3.1: Relative Reliability Cost

Effector Failure Rate	0.1			
Effectors in Subsystem	1	2	3	4
Failure Rate of Subsystem	0.1	0.0667	0.0526	0.0445
Failure Rate of System	0.4	0.267	0.211	0.178
Increase in System Reliability	0	33%	47%	55%
Cost of System	4	8	12	16
Cost per % Increase		0.24	0.25	0.29

3.3 Linear Control Allocation

3.3.1 Unconstrained Control Allocation

The challenge of inverting the octorotor model input matrix (3.1) is that B is not a square matrix. We will assume that it has a non-trivial null space meaning there is an infinite number of vectors $\mathbf{u} \in \mathbb{R}^p$ satisfying (2.32) for a given $\tau \in \mathbb{R}^m$.

Neglecting control value saturations and rate constraints on the input and choosing a quadratic cost function leads to the control allocation cost function formulation [Oppenheimer et al., 2006]

$$\min_{\mathbf{u}} J = \min_{\mathbf{u}} \frac{1}{2}(\mathbf{u}+c)^T W(\mathbf{u}+c), \quad \text{subject to } \tau = B\mathbf{u} \tag{3.13}$$

where $W \in \mathbb{R}^{p\times p}$ is a positive definite weighting matrix and c is an offset vector used to represent failed effector controls. Taking partial derivatives of the Hamiltonian [Oppenheimer et al., 2006] gives the generalised inverse

$$\mathbf{u} = -c + W^{-1}B^T(BW^{-1}B^T)^{-1}(\tau + Bc) \tag{3.14}$$

For the case when $W = I$ the solution to (2.32) is of the form $\mathbf{u} = B^\dagger\tau$ where $B^\dagger$ is the Moore-Penrose psuedo inverse [Oppenheimer et al., 2006].

3.4 Effector Constraints

The maximum thrust that can be generated by the octorotor effectors is limited by the values of the rotor speeds $\Omega_i(t)$ which are limited between absolute lower and uper bounds $\Omega_{i,\min}$ and $\Omega_{i,\max}$ such that

$$\Omega_{i,\min} \leq \Omega_i(t) \leq \Omega_{i,\max} \tag{3.15}$$

holds for all t. There is a maximum thrust that can be generated by each motor-propeller combination due to the constraint on the maximum rotational speed, as well as a minimum thrust due to the lowest rotation speed of the motor. The

maximum rotational speed of the motor can be determined by multiplying the kv rating (supplied by the manufacturer) by the supplied voltage (7.4 or 11.1 volts are commonly used). This gives the maximum speed in rpm which is converted to rad/s by multiplying by 2π. Data for a typical motor are shown in Table 3.2.

Table 3.2: Turnigy Motor Specifications [tur]

kv [rpm/volt]	980
Lipo cells	2-3s
Max current	10 Amps

Connecting a 2S Lipo battery (7.4 volts) to this motor gives a theoretical maximum rotational speed of 736 rad/s. For simulation work the limit was set to 700 rad/s since this is a realistic real-life limitation.

With fixed pitch propellers and brushless motors that are unidirectional, a negative thrust cannot be generated, so the constraint becomes

$$0 \leq \Omega_i(t) \leq \Omega_{\max} \tag{3.16}$$

and the rate limit constraint is

$$\dot{\Omega}_{i,\min} \leq \dot{\Omega}_i \leq \dot{\Omega}_{i,\max} \tag{3.17}$$

The control law is considered to operate as a discrete time system with sample period T. The rate of change of the effector response is approximated by a first order difference approximation [Harkegard, 2003, Gai and Wang, 2013, Kishore et al., 2013] as

$$\dot{\Omega} = \frac{\Omega(t) - \Omega(t-T)}{T} \tag{3.18}$$

The rate constraints can be rewritten by combining (3.17), (3.18)

$$\dot{\Omega}_{i,\min} \leq \dot{\Omega}_i = \frac{\Omega_i(t) - \Omega_i(t-T)}{T} \leq \dot{\Omega}_{i,\max} \tag{3.19}$$

This enables rate constraints to be rewritten as position constraints over the interval T. Combining with the position saturation yields

$$\Omega_{i,\min} \leq \Omega_i \leq \Omega_{i,\max} \tag{3.20}$$

where

$$\begin{aligned} \Omega_{i,\min} &= \max\left(\Omega_{i,\min}, \Omega_i(t-T) + \dot{\Omega}_{i,\min}T\right) \\ \Omega_{i,\max} &= \min\left(\Omega_{i,\max}, \Omega_i(t-T) + \dot{\Omega}_{i,\max}T\right) \end{aligned} \tag{3.21}$$

give the overall position saturation constraint at time t.

Test bed modeling can reveal the limit to the rate at which the motors can respond but in this thesis no motor dynamics are modelled. This is because the work is

purposely as generic as possible so that it can be applied to real life effectors and is not restricted to one motor-rotor combination. The effectors are therefore assumed to respond instantaneously, i.e. $\dot{\Omega}_i(t)$ is unbounded and $\Omega_{i,\min} \leq \Omega_i \leq \Omega_{i,\max}$. From (2.35), (3.15) can be rewritten as

$$\mathbf{u}_{i,\min} \leq \mathbf{u}_i(t) \leq \mathbf{u}_{i,\max} \tag{3.22}$$

The maximum and minimum values define the closed subset $\mathcal{F}$ [Bordignon, 1996]

$$\mathcal{F} = \{\mathbf{u} \in \mathbb{R}^p | \mathbf{u}_{i,\min} \leq \mathbf{u}_i \leq \mathbf{u}_{i,\max}\} \subset \mathbb{R}^p \tag{3.23}$$

$\mathcal{F}$ is a closed and bounded set. The subset of controls which lie on the boundary of $\mathcal{F}$ are denoted $\partial\mathcal{F}$. If an element of the control vector $\mathbf{u}$ is equal to one of its saturation values it is a saturated control [Bordignon, 1996].

The controls generate a force and moment combination through a linear mapping of the control effectiveness matrix B onto the m-dimensional force-moment space through $B\mathbf{u} = \tau$ where $B : \mathbb{R}^p \to \mathbb{R}^m$. The class of overactuated control allocation problems examined here involves redundant controls, $p > m$.

3.5 Constrained Control Allocation

The difference between unconstrained and constrained linear control allocation is the inclusion of position and rate limits. In constrained linear control allocation the goal is to find $\mathbf{u}$ such that $B\mathbf{u} = \tau$ subject to $\mathbf{u}_{\min} \leq \mathbf{u} \leq \mathbf{u}_{\max}, |\dot{\mathbf{u}}| \leq \dot{\mathbf{u}}_{\max}$. Constraining the effector outputs $\mathbf{u} \subset \mathcal{F}$ means that the total forces and moments that can be generated by the effectors is constrained $\mathcal{A} \subset \tau$.

We define a control allocation method to be successful if the Kalman controllability analysis returns $\text{rank}(R) = n$ and the controls are allocated within the saturation limits. If the control demands cannot be allocated we describe it as unsuccessful or unallocatable.

3.5.1 Daisy Chaining

The daisy chaining method aims to solve the control allocation problem (3.1) by grouping the effectors together and then ranking the groups so that the control allocation problem is solved for the highest priority group. If any of the effectors saturate then the values for the group are set and the allocation problem passes on to the next group to solve the residual between the required forces and the allocated forces. This continues until a solution is found or a solution is not feasible:

$$\tau = B\mathbf{u} = B_1\mathbf{u}_1 + B_2\mathbf{u}_2 + \ldots + B_M\mathbf{u}_M \tag{3.24}$$

where M is the number of groups. This is generally formulated as

$$\mathbf{u}_i = \text{sat}_{\mathbf{u}_i}(B_i^{\dagger}(\tau - \sum_{k=1}^{M-1} B_k U_k)) \tag{3.25}$$

where the saturation function

$$\text{sat}_{\mathbf{u}_i} = \begin{cases} \mathbf{u}_{\min} & \mathbf{u} \leq \mathbf{u}_{\min} \\ \mathbf{u} & \mathbf{u}_{\min} < \mathbf{u} < \mathbf{u}_{\max} \\ \mathbf{u}_{\max} & \mathbf{u} \geq \mathbf{u}_{\max} \end{cases} \quad i = 1, \ldots, M \tag{3.26}$$

The order in which this allocation occurs can be important as shown in Kim et al. [2011] where a modified daisy chain method is used to allocate controls for a model of the F-18 HARV. If smart effectors (which can detect their failure state) are used then grouping the failed effectors and functional effectors into different groups and then ranking the failed effectors into the first allocation group leads to better performance than if they are ranked according to their nominal performance groups. Regardless to the control allocation method, the control effectiveness matrix for a specific vehicle remains constant. For the following examples this is found in Section 2.6.1, (2.36).

Example 3 It could be suggested that this can be applied to the case of the octorotor where the vehicle is considered to be two superimposed and offset quadrotor vehicles so that the control allocation problem is split between $M = 2$ groups and becomes

$$\begin{aligned} \tau = B_1\mathbf{u}_1 + B_2\mathbf{u}_2 = &\begin{bmatrix} b & b & b & b \\ -bls_{\gamma_0} & -bls_{\gamma_2} & -bls_{\gamma_4} & -bls_{\gamma_6} \\ blc_{\gamma_0} & blc_{\gamma_2} & blc_{\gamma_4} & blc_{\gamma_6} \\ d & -d & d & -d \end{bmatrix} \begin{bmatrix} \sigma_0 \\ \sigma_2 \\ \sigma_4 \\ \sigma_6 \end{bmatrix} + \\ &\begin{bmatrix} b & b & b & b \\ -bls_{\gamma_1} & -bls_{\gamma_3} & -bls_{\gamma_5} & -bls_{\gamma_7} \\ blc_{\gamma_1} & blc_{\gamma_3} & blc_{\gamma_5} & blc_{\gamma_7} \\ -d & d & -d & d \end{bmatrix} \begin{bmatrix} \sigma_1 \\ \sigma_3 \\ \sigma_5 \\ \sigma_7 \end{bmatrix} \end{aligned} \tag{3.27}$$

This is shown in Figure 3.4

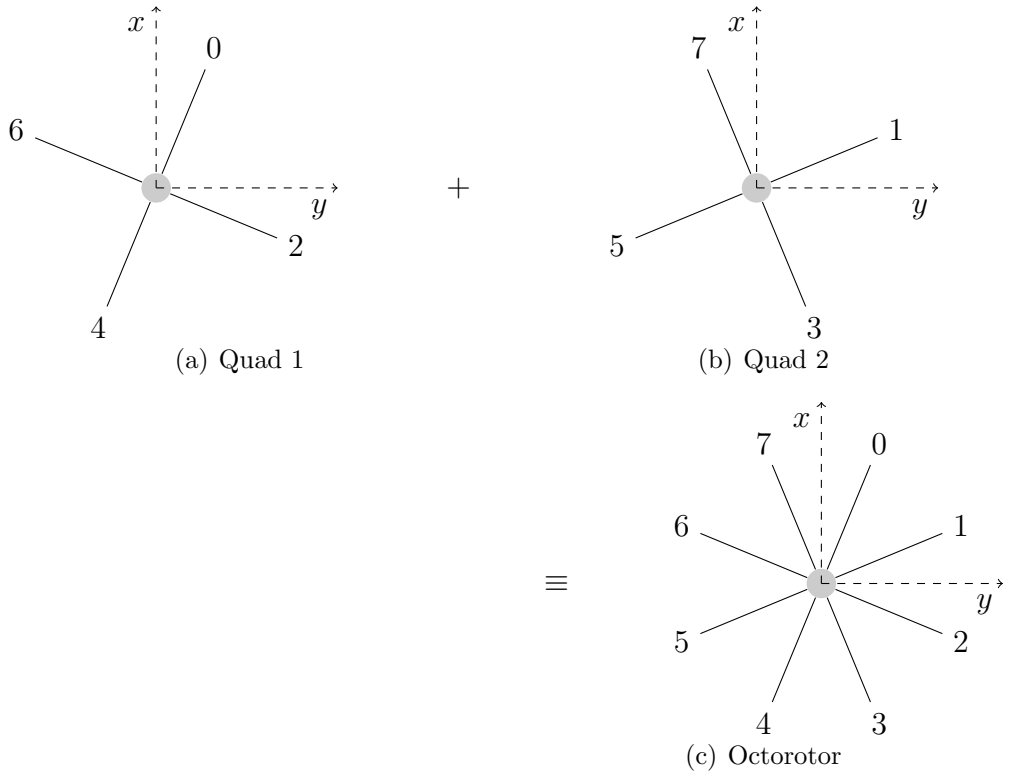

(a) Quad 1 (b) Quad 2

(c) Octorotor

Figure 3.4: 'Offset' Quadrotors Combined to form Octorotor

With this method priority will be given to the first group containing 4 effectors $\{0, 2, 4, 6\}$ unless an effector is saturated. When constructed in this manner it is clear to see that a nominal case could be where only four effectors are only ever used. The total energy expenditure in such a case will be the same as when eight effectors are used and it might be thought that this promising method would be applicable to the fault case of the octorotor. An example for level hover is shown in (3.28). The total vertical thrust is equal to the vehicle weight and no attitude moments are desired.

$$\tau = \begin{bmatrix} mg \\ 0 \\ 0 \\ 0 \end{bmatrix} = \begin{bmatrix} 11.72 \\ 0 \\ 0 \\ 0 \end{bmatrix} = B_1 \mathbf{u}_1 \tag{3.28}$$

Rearranging and taking the pseudo inverse gives the squared rotor speeds.

$$\mathbf{u}_1 = B_1^{\dagger} \begin{bmatrix} 11.772 \\ 0 \\ 0 \\ 0 \end{bmatrix} \tag{3.29}$$

$$\mathbf{u}_1 = \begin{bmatrix} b & b & b & b \\ -bls_{\gamma_0} & -bls_{\gamma_2} & -bls_{\gamma_4} & -bls_{\gamma_6} \\ blc_{\gamma_0} & blc_{\gamma_2} & blc_{\gamma_4} & blc_{\gamma_6} \\ d & -d & d & -d \end{bmatrix}^{\dagger} \begin{bmatrix} 11.772 \\ 0 \\ 0 \\ 0 \end{bmatrix} \tag{3.30}$$

$$\mathbf{u}_1 = \begin{bmatrix} 94,249 \\ 94,249 \\ 94,249 \\ 94,249 \end{bmatrix} \text{rad}^2/\text{s}^2 \tag{3.31}$$

Taking the square root of the individual squared rotor speeds gives the individual rotor speed.

$$\sqrt{\mathbf{u}_1} = \begin{bmatrix} 307 \\ 307 \\ 307 \\ 307 \end{bmatrix} \text{rad/s} \tag{3.32}$$

This is allocatable within the saturation limits $\Omega_{\max}$ =700 rad/s and so $\mathbf{u}_2 = [0\ 0\ 0\ 0]^T$.

Example 4 We consider the same scenario as Example 3, i.e. $\tau = [11.772\ 0\ 0\ 0]^T$ but this time apply a lower saturation limit so that $\Omega_{\max} = 250$ rad/s. The first step is to perform unconstrained control allocation using the first group of effectors so

$$\tau = B_1 \mathbf{u}_1 = \begin{bmatrix} b & b & b & b \\ -bls_{\gamma_0} & -bls_{\gamma_2} & -bls_{\gamma_4} & -bls_{\gamma_6} \\ blc_{\gamma_0} & blc_{\gamma_2} & blc_{\gamma_4} & blc_{\gamma_6} \\ d & -d & d & -d \end{bmatrix} \begin{bmatrix} \sigma_0 \\ \sigma_2 \\ \sigma_4 \\ \sigma_6 \end{bmatrix} \tag{3.33}$$

which gives the rotor speeds as

$$\sqrt{\mathbf{u}_1} = \begin{bmatrix} 307 \\ 307 \\ 307 \\ 307 \end{bmatrix} \text{rad/s} \tag{3.34}$$

Since these values are above the saturation limit of 250 rad/s they are set to the saturation value and the residual force is allocated to the remaining effectors:

$$\tau_{\text{res}} = \tau - (B_1 \mathbf{u}_{1,\max}) \tag{3.35}$$

$$= \begin{bmatrix} 11.771 \\ 0 \\ 0 \\ 0 \end{bmatrix} - \begin{bmatrix} b & b & b & b \\ -bls_{\gamma_0} & -bls_{\gamma_2} & -bls_{\gamma_4} & -bls_{\gamma_6} \\ blc_{\gamma_0} & blc_{\gamma_2} & blc_{\gamma_4} & blc_{\gamma_6} \\ d & -d & d & -d \end{bmatrix} \begin{bmatrix} 250^2 \\ 250^2 \\ 250^2 \\ 250^2 \end{bmatrix} \tag{3.36}$$

$$= \begin{bmatrix} 3.947 \\ 0 \\ 0 \\ 0 \end{bmatrix} \tag{3.37}$$

This control demand is allocated to the second group of effectors

$$\sqrt{\mathbf{u}_2} = \sqrt{B_2^{\dagger} \tau_{\text{res}}} = \begin{bmatrix} 178 \\ 178 \\ 178 \\ 178 \end{bmatrix} \text{ rad/s} \tag{3.38}$$

so in this case all of the effectors are used with 4 at their maximum and 4 below the constraint.

However there is an additional constraint imposed on this method in addition to that proposed in Kim et al. [2011]. It must be possible to allocate each individual control group using B_M, i.e. $\text{rank}(R) = n$ for each group in M. An example of this method was demonstrated in Adîr et al. [2011] where after the failure in one effector the control allocation scheme was switched to allocate to only four remaining effectors, i.e. $\{1, 3, 5, 7\}$. This has the effect of reducing the potential performance of the vehicle since the largest force that can be produced by the combined effectors is reduced. The daisy chain allocation is shown below for a complete failure of effector 0 ($f_1 = 0, f_{2,3} = 1$)

$$\begin{aligned} \tau = f_1 B_1 \mathbf{u}_1 + f_2 B_2 \mathbf{u}_2 + f_3 B_3 \mathbf{u}_3 = & f_1 \begin{bmatrix} b \\ -s_{\gamma_0} \\ c_{\gamma_0} \\ d \end{bmatrix} \sigma_0 + \\ & f_2 \begin{bmatrix} b & b & b \\ -bls_{\gamma_2} & -bls_{\gamma_4} & -bls_{\gamma_6} \\ blc_{\gamma_2} & blc_{\gamma_4} & blc_{\gamma_6} \\ -d & d & -d \end{bmatrix} \begin{bmatrix} \sigma_2 \\ \sigma_4 \\ \sigma_6 \end{bmatrix} + \\ & f_3 \begin{bmatrix} b & b & b & b \\ -bls_{\gamma_1} & -bls_{\gamma_3} & -bls_{\gamma_5} & -bls_{\gamma_7} \\ blc_{\gamma_1} & blc_{\gamma_3} & blc_{\gamma_5} & blc_{\gamma_7} \\ -d & d & -d & d \end{bmatrix} \begin{bmatrix} \sigma_1 \\ \sigma_3 \\ \sigma_5 \\ \sigma_7 \end{bmatrix} \end{aligned} \tag{3.39}$$

Since $f_1 = 0$ the first group is not allocated. It is not possible to allocate to the second group since $\text{rank}(R) \neq n$ for this group and so they will not be used post-failure, leaving the effective control allocation as

$$\mathbf{u}_3 = f_3 B^{\dagger} \tau \tag{3.40}$$

$$\sqrt{\mathbf{u}_3} = \begin{bmatrix} 307 \\ 307 \\ 307 \\ 307 \end{bmatrix} \text{ rad/s} \tag{3.41}$$

Considering the original constraints o $\Omega_{\max} = 700$ rad/s, this is a successful control allocation.

The disadvantage of the daisy chaining scheme is that not all of the effectors will be used if the first group is able to solve the control allocation problem. Such an approach may cause large deflections in aircraft control surfaces where a different combination of effectors could provide a faster response to a control input. This can be somewhat solved through careful selection of effector groups, but after a failure there is no guarantee that the groups will still provide the desired response. A more severe outcome of this method is if a failure occurs once the control scheme uses (3.40). In such a case the vehicle will have suffered two failures and will be uncontrollable unless the effectors are regrouped. This method would then resemble a cascade redistributed pseudo inverse method or an intractable number of groupings will have to be constructed which are capable or solving the control allocation for any failure scenario. For these reasons the daisy chaining control allocation method is not implemented to provide fault tolerant control for the octorotor.

3.5.2 Redistributed Pseudo Inverse Method

The redistributed pseudo inverse method is used when considering constrained control allocation. In constrained control allocation, the goal is to find $\mathbf{u}$ such that $\tau = B\mathbf{u}$ subject to $\mathbf{u}_{\min} \leq \mathbf{u} \leq \mathbf{u}_{\max}, |\dot{\mathbf{u}} \leq \dot{\mathbf{u}}_{\max}$. The redistributed pseudo inverse works in a fashion similar to the pseudo inverse, with the addition of position and rate limits. For the redistributed pseudo inverse the process is iterative and position saturated control effectors are removed from subsequent pseudo inverse solution. The idea is that if an inverse allocates a control which exceeds the saturation limit the control is set to the saturation value and the remainder of the controls are redistributed to achieve the desired force and moments. The first step is to solve the control allocation problem using the pseudo inverse solution in Equation (3.42) with c initially a vector of zeros and $W = I$ since the effectors are identical [Oppenheimer et al., 2006]

$$\mathbf{u} = -c + W^{-1} B^T (B W^{-1} B^T)^{-1} [\tau + Bc] = -c + B_{\text{red}}^{\dagger} [\tau + Bc] \tag{3.42}$$

where initially $B_{\text{red}} = B$. If no controls exceed their maximum or minimum position limits then the process stops and the solution from (3.42) is used. However, if one or

more controls saturate the problem is solved again, this time zeroing out the columns of the B_{red} matrix corresponding to the saturated controls and placing the negative of the saturated values in the vector c. For example, if the i-th control saturates by allocating a value above the maximum allowed, $c_i = -\Omega_{\max}$, $B_{\text{red},i} = 0_{4\times 1}$. The controls are then reallocated whilst leaving the i-th control at the saturation value.

If any additional control effectors saturate, the corresponding columns of B_{red} are zeroed out, the negative of the saturated value is inserted in c and the problem is solved again. This process continues until all control effectors saturate or a solution is found that does not violate the constraints. One must be cautious here because when saturation occurs there are two B matrices in (3.42), one for the pseudo inverse solution and one for the offset or saturated contribution Bc. When zeroing out a column corresponding to a saturated effector, only the pseudo inverse $B_{\text{red}}^{\dagger}$ matrix is modified, while the Bc term uses the original B matrix. The advantage of the pseudo inverse method over the daisychaining method is that the initial control allocation matrix is used regardless of effector saturations and failures. If the daisy chain method is used then an intractable number of allocation matrices are possibl and must be instantaneously solved.

The folllowing example demonstrates the redistributed pseudo inverse method utilising the Moore-Penrose pseudo inverse.

Example 5 The octorotor effectors saturation limits are $\Omega_{i\max} = 250$ rad/s,$\rightarrow$ $\mathbf{u}_{\max} = 62,500$ rad^2/s^2 and there is an altitude step demand such that

$$\tau = \begin{bmatrix} 59.772 \\ 0 \\ 0 \\ 0 \end{bmatrix} \tag{3.43}$$

The control allocation matrix B is given in (2.36). The first step is calculated using (3.42) with $W = I$ and c a vector of zeros. The first iteration gives

$$\Omega = \sqrt{\mathbf{u}} = \sqrt{B^{\dagger}\tau} = \begin{bmatrix} 489 \\ 489 \\ 489 \\ 489 \\ 489 \\ 489 \\ 489 \\ 489 \end{bmatrix} \text{ rad/s} \tag{3.44}$$

Since $489 > 250$ and exceeds the saturation limit, the negative values of the maximum control are inserted in c which becomes

$$c = \begin{bmatrix} -250 \\ -250 \\ -250 \\ -250 \\ -250 \\ -250 \\ -250 \\ -250 \end{bmatrix} \text{ rad/s} \tag{3.45}$$

$B_{\text{red}}^{\dagger}$ is modified to become a zero matrix since all of the effectors are saturated. The problem (3.42) becomes

$$\sqrt{\mathbf{u}} = -c \tag{3.46}$$

$$= \begin{bmatrix} 250 \\ 250 \\ 250 \\ 250 \\ 250 \\ 250 \\ 250 \\ 250 \end{bmatrix} \text{ rad/s} \tag{3.47}$$

and so the rotor speeds are set to the maximum. This leads to a disparity between the output of the controller τ and the force output of the effectors U where

$$U = B\mathbf{u} = \begin{bmatrix} 25 \\ 0 \\ 0 \\ 0 \end{bmatrix} \neq \tau \tag{3.48}$$

This means that the performance is degraded compared to an effector model with higher saturation limits and the control allocation is not perfect since the effectors are saturated. Since all of the effector outputs are set to their maximum values there is nothing else that the allocation scheme can do and so this continues until the controller output is allocatable and $U = \tau$ such as when considering the thrust requirements for a smaller altitude step or for the vehicle in the hover. A future topic for research can be towards limiting the altitude error value such that the altitude step demand does not saturate all of the effectors. This could prove to be extremely useful.

3.5.3 The Attainable Force Set

The effector constraints can be applied at the effector level as opposed to the overal moment set, and this implementation is in contrast to various face searching algorithm techniques which are computationally intensive and must be computed online

for every failure scenario. These rely on the image $\mathcal{A} \in \mathbb{R}^m \subset \mathbb{R}^m$ of $\mathcal{F} \subset \mathbb{R}^p$, which is mapped using B. The subset $\mathcal{A}$ represents all of the forces and moments which can be attained within the constraints of the controls. This is denoted the attainable force set. Forces and moments lying on the boundary of $\mathcal{A}$ are denoted by $\partial\mathcal{A}$.

There may be times when the control allocation problem cannot be solved. In such a case it might be desirable to obtain a scaled force so that the effectors are not saturated. The resultant forces and moments lie in the attainable force set $\mathcal{A}$. This method starts with the unconstrained control allocation using a pseudo inverse method $\tilde{\mathbf{u}} = B^{\dagger}\tau$ [Durham, 1994, Johansen and Fossen, 2013]. If $\tilde{\mathbf{u}} \in \mathcal{F}$ no further steps are needed and $\mathbf{u} = \tilde{\mathbf{u}}$. Otherwise the directional sense of τ is preserved but the force $B\mathbf{u}$ is scaled to be on the boundary of $\mathcal{A}$. A case of two variables and each variable is limited to ± 1 and is shown in Figure 3.5. The scaled resultant

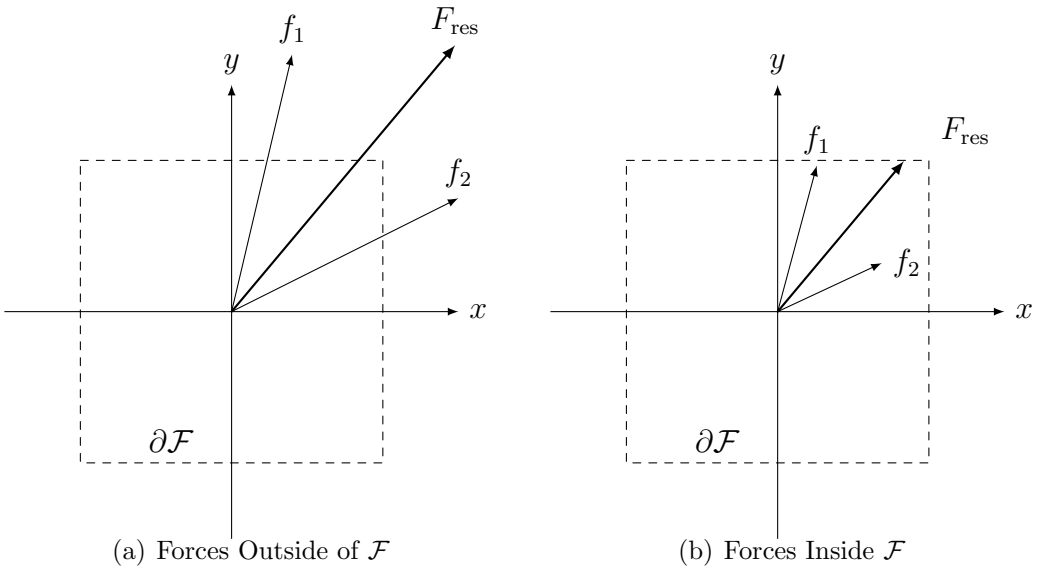

(a) Forces Outside of $\mathcal{F}$ (b) Forces Inside $\mathcal{F}$

Figure 3.5: Attainable Force Set, Constrained to $\mathcal{F}$

force lies inside the constrained set $\mathcal{F}$. If both of the variables (f_1 and f_2) are initially allocated outside of $\mathcal{F}$ then the directional sense of F_{res} is maintained after constraining. However, consider the example of Figure 3.6 where initially only one of the variables exceeds $\mathcal{F}$. This force is scaled to be on the boundary $\partial\mathcal{F}$ but the other force is not scaled.

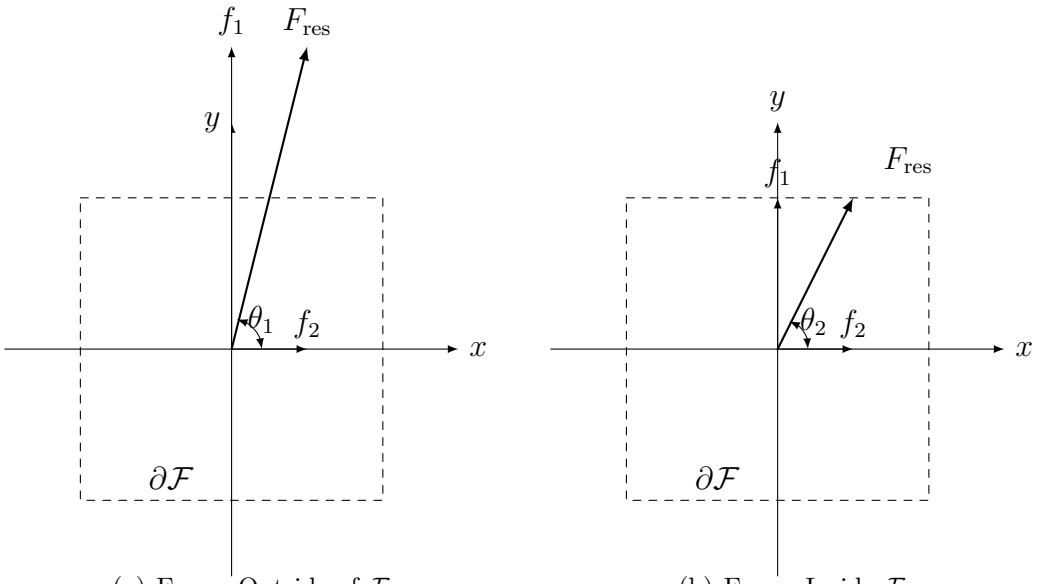

(a) Forces Outside of $\mathcal{F}$ (b) Forces Inside $\mathcal{F}$

Figure 3.6: Attainable Force Set, Constrained to $\mathcal{F}$, Rotated Resultant

Here $\theta_2 < \theta_1$ and the direction of the resultant force has changed. In order to preserve the directional sence of F_{res} the following condition is imposed:

- If any control lies outside of $\mathcal{F}$ then all controls are equally scaled in order to preserve the direction of F_{res}.

Implementing this condition is shown graphically in Figure 3.7 where $\theta_2 = \theta_1$.

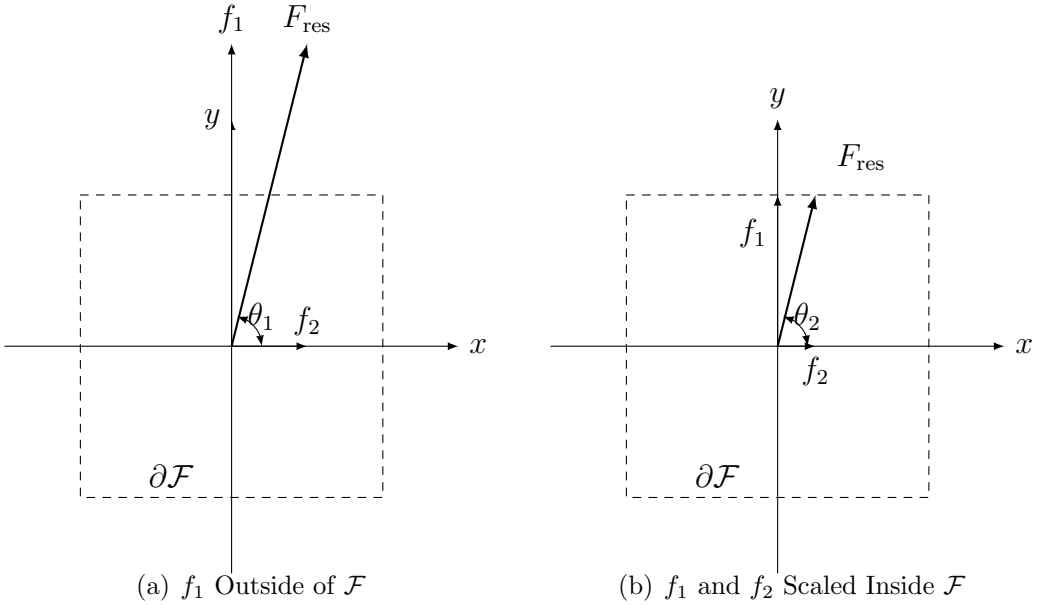

(a) f_1 Outside of $\mathcal{F}$ (b) f_1 and f_2 Scaled Inside $\mathcal{F}$

Figure 3.7: Attainable Force Set, Constrained to $\mathcal{F}$, Resultant Direction Conserved

This can be applied to the linear mapping such as shown in Figure 3.8 where the forces and moments are mapped from the effectors through $\mathcal{A} = 2f_1 + 2f_2$.

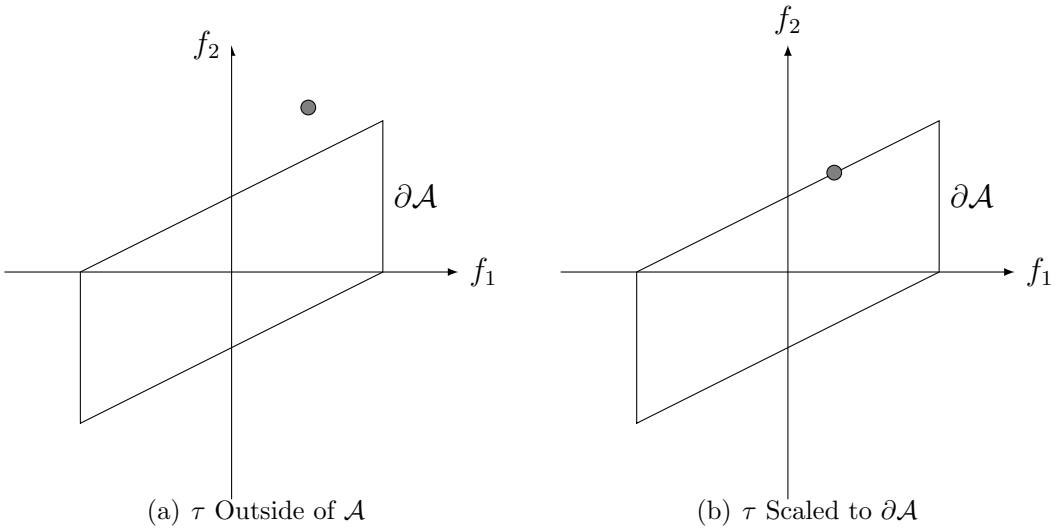

(a) τ Outside of $\mathcal{A}$ (b) τ Scaled to $\partial\mathcal{A}$

Figure 3.8: Attainable Force Set, Constrained to $\mathcal{A}$

Note that the magnitude of τ is reduced but the direction is maintained. If you are inside $\partial\mathcal{A}$ then you will be inside $\partial\mathcal{F}$. This can be applied to the linear mapping of the octorotor where all effectors are equal and the constraints on $\mathcal{A}$ are related to the constraints on $\mathcal{F}$ and for this reason the constraints are applied directly to $\mathcal{F}$ to avoid computationally intensive face searching algorithms to determine $\mathcal{A}$ for every subset of $\mathbf{u}$.

It should be pointed out that the scaling is only performed if the allocated control values lie outside of the set $\mathcal{F}$. If they are all inside this set then scaling to force one to the boundary of the set will mean that any manoeuvre will be performed with the maximum available resultant force. This may not be desirable for dealing with delicate cargo or when manoeuvring close to obstacles and indeed will not allow for a single thruster to be set below its maximum value - hovering would become impossible!

The following method which constrains the effectors to be inside $\mathcal{F}$ may be used in order to maintain the direction of the control demand. It is based on de Lamberterie et al. [2011] but has been adapted to the octorotor and relies on knowing the outputs of each effector. This method is only suitable if

- all of the effectors are equal (they have the same voltage-thrust relationship),
- are aligned with z_b, and
- are unidirectional so cannot produce a negative thrust.

The method is as follows:

Step 1 Perform the constrained control allocation using a suitable method (such as redistributed pseudo inverse). If this is successful (i.e. $U = \tau$) then stop.

Step 2 If the constrained control allocation is not successful ($U \neq \tau$) then perform the unconstrained control allocation, $\mathbf{u} = B^{\dagger}\tau$.

Step 3 Calculate $\lambda_i = \mathbf{u}_i/\mathbf{u}_{\mathrm{i,max}}$ for all $i \in p$. Then, if $\lambda_{\max} > 1, \tau_{c,m} = \tau_m/\lambda_{\max}$ where $\tau_{c,m}$ is the m-th constrained control demand.

Step 4 Perform unconstrained control allocation on the constrained control demands τ_c to give $\mathbf{u}_c$ where τ_c is allocatable.

Step 5 The effector outputs are

$$U = B^{\dagger}\mathbf{u}_c = \tau_c = \lambda\tau_u \tag{3.49}$$

which are the constrained force and moment outputs.

If the scheme stops at step 1 then nominal performance is maintained ($\lambda = 1$ and perfect allocation is achieved). If the scheme continues through to the end then the performance is degraded, however, the direction of the constrained output is the same as the unconstrained demand.

Example 6 We consider the controller output $\tau = [11.772\ 5\ 0\ 0]^T$ which represents level hover and a large step demand in roll. The pseudo inverse control allocation method is used to give the unconstrained control allocation as

$$\sqrt{\mathbf{u}} = \sqrt{B^{\dagger}\tau} = \begin{bmatrix} 178 \\ 101 \\ 101 \\ 178 \\ 250 \\ 290 \\ 290 \\ 250 \end{bmatrix} \text{ rad/s} \tag{3.50}$$

$\lambda_{\max}$ is the ratio between the highest allocated squared rotor speed and the upper saturation squared rotor speed.

$$\lambda_{\max} = \frac{290^2}{250^2} = 1.3456 \tag{3.51}$$

The constrained control demands are

$$\tau_c = \frac{\tau}{\lambda_{\max}} = \begin{bmatrix} 8.7485 \\ 3.7158 \\ 0 \\ 0 \end{bmatrix} \tag{3.52}$$

The unconstrained control allocation is performed and the rotor speeds are within the saturation limits:

$$\sqrt{\mathbf{u}} = \sqrt{B^{\dagger}\tau_c} = \begin{bmatrix} 154 \\ 87 \\ 87 \\ 154 \\ 215 \\ 250 \\ 250 \\ 215 \end{bmatrix} \text{ rad/s} \tag{3.53}$$

This method only runs once (it is not iterative like the RPI method). The direction of the thrust vector remains aligned with the control demand, but the magnitude is reduced. This is compared to the RPI method where the effector outputs are shown in Example 7.

Example 7 In this example the controller output is $\tau = [11.772\ 5\ 0\ 0]^T$ corresponding to a large roll demand. The maximum rotor speed is the same as the previous example, $\Omega_{\max} = 250$rad/s. The first step is to perform the unconstrained control allocation using the Moore-Penrose pseudo inverse:

$$\sqrt{\mathbf{u}} = \sqrt{B^{\dagger}\tau} = \begin{bmatrix} 178 \\ 101 \\ 101 \\ 178 \\ \mathbf{250} \\ \mathbf{290} \\ \mathbf{290} \\ \mathbf{250} \end{bmatrix} \text{ rad/s} \tag{3.54}$$

The effectors exceeding the saturation limit are delineated in bold and are $\mathbf{u}_{4,5,6,7}$. Their values are set to the maximum (250 rad/s) and their influence is removed from the next allocation where the residual commands are

$$\tau_{a2} = \tau - B_5(\mathbf{u}_{\max}) - B_6(\mathbf{u}_{\max}) - B_7(\mathbf{u}_{\max}) - B_8(\mathbf{u}_{\max}) \tag{3.55}$$

$$= \begin{bmatrix} 3.947 \\ -0.1119 \\ 0 \\ 0 \end{bmatrix} \tag{3.56}$$

where B_i denotes the ith column of the control effectiveness matrix B. This is allocated to the remaining effectors where the reduced control effectiveness matrix B_{red} is

$$B_{\text{red}} = \begin{bmatrix} b & b & b & b \\ -bls_{\gamma_0} & -bls_{\gamma_1} & -bls_{\gamma_2} & -bls_{\gamma_3} \\ blc_{\gamma_0} & blc_{\gamma_1} & blc_{\gamma_2} & blc_{\gamma_3} \\ d & -d & -d & d \end{bmatrix} \tag{3.57}$$

The unconstrained rotor speeds are

$$\sqrt{\mathbf{u}} = \sqrt{B_{\text{red}}^{\dagger}\tau_{a2}} = \begin{bmatrix} \mathbf{321} \\ \mathbf{-201} \\ \mathbf{-201} \\ \mathbf{321} \end{bmatrix} \text{ rad/s} \tag{3.58}$$

Once again, the effectors exceeding the saturation limits are set to the limit and the unallocated remaining force is

$$\tau_{a3} = \tau_{a2} – B_1(\mathbf{u}_{\max}) - B_4(\mathbf{u}_{\max}) \tag{3.59}$$

$$= \begin{bmatrix} 0.0345 \\ 1.3853 \\ 0 \\ -0.0938 \end{bmatrix} \tag{3.60}$$

The total force and moments that are allocated are

$$U = \tau - \tau_{a3} = \begin{bmatrix} 11.7375 \\ 3.6147 \\ 0 \\ 0.0938 \end{bmatrix} \tag{3.61}$$

We can obtain the final allocation values from

$$\sqrt{\mathbf{u}} = \sqrt{(B – B_{\text{red}})^{\dagger}U} = \begin{bmatrix} 250 \\ 0 \\ 0 \\ 250 \\ 250 \\ 250 \\ 250 \\ 250 \end{bmatrix} \text{ rad/s} \tag{3.62}$$

All of the effectors are within the constraints but the thrust vector is being rotated ($U_4 \neq 0$). This leads to a deviation from the required flightpath and is undesirable.

A solution to this is to change physical setup of the vehicle (and the corresponding control effectiveness matrix) so that the rotational sense of the motors alternates every motor instead of grouping motors into corotating pairs. This effects the bottom row of the control allocation matrix and leaves the rest of the matrix unchanged. The control allocation matrix B becomes

$$B = \begin{bmatrix} b & b & b & b & b & b & b & b \\ -bls_{\gamma_0} & -bls_{\gamma_1} & -bls_{\gamma_2} & -bls_{\gamma_3} & -bls_{\gamma_4} & -bls_{\gamma_5} & -bls_{\gamma_6} & -bls_{\gamma_7} \\ blc_{\gamma_0} & blc_{\gamma_1} & blc_{\gamma_2} & blc_{\gamma_3} & blc_{\gamma_4} & blc_{\gamma_5} & blc_{\gamma_6} & blc_{\gamma_7} \\ d & -d & d & -d & d & -d & d & -d \end{bmatrix} \tag{3.63}$$

The manoeuvres are achieved similarly to as shown in Figure 3.9 with the difference being in the effectors for yaw control where they are no longer grouped but are alternate:

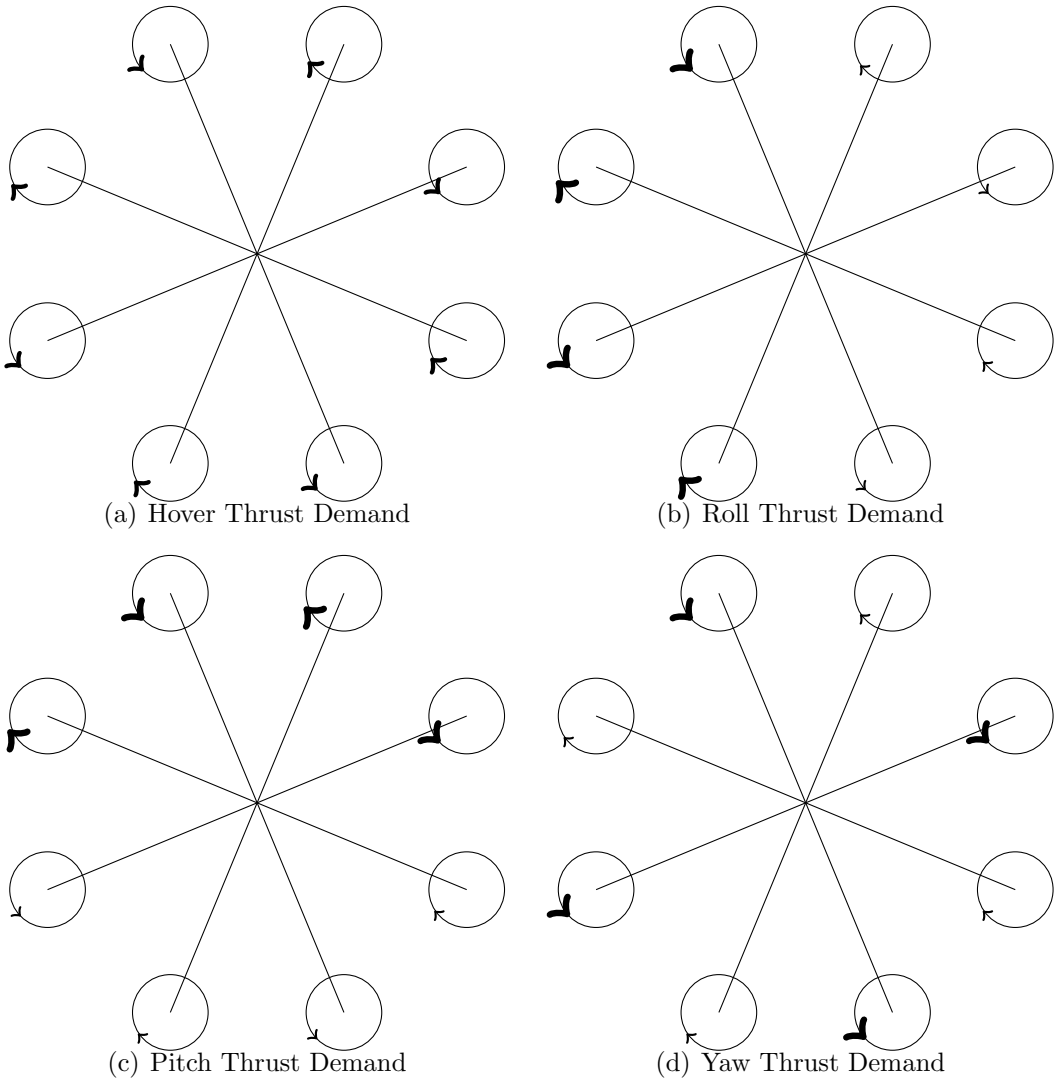

(a) Hover Thrust Demand (b) Roll Thrust Demand

(c) Pitch Thrust Demand (d) Yaw Thrust Demand

Figure 3.9: Thrust Demands for Alternating Motor Directions

We consider the same allocation problem as before with $\tau = [11.772\ 5\ 0\ 0]^T$. The control allocation using the RPI method gives the result

$$\mathbf{u} = \begin{bmatrix} 250 \\ 0 \\ 0 \\ 250 \\ 250 \\ 250 \\ 250 \\ 250 \end{bmatrix} \tag{3.64}$$

and the effector output to the dynamic model is

$$U = B\mathbf{u} = \begin{bmatrix} 11.7375 \\ 3.6147 \\ 0 \\ 0 \end{bmatrix} \neq \tau \tag{3.65}$$

The allocated force and moments are not equal to the controller output but this situation is favourable to rotating the force vector. Indeed, this method gives a better result than that obtained using the attainable force set in Example 6. Comparing the results from Example 4 and Example 6 to the controller output shows that as the constrained moment command is similar for both configurations, the overall thrust command from Example 4 is lower than for Example 6. This will lead to a drop in altitude and a slower translation of the vehicle. However, the configuration of Example 6 is not favourable for the grouping of the effectors for a daisy chaining method as outlined in Example 3 (the two overlapping quadrotors) where the signs of the bottom row of the individual control allocation matrices are the same in each group and so the controls cannot be allocated to just a single group. This means that the groups must be redefined as in Figure 3.10 so that each group contains two clockwise and two counter-clockwise rotating motors.

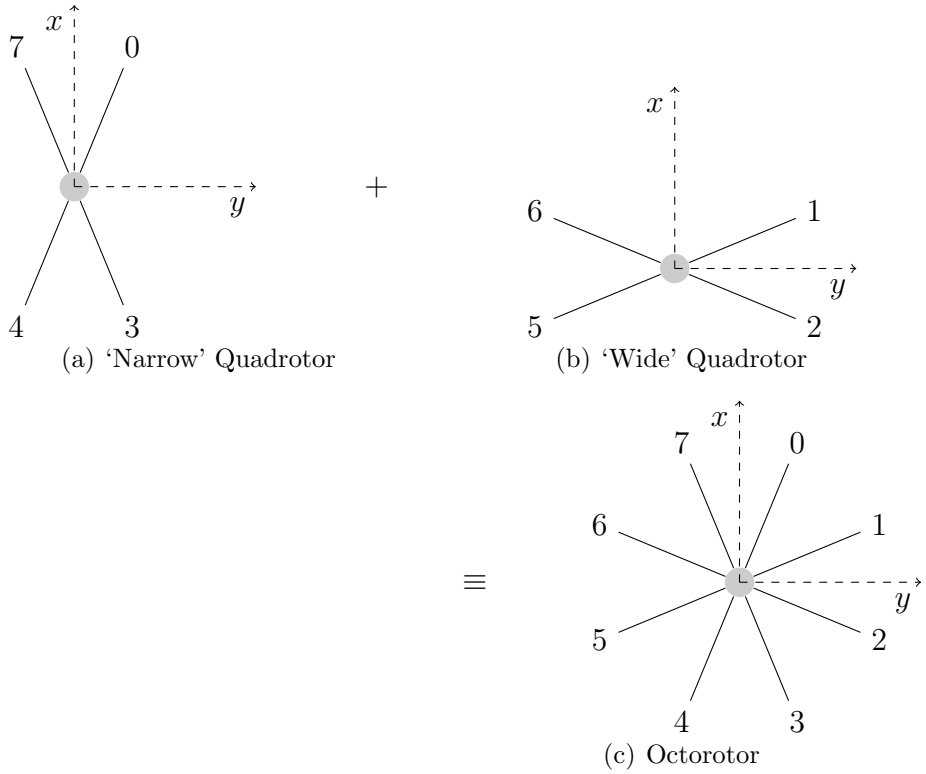

(a) 'Narrow' Quadrotor (b) 'Wide' Quadrotor

(c) Octorotor

Figure 3.10: 'Offset' Quadrotors Combined to form Octorotor, Alternating Rotation

The component quadrotors are no longer axisymmetric as they once were and possess only two planes of symmetry where they once had four. The quadrotor as shown in Figure 3.10a is more maneuvrable in pitch whilst the one in Figure 3.10b is more

maneuvrable in roll compared to pitch. If the controls are allocated so that only one group is utilised this will lead to the possibility that the second group will need to be temporatily used for roll control which means that the effectors will be switching on and off sporadically which causes vibration through the structure.

An optimum physical layout of the vehicle and the location of the effectors is an area for future study.

3.6 Conclusion

- This section has described how the linear control allocation is applied to the octorotor. The control allocation problem has been solved for the unconstrained and the constrained cases, and this lead to an investigation into novel application of the constraints to the individual effectors instead of on to the virtual controls. The result is that the control allocation can be considered to be the unconstrained problem which is simpler to solve and is guaranteed to be successful.
- Examples are given to demonstrate the control allocation scheme and how the effector constraints are implemented to provide successful allocation.
- The rotation of the thrust vector after allocation was discovered and is due to the physical setup of the vehicle where the effectors are grouped in to co-rotating pairs. If they are set as counter-rotation pairs then the adverse yaw is removed and the allocation is successful. This grouping has implications for the daisy chaining method as well as post-failure controllability analysis and will be the topic of future work.

Chapter 4

Controller

4.1 Introduction

This chapter discusses how closed loop control is implemented on the octorotor. The linearized model of the octorotor (2.67) is analysed by finding the eigenvalues of the linearized A matrix. This produces 12 poles, all of which are at the origin showing that the linearized system has marginal stability. For this reason a closed loop controller is implemented. As discussed in Chapter 2 the Euler angle attitude representation is valid for small perturbations about hover. Since the translational components of the vehicle depend on the vehicle attitude it is possible to implement a 'nested' control structure whereby position commands are converted directly to attitude commands. However, when the vehicle is away from the near-hover region the small angle approximations used for the simplified controller are no longer valid and do not give good results. For this reason a global controller utilising the quaternion attitude reference system is implemented.

Section 4.3 discusses how the error quaternion is derived and how pure attitude tracking is achieved. It is possible to calculate the desired pose of the vehicle in a quaternion frame and obtain the error from the current vehicle quaternion attitude. The quaternion attitude controller generates three constrained moment commands corresponding to the three attitude axes and provides for suitable attitude control, either to level hover or to a specified vehicle attitude.

The thrust required to track the vehicle altitude is determined by the altitude demand from the pilot. This demand is converted to the body centric axis scheme and a constraint is applied so that large altitude commands are ignored when the vehicle attitude is far from level, i.e. when the thrust vector is pointed far from vertical. This reduces the amount of lateral position perturbations when the vehicle recovers from an initial inverted condition.

4.2 Euler Control Scheme

A PD control scheme around a linear operating point is chosen for the first step in providing closed loop attitude control. The main purpose of the controller is to design the required accelerations around the three body axes and to provide sufficient overall thrust to track an altitude command. The vehicle is axisymmetric in x_b and y_b, which means that manoeuvres in those planes are attitude indifferent unless another restriction is enforced (such as carrying a gimbal mount for a camera with slew limits constrained by the platform).

It is possible to see from the equations of motion that the Euler angles and their time derivatives do not depend on the translation components. On the other hand, the translations depend on the angles. It is possible to use a 'nested' control design shown in Figure 4.1 (adapted from Bouabdallah et al. [2004b])

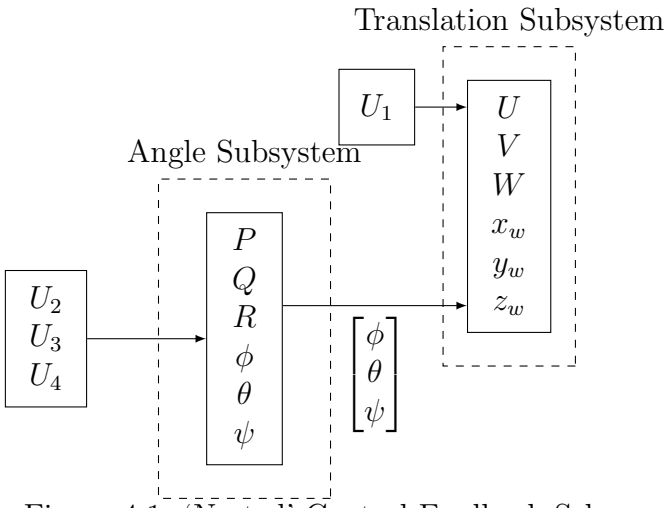

Figure 4.1: 'Nested' Control Feedback Scheme

The attitude demands are given by the reference signal r and can be generated by a pilot-in-the-loop or by a path planning algorithm. These are converted to the body axes using the rotation matrix R so that they are expressed in the body fixed reference system. Various measurements and calculations are performed in either the inertial or body frame. This is demonstrated in Figure 4.2.

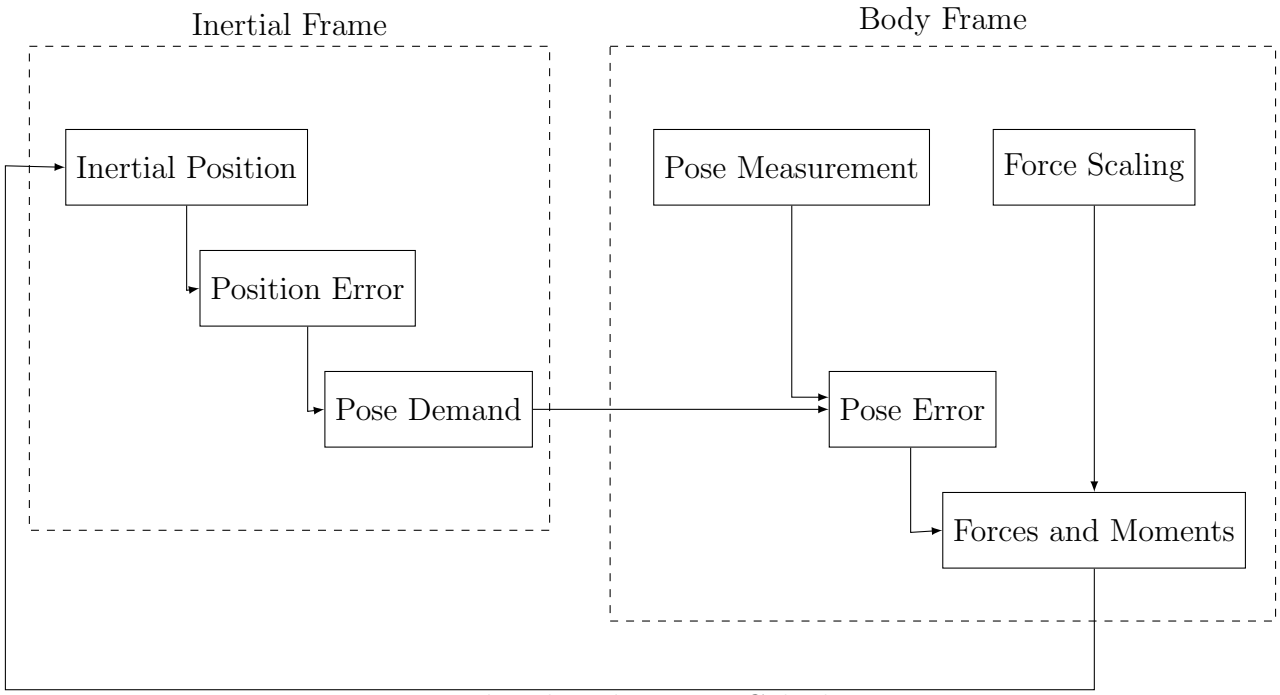

Figure 4.2: Inertial and Body Frame Calculations

For the vehicle operating in the linear region close to hover it is possible to remove cross coupling terms from the attitude state variable in (2.27) and the state derivatives $\dot{P}, \dot{Q}, \dot{R}$ are assumed to be proportional to the controller demands

$$\begin{bmatrix} \dot{P} \\ \dot{Q} \\ \dot{R} \end{bmatrix} = \text{diag}\left(\frac{1}{J_x}, \frac{1}{J_y}, \frac{1}{J_z}\right) \begin{bmatrix} \tau_2 \\ \tau_3 \\ \tau_4 \end{bmatrix} \tag{4.1}$$

Similar approximations are made to (2.22) and (2.24) to obtain

$$\dot{z} = W \tag{4.2}$$
$$\dot{\phi} = P \tag{4.3}$$
$$\dot{\theta} = Q \tag{4.4}$$
$$\dot{\psi} = R \tag{4.5}$$

For the position controller the demands are given in the inertial frame where the reference command is $\tau \in \mathbb{R}^4$ and consists of a latitude/longitude position (x_d, y_d), an altitude (z_d), and a yaw angle (Ψ_d). This generates the desired vehicle pose in the intertial frame which are described using the Euler notation for roll, pitch, and yaw angles as Φ_d, Θ_d, Ψ_d.

$$\begin{bmatrix} \tau_1 \\ \Phi_d \\ \Theta_d \\ \psi_d \end{bmatrix} = \begin{bmatrix} \frac{m}{\cos\phi\cos\theta}(K_{pz}(z_d - z) - K_{dz}(\dot{z}) + g) \\ K_{py}(y - y_d) + K_{dy}(\dot{y}) \\ -K_{px}(x - x_d) - K_{dx}(\dot{x}) \\ -\Psi_d \end{bmatrix} \tag{4.6}$$

Note that the interial frame Euler angle pose must now be rotated to the body frame Euler angle pose using the rotation matrix (2.7) to give ϕ_d, θ_d, and ψ_d. These body frame Euler angles are then used to determine the body frame attitude control moments τ_2, τ_3, and τ_4.

$$\tau_2 = (K_{p\phi}(\phi_d - \phi) - K_{d\phi}(\dot{\phi})) \tag{4.7}$$
$$\tau_3 = (K_{p\theta}(\theta_d - \theta) - K_{d\theta}(\dot{\theta})) \tag{4.8}$$
$$\tau_4 = (K_{p\psi}(\psi_d - \psi) - K_{d\psi}(\dot{\psi})) \tag{4.9}$$

The gain values were tuned by trial and error so as to be adaptable to different vehicle models and parameters. Gains in the roll and pitch controller (4.7) and (4.8) are identical since the vehicle has planes of symmetry along x_b and y_b. The gain values for the yaw controller, (4.9), are set lower than for the roll and pitch since the gyroscopic drag generated by the rotor turning is lower than the moment created when a rotor speed is increased. A high yaw rate demand is more likely to saturate the effectors. This means that the yaw response is more sluggish than the roll and pitch response. For most applications this is not a problem since the vehicle is axisymmetric and highly manoeuvrable in roll and pitch and can easily track global demands x_d, y_d.

The control allocation and effector saturations are not included in the analysis of the PD controller. This task is done in the control allocation block of the system. This means that it is possible that unfeasible control demands τ are output from the controller there will be a discrepancy between this and the output of the control allocation block $\mathbf{u}$ meaning $U \neq \tau$. If the controller is model based there will be a difference between the expected model output and the actual output. A different control method is used which utilises the quaternion attitude representation and accounts explicitly for effector saturation limits.

4.3 The Error Quaternion

Utilising the sequential rotation properties of quaternions [Diebel, 2006] the desired vehicle attitude can be represented as a rotation from the inertial frame to the body frame of the vehicle followed by a rotation from the body frame to the desired body orientation

$$\underbrace{\bar{q}_d}_{\text{inertial frame}} = \underbrace{\bar{q}}_{\text{inertial frame}} \otimes \underbrace{\bar{q}_e}_{\text{body frame}} \tag{4.10}$$

The quaternion $\bar{q}_e$ represents the error quaternion expressed in the body frame. Rearranging (4.10) using the conjugate properties of the quaternion yields the error quaternion expressed in the body frame as a quaternion multiplication between the actual attitude and the desired attitude:

$$\underbrace{\bar{q}_e}_{\text{body frame}} = \underbrace{\bar{q}^{-1}}_{\text{inertial frame}} \otimes \underbrace{\bar{q}_d}_{\text{inertial frame}} \tag{4.11}$$

With the error expressed in the body frame the elements of the quaternion directly map to the body forces and moments and a suitable control allocation method is used to generate commands for individual effectors.

4.4 Problem Statement, Pure Attitude Tracking

The objective is to implement a controller for the system (2.70),(2.71) to guarantee that the quaternion $\bar{q}$ of the vehicle can track a signal $\bar{q}_d$ by reducing q_e to $[0\ 0\ 0]^T$ as $t \to \infty$ regardless of attitude $\bar{q}$. If the desired quaternion coincides with the inertial frame then this objective is

$$\bar{q} \to [\pm 1\ 0\ 0\ 0]^T, \quad \vec{\omega} \to 0, \quad \text{as } t \to \infty \tag{4.12}$$

Note that (4.12) represents two equilibrium points ($q_0 = 1, q = [0\ 0\ 0]^T$ and $q_0 = -1, q = [0\ 0\ 0]^T$). These points represent the same point in physical space since quaternions double cover the set of attitudes $SO(3)$ in the sense that each attitude corresponds to two different quaternion vectors. Specifically, a physical attitude $R \in SO(3)$ is represented by a pair of antipodal quaternions $\pm\bar{q} \in \mathbb{S}^3$. Because of this we manipulate the control law formulation as demonstrated in the following section.

4.5 Control Law Formulation

This section introduces a bounded control law stabilising (2.70),(2.71). For this purpose a saturation function σ_M is introduced.

Definition 6. *Let $\sigma_M : \mathbb{R} \to [-\bar{M}, \bar{M}]$ denote the saturation function defined by:*

1. *$\sigma_M(s) = s$ if $|s| < \bar{M}$,*
2. *$\sigma_M(s) = sign(s)\bar{M}$ elsewhere.*

where $\bar{M}$ is the upper bound on the torque, M.

With this definition we obtain an expression for a bounded PD controller providing the controls $M = [M_1\ M_2\ M_3]^T$:

$$M_i = -\sigma_{\bar{M}_i}\left(\frac{\kappa\omega_i}{\rho_i} + \kappa q_i\right) \tag{4.13}$$

where $\sigma(\cdot)$ represents a saturation function described in Definition 6, $\bar{M}_i$ with $i \in \{1, 2, 3\}$ is the upper bound on the torque $|M_i|$, κ and ρ are variables which are used to tune the controller's sensitivity to angle and angular velocity errors such that $0 < \kappa \leq \min |M_i|/2$ and $\rho_i > 0$. The inputs (4.13) almost globally asymptotically stabilise the rigid body to the origin ($q_0 = 1, q = [0\ 0\ 0]^T$, and $\vec{\omega} = 0$).

Proof. We consider a Lyapunov function:

$$V = \frac{1}{2}\vec{\omega}^T J\vec{\omega} \tag{4.14}$$

Along the trajectories of the system we obtain

$$\dot{V} = \underbrace{\vec{\omega}^T(-\vec{\omega} \times J\vec{\omega})}_{=0} + \vec{\omega}^T M = \underbrace{\vec{\omega}_1\ M_1}_{\dot{V}_1} + \underbrace{\vec{\omega}_2\ M_2}_{\dot{V}_2} + \underbrace{\vec{\omega}_3\ M_3}_{\dot{V}_3} \tag{4.15}$$

Substituting (4.13) into (4.15) gives

$$\dot{V} = -\omega_i \sigma_{\bar{M}_i}\left(\frac{\kappa\omega_i}{\rho_i} + \kappa q_i\right) \tag{4.16}$$

with $i \in \{1,2,3\}$. Let $\Phi_i = \{\omega_i : |\omega_i| \leq \rho_i + \epsilon\}$ for some small $\epsilon > 0$. Outside Φ_i, using the normalised quaternion norm condition (2.51) it follows that $|\frac{\kappa\omega_i}{\rho_i} + \kappa q_i| \geq \frac{\kappa\epsilon}{\rho_i}$ and that $\frac{\kappa\omega_i}{\rho_i} + \kappa q_i$ and ω_i have the same sign. Therefore

$$\dot{V}_i = -\omega_i \sigma_{\bar{M}_i}\left(\frac{\kappa\omega_i}{\rho_i} + \kappa q_i\right) \leq -\frac{\kappa\epsilon}{\rho_i}|\omega_i| < -\frac{\kappa\epsilon(\rho_i + \epsilon)}{\rho_i} < -\kappa\epsilon < 0 \tag{4.17}$$

Consequently ω_i enters Φ_i in a finite time and remains in it. The unit quaternion cannot diverge since it is structurally unitary and therefore bounded.

Once in Φ_i we consider a new Lyapunov function

$$W = \frac{1}{2}\vec{\omega}^T J\vec{\omega} + \kappa\left((1-q_0)^2 + q^T q\right) = \frac{1}{2}\vec{\omega}^T J\vec{\omega} + 2\kappa(1-q_0) \tag{4.18}$$

Since J is positive definite, the Lyapunov function W is positive definite, radially unbounded, and belongs to the class C^2 [Guerrero-Castellanos et al., 2007]. The derivative of (4.18) is given by

$$\begin{aligned} \dot{W} &= \vec{\omega}^T J\dot{\vec{\omega}} - 2\kappa\dot{q}_0 = \underbrace{\vec{\omega}^T J(-\vec{\omega} \times J\vec{\omega}}_{=0} + \vec{\omega}^T M + \kappa q^T\vec{\omega} = \vec{\omega}^T M + \kappa q^T\vec{\omega} \\ &= \underbrace{\omega_1 M_1 + \kappa q_1\omega_1}_{\dot{W}_1} + \underbrace{\omega_2 M_2 + \kappa q_2\omega_2}_{\dot{W}_2} + \underbrace{\omega_3 M_3 + \kappa q_3\omega_3}_{\dot{W}_3} \end{aligned} \tag{4.19}$$

Similarly to V, $\dot{W}$ is a sum of three terms $\dot{W}_1, \dot{W}_2, \dot{W}_3$. Analysing $\dot{W}_i$ for $i \in \{1,2,3\}$ in a similar way done for $\dot{V}_i$ and using the definition of M_i from (4.13) gives

$$\dot{W}_i = -\omega\sigma_{\bar{M}_i}\left(\frac{\kappa\omega_i}{\rho_i} + \kappa q_i\right) + \kappa q_i\omega_i \tag{4.20}$$

In Φ_i we have

$$\left|\frac{\kappa\omega_i}{\rho_i} + \kappa q_i\right| \leq 2\kappa + \frac{\kappa\epsilon}{\rho_i} \tag{4.21}$$

If ϵ is sufficiently small and assuming that $2\kappa < M_i$

$$\left|\frac{\kappa\omega_i}{\rho_i} + \kappa q_i\right| \leq M_i \tag{4.22}$$

Consequently σ operates in a linear region

$$M_i = -\frac{\kappa}{\rho_i}[\omega_i + \rho_i q_i] \tag{4.23}$$

As a result (4.20) becomes

$$\dot{W}_i = -\frac{\kappa}{\rho_i}\omega_i^2 \tag{4.24}$$

therefore (4.19) becomes

$$\begin{aligned} \dot{W} &= \dot{W}_1 + \dot{W}_2 + \dot{W}_3 \\ &= -\kappa\left(\frac{\omega_1^2}{\rho_1} + \frac{\omega_2^2}{\rho_2} + \frac{\omega_3^2}{\rho_3}\right) \leq 0 \end{aligned} \tag{4.25}$$

The LaSalle Invariance Principle is invoked to complete this proof. All the trajectories converge to the largest invariant set $\bar{\Omega}$ in $\Omega = \{(q, \vec{\omega}) : \dot{V} = 0\} = \{(q, \vec{\omega}) : \vec{\omega} = 0\}$ In the invariant set, $J\dot{\vec{\omega}} = -\kappa q = 0$. To remain in $\bar{\Omega}$ one must satisfy $q = 0$ and $q_0 = \pm 1$ from the nomalised quaternion condition. These points correspond to a minimum ($W = 0$) and a local maximum ($W = 4$) of the Lyapunov function (4.18). $\dot{W} = 0$ at these points. If at $t_0 = 0$, the closed loop system lies at a local maximum it remains at this point for $t > t_0$. If at t_0 the closed loop system is away from these equilibrium points, and since $\dot{W} < 0$ outside the two equilibrium points then the system state will converge to the equilibrium point $\bar{q} = [1\ 0\ 0\ 0]^T, \vec{\omega} = 0$ and will remain there for all subsequent time since at this point $W = \dot{W} = 0$. □

A number of other Lyapunov functions are suggested for general attitude control Fragopoulos and Innocenti [2004], Hu et al. [2006], control of underwater vehicles [Fjellstad and Fossen, 1994, Yang et al., 2013], and spacecraft [Wie and Barba, 1985, Boskovic et al., 1999, Li et al., 2006, Bajodah, 2011].

Remark 1 As shown above $\bar{q} = [1\ 0\ 0\ 0]^T, \vec{\omega} = 0$ is a point of attraction. The point $\bar{q} = [-1\ 0\ 0\ 0]^T, \vec{\omega} = 0$ is considered a repelling point even though they both represent the same pose in $SO(3)$ (this can lead to unwinding). It is possible to reverse the attraction of these two points (with reference to (4.13)) by using the control

$$M_i = -\sigma_{\bar{M}_i}\left(\frac{\kappa\omega_i}{\rho_i} - \kappa q_i\right) \tag{4.26}$$

However, it is best to chose the shortest angular path and this is achieved using the control

$$M_i = -\sigma_{\bar{M}_i}\left(\frac{\kappa\omega_i}{\rho_i} + \text{sign}(q_0)\kappa q_i\right) \tag{4.27}$$

where the shorter of the rotation angles η and $2\pi - \eta$ is chosen. The control (4.27) stabilises globally asymptotically the two-point set in the quaternion space. This can be proven by using the Lyapunov function

$$W = \frac{1}{2}\vec{\omega}^T J\vec{\omega} + \begin{cases} 2\kappa(1 - q_0) & \text{if } q_0 \geq 0 \\ 2\kappa(1 + q_0) & \text{if } q_0 < 0 \end{cases} \tag{4.28}$$

The proposed control law (4.27) stabilises the vehicle to the inertial orientation with the shortest rotation. This is a desireable situation, however it is assumed that $\vec{\omega}$ can be controlled directly and instantly which is not true in practise. Consider a scenario where the yaw error is close to 180°. If the vehicle is steady then it does not make much time difference if the vehicle rotates around clockwise or counterclockwise. However if the vehicle has a high rotational speed (ω_z) around the z axis then it may be faster to rotate further in the same direction as the rotation than to stop the initial motion and then accelerate in the other direction. Heuristic methods can be used to find logic thresholds and then implement a non continuous control scheme [Schlanbusch et al., 2010, Mayhew et al., 2011, Bouhired et al., 2013].

If the control is applied as a continuous-time controller an arbitrarily small noise in the attitude measurements could cause chattering and therefore Mayhew et al. [2011] propose introducing a hysteretic regulation of the unit quaternion to the set ± 1. In practical terms this point represents when the vehicle is 180° away from the desired attitude, i.e. $q_0 = 0$. It is highly unlikely that the vehicle could be at such an attitude with no residual angular velocity since it would require a large external force in order to introduce such an error in the first place. This potential chattering is therefore not a concern for the practical application to the octorotor. In practice, a hysteric memory state is not required if the control law is implemented on a discrete-time controller since the output of a discrete-time controller is constant between two updates, the rotation direction is not changed during that period and so the discrete-time controller is analogous to a continuous-time controller with hysteresis [Bresciani, 2008].

Furthermore the definition of the $\text{sign}(q_0)$ function used here has a slight bias towards $\bar{q} = [1\ 0\ 0\ 0]^T$ since

$$\text{sign}(q_0) = \begin{cases} 1 & \text{if } q_0 \geq 0 \\ -1 & \text{if } q_0 < 0 \end{cases} \tag{4.29}$$

Remark 2 The stability analysis is carried out where the desired final orientation of the vehicle is algined with the inertial axes, $q \to q_d = [1\ 0\ 0\ 0]^T$. If the desired orientation is other than this then the control with reference to (4.11) is

$$M_i = -\sigma_{\bar{M}_i} \left(\frac{\kappa \omega_i}{\rho_i} + \text{sign}(q_{e0}) \kappa q_{ei} \right) \tag{4.30}$$

gives almost global unique solution to the problem.

Previous work (for example Guerrero-Castellanos et al. [2007] and Fresk and Nikolakopoulos [2013]) implemented a similar controller to solve the attitude control problem with no extension to implementing it to a position control system. This approach could be considered for a satellite or underwater vehicle, but is not suitable when controlling a vehicle in atmospheric flight. This is because the thrust vector must directed below the horizontal in order to provide any vertical force to counter gravity, else the vehicle will accelerate towards the ground.

In order to implement a position controller the error quaternion (4.11) is used to determine the required body moments in the body frame (4.30).

The vertical force is calculated in the inertial frame such that

$$\tau_{1i} = K_{pz}(z_d - z) - K_{dz}\dot{z} + mg \tag{4.31}$$

This is used to create the inertial thrust vector T_i. Since the effectors are vertically aligned with the vehicle body there can only be a force generated in the z_b direction leaving

$$T_i = \begin{bmatrix} 0 \\ 0 \\ \tau_{1i} \end{bmatrix} \tag{4.32}$$

This vector is rotated by the body attitude as in (2.61) to give the total thrust in the body frame T_b

$$T_b = \bar{q} \otimes \begin{bmatrix} 0 \\ T_i \end{bmatrix} \tag{4.33}$$

The control allocation problem becomes

$$\tau = B\mathbf{u} \tag{4.34}$$

$$\mathbf{u} = B^{\dagger} \begin{bmatrix} T_b \\ M_i \end{bmatrix} \tag{4.35}$$

with $T_b \in \mathbb{R}$ and $M_i \in \mathbb{R}^3$.

4.6 Attitude Control and Full Position Control

Definition 7. *Attitude control refers to the vehicle tracking a desired attitude and does not consider vertical tracking, i.e.* $\tau = M_i \in \mathbb{R}^3$. *Full position control is used where the altitude tracking is included in the control demands such that* $\tau = [T_b \ M_i]^T \in \mathbb{R}^4$.

4.6.1 Attitude Control

The α function is used to determine the 'switching' in the control logic whereby attitude control is prioritised over full position control. The rationale behind this is that when the vehicle is far away from a linear operating point (such as hover) a demand to maintain altitude will result in a large thrust demand in the body axis. This leads to two linked outcomes:

- the effectors will reach their saturation limits and will likely attempt to produce maximum thrust, leading to
- the vehicle not performing an attitude control manoeuvre and instead will travel in the direction of the non-rotating thrust vector leading to large position error.

One case where this happens is when the vehicle is initialised with an inverted attitude. In such a case the body centric thrust demand will be $T_b = -T_i$ which, due to the physical restrictions of the motors, is un-allocate-able.

The idea is therefore to ascertain a maximum upset condition away from level flight at which the controller switches from providing 4 control inputs ($\tau \in \mathbb{R}^4$) and instead provides only attitude control ($\tau \in \mathbb{R}^3$) for allocation. This condition is termed $\alpha_{\max}$. The upset condition α is based on the norm constraint on the quaternion attitude representation and is calculated as

$$\alpha = \sqrt{q_1^2 + q_2^2} \tag{4.36}$$

It can be seen from Figure 4.3 (representing a 2-d frame) that as the vehicle rotates, the thrust vector generated in the body frame T_b rotates in the inertial frame and provides a force contribution in the inertial frame, T_i. This inertial force accelerates the vehicle away from the desired final position. The higher values of α give a larger disturbing force in the inertial frame for two reasons:

- the thrust vector is further away from the vertical, and
- at higher values of α the force required to maintain altitude (described in the body frame) is large.

For this reason the lower values of $\alpha_{\max}$ can contribute smaller positional disturbances since the full position control is only implemented at low values of α. When $\alpha \leq \alpha_{\max}, \tau \in \mathbb{R}^4$, else $\tau \in \mathbb{R}^3$. However, this is a trade off with altitude tracking since the vehicle will be performing an attitude control manoeuvre for a longer time and therefore will accelerate with gravity for that duration.

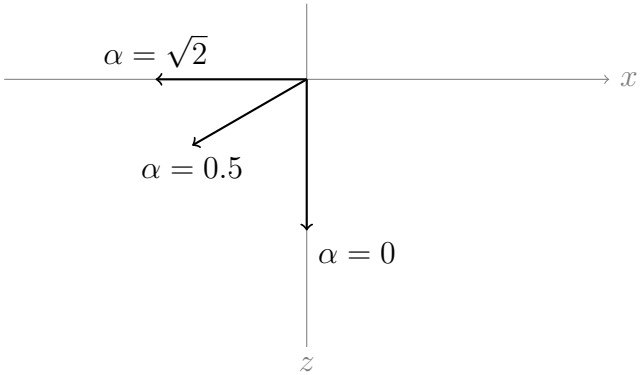

Figure 4.3: Demonstration of Thrust Vector Rotation in the Inertial Frame

4.6.2 Constraints for Attitude Commands

Generating the error quaternion for position control must be done with care if the position error or inertial velocity of the vehicle is high. For this reason a saturation

term β is introduced to $\bar{q}_d$ in (4.10) such that the desired inertial body attitude Φ is restricted such that

$$\Phi = \min(\Phi,\ \text{sign}(\Phi)\beta) \tag{4.37}$$

where β is specified in the controller. A high value of β can lead to instabilities if it is much higher than $\alpha_{\max}$ since the controller will be setting a desired attitude which will generate an output $\tau \in \mathbb{R}^3$ and full position tracking is lost. A low value of β leads to poor response and tracking of position and altitude reference signals since the constraint will be applied even for small manoeuvres. β is also implemented for Θ. An example is given below.

Example 8 Initial conditions $x_w = y_w = z_w = \psi = 0$. Desired final position $x_d = 20, y_d = z_d, \psi_d = 0$.

Using (4.6) and (4.8) and considering the first time step in the simulation so that the initial states where all zero:

$$\begin{aligned} \Theta_d &= -K_{px}(x - x_d) - K_{dx}\dot{x} && (4.38)\\ &= -0.15(0 - 20) - 0.25 \times 0 && (4.39)\\ \Theta_d &= 3 > \beta && (4.40) \end{aligned}$$

Therefore the restriction is invoked and $\Theta_d = \beta$. Considering the first time step in the simulation the rotation matrix $R = I$ and so $\theta_d = \Theta_d$.

$$\begin{aligned} \tau_3 &= K_{p\theta}(\theta_d - \theta) - K_{d\theta}\dot{\theta} && (4.41)\\ \tau_3 &= 0.35(\beta - \theta) - 0.07\dot{\theta} && (4.42) \end{aligned}$$

In general the errors on the position demands will be small so Φ_d and Θ_d should not exceed β. However the constraint term is still included because:

- after a failure the vehicle may be far from its original path and the error is large,
- a collision may disturb the vehicle a long way from the initial path, and
- a software glitch or loss of GPS signal could generate a very large error. Applying a constraint allows for some software protection.

4.7 Conclusion

- It is feasible that large body angles can be encountered during an effector failure and so an Euler angle control strategy is rejected and a quaternion controller is used. This controller does not suffer from gimbal lock and also does not experience 'unwinding' due to the way in which the error quaternion is defined.
- Two novel terms are introduced to limit potential flightpath divergence after effector failure or software malfunction.

Chapter 5

Simulation Results

5.1 Introduction

This section contains simulation results to demonstrate the quaternion attitude controller. The first missions demonstrate how the values of $\alpha_{\max}$ and β affect the position control of the vehicle when recovering from an initial disturbed attitude. These values are chosen from the simulation cases and three further missions are flown to demonstrate how the vehicle tracks position control demands. The effect of the effector saturation limits are demonstrated by reducing the upper constraint so that for an altitude step the virtual control exceeds the constraint. The settling time of the system is increased when the virtual controls exceed the constraints.

5.2 Mission Outlines

The first stage in selecting the values of $\alpha_{\max}$ and β was to consider a number of mission scenarios where the desired final vehicle position is $x_d = 0, y_d = 0, z_d = 0$ in the inertial frame, and initial attitudes are:

Mission 1 : $\phi = 0,\ \theta = \frac{\pi}{2},\ \psi = 0$

Mission 2 : $\phi = \frac{\pi}{2},\ \theta = \frac{\pi}{2},\ \psi = 0$

Mission 3 : $\phi = 0,\ \theta = \pi,\ \psi = 0$

Mission 4 : $\phi = 0,\ \theta = 0,\ \psi = \pi$

These scenarios cover the most extreme of initial body attitudes and so represent the threshold performance required for the vehicle to rotate the thrust vector in any direction to follow a flight path.

A number of position missions are specified with the vehicle initially at a level hover and tasked to reach the following positions:

Mission 5 : $x_{\mathrm{d}} = 2,\ y_{\mathrm{d}} = 0,\ z_{\mathrm{d}} = 0$

Mission 6 : $x_{\mathrm{d}} = 10,\ y_{\mathrm{d}} = 0,\ z_{\mathrm{d}} = 0$

Mission 7 : $x_{\mathrm{d}} = 0,\ y_{\mathrm{d}} = 0,\ z_{\mathrm{d}} = 10$

Using the axisymmetric property of the octorotor any position change demand in x_w is equivalent to a position change demand in y_w and so missions 5 and 6 represent a scenario where the vehicle is away from the target in either x_w or y_w. Mission 7 is used to show how the vehicle tracks an altitude demand and is a simple vertical ascent. For all missions the desired outcome is that the vehicle state variables shall be

$$X = \begin{bmatrix} x_w \\ y_w \\ z_w \\ \dot{x}_w \\ \dot{y}_w \\ \dot{z}_w \\ q_0 \\ q_1 \\ q_2 \\ q_3 \\ \omega_x \\ \omega_y \\ \omega_z \end{bmatrix} = \begin{bmatrix} x_d \\ y_d \\ z_d \\ 0 \\ 0 \\ 0 \\ \pm 1 \\ 0 \\ 0 \\ 0 \\ 0 \\ 0 \\ 0 \end{bmatrix} \tag{5.1}$$

as $t \to \infty$. This is representative of a level hover at the desired position x_d, y_d, z_d. The initial state variables X_{initial} and desired final state variables X_{desired} for the Missions are given in each Mission's subsection. The plots show 'corridors' which define the limits of the deviation from the desired flightpath. This representation makes it possible to show how the values of $\alpha_{\max}$ and β cannot be considered in isolation, but carefully selected to ensure that the vehicle is controllable.

5.3 Mission 1

$$X_{\text{initial}} = \begin{bmatrix} 0 \\ 0 \\ 0 \\ 0 \\ 0 \\ 0 \\ 0.7071 \\ 0 \\ 0.7071 \\ 0 \\ 0 \\ 0 \\ 0 \end{bmatrix}, \quad X_{\text{desired}} = \begin{bmatrix} 0 \\ 0 \\ 0 \\ 0 \\ 0 \\ 0 \\ 1 \\ 0 \\ 0 \\ 0 \\ 0 \\ 0 \\ 0 \end{bmatrix} \tag{5.2}$$

In this mission the initial attitude represents a 90° positive pitch angle around the y_b axis leaving z_b aligned with x_w and x_b opposite to z_w. As shown in Section 2.8 if the Euler representation is used for the controller then this results in gimbal lock as the roll and the yaw axes are collocated.

When $\alpha > \alpha_{\max}$ the controller is in attitude control mode only ($\tau \in \mathbb{R}^3$) and the altitude tracking is ignored.Only when $\alpha \leq \alpha_{\max}$ does the vehicle regain lost altitude with $\tau \in \mathbb{R}^4$. Figure 5.1 shows the 'corridor' of the flight path as the vehicle deviates from the original position as the values of $\alpha_{\max}$ and β are changed. This corridor represents the extreme values of x_w and shows the position is successfully controlled.

The x_w corridor widens as the value of $\alpha_{\max}$ increases since the full position control $\tau \in \mathbb{R}^4$ is used with a higher body attitude α leading to a larger non-zero term in T_i. When $\alpha_{\max} > 0.20$ there is no overshoot when returning to the original position.

β has a small effect on the flight path because the overall position error remains small and the vehicle does not deviate more than 0.9m away from the initial position. The only real effect is seen when $\alpha_{\max} = 0.35$ and $\alpha_{\max} = 0.40$. This is because T_i is large in this scenario and so the x_w velocity is large, which could introduce the saturation function β.

For this pure pitch recovery manoeuvre there is no deviation in y_w and these plots are therefore not included. The altitude tracking is shown in Figures 5.2(a), 5.2(b).

As $\alpha_{\max}$ increases the maximum $-z_w$ position (the altitude drop) decreases. This is because the vehicle is in the free-fall, attitude control state for a shorter time. None of the simulations showed overshoot of the altitude position and so only the altitude drop is shown on the Figures 5.2(a), 5.2(b).

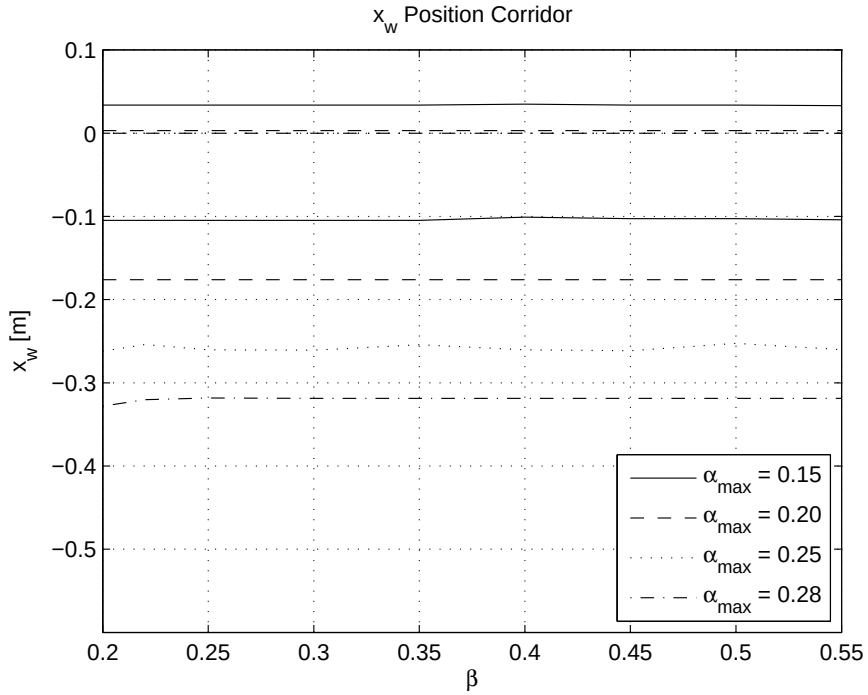

(a) $0.15 \leq \alpha_{\max} \leq 0.30$

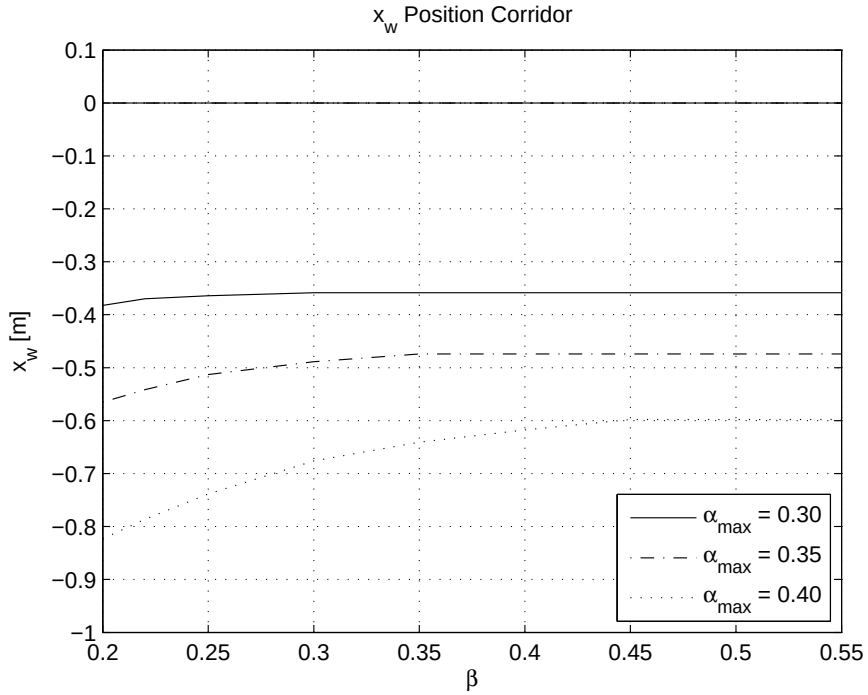

(b) $0.30 \leq \alpha_{\max} \leq 0.40$

Figure 5.1: Mission 1, x_w Corridor

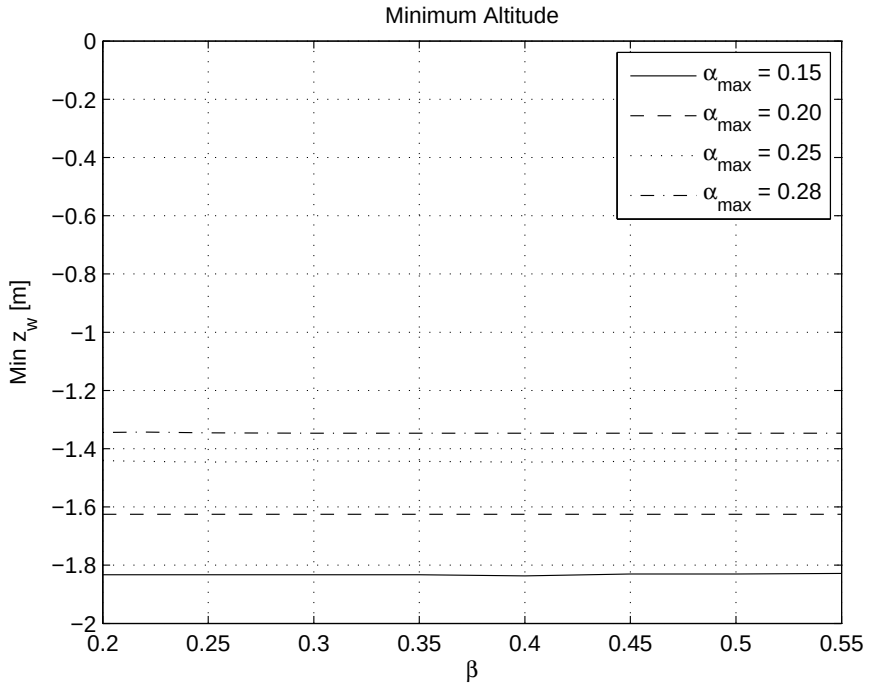

(a) $0.15 \leq \alpha_{\max} \leq 0.30$

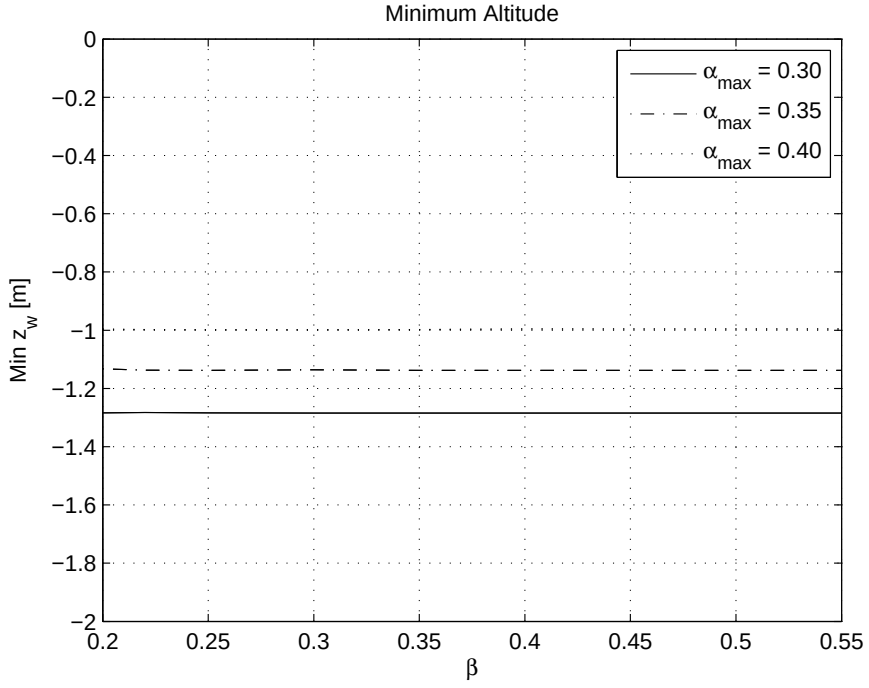

(b) $0.30 \leq \alpha_{\max} \leq 0.40$

Figure 5.2: Mission 1, Minimum Altitude

5.4 Mission 2

$$X_{\text{initial}} = \begin{bmatrix} 0 \\ 0 \\ 0 \\ 0 \\ 0 \\ 0 \\ 0.5 \\ -0.5 \\ 0.5 \\ 0.5 \\ 0 \\ 0 \\ 0 \end{bmatrix}, \quad X_{\text{desired}} = \begin{bmatrix} 0 \\ 0 \\ 0 \\ 0 \\ 0 \\ 0 \\ 1 \\ 0 \\ 0 \\ 0 \\ 0 \\ 0 \\ 0 \end{bmatrix} \tag{5.3}$$

This mission is representative of the vehicle pitching 90° and then rolling 90°. It can also be described as yawing 90° and then pitching 90°. The quaternion representation avoids gimbal lock and allows for the controller to bring the vehicle back to level hover over the initial position. This scenario shows that the controller is able to return the vehicle to the initial position when it is perturbed in two inertial axes, x_w and y_w.

None of the combinations of $\alpha_{\max}$ and β show overshoot in the x_w position shown in Figure 5.3. As $\alpha_{\max}$ is increased the vehicle is further perturbed from the desired x_w position due to the orientation of the thrust vector. Since the initial attitude is a combination of roll and pitch the y_w position is considered in Figures 5.4.

Increasing the value of $\alpha_{\max}$ increases the overshoot of the y_w recovery. The perturbations away from the desired position are slightly affected by choice of $\alpha_{\max}$. All combinations of $\alpha_{\max}$ and β are shown to bring the vehicle back to the desired position.

As $\alpha_{\max}$ is increased the altitude drop decreases as shown in Figure 5.5. This is because the vehicle is in the free-fall, attitude control state for a shorter time. None of the simulations showed overshoot of the altitude position and so this is not shown on the Figures 5.5 where the minimum value of z_w is plotted.

The altitude drop in Mission 2 is larger than for Mission 1 due to the definition of $\alpha_{\max}$ (Section 4.5). Here the attitude is a compound of the two rotations and so it takes longer until $\alpha \leq \alpha_{\max}$.

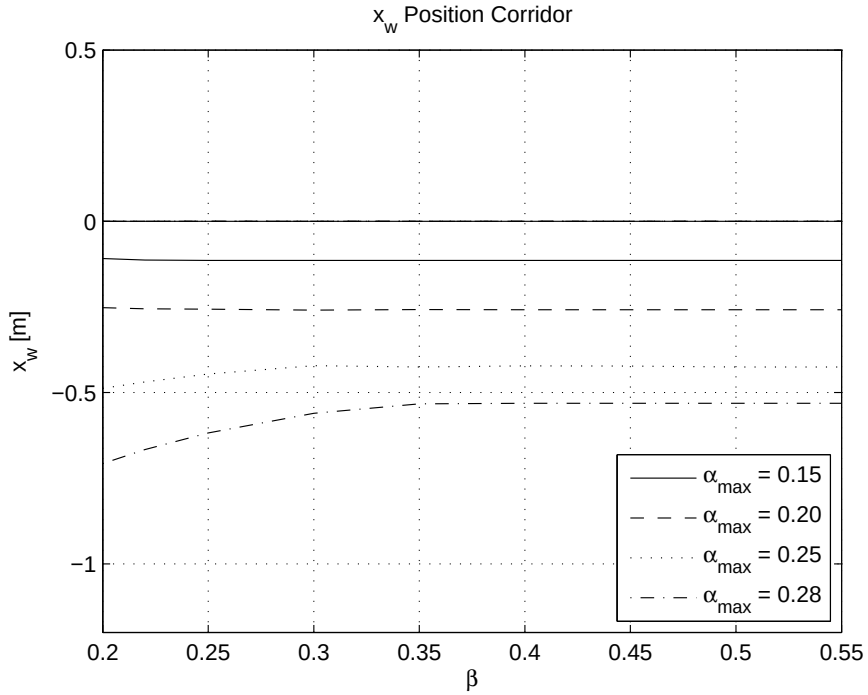

(a) $0.15 \leq \alpha_{\max} \leq 0.30$

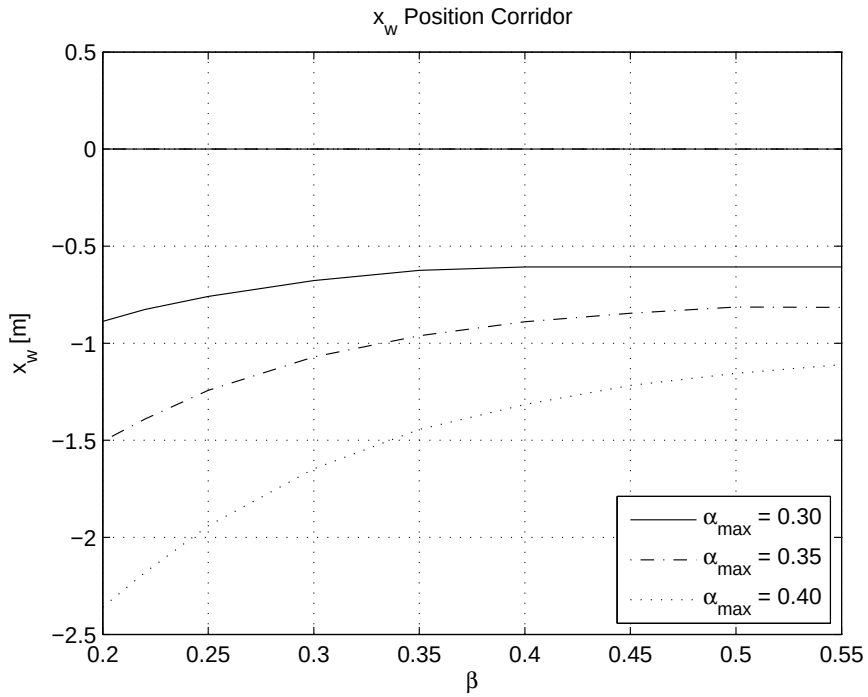

(b) $0.30 \leq \alpha_{\max} \leq 0.40$

Figure 5.3: Mission 2, x_w Corridor

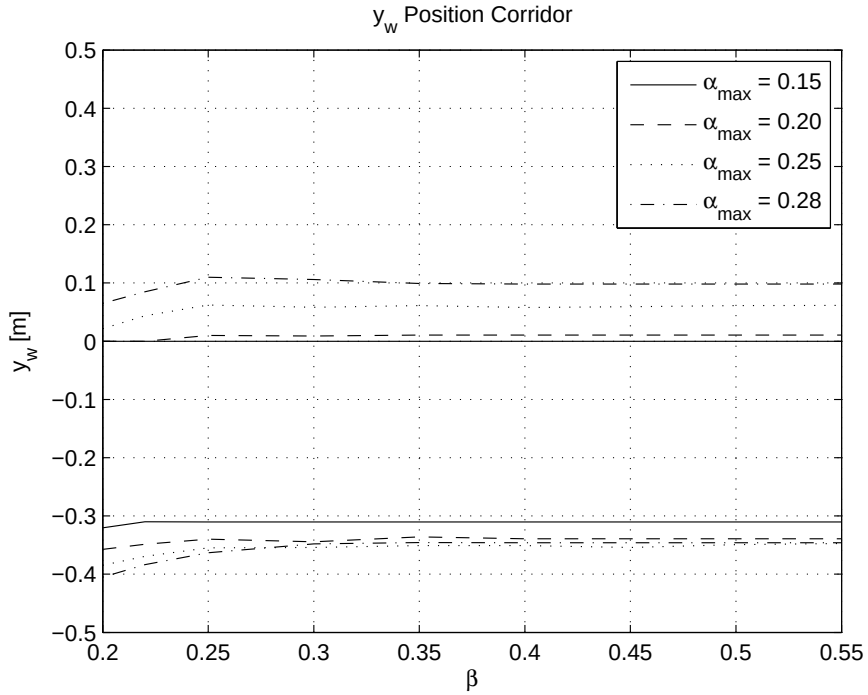

(a) $0.15 \leq \alpha_{\max} \leq 0.30$

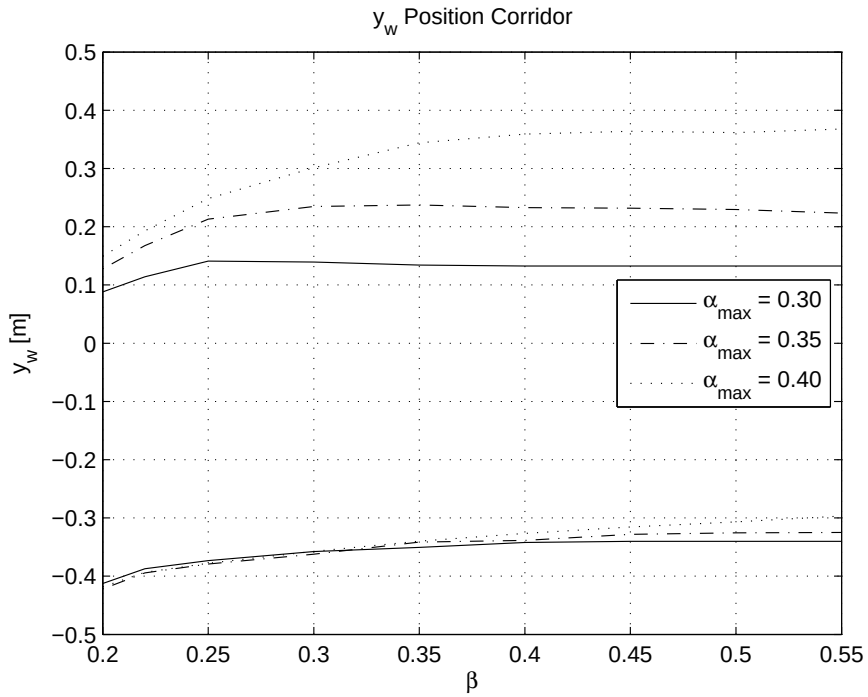

(b) $0.30 \leq \alpha_{\max} \leq 0.40$

Figure 5.4: Mission 2, y_w Corridor

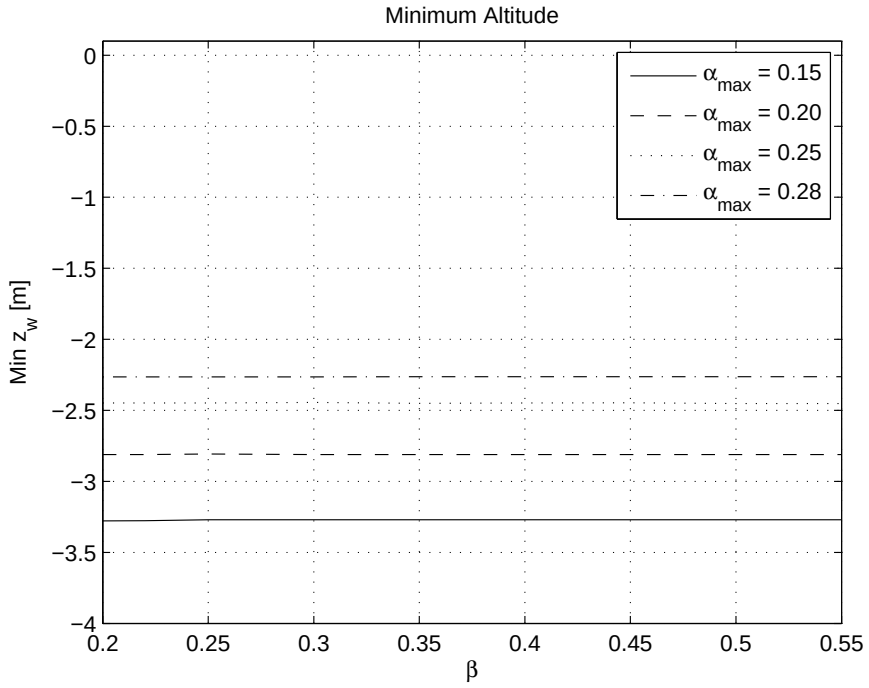

(a) $0.15 \leq \alpha_{\max} \leq 0.30$

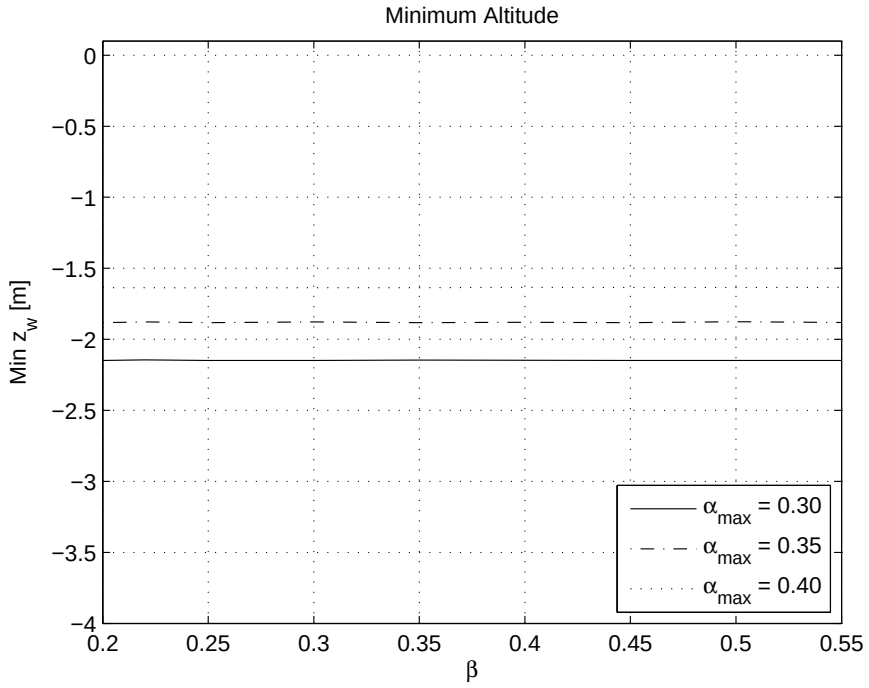

(b) $0.30 \leq \alpha_{\max} \leq 0.40$

Figure 5.5: Mission 2, Minimum Altitude

5.5 Mission 3

$$X_{\text{initial}} = \begin{bmatrix} 0 \\ 0 \\ 0 \\ 0 \\ 0 \\ 0 \\ 0 \\ 0 \\ 1 \\ 0 \\ 0 \\ 0 \\ 0 \end{bmatrix}, \quad X_{\text{desired}} = \begin{bmatrix} 0 \\ 0 \\ 0 \\ 0 \\ 0 \\ 0 \\ 1 \\ 0 \\ 0 \\ 0 \\ 0 \\ 0 \\ 0 \end{bmatrix} \tag{5.4}$$

In this mission the vehicle is initialised inverted over the desired position. Since the rotor blades are fixed pitch they cannot produce a negative T_b. If they are constrained to only produce a positive T_b then without adapting the control laws to include $\alpha_{\max}$ the resultant thrust values will be allocated to zero and no attitude manoeuvre will take place – the vehicle will simply accelerate with gravity.

By including $\alpha_{\max}$ the vehicle performs an attitude control manoeuvre so that the thrust vector is pointing below the horizon and then completes the manoeuvre by considering the altitude and returning to level hover over the starting position. As $\alpha_{\max}$ is increased for a given β the maximum negative x_w position increases. This is because the thrust vector is rotated further from the vertical as explained in Section 4.6.1. When β is much higher than $\alpha_{\max}$ the vehicle overshoots when recovering position and as shown for example $\alpha_{\max} = 0.15, \beta > 0.3$ in Figure 5.6(a) does not recover. The $\alpha_{\max}, \beta$ combination is therefore not suitable.

As with Mission 1 the vehicle recovers by pitching and so there is no motion in the y_w axis. Figures showing the y_w position are therefore not included. The loss of altitude was considered and is shown in Figure 5.7. Note that in this scenario the lower values of $\alpha_{\max}$ coupled with the higher values of β results in vehicles that are not controllable and are in free-fall. This is shown in Figure 5.7a for $\alpha_{\max} \leq 0.25$. The minimum altitude far exceeds the limits of the plot and therefore the combination of $\alpha_{\max}$ and β would result in destruction of the vehicle.

Overall the values of $\alpha_{\max}$ do not have a significant impact on the altitude loss provided that, as when considering the x_w position, β is not much larger than $\alpha_{\max}$ where in such a case the altitude control is lost and the vehicle accelerates towards the ground. For $\alpha_{\max} \geq 0.28$ the vehicle stabilises and returns to the desired altitude.

Based on the selected missions and from the results of the simulations the value of $\alpha_{\max}$ was selected as 0.28, and $\beta = 0.22$. The following figures show the vehicle attitude quaternion $\bar{q}$ and position (x_w, y_w, z_w) plots for Mission 1, Mission 2, and Mission 3.

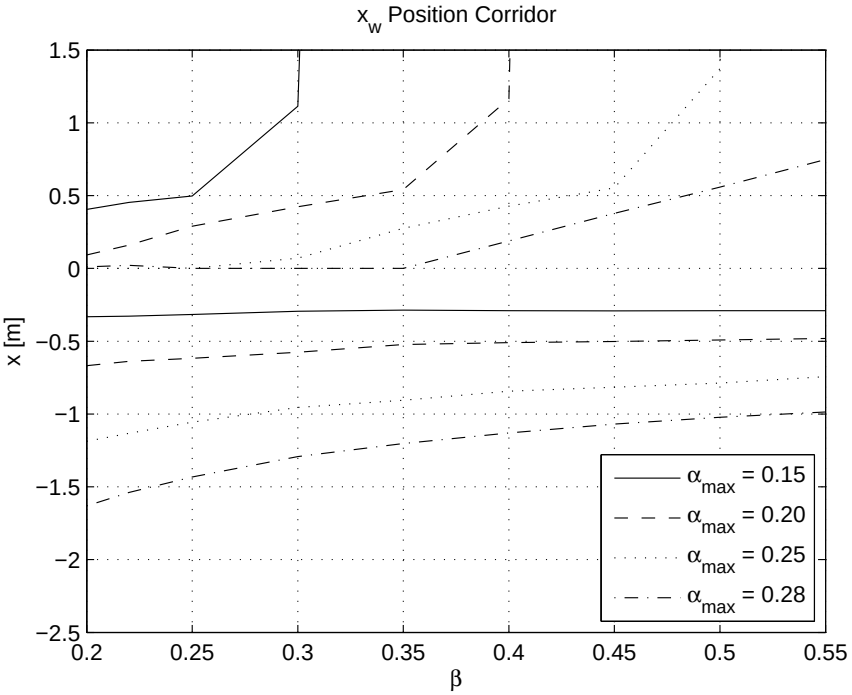

(a) $0.15 \leq \alpha_{\max} \leq 0.30$

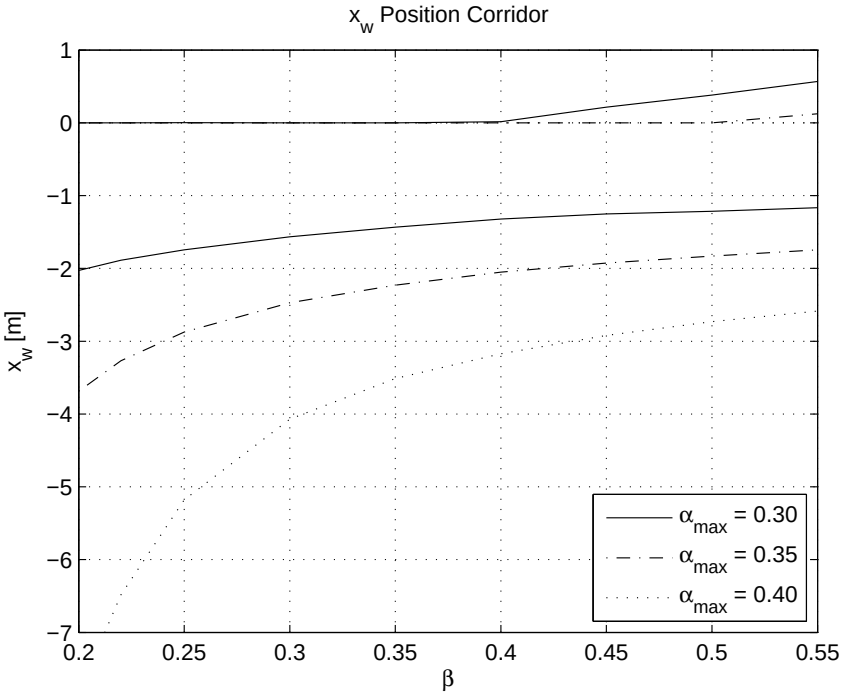

(b) $0.30 \leq \alpha_{\max} \leq 0.40$

Figure 5.6: Mission 3, x_w Corridor

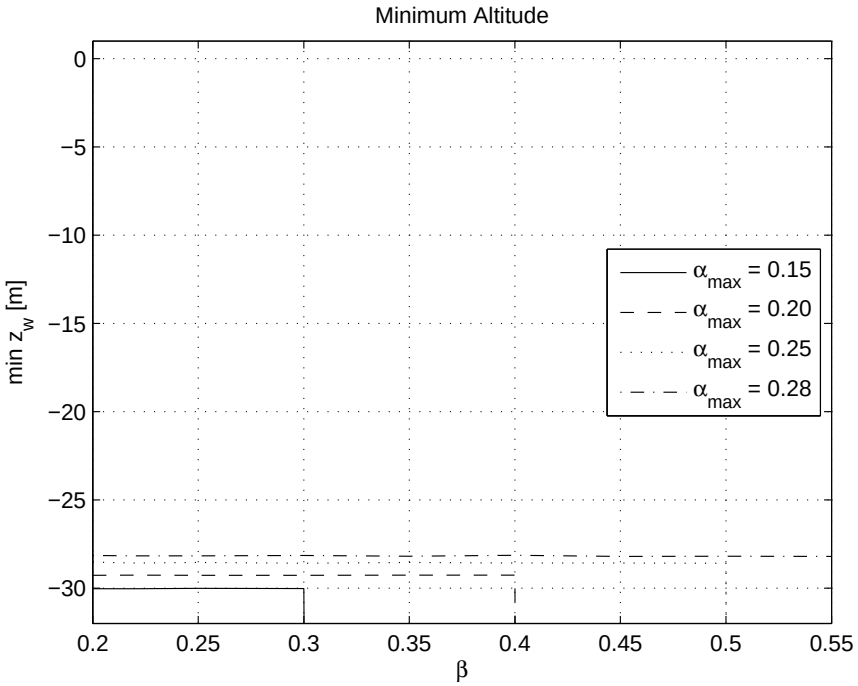

(a) $0.15 \leq \alpha_{\max} \leq 0.30$

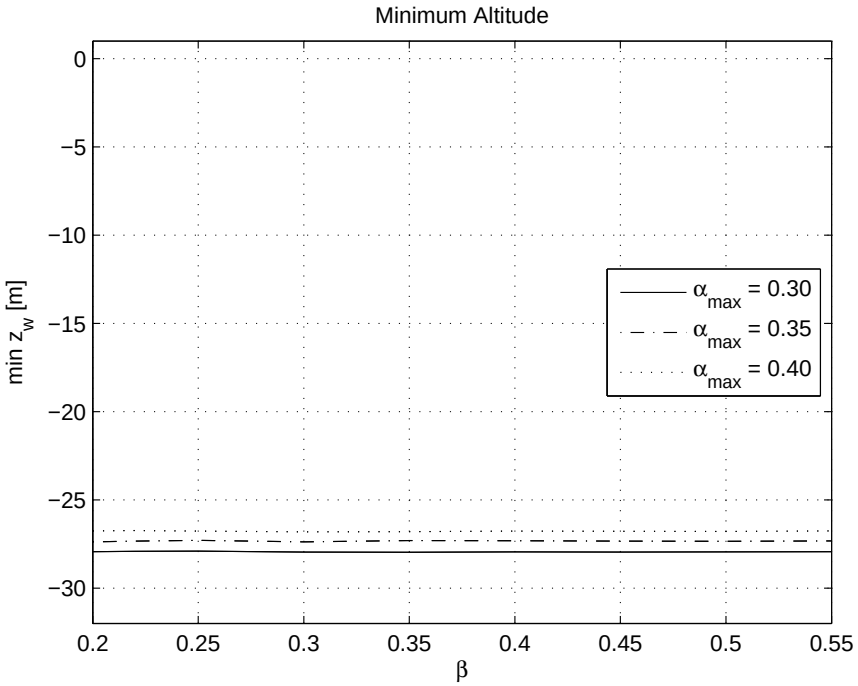

(b) $0.30 \leq \alpha_{\max} \leq 0.40$

Figure 5.7: Mission 3, Minimum Altitude

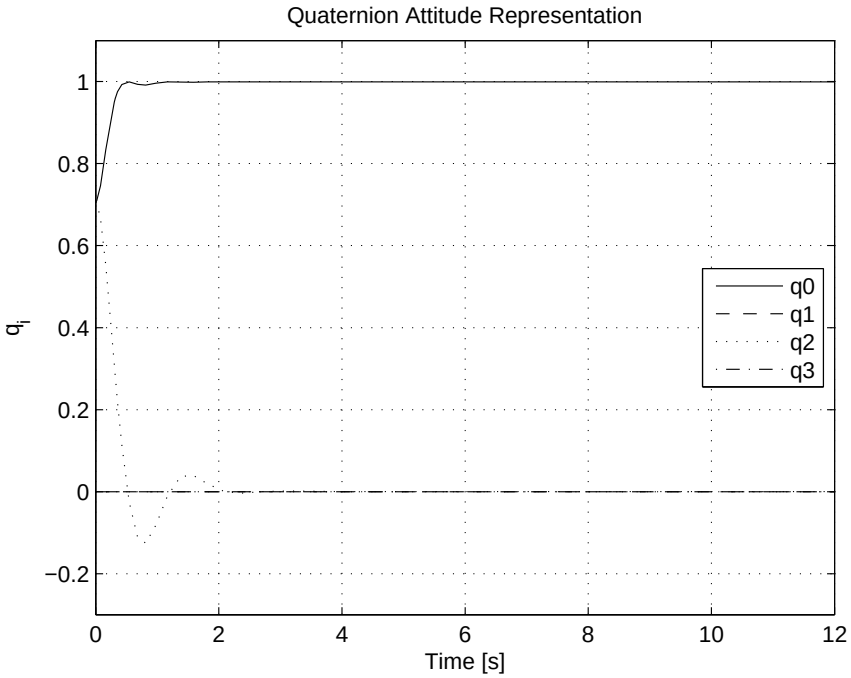

(a) Quaternion Attitude Response

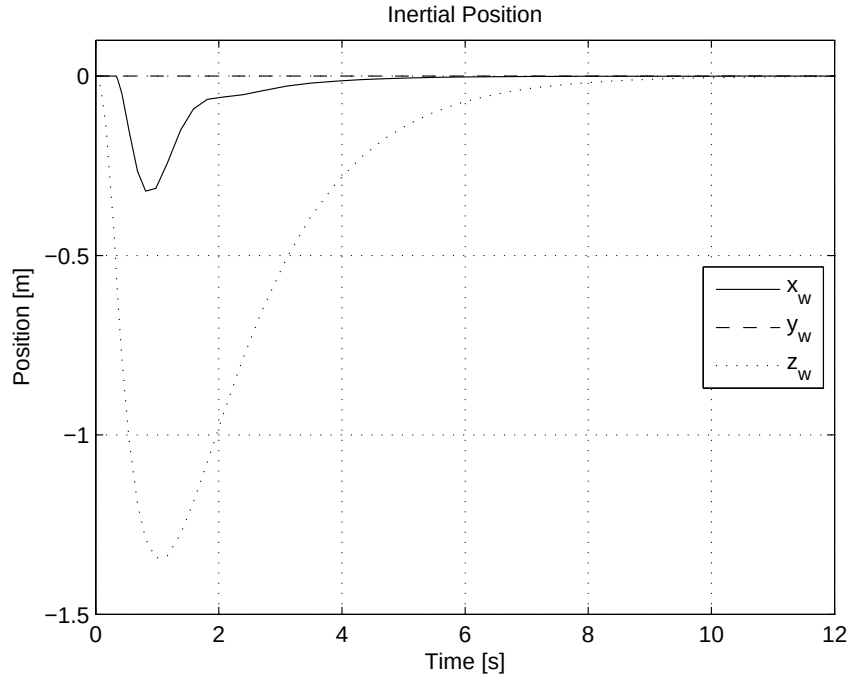

(b) Position Response

Figure 5.8: Mission 1

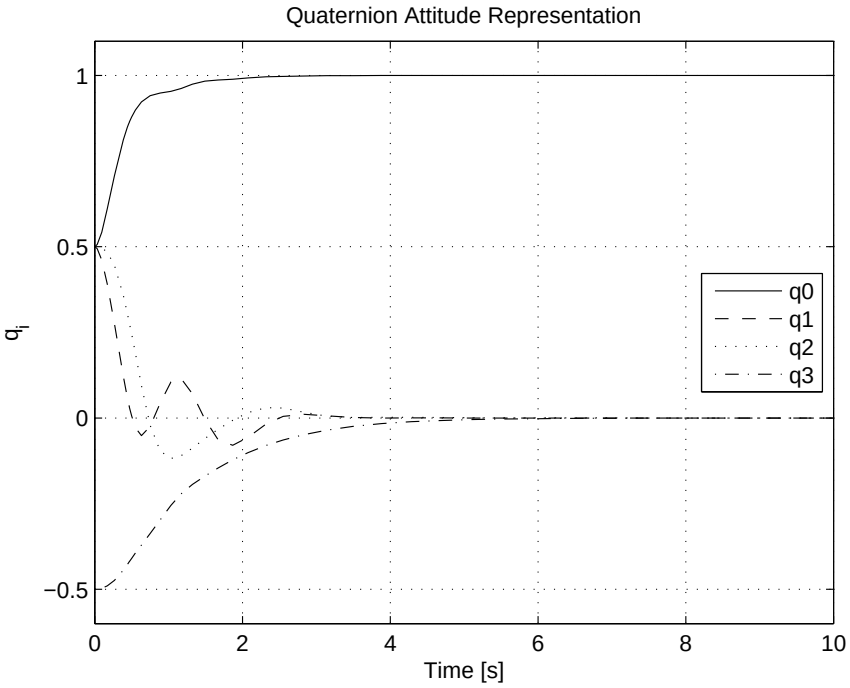

(a) Quaternion Attitude Response

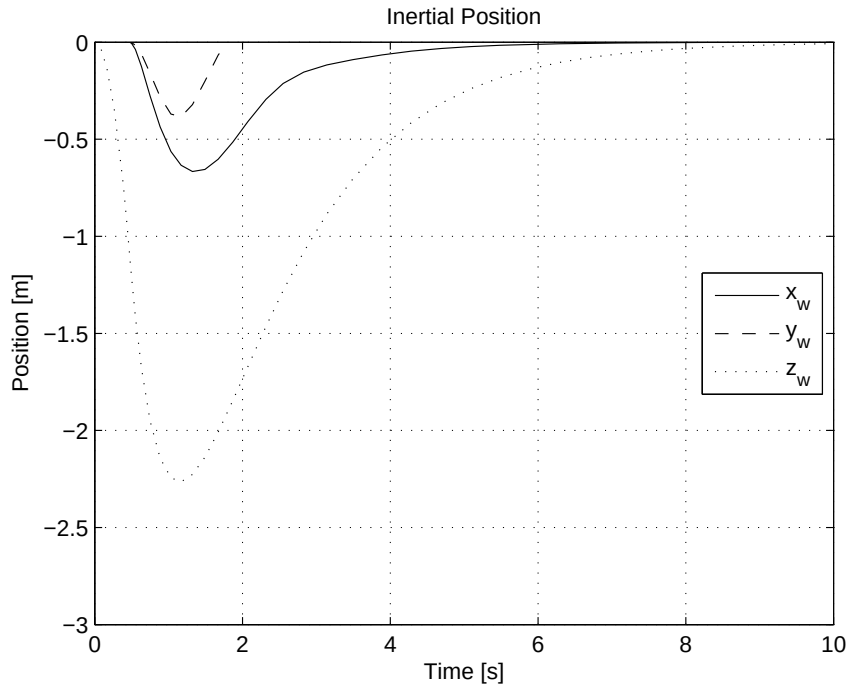

(b) Position Response

Figure 5.9: Mission 2

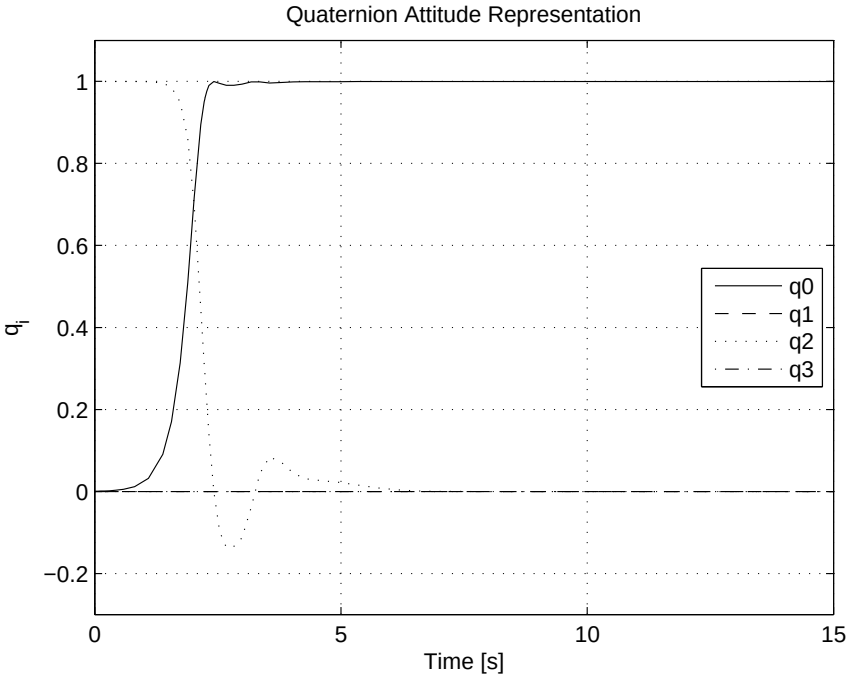

(a) Quaternion Attitude Response

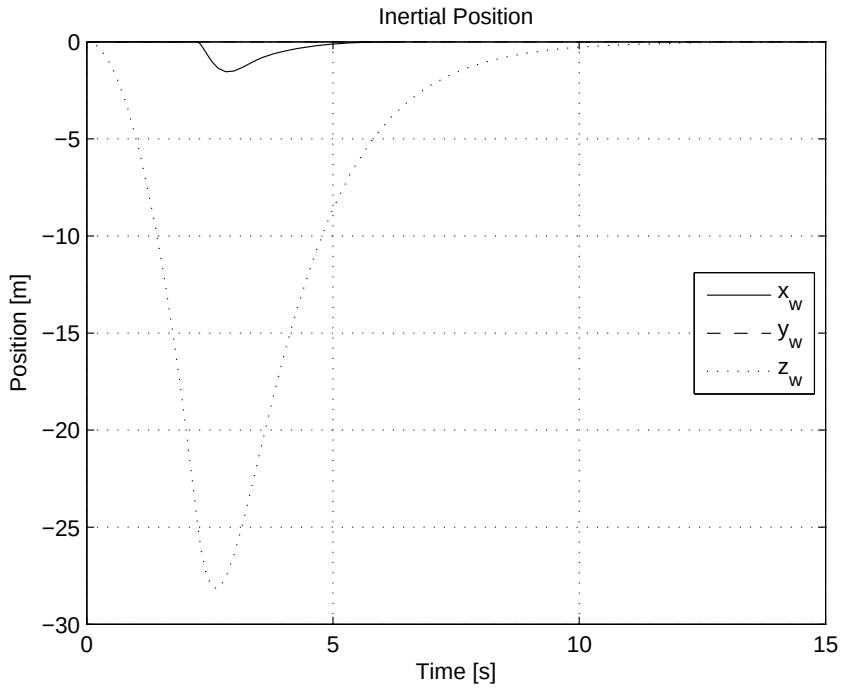

(b) Position Response

Figure 5.10: Mission 3

The position response of the vehicle may appear sluggish. This is due to the fact that the large initial perturbation must first be countered before position control is implemented. Nominal position response is demonstrated in Missions 5, 6, amd 7.

5.6 Mission 4

$$X_{\text{initial}} = \begin{bmatrix} 0 \\ 0 \\ 0 \\ 0 \\ 0 \\ 0 \\ 0 \\ 0 \\ 1 \\ 0 \\ 0 \\ 0 \end{bmatrix}, \quad X_{\text{desired}} = \begin{bmatrix} 0 \\ 0 \\ 0 \\ 0 \\ 0 \\ 0 \\ 1 \\ 0 \\ 0 \\ 0 \\ 0 \\ 0 \end{bmatrix} \tag{5.5}$$

Mission 4 is chosen to confirm that the value of $\alpha_{\max}$ and β do not impact the yaw control performance, and that the effectors are not saturated when tasked to rotate the vehicle through π radians. As defined in Section 4.5 the yaw component of the quaternion vector is not considered in deriving α due to the rotation order of the quaternion representation (the vehicle is first yawed and then pitched and rolled it does not matter what the yaw angle is since we are only interested in the direction of the thrust vector with respect to the inertial frame horizontal when considering whether we do attitude control $\tau \in \mathbb{R}^3$ or position control $\tau \in \mathbb{R}^4$).

The vehicle is initialised with a yaw angle of 180°, keeping z_b aligned with z_w and making $x_b = -x_w$ and $y_b = -y_w$. The inertial position of the vehicle does not change during this manoeuvre and so is not shown. The quaternion attitude representation of the vehicle is shown in Figure 5.11.

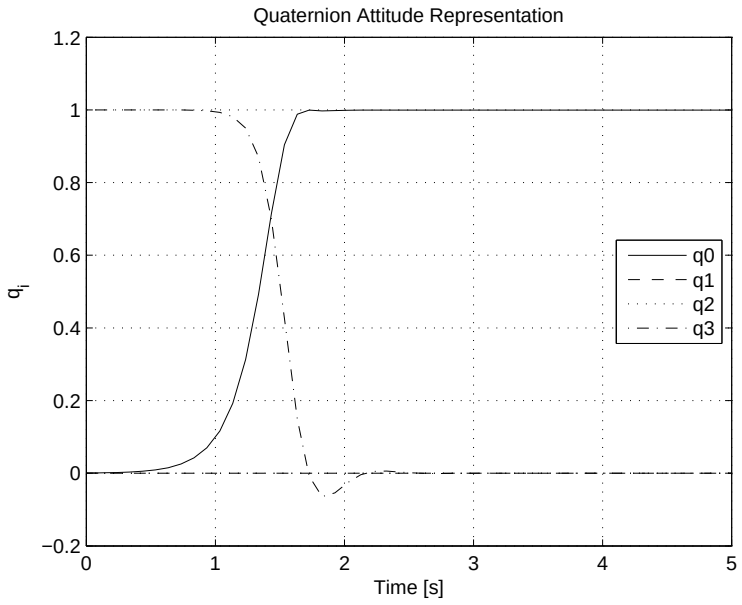

Figure 5.11: Quaternion Attitude

The vehicle rotates about the z_b axis and reaches the equilibrium $\bar{q} = [1\ 0\ 0\ 0]^T$ with a small overshoot. A sweep of initial yaw angles such that $-\pi \leq \psi \leq \pi$ is performed and the q_3 response is shown in Figure 5.12. For all initial values of ψ the yaw is reduced to zero.

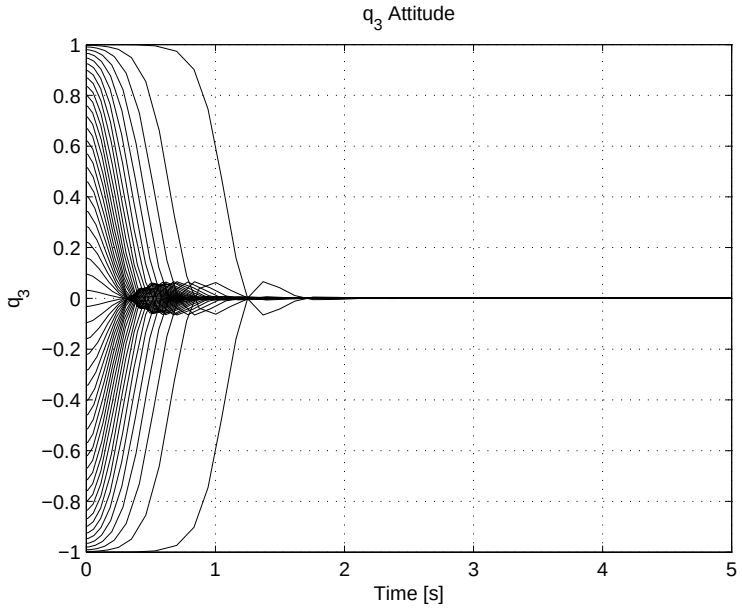

Figure 5.12: Quaternion Attitude q_3

The sign function used in deriving the error quaternion means that there is a slight bias so that $q_d = [1\ 0\ 0\ 0]^T$ (as opposed to $q_d = [-1\ 0\ 0\ 0]^T$). For the complete sweep of initial yaw angles the value of q_0 tracks so that $q_0 = 1$ as $t \to \infty$ as shown in Figure 5.13.

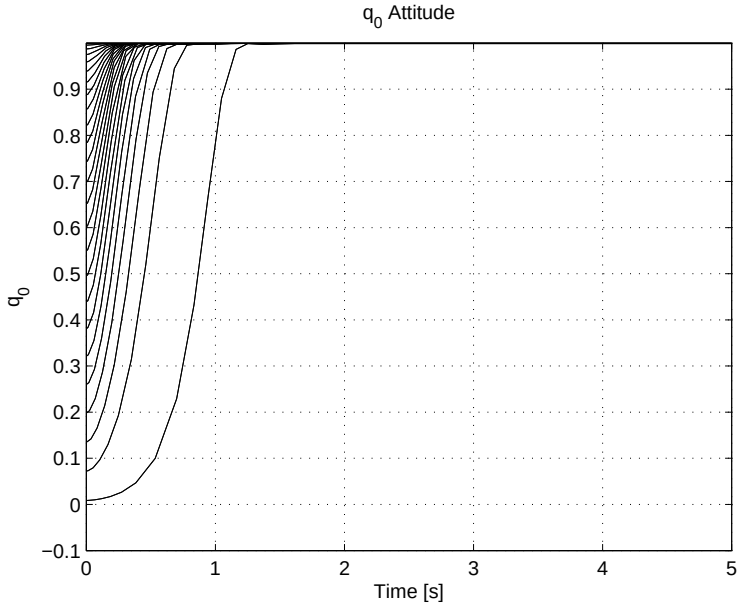

Figure 5.13: Quaternion Attitude q_0

If an initial angular velocity ω_z is applied then depending on the rotational sense of the applied initial angular velocity the vehicle attitude is controlled to the equilibrium point $\bar{q} = [\pm 1\ 0\ 0\ 0]^T$ as shown in Figure 5.14. For this sweep the initial yaw angle was set so that $\psi = \pi$ and the angular rate varied between -5rad/s and 5rad/s. There was no other intial body attitude or angular rate.

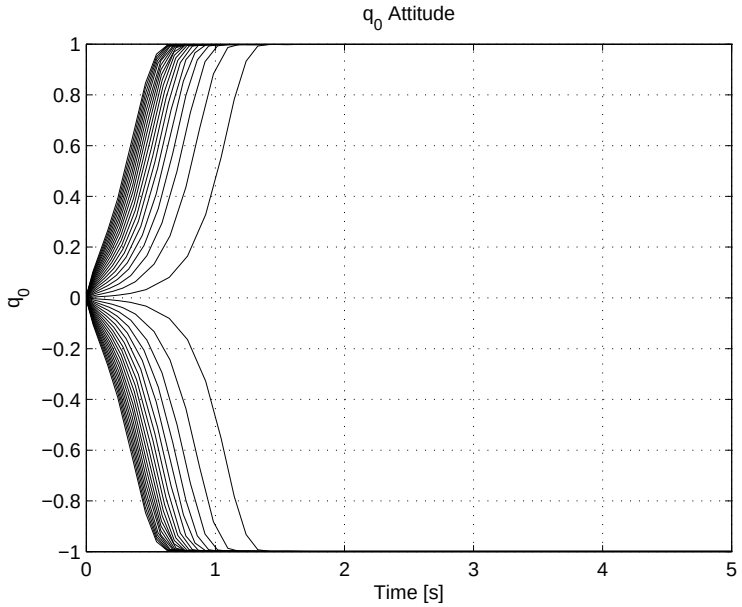

Figure 5.14: Quaternion Attitude q_0

It can be seen that the initial angular rate means that the quaternion is driven to $\bar{q} = [\pm 1\ 0\ 0\ 0]^T$ depending on the sense of the initial rotation. The attitude q_3 goes to zero as $t \to \infty$ as shown in Figure 5.15.

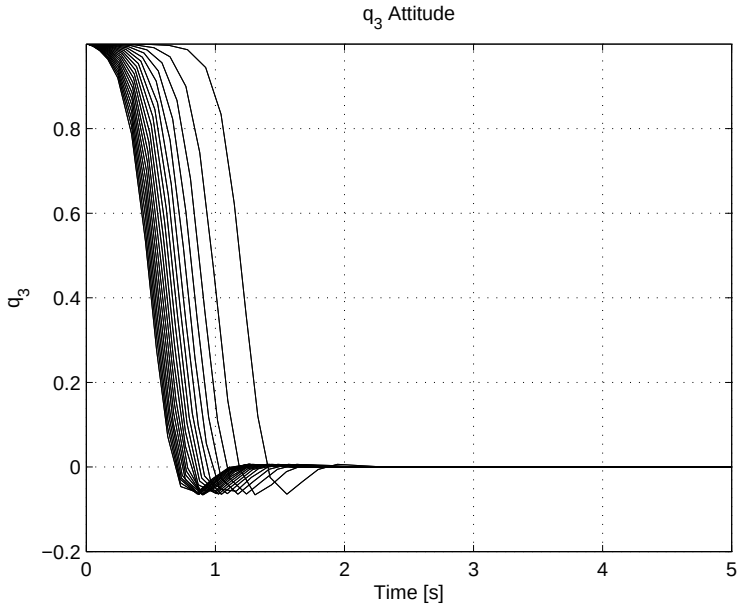

Figure 5.15: Quaternion Attitude q_3

The longest settling time is taken when the initial angular rate is zero with the shortest time taken when the initial angular rate was highest. This is because the controller utilises the initial angular velocity and controls the vehicle so that it follows the rotational sense imparted on it by the external stimulus. The following example shows the scenario where the vehicle is initialised with a yaw angle close to π. A sweep on angular rates are applied to the vehicle and the controller is tasked with bringing the vehicle to $\bar{q}_d = [\pm 1\ 0\ 0\ 0]^T$. Firstly the angular rates are between $\pm$ 2rad/s. This is shown in Figure 5.16.

The initial angular rate is not sufficient to ever allow for $q_0 = -1$ so the angular rate sweep was increased to -5rad/s to 5rad/s. This is shown in Figure 5.17. The controller allows the vehicle to follow the 'long way round' since it is optimal over stopping the initial rotation and reversing the rotation.

The closeup analysis of this simulation (Figure 5.17(b)) shows that the desired value of q_0 is set at every time step. If $q_0 \geq 0$ then $q_{0d} = 1$, else $q_{0d} = -1$, meaning that the vehicle may rotate through a larger angle if the initial angular rate is sufficiently high such that sign q_0 changes throughout the simulation.

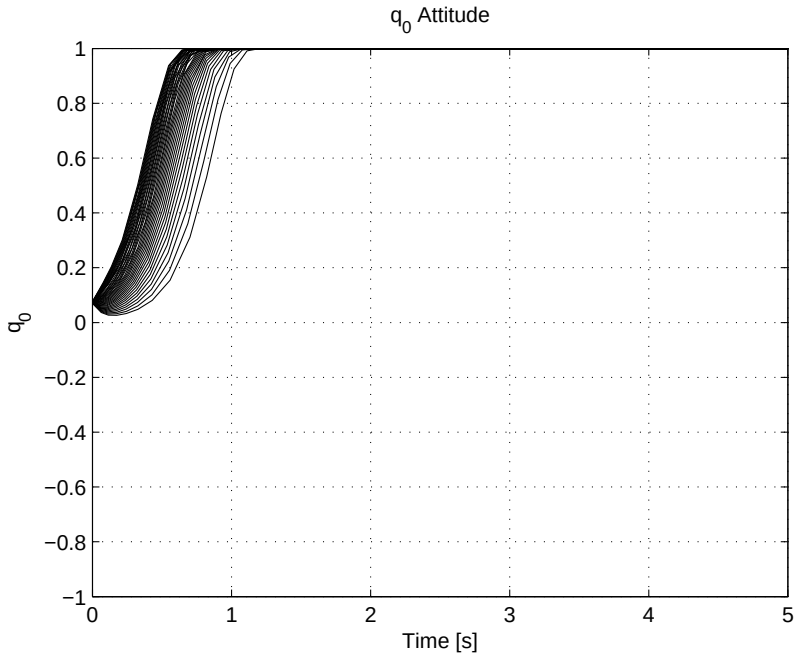

(a) Overall Simulation

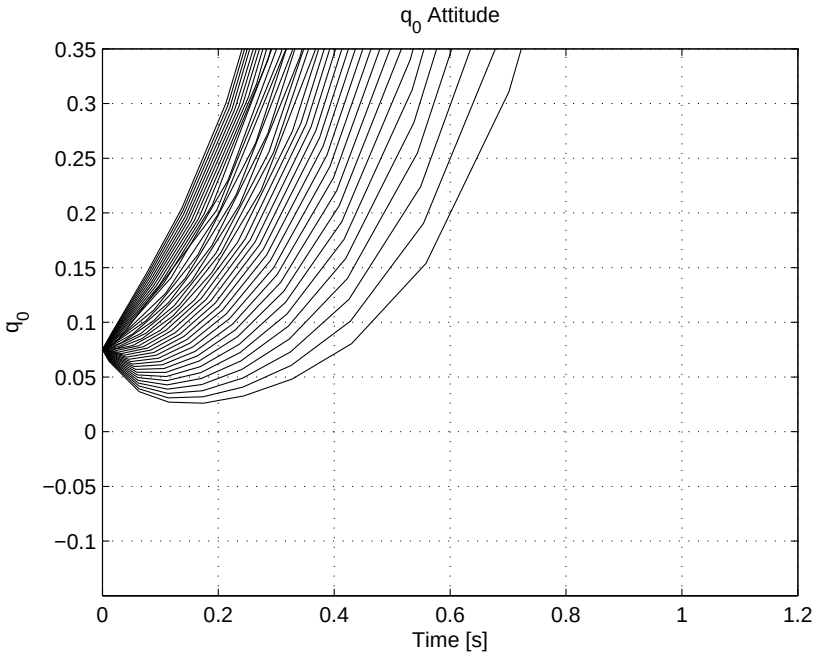

(b) Closeup of Initial Simulation Run

Figure 5.16: Variation of q_0 with initial angular rate -2rad/s $\leq \omega_z \leq$ 2rad/s. Initial $\psi = \pi - 0.15$

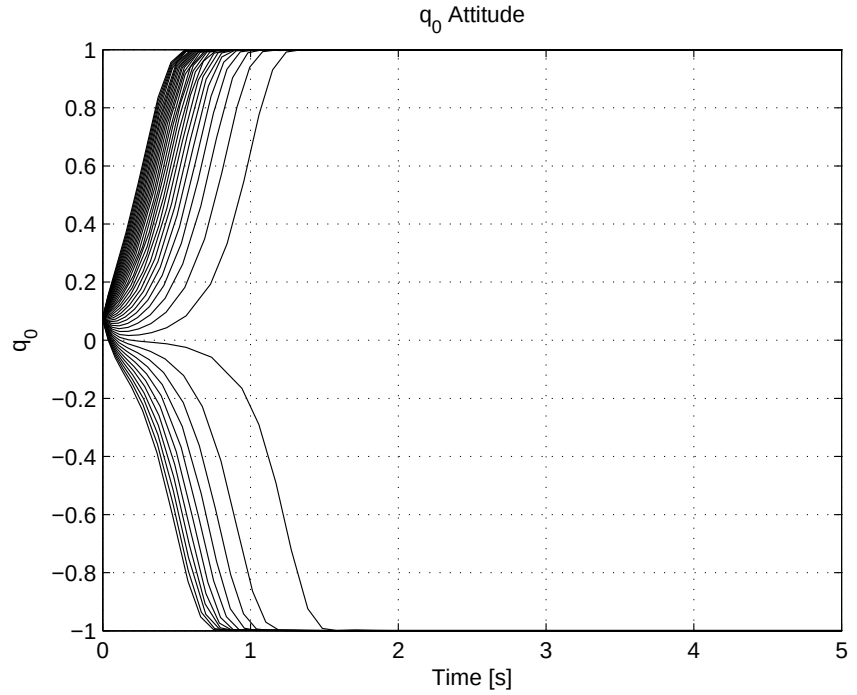

(a) Overall Simulation

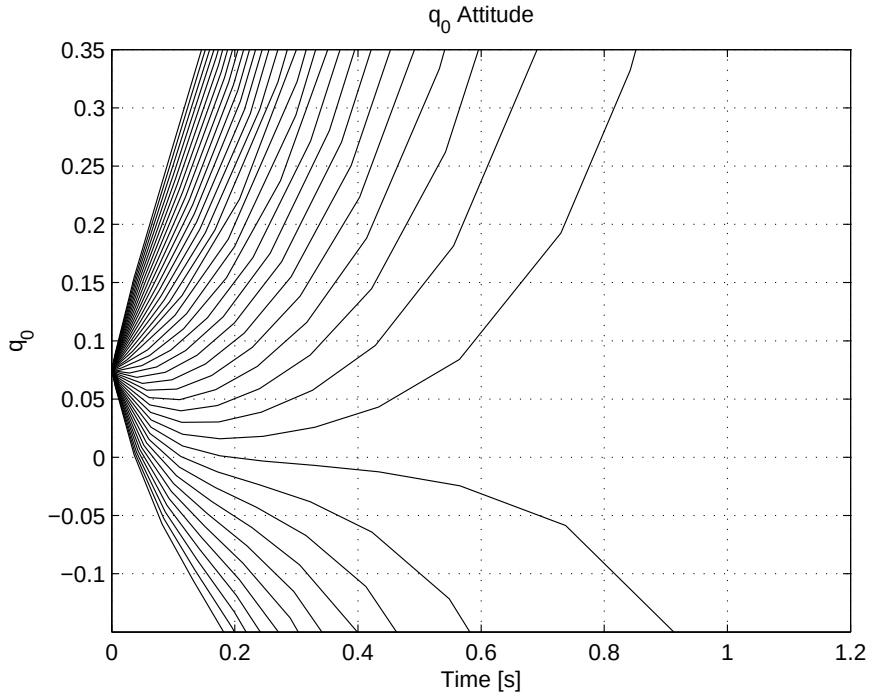

(b) Closeup of Initial Simulation Run

Figure 5.17: Variation of q_0 with initial angular rate -5rad/s $\leq \omega_z \leq$ 5rad/s. Initial $\psi = \pi - 0.15$

5.7 Mission 5

$$X_{\text{initial}} = \begin{bmatrix} 0 \\ 0 \\ 0 \\ 0 \\ 0 \\ 0 \\ 1 \\ 0 \\ 0 \\ 0 \\ 0 \\ 0 \\ 0 \end{bmatrix}, \quad X_{\text{desired}} = \begin{bmatrix} 2 \\ 0 \\ 0 \\ 0 \\ 0 \\ 0 \\ 1 \\ 0 \\ 0 \\ 0 \\ 0 \\ 0 \\ 0 \end{bmatrix} \tag{5.6}$$

This mission represents a small error between the current position and the desired final position. The effect of varying $\alpha_{\max}$ and β are negligible in this scenario since the error is small enough that $\alpha \leq \beta \leq \alpha_{\max}$ and no saturation functions are used to determine the error quaternion function.

The vehicle is initialised in a level hover (all states set to zero apart from $q_0 = 1$) and tasked to travel to $x_w = 2$. The vehicle pitches forwards (negative) which rotates the thrust vector to provide an acceleration in the x_w direction and then pitches backwards (positive) to slow the motion and arrive at the desired position.

Since the motion is purely pitching the only varying element of the quaternion attitude vector is q_2. Only one value of $\alpha_{\max}$ is shown since α is low throughout the manoeuvre and it is performed in the same time and with the same α regardless.

The position of the vehicle is shown in Figure 5.19. The aircraft tracks the response with no overshoot and arrives at x_d without deviating in y_w and z_w.

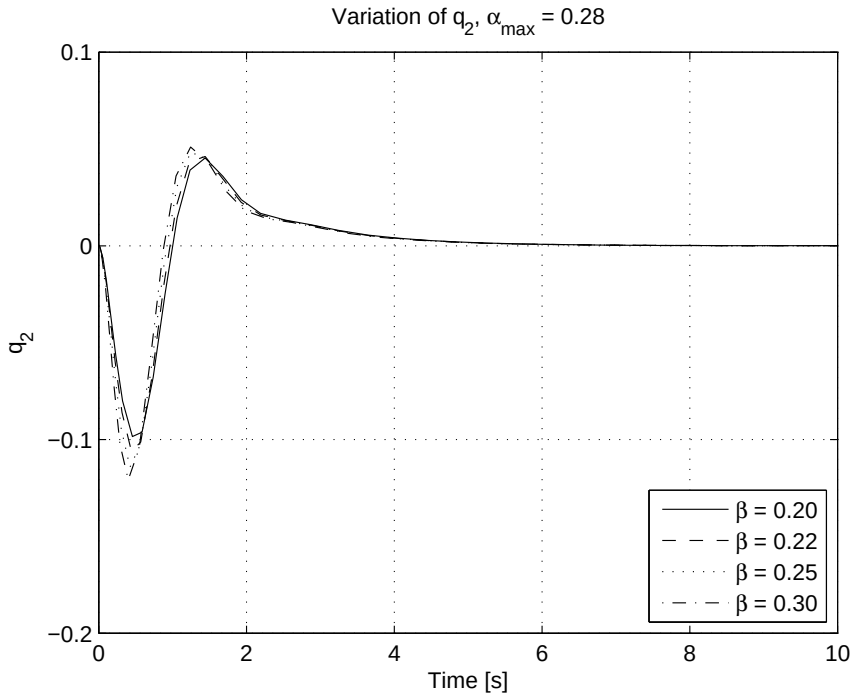

(a) $0.20 \leq \beta \leq 0.30$

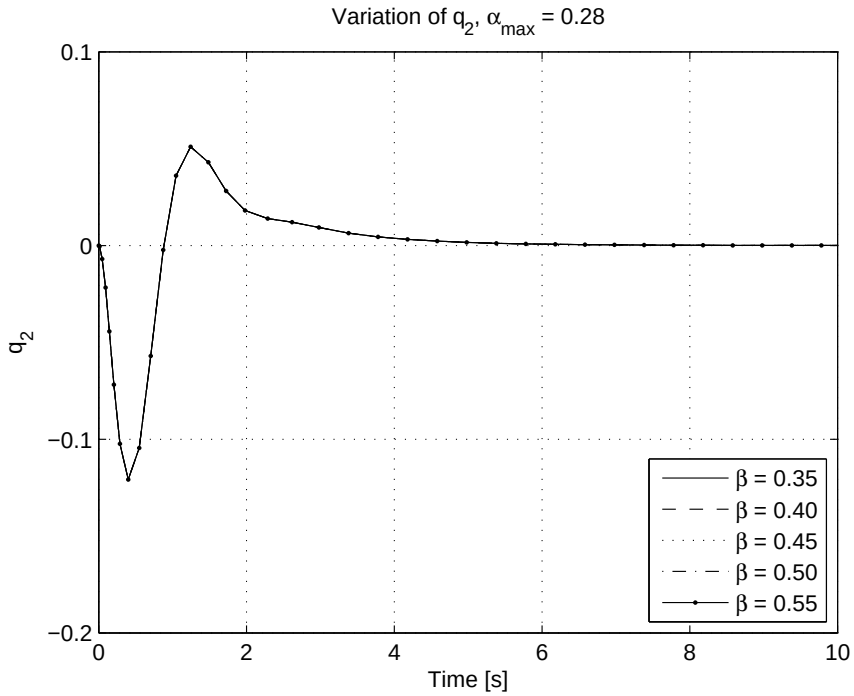

(b) $0.35 \leq \beta \leq 0.55$

Figure 5.18: Variation of q_2 for changing β

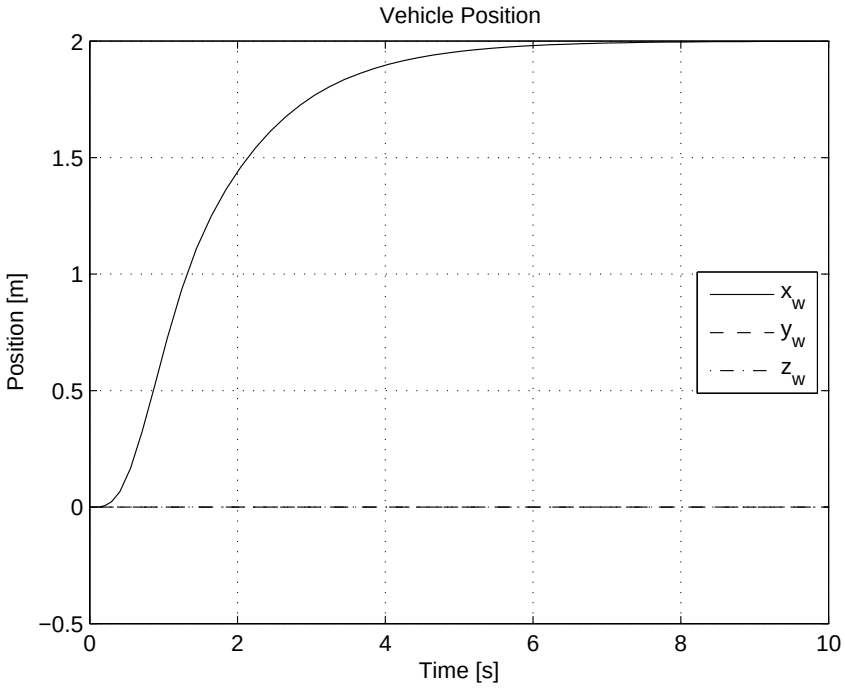

Figure 5.19: Vehicle Position

5.8 Mission 6

$$X_{\text{initial}} = \begin{bmatrix} 0 \\ 0 \\ 0 \\ 0 \\ 0 \\ 0 \\ 1 \\ 0 \\ 0 \\ 0 \\ 0 \\ 0 \\ 0 \end{bmatrix}, \quad X_{\text{desired}} = \begin{bmatrix} 10 \\ 0 \\ 0 \\ 0 \\ 0 \\ 0 \\ 1 \\ 0 \\ 0 \\ 0 \\ 0 \\ 0 \\ 0 \end{bmatrix} \tag{5.7}$$

This mission demonstrates the vehicle recovering to a desired track or location after a large position perturbation. This may occur after an effector failure when the controls have been reallocated and the vehicle is recovering to the nominal planned flight path. For normal flight and path following such a large error should not occur since the horizon time can be reduced and the error will be smaller. However if the failure perturbation is large either due to the reduction in effector thrust or through a collision with an object the simulations show that the vehicle is controllable and able to follow the desired body attitude.

As with Mission 5 the vehicle pitches forwards (negative) which rotates the thrust

vector to provide an acceleartion in the x_w direction and then pitches backwards (positive) to slow the motion and arrive at the desired position.

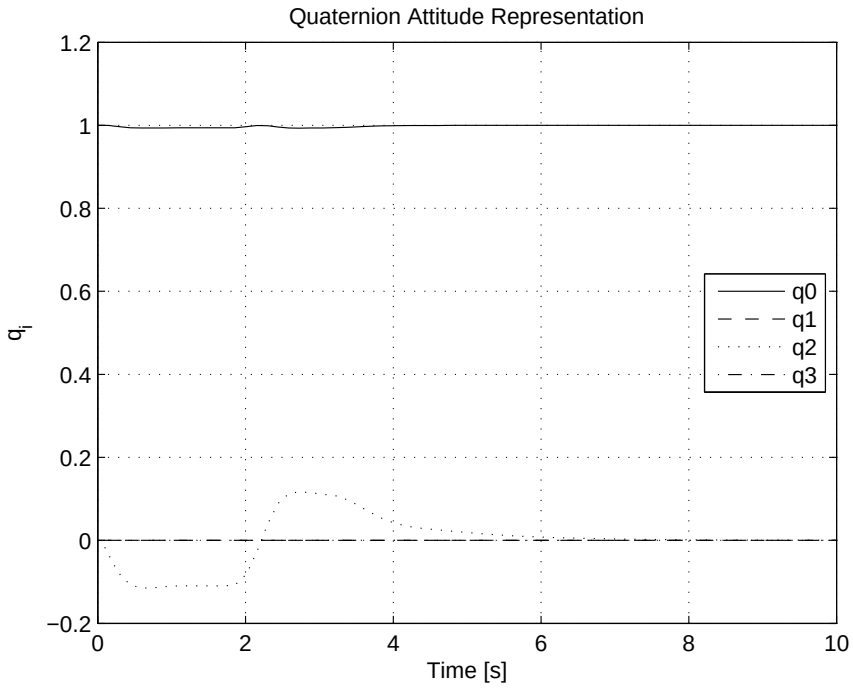

Figure 5.20: Quaternion Attitude Response

The position tracking of the vehicle is shown in Figure 5.21. The vehicle is able to track the large position error and arrive at the desired position.

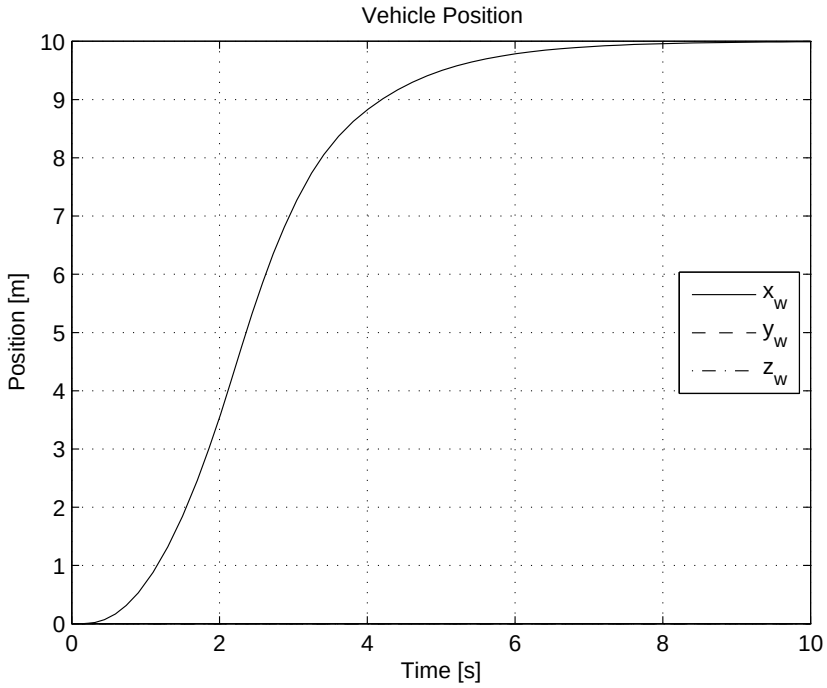

Figure 5.21: Vehicle Position

5.9 Mission 7

$$X_{\text{initial}} = \begin{bmatrix} 0 \\ 0 \\ 0 \\ 0 \\ 0 \\ 0 \\ 1 \\ 0 \\ 0 \\ 0 \\ 0 \\ 0 \\ 0 \end{bmatrix}, \quad X_{\text{desired}} = \begin{bmatrix} 0 \\ 0 \\ 10 \\ 0 \\ 0 \\ 0 \\ 1 \\ 0 \\ 0 \\ 0 \\ 0 \\ 0 \\ 0 \end{bmatrix} \tag{5.8}$$

This mission simulation represents a step change demand in altitude. The performance of the vehicle is limited by design features such as its mass and thrust to weight ratio, and constraints such as effector saturation which limits the thrust in the body frame to be bound positive only. The first simulation is for a 10m step change demand in altitude and is shown in Figure 5.22.

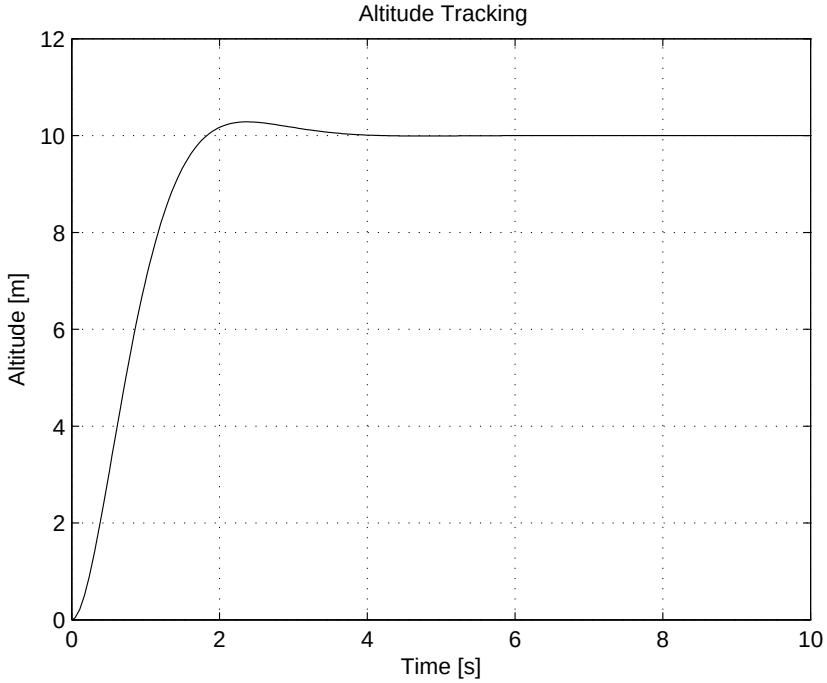

Figure 5.22: Altitude Tracking Performance

The quaternion attitude remains constant throughout the manoeuvre and is shown in Figure 5.23. The rotor speeds for the altitude step change are shown in Figure 5.24. The rotor speeds are initially high to accelerate the vehicle in z_b and reduce to below the trimmed hover speed so that the overshoot is not excessive. The rotational

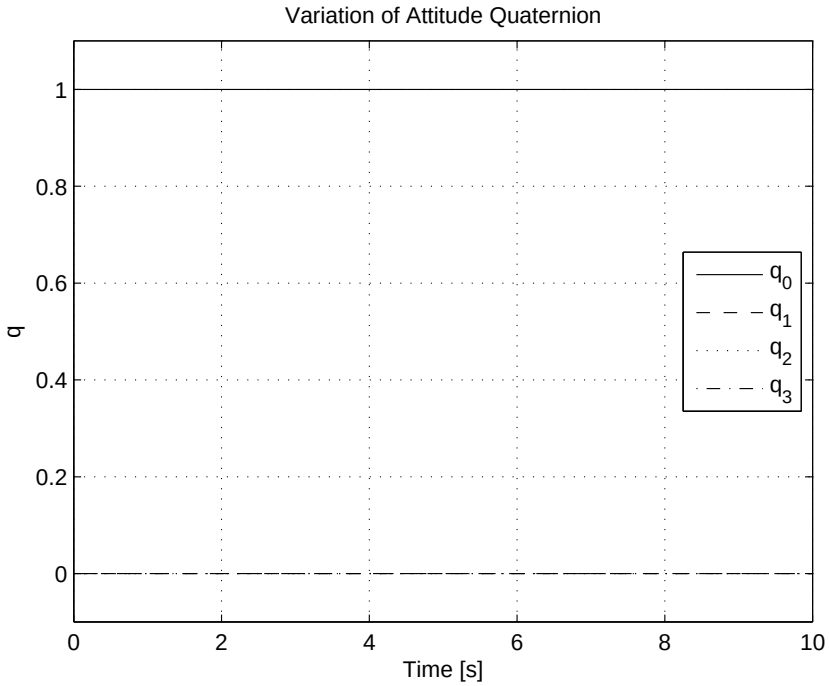

Figure 5.23: Attitude Tracking Performance During Altitude Change

speeds during the hover are constant. Note that all rotor speeds are identical so that the overall moments across the vehicle body are zero and the thrust opposes gravity and accelerates the vehicle upwards to track z_d. Applying a lower saturation limit to the effectors ($\Omega_{\max} = 250$ rad/s) changes the performance of the vehicle. The altitude tracking is shown in Figure 5.25 with rotor speeds shown in Figure 5.26. The settling time is increased compared to the nominal case and the rotor speeds are set to the saturation limit for the first portion of the flight where $t < 1.85s$. As before the motor speeds are reduced to below the value required for level hover so as to slow the acceleration and reduce the altitude overshoot. The change to the vehicle response is performed solely by changing the saturation limit in the allocation block and the controller remains invariant.

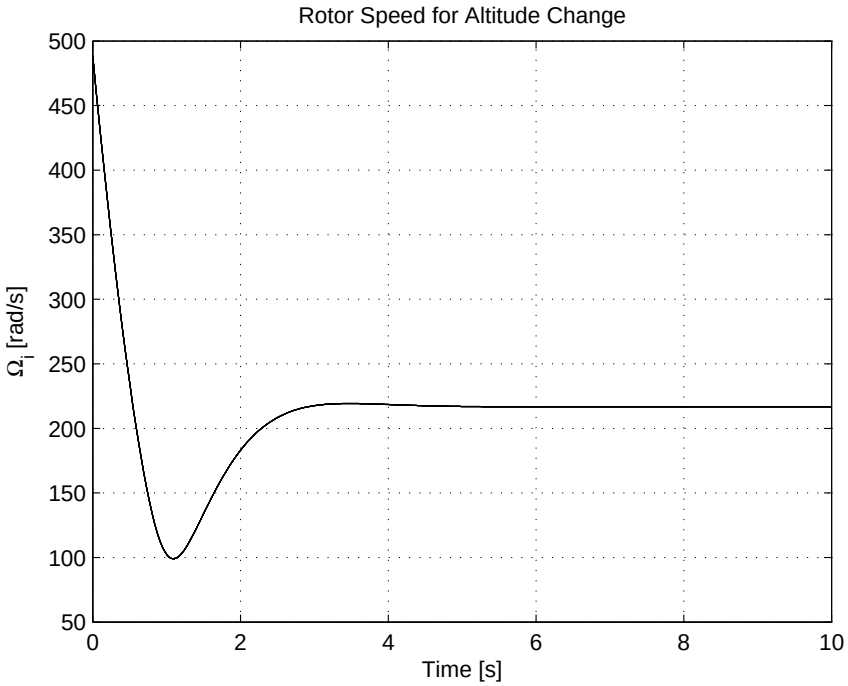

Figure 5.24: Rotor Speed For 10m Altitude Change. $\Omega_{\max} = 700$ rad/s

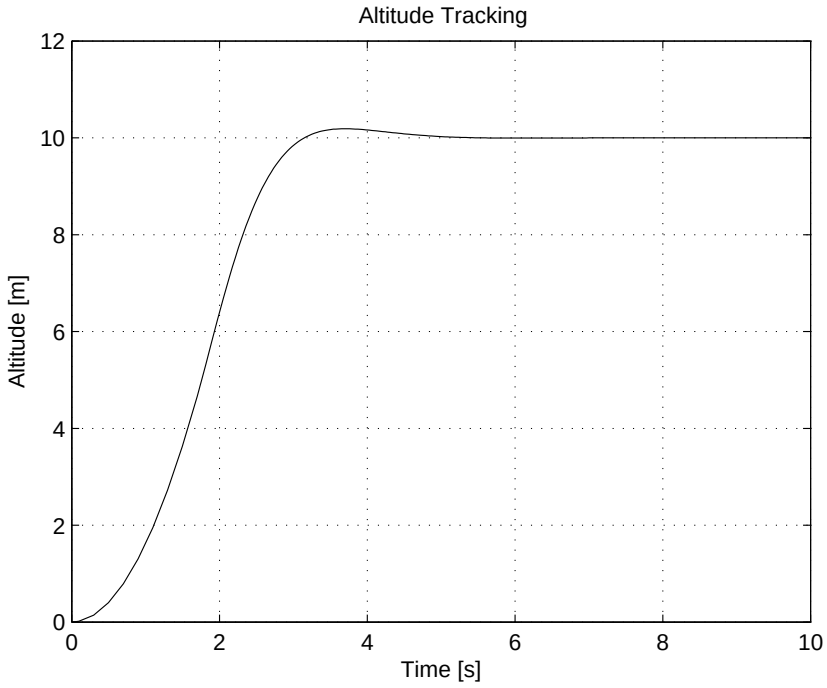

Figure 5.25: Altitude Tracking Performance During Altitude Change

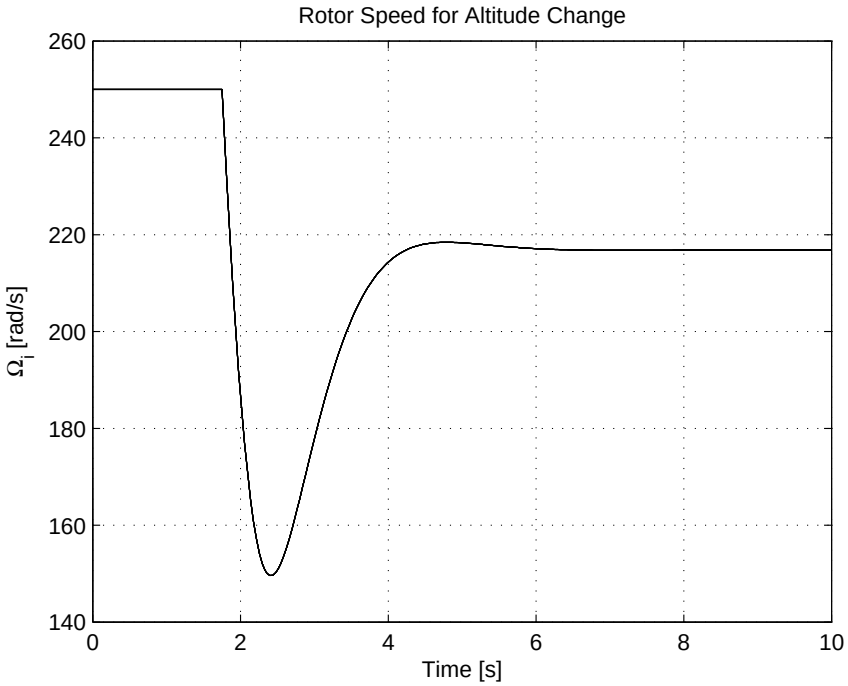

Figure 5.26: Rotor Speed For 10m Altitude Change. $\Omega_{\max} = 250$ rad/s

5.10 Conclusion

- The difference between attitude and full position control is defined and the values of $\alpha_{\max} = 0.28$ and $\beta = 0.22$ are derived through a parametric study of a number of scenarios where the initial attitude is far away from the hover attitude.
- Results show that the quaternion controller is able to return the vehicle to a level hover over at a desired position even when recovering from a large initial upset such as an inversion.
- The attainable force set constraints are successfully applied and the impact on flight performance is noted.
- The controller is suitable for application to the octorotor and tracks position and altitude demands.

Chapter 6

Failure Modelling

6.1 Introduction

This chapter discusses the subject of effector failures. It begins by describing how the Simulink vehicle model is built so that failures can be modelled, as well as how the delay in failure detection is simulated. This delay is the reason for a perturbation away from a desired position since the control allocation algorithm is initially allocating to all of the effectors (including the failed ones). The number and position of the failure will determine the perturbation, with a higher number and closer grouped effectors providing larger disturbing forces than single failures.

An objective of this thesis is to provide a fault hiding approach to fault tolerant control and so the post-failure controllability and manoeuvrability should be the same as the no-failure, nominal vehicle condition. Linear controllability analysis is performed to determine the combination of effector failures after which the vehicle is still fully controllable. This is valid since the vehicle is controllable around the linear operating point, level hover.

The fault hiding approach is further described and this involves moving the control allocation into the 'plant' so that the controller is designed for the nominal vehicle and the virtual controls are suitably allocated to the functioning effectors. This provides for failure indifferent flight performance.

This chapter concludes with a few examples of flight manoeuvres conducted with different combinations of failed effectors. This illustrates how the same performance is achieved by implementing the virtual controls to the effectors so that the overall forces and moments generated is the same.

6.2 Modelling in Simulation

In this thesis, a failure is modelled as a total and instantaneous loss of thrust from an effector (or number of effectors). A physical scenario where this might occur is if the rotor blades separate from the motor. Due to the physical setup of the 'cross' vehicle a single failure will contribute an adverse roll, pitch, and yaw moment.

A failure in an effector can be described by a change in the control effectiveness matrix as in Zhang et al. [2007] and Ma et al. [2008] where

$$B_f = B(I_p - \Delta) \tag{6.1}$$
$$\Delta = \text{diag}[\delta_0, \delta_1, \ldots, \delta_{p-1}] \tag{6.2}$$

where δ_i denotes the health of the ith effector with $\delta_i = 0$ representing a healthy ith effector, $\delta_i = 1$ a failure in the ith effector, and $0 < \delta_i < 1$ is a fault in the ith effector. First, the nominal control allocation method is shown in Figure 6.1 which is part of a closed loop feedback system.

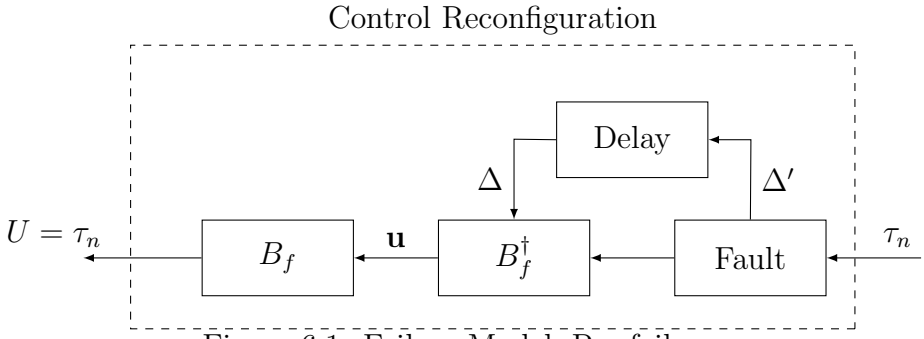

Figure 6.1: Failure Model, Pre-failure

Firstly the rotor speeds are allocated using a control allocation scheme where $\mathbf{u} = B_f^\dagger \tau_n$. A suitable fault detection method is used (either a sensor or a model-based system) to determine the failure state of each effector, along with a delay. For the nominal case $\delta_i = 0$ for all i. The modified control effectiveness matrix is then used to determine the forces and moments that are generated with the allocated motor speeds, i.e. $U = B_f \mathbf{u}$. These are passed to the vehicle dynamics. For the perfect control allocation case with no delay in the failure detection $U = \tau_n$.

For the nominal case the effectors are all healthy ($\delta_i = 0$) and B_f does not change throughout the simulation. Considering the octorotor vehicle with the parameters

given in Table 2.1 the rotor speeds for level hover are

$$\sqrt{\mathbf{u}} = \begin{bmatrix} 217 \\ 217 \\ 217 \\ 217 \\ 217 \\ 217 \\ 217 \\ 217 \end{bmatrix} \text{ rad/ s} \tag{6.3}$$

which are within the saturation limits. Note that in the octorotor configuration the rotor speeds are all equal to each other to provide a balance to the overall moments about the body axis and to generate sufficient lift for level hover.

When simulating a failure the delay in the fault detection system means that the failure state of the effectors is not current. In such a case the control effectiveness matrix is not instantly modified and the allocation is performed as for the nominal case and $U \neq \tau_n$. There is an imbalance in the forces and moments and the vehicle deviates away from the initial position or flightpath. For example, a failure in effector 7 is represented as

$$\sqrt{\mathbf{u}} = \begin{bmatrix} 217 \\ 217 \\ 217 \\ 217 \\ 217 \\ 217 \\ 217 \\ 0 \end{bmatrix} \text{ rad/ s} \tag{6.4}$$

The controller output τ_n and the forces and moments U are

$$\tau_n = \begin{bmatrix} 11.772 \\ 0 \\ 0 \\ 0 \end{bmatrix}, \quad U = B_f \mathbf{u} = \begin{bmatrix} 10.3005 \\ -0.5631 \\ -1.3595 \\ -0.0353 \end{bmatrix} \tag{6.5}$$

where B_f is the control allocation matrix for the nominal condition. The force imbalance will cause a negative roll, pitch, and yaw as well as a reduction in overall thrust leading to a drop in altitude. For the control reconfiguration case the modified control effectiveness matrix is updated with the current failure state of the effectors (i.e. $\delta_7 = 1$). Using a suitable control allocation method the rotor speeds are determined between the remaining effectors giving

$$\sqrt{\mathbf{u}} = \begin{bmatrix} 295 \\ 217 \\ 174 \\ 217 \\ 232 \\ 217 \\ 252 \end{bmatrix} \text{ rad/s} \tag{6.6}$$

and

$$U = \tau_n = \begin{bmatrix} 11.772 \\ 0 \\ 0 \\ 0 \end{bmatrix} \tag{6.7}$$

6.3 Linear Controllability Analysis After Failure

To investigate the controllability of the vehicle after control reallocation the control effectiveness matrix is constructed by removing the columns with zeros which represent the failed effectors. The controllability conditions apply to the reconfigured system as to the nominal system, that is

$$\dot{\mathbf{x}}_f = A_f \mathbf{x}_f + \hat{B}_f \mathbf{u}_f, \quad t \in [t_0, \infty) \tag{6.8a}$$
$$\mathbf{y}_f = C_f \mathbf{x}_f + D\mathbf{u}_f \tag{6.8b}$$

where

$$\mathbf{u}_f = B_f^{\dagger} \tau \tag{6.9}$$

is controllable if and only if the $n \times nm$ controllability matrix

$$R_f = [\hat{B}_f \; A_f \hat{B}_f \; A_f^2 \hat{B}_f \; \ldots \; A_f^{n-1} \hat{B}_f] \tag{6.10}$$

has full rank, i.e. $\text{rank}(R_f) = n$. If $\dot{\mathbf{x}}_f = \dot{\mathbf{x}}$ then the control reallocation has been successfully achieved and the performance of the vehicle after the failure is identical to the prefailure performance.

Similar to the nominal vehicle, the input matrix $\hat{B}_f$ is constructed with reference to the control allocation matrix B_f. The input matrix for the failure scenarios can be obtained by deleting the respective column from the nominal vehicle. See Example 7.

Example 7, Fail $\{7\}$ For this scenario a failure in effector 7 ($\delta_7 = 1$) means that the control effectiveness matrix is reduced from $B \in \mathbb{R}^{4\times 8}$ to $B \in \mathbb{R}^{4\times 7}$. The dimension of $\mathbf{u}$ is similarly reduced from $\mathbf{u} \in \mathbb{R}^8$ to $\mathbf{u}_f \in \mathbb{R}^7$. The dimension of τ remains the same for the nominal and post-failure case with $U = \tau_n \in \mathbb{R}^4$ representing the successful control reallocation. The pseudo inverse method is used for this failure case. Firstly the control allocation matrix B_f is constructed to give

$$B_f = \begin{bmatrix} b & b & b & b & b & b & b \\ -bls_{\gamma_0} & -bls_{\gamma_1} & -bls_{\gamma_2} & -bls_{\gamma_3} & -bls_{\gamma_4} & -bls_{\gamma_5} & -bls_{\gamma_6} \\ blc_{\gamma_0} & blc_{\gamma_1} & blc_{\gamma_2} & blc_{\gamma_3} & blc_{\gamma_4} & blc_{\gamma_5} & blc_{\gamma_6} \\ d & -d & -d & d & d & -d & -d \end{bmatrix} \tag{6.11}$$

The trimmed rotor speeds are found using

$$\mathbf{u}_f = B_f^{\dagger}\tau \tag{6.12}$$

$$\sqrt{\mathbf{u}}_f = \begin{bmatrix}\Omega_0\\ \Omega_1\\ \Omega_2\\ \Omega_3\\ \Omega_4\\ \Omega_5\\ \Omega_6\end{bmatrix} = \begin{bmatrix}295\\ 217\\ 174\\ 217\\ 232\\ 217\\ 252\end{bmatrix} \text{ rad/s} \tag{6.13}$$

Since all of the rotor speeds are within the saturation limits the pseudo-inverse method is suitable for this step. Note that the trimmed rotor speeds are not the same for each effector. This is in order to counteract against the adverse roll, pitch, and yaw which is generated when the axisymmetric property of the vehicle is removed after experiencing a complete effector failure.

For the controllability analysis the input matrix $\hat{B}_f \in \mathbb{R}^{12\times 7}$ is derived by deleting the last column of the nominal input matrix $\hat{B}$ to give

$$\hat{B}_f = \begin{bmatrix} 0_{2\times1} & 0_{2\times1} & 0_{2\times1} & 0_{2\times1} & 0_{2\times1} & 0_{2\times1} & 0_{2\times1}\\ b_1\hat{\sigma_0} & b_1\hat{\sigma_1} & b_1\hat{\sigma_2} & b_1\hat{\sigma_3} & b_1\hat{\sigma_4} & b_1\hat{\sigma_5} & b_1\hat{\sigma_6}\\ -b_2\hat{\sigma_0} & -b_2\hat{\sigma_1} & -b_2\hat{\sigma_2} & -b_2\hat{\sigma_3} & -b_2\hat{\sigma_4} & -b_2\hat{\sigma_5} & -b_2\hat{\sigma_6}\\ b_3\hat{\sigma_0} & b_3\hat{\sigma_1} & b_3\hat{\sigma_2} & b_3\hat{\sigma_3} & b_3\hat{\sigma_4} & b_3\hat{\sigma_5} & b_3\hat{\sigma_6}\\ b_4\hat{\sigma_0} & b_4\hat{\sigma_1} & b_4\hat{\sigma_2} & b_4\hat{\sigma_3} & b_4\hat{\sigma_4} & b_4\hat{\sigma_5} & b_4\hat{\sigma_6}\\ 0_{6\times1} & 0_{6\times1} & 0_{6\times1} & 0_{6\times1} & 0_{6\times1} & 0_{6\times1} & 0_{6\times1}\end{bmatrix} \tag{6.14}$$

Kalman controllability analysis shows this to be controllable with $\text{rank}(R_f) = n$ and so demonstrates the resistance to a failure.

Example 8, Fail $\{7, 6, 5\}$ This example is used to show how the analysis is sensitive to a suitable control allocation method which takes effector saturations into account. This scenario is one where three consecutive effectors suffer simultaneous failures. As before the first step is to construct the control effectiveness matrix B_f with $\delta_5 = \delta_6 = \delta_7 = 1$.

$$B_f = \begin{bmatrix} b & b & b & b & b\\ -bls_{\gamma_0} & -bls_{\gamma_1} & -bls_{\gamma_2} & -bls_{\gamma_3} & -bls_{\gamma_4}\\ blc_{\gamma_0} & blc_{\gamma_1} & blc_{\gamma_2} & blc_{\gamma_3} & blc_{\gamma_4}\\ d & -d & -d & d & d\end{bmatrix} \tag{6.15}$$

The pseudo inverse method gives the rotor speeds as

$$\sqrt{\mathbf{u}_f} = \begin{bmatrix}\Omega_0\\ \Omega_1\\ \Omega_2\\ \Omega_3\\ \Omega_4\end{bmatrix} = \begin{bmatrix}266\\ 388\\ 193\\ -451\\ 567\end{bmatrix} \text{ rad/s} \tag{6.16}$$

Note that the rotational speed Ω_3 is set below zero, i.e. to reverse rotational sense from its installed value. For the unconstrained analysis the input matrix is

$$\hat{B}_{f,\text{unconstrained}} = \begin{bmatrix} 0_{2\times1} & 0_{2\times1} & 0_{2\times1} & 0_{2\times1} & 0_{2\times1} \\ b_1\hat{\sigma_0} & b_1\hat{\sigma_1} & b_1\hat{\sigma_2} & b_1\hat{\sigma_3} & b_1\hat{\sigma_4} \\ -b_2\hat{\sigma_0} & -b_2\hat{\sigma_1} & -b_2\hat{\sigma_2} & -b_2\hat{\sigma_3} & -b_2\hat{\sigma_4} \\ b_3\hat{\sigma_0} & b_3\hat{\sigma_1} & b_3\hat{\sigma_2} & b_3\hat{\sigma_3} & b_3\hat{\sigma_4} \\ b_4\hat{\sigma_0} & b_4\hat{\sigma_1} & b_4\hat{\sigma_2} & b_4\hat{\sigma_3} & b_4\hat{\sigma_4} \\ 0_{6\times1} & 0_{6\times1} & 0_{6\times1} & 0_{6\times1} & 0_{6\times1} \end{bmatrix} \tag{6.17}$$

Kalman controllability analysis shows that this system is controllable. However, this method does not explicitely account for the saturation limits and this is seen in the allocation of the rotor speeds in (6.16). For this reason the redistributed pseudo inverse method is used. Using the RPI method it is not possible to trim the vehicle about the linear operating point. The allocated rotor speeds are

$$\sqrt{\mathbf{u}_f} = \begin{bmatrix} \Omega_0 \\ \Omega_1 \\ \Omega_2 \\ \Omega_3 \\ \Omega_4 \end{bmatrix} = \begin{bmatrix} 266 \\ 388 \\ 193 \\ 0 \\ 567 \end{bmatrix} \text{ rad/s} \tag{6.18}$$

Since $\Omega_3 = 0$, the input matrix $\hat{B}_{f,\text{constrained}}$ is

$$\hat{B}_{f,\text{constrained}} = \begin{bmatrix} 0_{2\times1} & 0_{2\times1} & 0_{2\times1} & 0_{2\times1} \\ b_1\hat{\sigma_0} & b_1\hat{\sigma_1} & b_1\hat{\sigma_2} & b_1\hat{\sigma_4} \\ -b_2\hat{\sigma_0} & -b_2\hat{\sigma_1} & -b_2\hat{\sigma_2} & -b_2\hat{\sigma_4} \\ b_3\hat{\sigma_0} & b_3\hat{\sigma_1} & b_3\hat{\sigma_2} & b_3\hat{\sigma_4} \\ b_4\hat{\sigma_0} & b_4\hat{\sigma_1} & b_4\hat{\sigma_2} & b_4\hat{\sigma_4} \\ 0_{6\times1} & 0_{6\times1} & 0_{6\times1} & 0_{6\times1} \end{bmatrix} \tag{6.19}$$

Constrained controllability analysis using $\hat{B}_{f,\text{constrained}}$ gives $\text{rank}(R) < n$ and the system is not controllable. Table 6.1 shows the combination of failures after which the vehicle is still controllable.

Table 6.1: Combination of Controllable Effector Failures

Combination	Effectors
Single Effector	{7}
Two Effectors	{7,6} , {7,5}, {7,4}, {7,3}
Three Effectors, Two Consecutive	{7,6,4}, {7,6,3}
Three Effectors	{7,5,3}, {7,5,2}
Four Effectors, Two Consecutive	{7,6,4,2}, {7,6,4,1}, {7,6,3,2}, {7,6,3,1}
Four Effectors, Alternate	{7,5,3,1}

The combinations of uncontrollable failures is shown in Table 6.2.

Table 6.2: Combination of Uncontrollable Effector Failures

Combination	Effectors
Two Effectors	{7,0}
Three Effectors, Two Consecutive	{7,6,5}
Four Effectors, Two Consecutive	{7,6,4,3}, {7,6,2,1}, {7,4,3,0}, {7,5,2,0}
Four Effectors, Three Consecutive	{7,6,5,3}, {7,6,5,2}

In general for the 'cross' type octorotor we define the fully functioning rotor set as

$$\mathcal{M} = \{\mathcal{M}_a, \mathcal{M}_b, \mathcal{M}_c, \mathcal{M}_d\} \tag{6.20}$$

where

$$\mathcal{M}_a = \{7, 0\},\ \mathcal{M}_b = \{1, 2\},\ \mathcal{M}_c = \{3, 4\},\ \mathcal{M}_d = \{5, 6\} \tag{6.21}$$

are the co-rotating rotor pair indices as shown in Figure 2.3. Let $\mathcal{M}_F \subseteq \mathcal{M}$ denote the set of failed rotors and $\mathcal{M}_G \subseteq \mathcal{M}$ denote the set of working rotors. Hence $\mathcal{M}_F \cup \mathcal{M}_G = \mathcal{M}$, $\mathcal{M}_F \cap \mathcal{M}_G = \emptyset$ and the cardinality of $\mathcal{M}_F$ is q.

By means of the Kalman controllability test the following conditions are established on the constrained Kalman controllability of the vehicle:

1. If $q \leq 1$ then $\text{rank}(R_f) = n$ and the vehicle is controllabile.
2. If $2 \leq q \leq 4$ then if two failures are in the same set $\mathcal{M}_{a,b,c,d}$ then the vehicle is not controllable, else it is controllable.
3. If $q \geq 5$ then $\text{rank}(R_f) < n$ and the vehicle is not controllable.

To summarise, provided that two failures do not occur in the same set $\mathcal{M}_{a,b,c,d}$ the vehicle is controllable. The rotor speeds for level hover after failures in each case are given in the results Section 6.5.

6.4 Fault Hiding

The concept of fault hiding allows us to keep the nominal controller in the reconfigured closed-loop system which has the advantage that the controller need only be designed once and can be applied to the nominal and post-failure systems. Furthermore, the opererator does not need to be trained to counter every failure scenario. Finally, if the failure affects only a small subsystem in the plant it is not necessary to redesign the entire controller. Recall the nominal system shown in Figure 6.2.

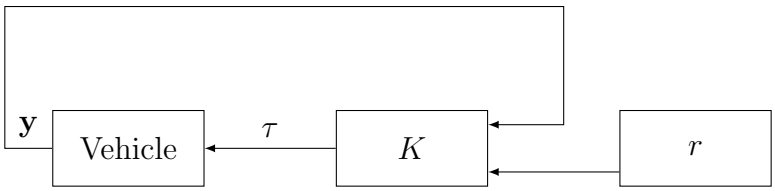

Figure 6.2: Nominal System Diagram

The reconfiguration block is inserted between the controller and the dynamics as shown in Figure 6.3.

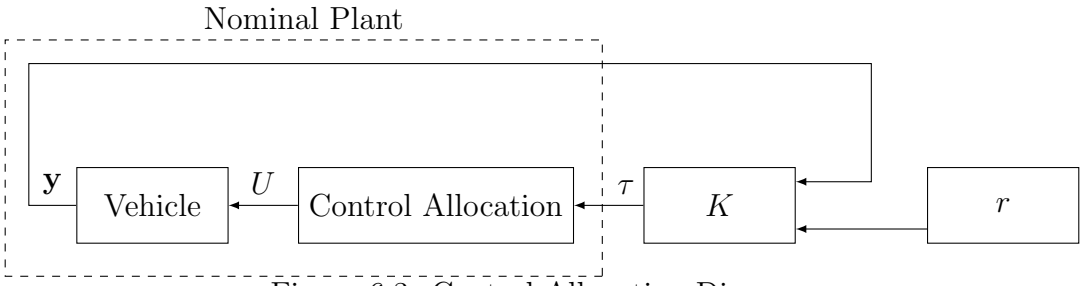

Figure 6.3: Control Allocation Diagram

The reconfiguration scheme can also be part of a control reallocation scheme such as shown in Figure 6.4 which is part of a closed loop feedback system.

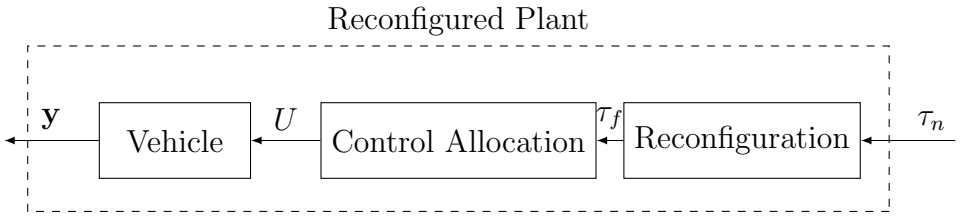

Figure 6.4:
Control Re-Allocation Diagram

The fault hiding method considers the allocation block as part of the reconfigured plant. The fault hiding goal is satisfied if the input/output (I/O) of the reconfigured plant is identical to the nominal plant for a suitable initial state of the allocation block [Lunze and Richter, 2008].

It is assumed that a suitable fault detection system is in use which is sensitive to detect effector failures yet does not produce false alarms. In practice a physical sensor (such an infra-red or LED emitter/detector combination) or a Hall sensor could be used to detect a specific failure where the rotor blades separate from the motor shaft. This will cause an instantaneous loss of thrust from the effector and it is this scenario which is investigated in this thesis.

6.5 Failure Recovery

The failure cases which are investigated are

- failure in a single effector,
- failure in two consecutive effectors,

- failure in two non-consecutive effectors,
- failure in three effectors where two are consecutive,
- failure in three non-consecutive effectors, and
- failure in four effectors

6.5.1 Failure in a Single Effector

In this scenario a failure occurs in effector 7. The failure causes a rolling, pitching, and yawing moment as well as a loss of overall lift which leads to a drop in altitude. This is further exacerbated as $\alpha \geq \alpha_{\max}$ before the controls are reallocated and the vehicle recovers to the initial position. The motion of the vehicle is the same for any effector failure as it 'tips' towards the failure and experiences an adverse yaw depending on the rotational sense of the failed effector. The adverse yaw is smaller than the adverse roll and pitch because the imbalance in the overall gyroscopic forces is of a smaller magnitude than the imbalance in overall thrust which causes the vehicle to roll and pitch.

The rotor speeds required for hover with a failure in effector 7 are

$$\sqrt{\mathbf{u}_{\{7\}}} = \begin{bmatrix} \Omega_0 \\ \Omega_1 \\ \Omega_2 \\ \Omega_3 \\ \Omega_4 \\ \Omega_5 \\ \Omega_6 \end{bmatrix} = \begin{bmatrix} 295 \\ 217 \\ 174 \\ 217 \\ 232 \\ 217 \\ 252 \end{bmatrix} \text{ rad/s} \tag{6.22}$$

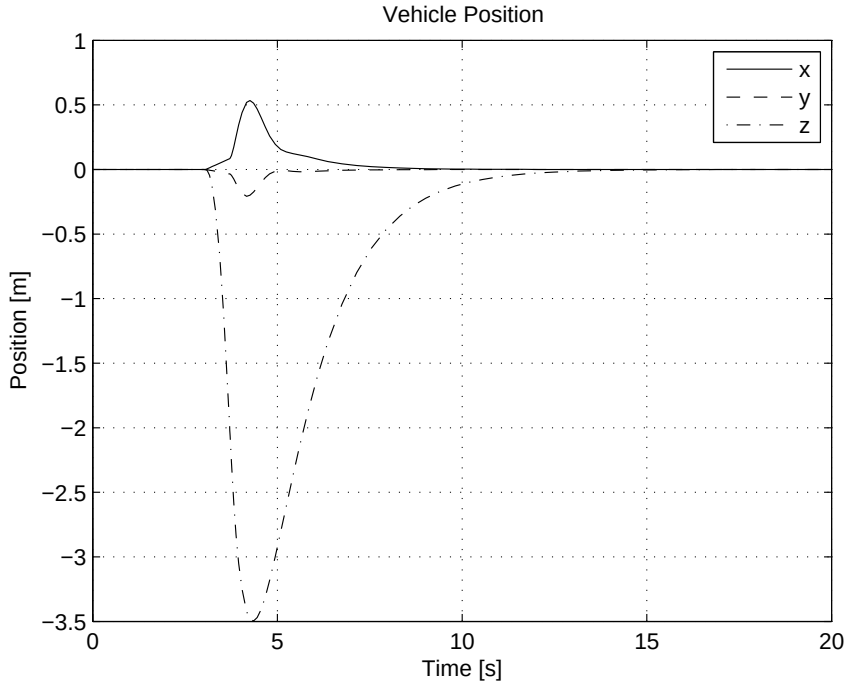

(a) Position Recovery

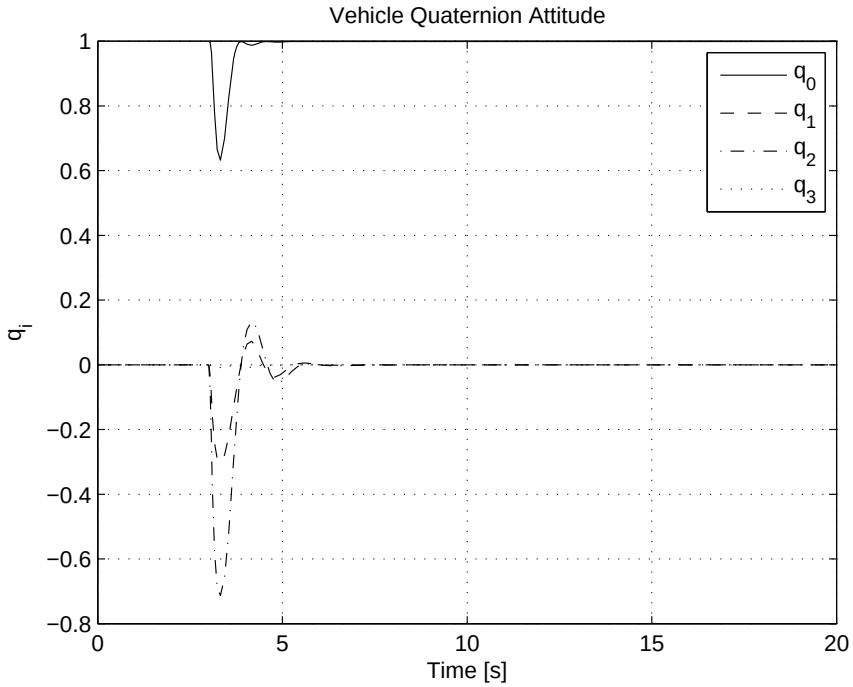

(b) Quaternion Attitude

Figure 6.5: Recovery for Failure in Effector 7

6.5.2 Failure in Two Consecutive Effectors

For this scenario two cases are considered

- two consecutive effectors that lie across a body axis line (Figure 6.6), and
- two consecutive effectors that are contained in a single body axis quadrant (Figure 6.7).

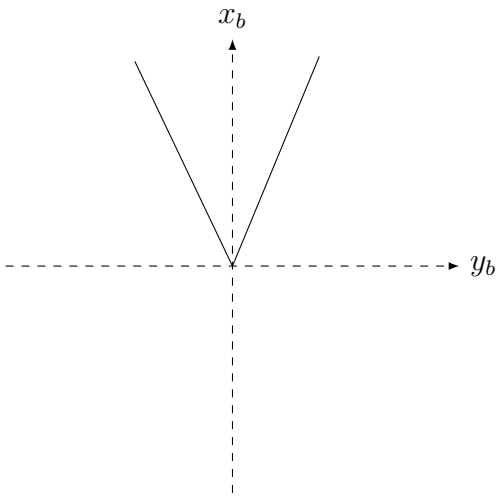

Figure 6.6: Failure across a body axis line

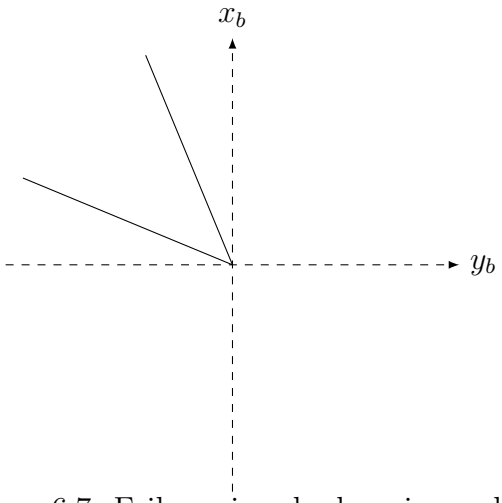

Figure 6.7: Failures in a body axis quadrant

The failure for this analysis is Fail {7,6} since failures in two effectors in the same set $\mathcal{M}_{a,b,c,d}$ was shown in Section 6.3 to not be controllable. When the failures occur in a body axis quadrant then there is a compound perturbation in roll and pitch, as well as a possibility that there is a yaw perturbation as well.

Position Response The vehicle pitches towards the failed effectors. Since the failures occur in a body axis quadrant this generates a compound perturbation in roll, and pitch. The vehicle loses altitude for two reasons:

- there is a reduction in overall thrust, and
- the vehicle attitude exceeds $\alpha_{\max}$ and so the controller switches to pure attitude mode.

The deviation in x_w and y_w are minimal compared to the reduction in altitude and this is achieved through the choice of $\alpha_{\max}$ as explained elsewhere in this thesis.

The rotor speeds for hover are

$$\sqrt{\mathbf{u}_{\{7,6\}}} = \begin{bmatrix} \Omega_0 \\ \Omega_1 \\ \Omega_2 \\ \Omega_3 \\ \Omega_4 \\ \Omega_5 \end{bmatrix} = \begin{bmatrix} 330 \\ 240 \\ 146 \\ 146 \\ 240 \\ 330 \end{bmatrix} \text{ rad/s} \tag{6.23}$$

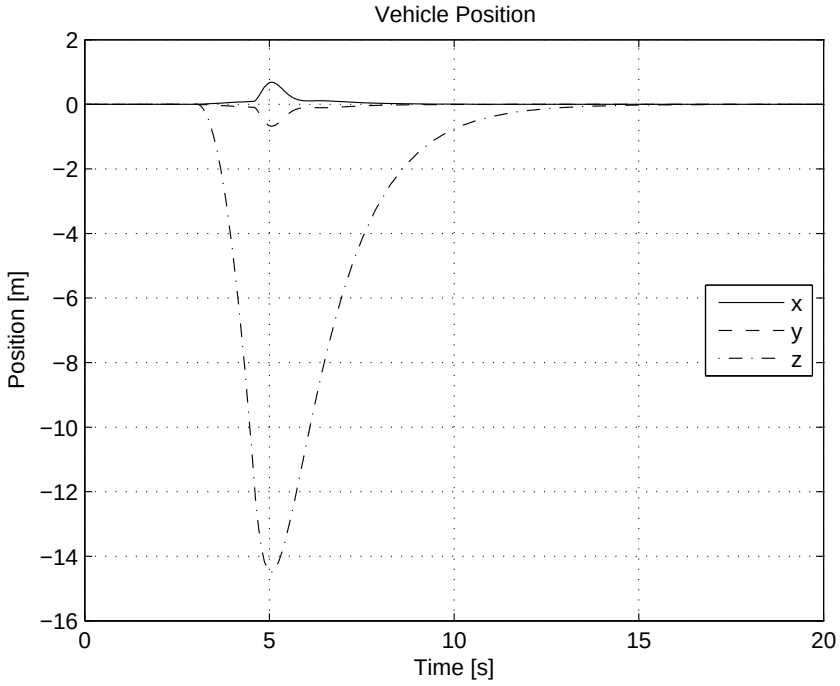

Figure 6.8: Position Recovery for Failures in 2 Consecutive Effectors, {7,6}

Attitude Response The initial rotational perturbation is stopped and the rotation is reversed to return to the initial position. There is possible scope in future work to 'tune' the choice of $\bar{q}_d$ depending on $\dot{\bar{q}}$ and was discussed in Section 5.6 so that the recovery could be faster and the altitude drop could be reduced.

The overshoot on the attitude is required in order to return the vehicle to the initial position since the failure perturbation generates an acceleration in x_w, y_w, and z_w.

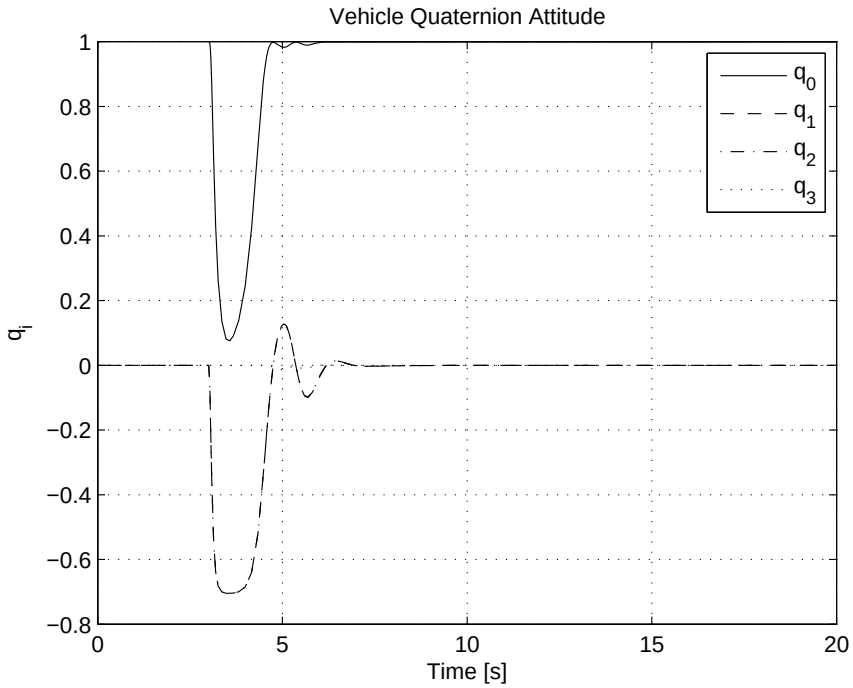

Figure 6.9: Attitude Recovery for Failures in 2 Consecutive Effectors, {7,6}

6.5.3 Failure in Two Non-Consecutive Effectors

This scenario concerns failures in two non-consecutive effectors. Because of the number of effectors on the octorotor and the physical layout of the vehicle there are three possible ways in which this failure can occur and still leave a controllable vehicle after control reconfiguration:

- Fail $\{7, 5\}$,
- Fail $\{7, 4\}$, and
- Fail $\{7, 3\}$.

The rotor speeds required for hover are

$$\sqrt{\mathbf{u}_{\{7,5\}}} = \begin{bmatrix}\Omega_0\\ \Omega_1\\ \Omega_2\\ \Omega_3\\ \Omega_4\\ \Omega_6\end{bmatrix} \begin{bmatrix}266\\ 217\\ 193\\ 217\\ 266\\ 322\end{bmatrix} \text{rad/s} \tag{6.24}$$

$$\sqrt{\mathbf{u}_{\{7,4\}}} = \begin{bmatrix}\Omega_0\\ \Omega_1\\ \Omega_2\\ \Omega_3\\ \Omega_5\\ \Omega_6\end{bmatrix} \begin{bmatrix}307\\ 166\\ 166\\ 307\\ 258\\ 258\end{bmatrix} \text{rad/s} \tag{6.25}$$

$$\sqrt{\mathbf{u}_{\{7,3\}}} = \begin{bmatrix}\Omega_0\\ \Omega_1\\ \Omega_2\\ \Omega_4\\ \Omega_5\\ \Omega_6\end{bmatrix} \begin{bmatrix}307\\ 217\\ 217\\ 307\\ 217\\ 217\end{bmatrix} \text{rad/s} \tag{6.26}$$

Position Response The x_w disturbance in in Fail $\{7, 5\}$ is caused by the imbalance in the overall pitch thrust of the vehicle, whilst the perturbation in x_w for Fail $\{7, 4\}$ is due to the imbalance in the overall yaw moments acting on the vehicle and so is small. It is also not caused by the initial failure, rather by the reallocated recovery after rolling. Fail $\{7, 3\}$ is a special case where the effectors are diametrically opposite one another and so introduce no disturbing rolling or pitching moment onto the vehicle.

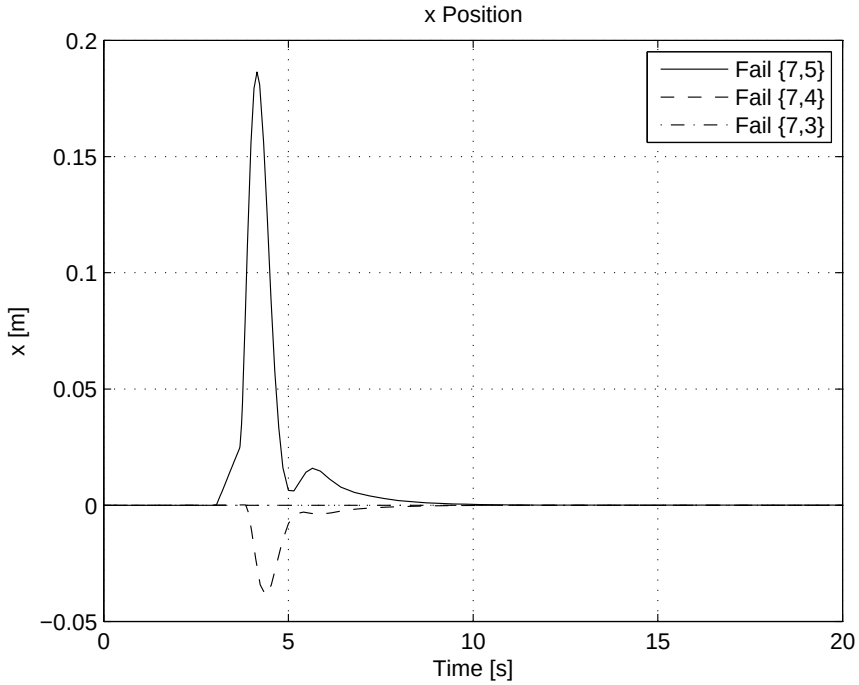

Figure 6.10: x_w Recovery for Failures in Two Non-Consecutive Effectors

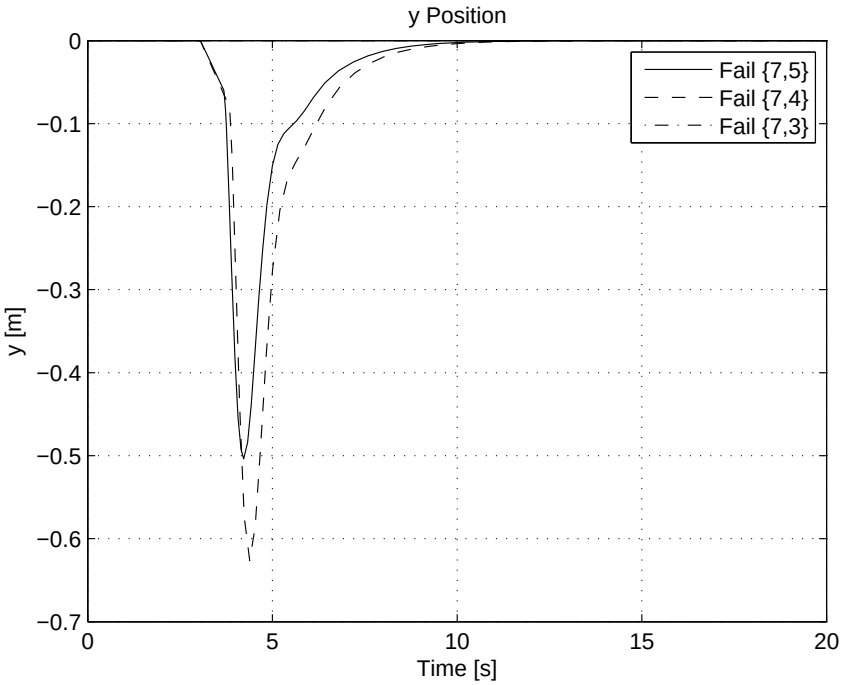

Figure 6.11: y_w Recovery for Failures in Two Non-Consecutive Effectors

The y_w recovery is similar for Fail $\{7, 5\}$ and Fail $\{7, 4\}$ since there is a large adverse rolling moment. It is slightly larger for Fail $\{7, 4\}$ because the failure provides a pure rolling disturbance instead of the roll and pitch disturbance with Fail $\{7, 5\}$. Fail $\{7, 3\}$ shows no movement in y_w since the effectors are opposite each other.

The altitude recovery shows that Fail $\{7, 4\}$ takes the longest to return $\alpha \leq \alpha_{\max}$. Fail $\{7, 3\}$ loses altitude due to the reduction in overall available thrust during the effector failure. This altitude drop is less than for the other failures because there is no disturbance to the vehicle attitude and so $\alpha \leq \alpha_{\max}$ for the duration of the failure and recovery.

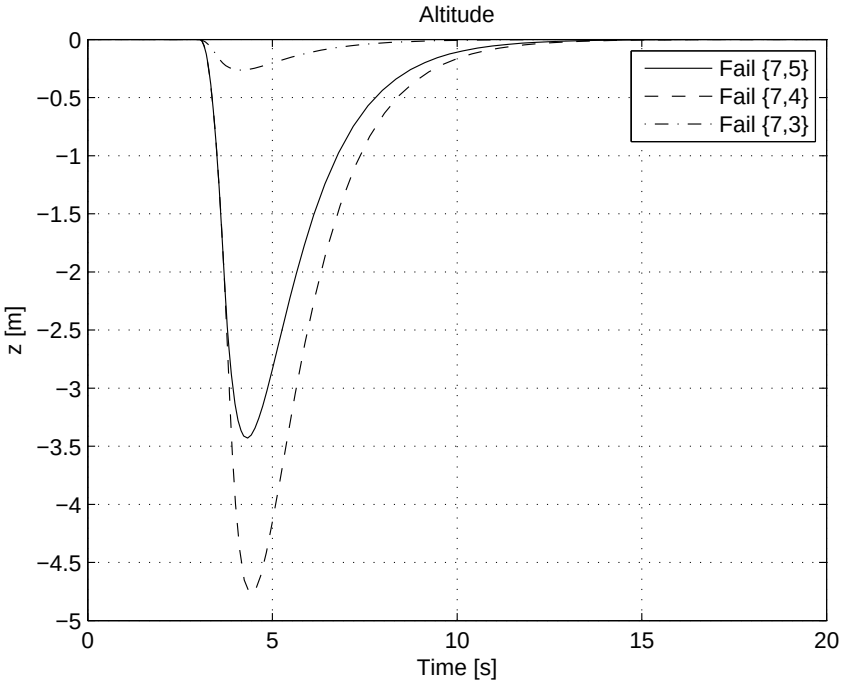

Figure 6.12: Altitude Recovery for Failures in Two Non-Consecutive Effectors

Attitude Response Fail $\{7, 5\}$ shows the combination of the roll and pitch disturbance. Fail $\{7, 4\}$ consists of a pure rolling motion, and Fail $\{7, 3\}$ is the special case where the failures are diametrically opposite each other and so the only disturbing force is an adverse yaw.

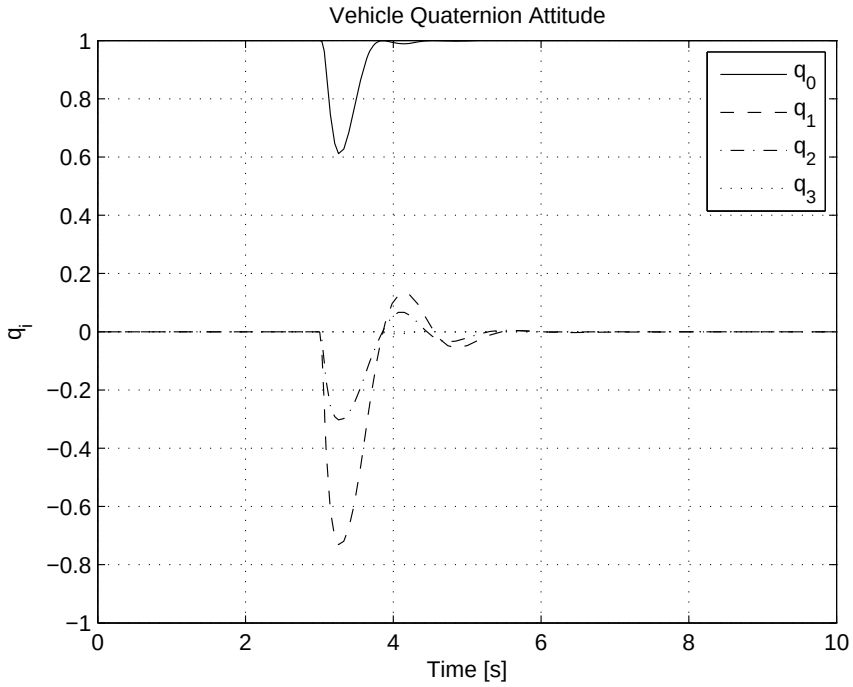

Figure 6.13: Vehicle Attitude Recovery for Fail $\{7, 5\}$

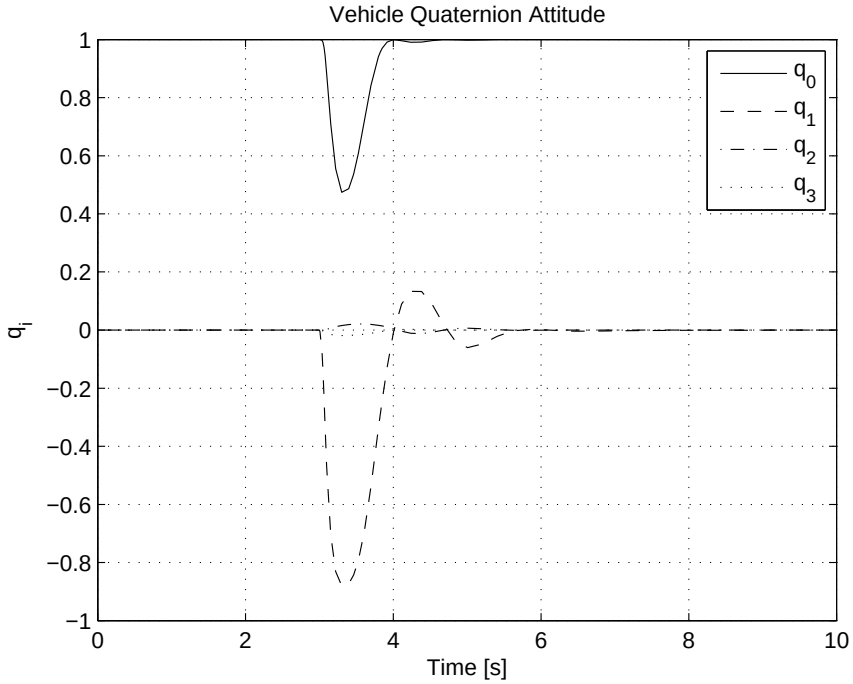

Figure 6.14: Vehicle Attitude Recovery for Fail $\{7, 4\}$

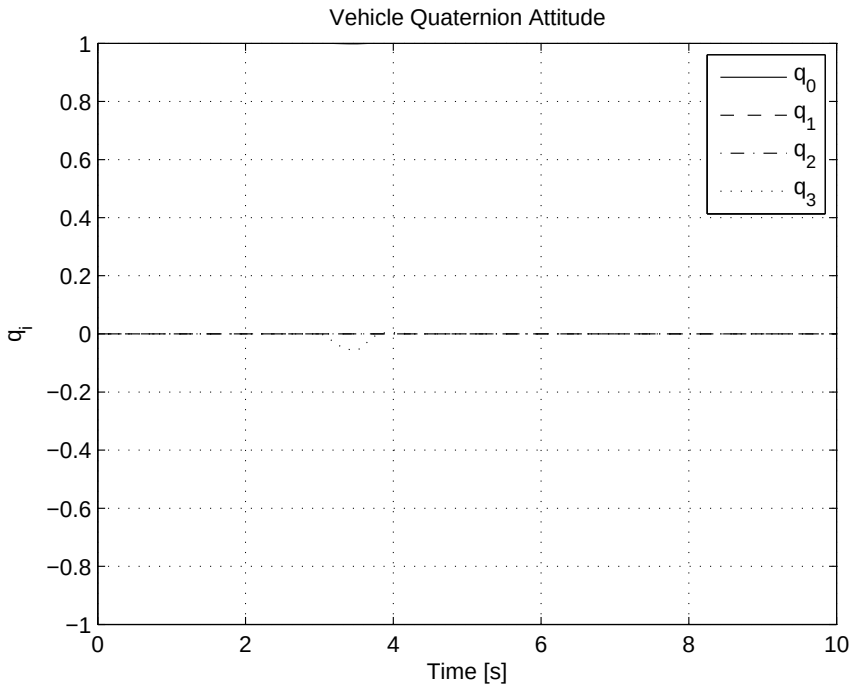

Figure 6.15: Vehicle Attitude Recovery for Fail $\{7, 3\}$

6.5.4 Failure in Three Effectors, Two Consecutive

For the octorotor there are two cases where this failure scenario is seen, Fail $\{7, 6, 4\}$ and Fail $\{7, 6, 3\}$.

The rotor speed required for hover are

$$\sqrt{\mathbf{u}_{\{7,6,3\}}} = \begin{bmatrix} \Omega_0 \\ \Omega_1 \\ \Omega_2 \\ \Omega_4 \\ \Omega_5 \end{bmatrix} = \begin{bmatrix} 331 \\ 237 \\ 177 \\ 280 \\ 317 \end{bmatrix} \text{ rad/s} \tag{6.27}$$

$$\sqrt{\mathbf{u}_{\{7,6,4\}}} = \begin{bmatrix} \Omega_0 \\ \Omega_1 \\ \Omega_2 \\ \Omega_3 \\ \Omega_5 \end{bmatrix} = \begin{bmatrix} 343 \\ 193 \\ 133 \\ 266 \\ 365 \end{bmatrix} \text{ rad/s} \tag{6.28}$$

Position Response Fail $\{7, 6, 4\}$ shows a larger x_w displacement since all three effectors fail in the same semicircle of the vehicle axes. This causes a large adverse rolling and pitching moment. The adverse pitching seen in Fail $\{7, 6, 3\}$ is due to the fact that three effectors failed at the same time (as seen earlier, Fail $\{7, 3\}$ does not show any characteristic of departing from the initial position) and there is an adverse yaw that must be overcome after control reallocation.

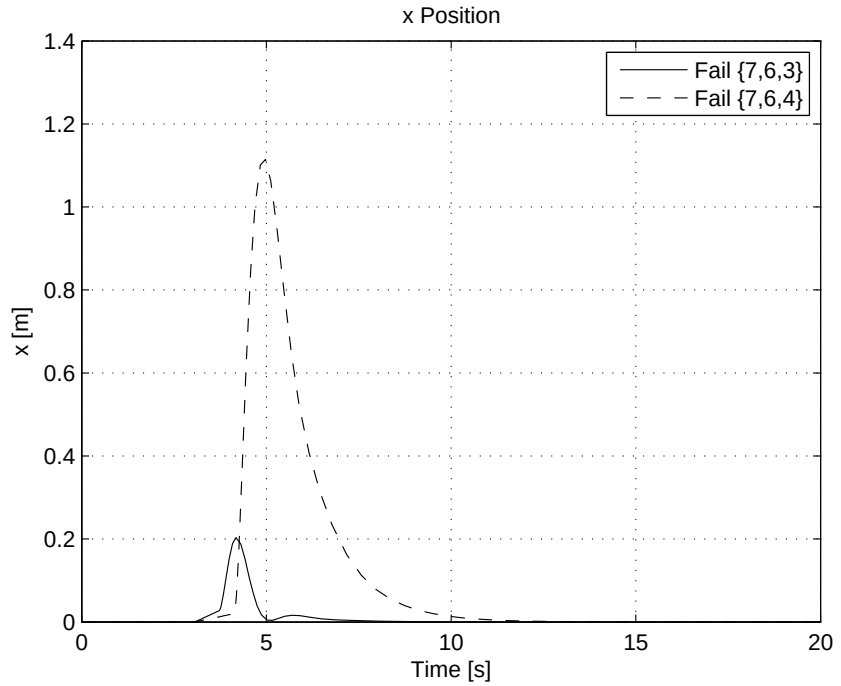

Figure 6.16: x_w Recovery for Failures in Three Effectors (Two Consecutive)

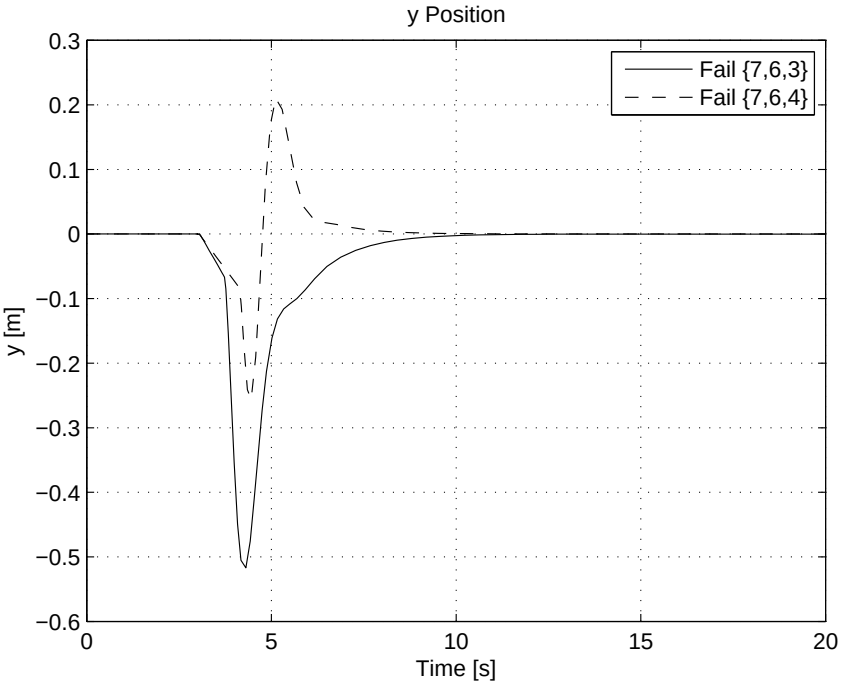

Figure 6.17: y_w Recovery for Failures in Three Effectors (Two Consecutive)

Fail $\{7, 6, 4\}$ undergoes a large perturbation on all three vehicle axes and so when control reallocation is complete the vehicle recovery is slower than for Fail $\{7, 6, 3\}$ where the initial disturbance is not too large and the applied rotational velocity is not so high that the vehicle cannot quickly stop the rotation and return to the initial position. The altitude recovery is shown in Figure 6.18.

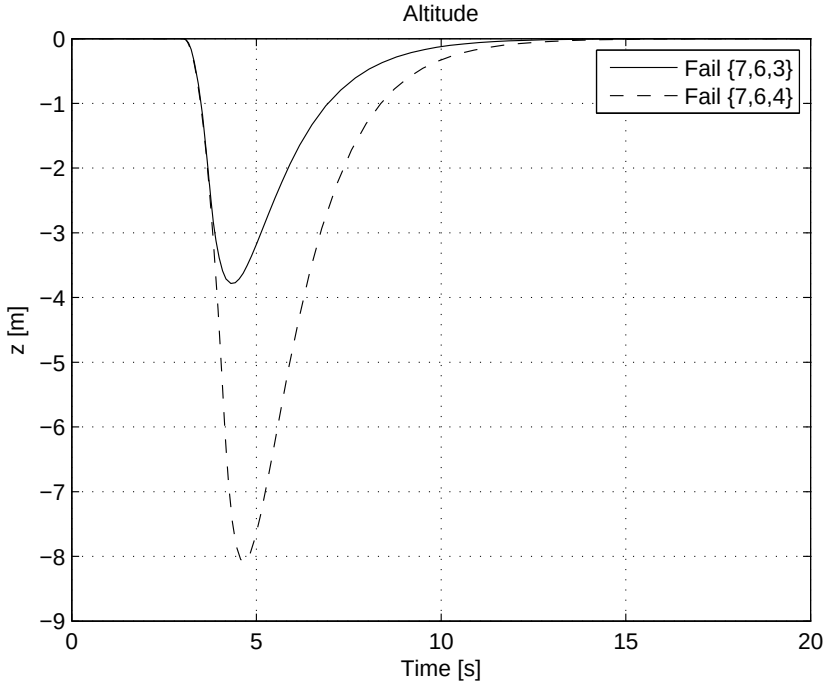

Figure 6.18: Altitude Recovery for Failures in Three Effectors (Two Consecutive)

Fail $\{7, 6, 3\}$ suffers a similar loss in altitude to Fail $\{7\}$ and there are parallels between the two scenarios. Fail $\{7, 6, 3\}$ can be considered as a special case of Fail $\{7\}$ where the failure occurs in effector 6 and with a small external disturbance in total thrust to represent the loss of effectors 7 and 3. Fail $\{7, 6, 4\}$ undergoes a larger altitude loss since the vehicle does not tumble over itself and the rotations are stopped and then returns to the initial position.

Attitude Response In Fail {7,6,3} the dominant disturbance is caused by the failure in effector 6 since the failures in effectors 7 and 3 'cancel out'. Fail {7,6,4} shows a more extreme disturbance in all three body axes - this is also seen in the position response figures where the time taken for the vehicle to return to the original position for Fail {7,6,4} takes longer than for Fail {7,6,3}.

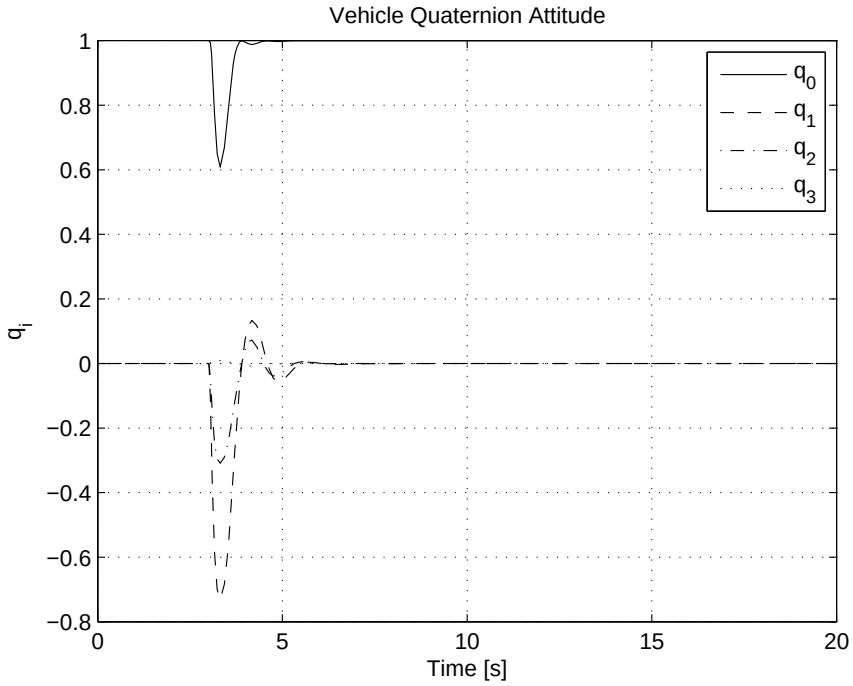

Figure 6.19: Attitude Recovery for Fail {7,6,3}

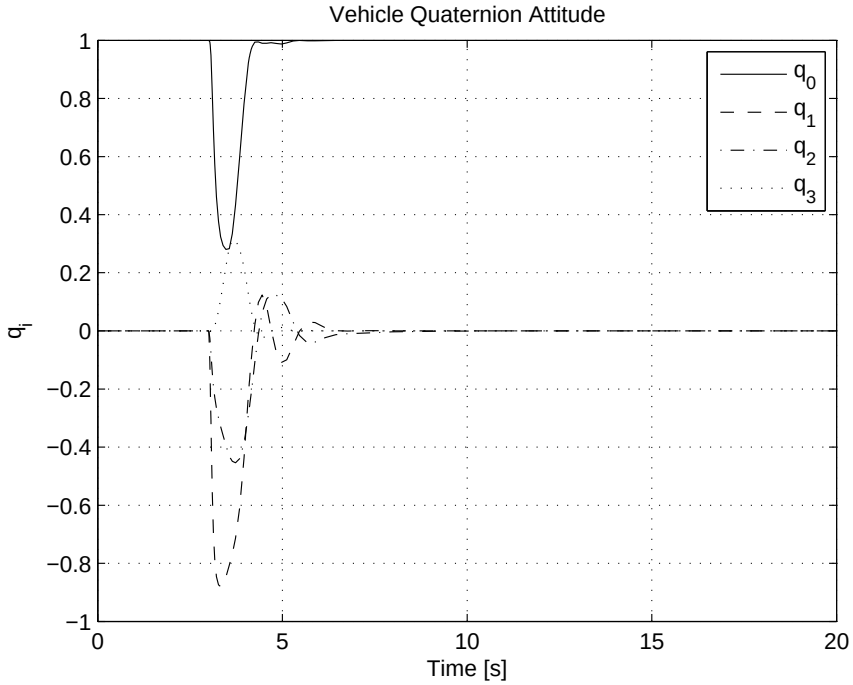

Figure 6.20: Attitude Recovery for Fail {7,6,4}

6.5.5 Failure in Three Effectors

Two scenarios are investigated for the octorotor, Fail {7,5,2} and Fail {7,5,3}.

The rotor speed required for hover are

$$\sqrt{\mathbf{u}_{\{7,5,2\}}} = \begin{bmatrix}\Omega_0\\ \Omega_1\\ \Omega_3\\ \Omega_4\\ \Omega_6\end{bmatrix} = \begin{bmatrix}235\\ 290\\ 250\\ 266\\ 322\end{bmatrix} \text{ rad/s} \tag{6.29}$$

$$\sqrt{\mathbf{u}_{\{7,5,3\}}} = \begin{bmatrix}\Omega_0\\ \Omega_1\\ \Omega_2\\ \Omega_4\\ \Omega_6\end{bmatrix} = \begin{bmatrix}278\\ 217\\ 232\\ 333\\ 295\end{bmatrix} \text{ rad/s} \tag{6.30}$$

Position Response The disturbance in the position for the two failure cases under consideration is not large since the failures are fairly evenly distributed around the body. This means that there is no overly large, dominant adverse moment that is generated when the failures occur.

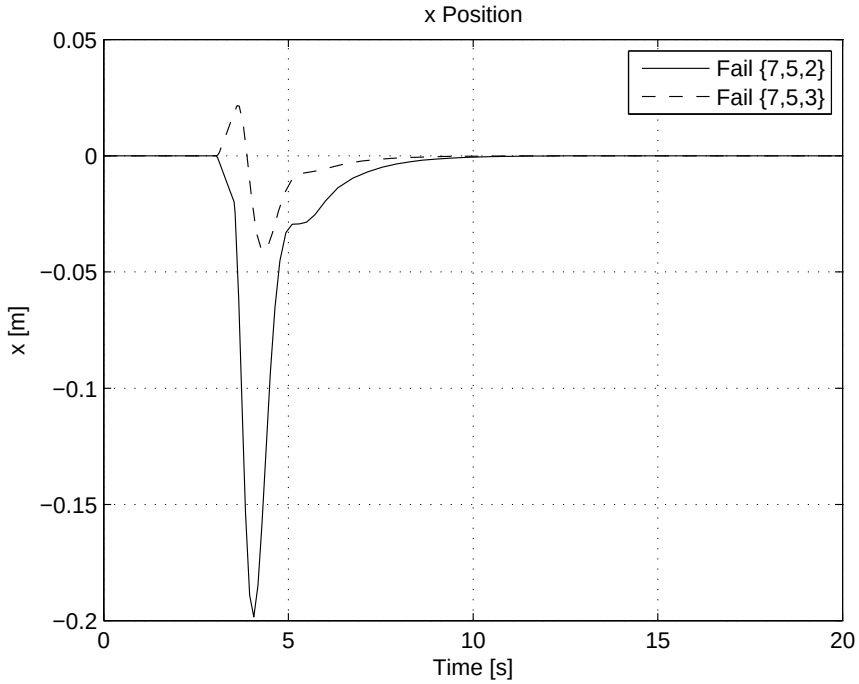

Figure 6.21: x_w Recovery for Failures in Three Effectors

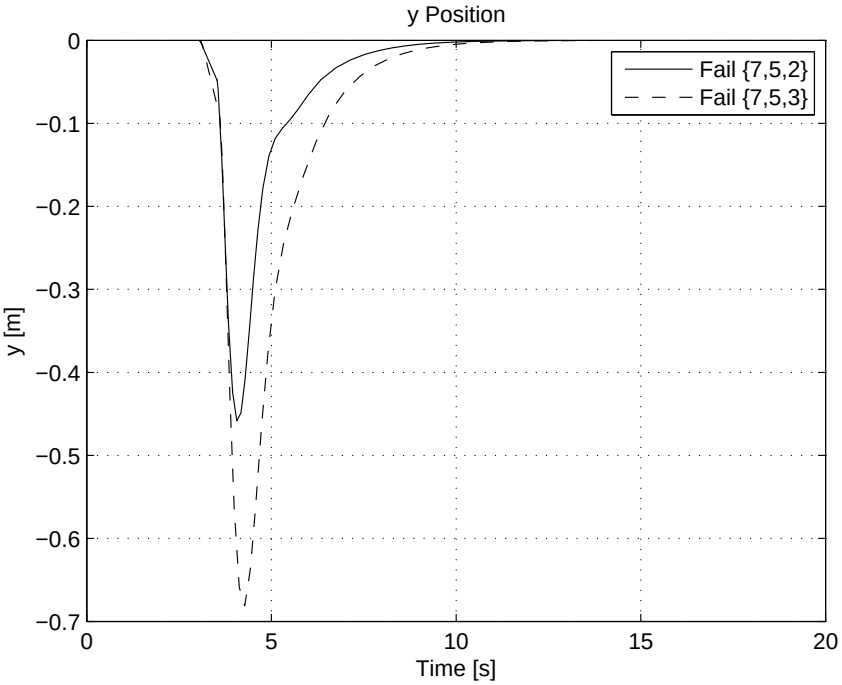

Figure 6.22: y_w Recovery for Failures in Three Effectors

Both failure cases introduce a disturbance in $-y_w$ due to the residual adverse roll from the effector failures. In Fail {7,5,3} this is because the adverse roll from effectors 7 and 3 cancel out, leaving the adverse roll from a failure in effector 5. In Fail {7,5,2} the roll disturbance is lower since the larger adverse roll caused by effectors 5 and 2 are cancelled out leaving the adverse roll from effector 7.

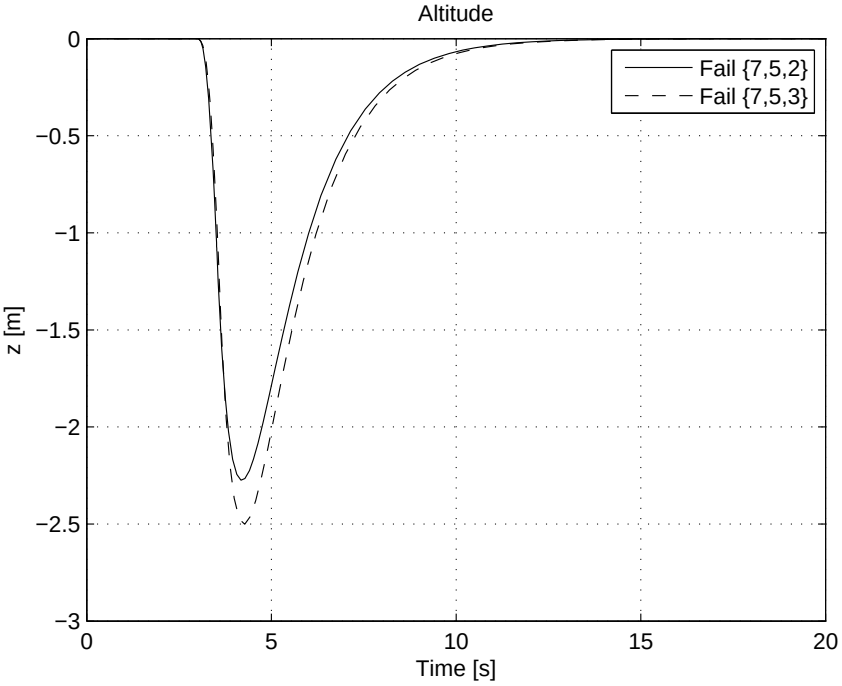

Figure 6.23: z_w Recovery for Failures in Three Effectors

The altitude drop is caused by a reduction in overall thrust from the effector failures as well as the time period where $\alpha > \alpha_{\max}$. The attitude disturbances are not overly large (see Section 6.5.5) and so the altitude drop is not large.

Attitude Response The disturbance for this failure is not too extreme as the failures are quite evenly spaced around the vehicle and so the adverse failure effects are in some ways evenly distributed around the body and the vehicle is quickly brought back to level hover over the original position.

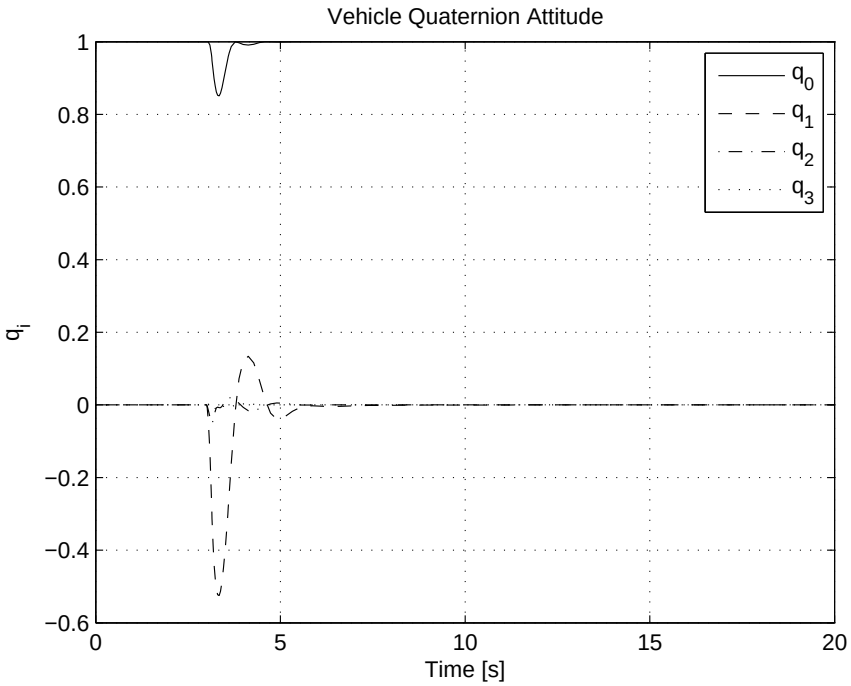

Figure 6.24: Attitude Recovery for Failures in Three Effectors, {7,5,2}

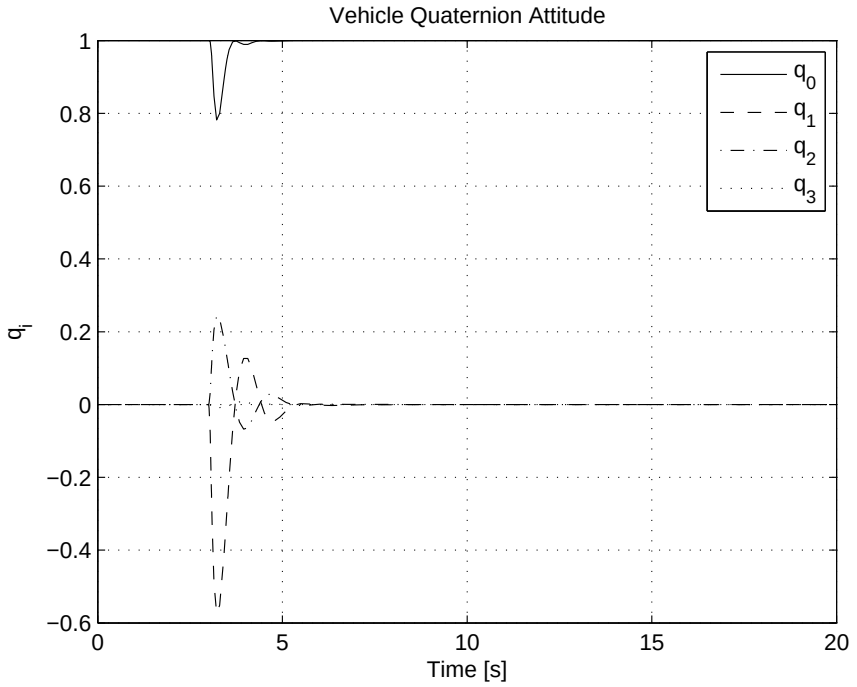

Figure 6.25: Attitude Recovery for Failures in Three Effectors, {7,5,3}

The attitude response of the vehicle for Fail {7,5,3} is similar to that of Fail {7,6,3} since the diametrically opposite failures 'cancel out' and do not have a large impact on the attitude response. The dominant effect is a negative adverse roll coupled with a smaller positive pitch caused by the failure in effector 5.

6.5.6 Failure in Four Effectors

The failure scenarios investigated are Fail {7,6,4,2}, Fail {7,6,4,1}, and Fail {7,6,3,1}. The special cases of Fail {7,6,3,2} and Fail {7,5,3,1} are considered by themselves since they are representative of a quadrotor.

The rotor speeds for hover for the failure cases are

$$\sqrt{\mathbf{u}_{\{7,6,4,2\}}} = \begin{bmatrix}\Omega_0\\ \Omega_1\\ \Omega_3\\ \Omega_5\end{bmatrix} = \begin{bmatrix}332\\ 235\\ 279\\ 365\end{bmatrix} \text{ rad/s} \tag{6.31}$$

$$\sqrt{\mathbf{u}_{\{7,6,4,1\}}} = \begin{bmatrix}\Omega_0\\ \Omega_2\\ \Omega_3\\ \Omega_5\end{bmatrix} = \begin{bmatrix}365\\ 235\\ 235\\ 365\end{bmatrix} \text{ rad/s} \tag{6.32}$$

$$\sqrt{\mathbf{u}_{\{7,6,3,1\}}} = \begin{bmatrix}\Omega_0\\ \Omega_2\\ \Omega_4\\ \Omega_5\end{bmatrix} = \begin{bmatrix}365\\ 279\\ 235\\ 332\end{bmatrix} \text{ rad/s} \tag{6.33}$$

Position Response With the combinations of effector failures there is a chance that some of the failures 'cancel' each other out and the disturbance to vehicle is less than for other cases (for example, the adverse pitch and roll disturbance applied to the vehicle for Fail {7,6} is the largest that is experienced). All three cases considered pitch forwards until reallocation where they return to the original position.

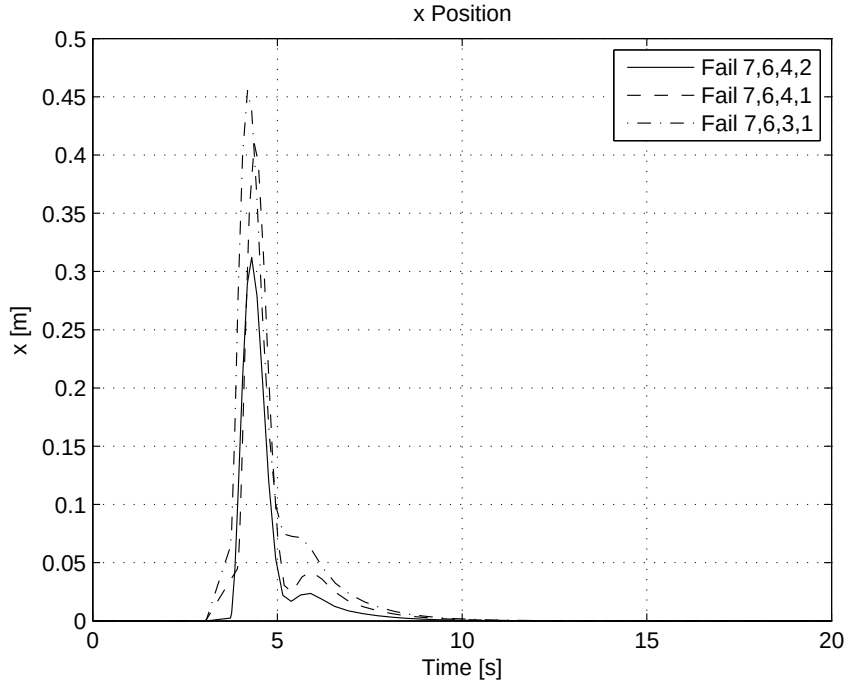

Figure 6.26: x_w Recovery for Failures in Four Effectors

The y_w response for all cases is similar where the vehicle rolls to the left towards the failed effectors.

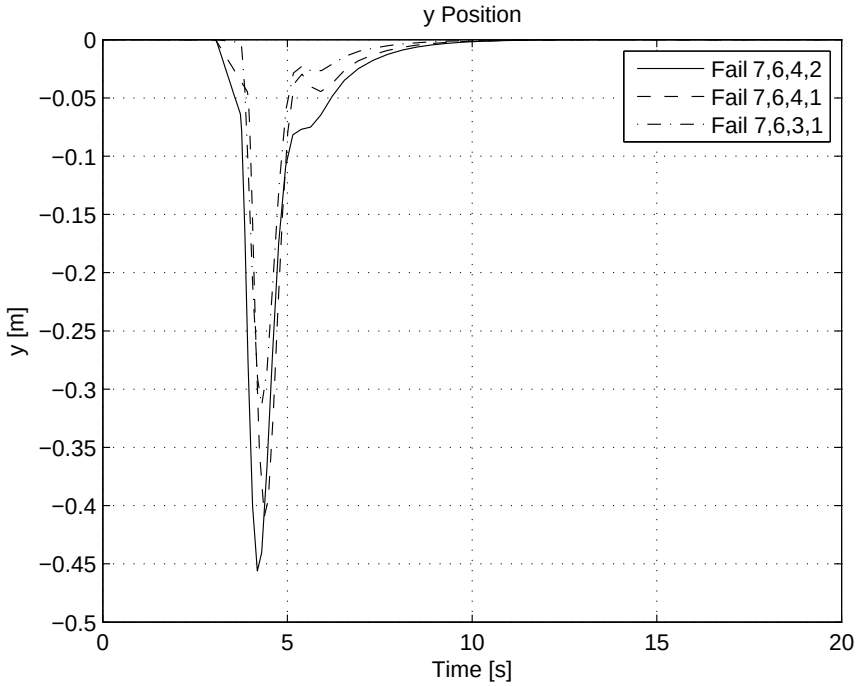

Figure 6.27: y_w Recovery for Failures in Four Effectors

The altitude recovery is shown in Figure 6.28 where the altitude recovery of Fail

{7,6,4,2} and Fail {7,6,3,1} are identical

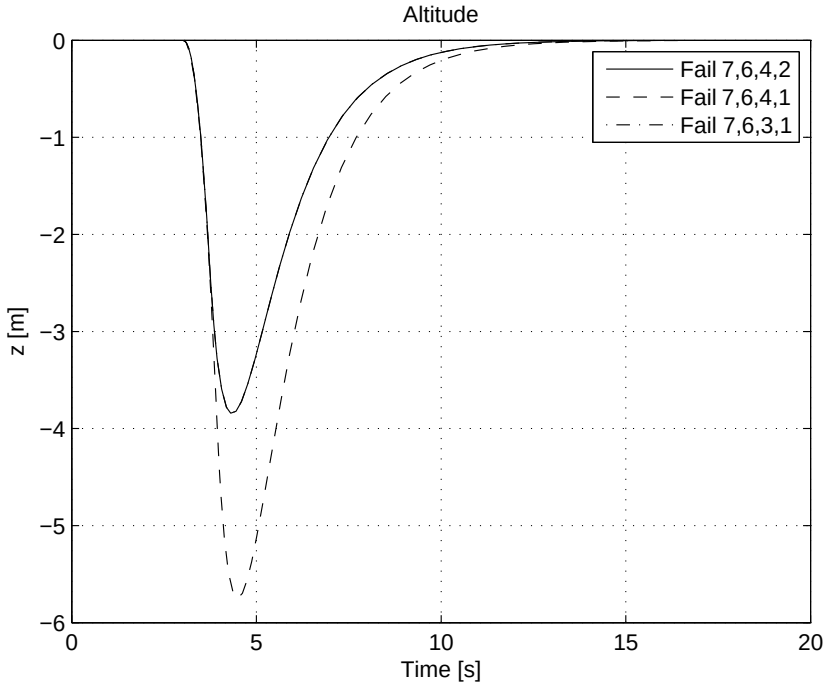

Figure 6.28: z_w Recovery for Failures in Four Effectors

Attitude Response The recovery after the considered failure cases are shown in the following figures.

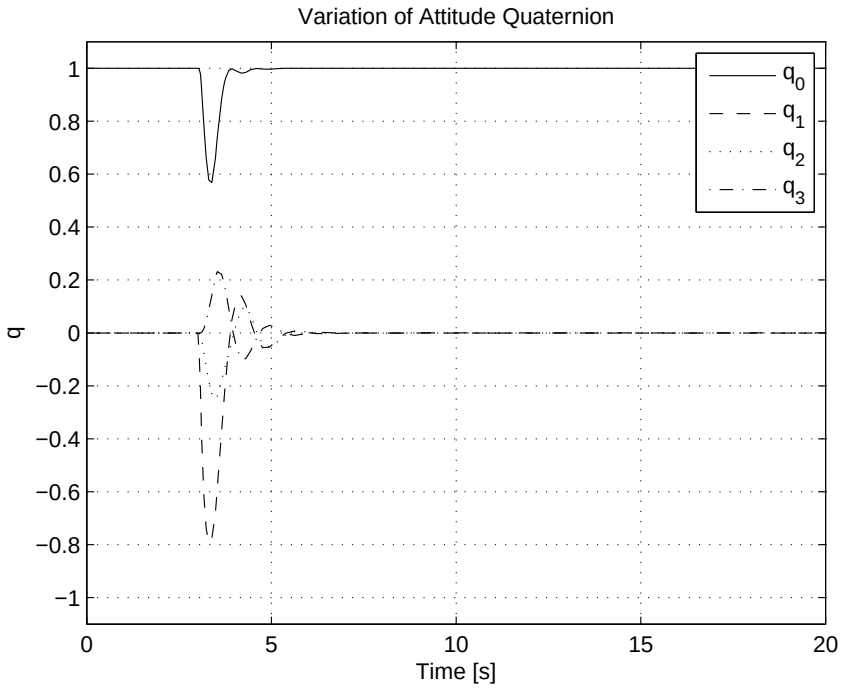

Figure 6.29: Attitude Recovery for Failures in Four Effectors, {7,6,4,2}

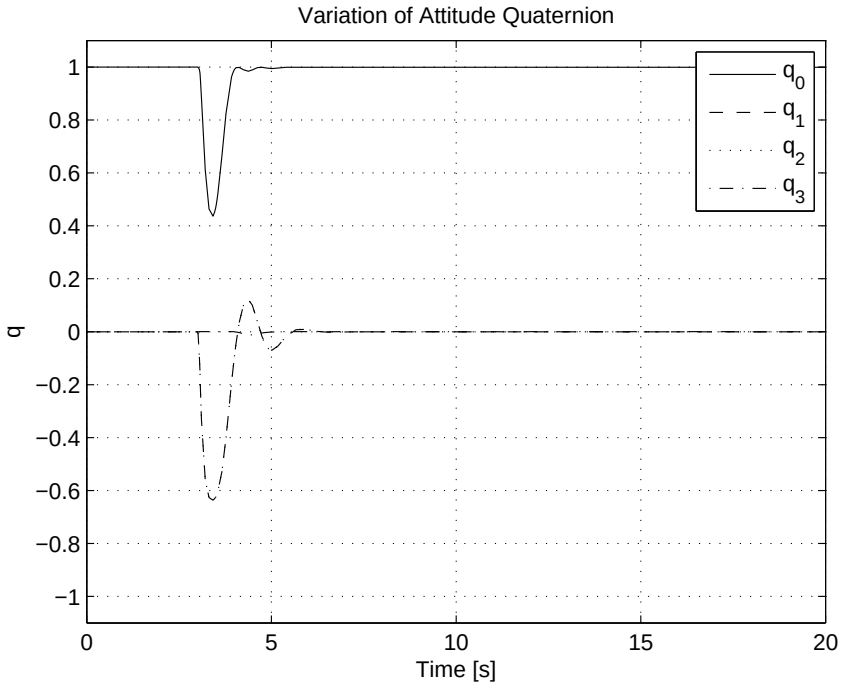

Figure 6.30: Attitude Recovery for Failures in Four Effectors, {7,6,4,1}

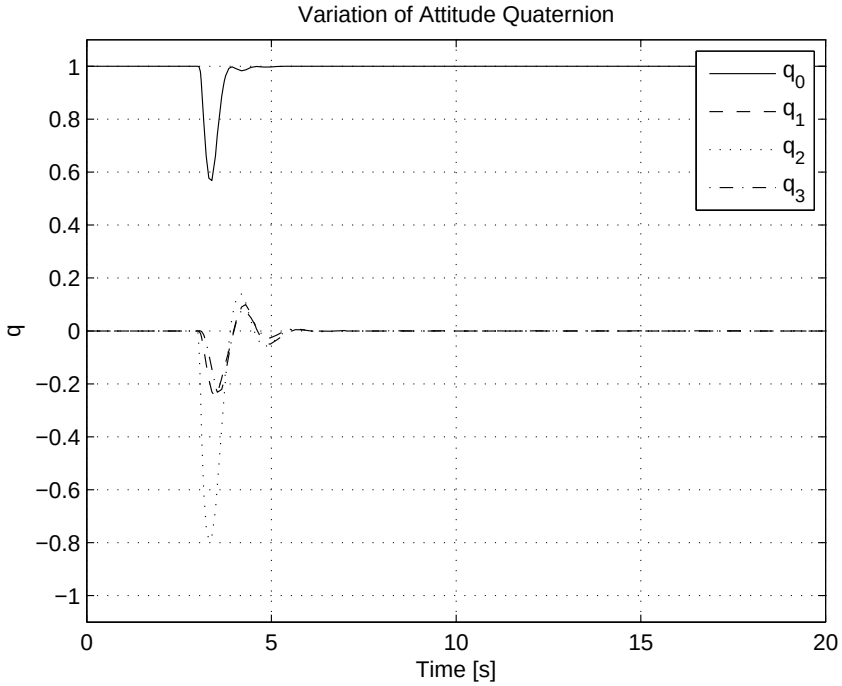

Figure 6.31: Attitude Recovery for Failures in Four Effectors, {7,6,3,1}

The two cases of Fail {7,6,3,2} and Fail {7,5,3,1} are shown separately because the vehicle setup after the control reallocation is a quadrotor. The position response is shown in Figure 6.32. There are no adverse moments generated and so the vehicle

does not deviate in x_w or y_w with the drop in altitude caused by the reduction in thrust from the four failed effectors. After reallocation the altitude drop is recovered.

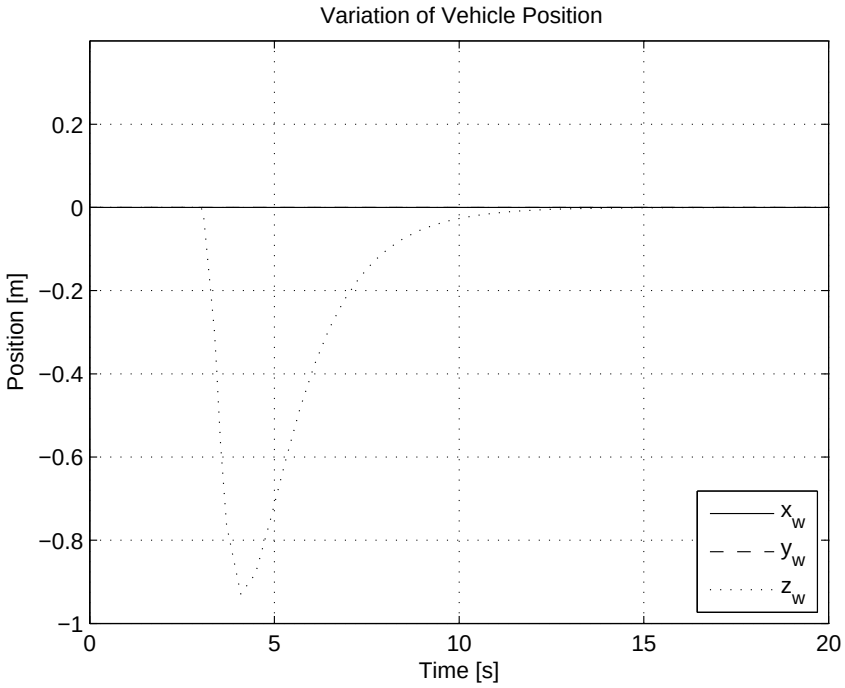

Figure 6.32: Position Recovery for Failures in Four Effectors

The failures leave a resultant quadrotor vehicle and the trimmed rotor speeds for level hover are

$$\sqrt{\mathbf{u}_{\{7,6,3,2\}}} = \begin{bmatrix}\Omega_0\\ \Omega_1\\ \Omega_4\\ \Omega_5\end{bmatrix} = \begin{bmatrix}307\\ 307\\ 307\\ 307\end{bmatrix} \text{ rad/s} \tag{6.34}$$

$$\sqrt{\mathbf{u}_{\{7,5,3,1\}}} = \begin{bmatrix}\Omega_0\\ \Omega_2\\ \Omega_4\\ \Omega_6\end{bmatrix} = \begin{bmatrix}307\\ 307\\ 307\\ 307\end{bmatrix} \text{ rad/s} \tag{6.35}$$

6.6 Conclusion

- The generation and detection of a failure is presented, and the fault hiding method is used to reconfigure the plant so that the controller remains invariant.
- A restriction is enforced so that the post-failure model must retain Kalman controllability. The combination of failures which ensure controllability is shown and the vehicle recovery for the controllable scenarios is presented.
- The simulations of the failure recovery take account of the failed effectors and constrain the control demand so that it is allocatable.
- The rotor speeds for trimmed flight for specific failure scenarios are given.

Chapter 7

Flight Testing

7.1 Introduction

This chapter discusses the implementation of the controller and a pseudo inverse allocation method to a flight test vehicle. The hardware selections are explained, and the challenges of the flight testing are described. The results from a number of representative flight tests are included, including hover, yaw control, and position control (translational) flights.

7.2 Choice of Hardware

The flight test equipment was not chosen through a rigorous comparison of requirements, rather the choice was based on availability of platform, a suitable open source controller, and local knowledge of components all of which combined to produce a suitable test vehicle. It is not intended for the components below to be taken as the optimum combination, and in an era where 3-d printing is prevalent the selection of suitable components (especially frames), is a dynamic challenge with new products and solutions emerging on a regular basis.

The controller for the flight vehicle is based on the Ardupilot Mega with APM1 IMU shield [Ardupilot, a]. The microcontroller is based on the ATmega2560 from Atmel [Atmel] and the full list of features of the IMU shield can be found on the Ardupilot wiki page [Ardupilot, b]. The key sensors are the 3-axis gyroscope, 3-axis accelerometer, magnetometer, and barometric pressure sensor. This control board was chosen due to its open source programming language and the flexibility to extract data from the sensors in their raw format. Over the course of this research the software and controller hardware have gone through various iterations and now are much more advanced than when initial flight testing occurred in 2011, to the point where initially the hardware was ideal for research opportunities and now is almost 'plug-and-play'. The code has had to be rewritten and restructured as

the ease of use and functionality has increased. The Ardupilot project has since moved on to supporting APM2.5+ hardware meaning that the APM1 hardware and software on the octorotor should be a stable platform for future investigations.

The vehicle frame is the Mikrokopter OktoXL [Mikrokopter] (photographs are included in Appendix C) and this has proven to be hard wearing and robust to impacts. The motor mounts allow for various sizes of brushless outrunner motor to be installed and there are numerous mounting options for the controller. Its modular design also means that it is possible to reconfigure this frame kit to create a desired vehicle layout. A number of companies offer competing products and allow for flexibility in choice between size, motor mounting options, and construction material.

Over the last few years the advances in lithium polymer battery technology have meant that battery capacity has increased whilst weight and charging time have decreased. All batteries used for the flight testing are attached to the underside of the vehicle between the landing gear legs and are aligned with x_b in order to have a low impact on off-diagonal inertia terms. Velcro is used as the main attachment method with a strap used as a secondary safeguard in case of a crash landing or delaminating of the glue holding the Velcro to the battery and mounting point which was seen to occur during a period of cold weather. A variety of batteries have been used for the flight testing and are of voltage class 3S with capacities of between 3000mAh-4000mAh and are of similar mass and shape.

Over the length of this research project the motors, electronic speed controllers (ESCs), and propellers have been changed due to wear-and-tear, obsolescence, crashes, and one notable electrical fire. It is shown in Section 4 that the controller is robust to variations in the plant where the inertias are not required (providing the saturation term is updated). The flight test results are therefore representative of any VTOL capable vehicle. The flight testing results are used to show that the controller is applicable to attitude control and that it can track pilot demands. Furthermore the flight testing was carried out indoors at Cranfield University, UK and Kitakyushu University, Japan where GPS data was not available so position tracking was not possible. Position control was achieved through manual control of the vehicle attitude - pitching forwards to move forwards, etc. Altitude measurement was performed using a barometric pressure sensor and is not as accurate as using a sonar-based or vision system therefore deviation from level flight is seen, particularly when manoeuvring indoors and close to the ground where the induced flow from the rotors had an impact on the altitude hold until a modification was made to the sensor by covering it loosely with cotton wool.

Rotor blades were chosen based on availability and suitability to the frame size. Initially there were not many choices available since the propeller size had to be available in both standard 'tractor' and negative pitch 'pusher' configuration since some rotate clockwise and some counter-clockwise. The diameter of the rotor blades was constrained so that neighbouring rotors did not overlap whilst still providing for a large enough disc area.

Control demands were transmitted using a Spektrum Dx8 transmitter [Spektrum,

b] and received using an 8 channel AR8000 Spektrum receiver [Spektrum, a] which were chosen for their numerous channels, high resolution, short frame rate, and high reliability. Stick scaling and mixing was also easy to implement and these proved useful for the initial flight testing where gains were being tuned. Four channels are needed to provide four reference inputs (x_d, y_d, z_d, ψ_d) where, for example, an increase in the x_d channel pitches the vehicle forwards and on releasing the spring-loaded control stick the vehicle stops its forward motion and hovers in place. A fifth channel is used to change the flight mode so that the control sticks directly control the body attitude rate where an increase in the pitch channel begins a pitch up manoeuvre and a change in position. As the stick is released the pitch rate stops but the pitch angle is maintained so the position of the vehicle continues to change. To return to level hover a corresponding negative pitch rate is manually commanded. Note than when used without GPS coverage (such as indoors) an increase in x_d maps directly to an increase in forwards position and y_d to an increase in right position. z_d and ψ_d are mapped as an increase in altitude or yaw angle and do not depend on GPS data.

Telemetry is sent through 900MHz XBee modules which have a range of up to 10km [XBee] and allow for two-way conversation between the modules. Flight logs are saved on-board in flash memory and also transmitted to a base station laptop and contain flight parameters and control demands. This communications setup allows for transmission and reception of flight planner commands where GPS coordinate and altitude waypoints can be uploaded to the vehicle. The GPS data was not available for the flight testing and is therefore not shown in the results section.

7.3 Challenges During Flight Testing

7.3.1 Bullet Connectors

One notable challenge occurred during the flight testing phases of this research where the bullet connectors that were initially used to connect the motors and the ESCs. This method was chosen since it allows for an easy way to change the rotational sense of a motor by swapping around any two connecting wires. When left for a period of time and also exposed to a particularly cold environment the connections between the ESCs and motors began to deteriorate and there was a delay in the flight testing program whilst all connections were checked and replaced as needed.

7.3.2 Testing Indoors

The restriction to test indoors is in place due to the close proximity of Cranfield Airport to Cranfield University. The test flights were performed inside a large sports facility. This had the advantage of alleviating any wind influence, but meant that GPS signal was blocked and so autonomous position control could not be demon-

strated. There were also some collisions with the walls which lead to protective arm extensions being attached in order to prevent damage to rotor blades. The green foam blocks seen in Figure 7.1 were added to provide an extra measure of protection to any obstacles which may have been hit but proved to be ineffective as they slid along the arm extensions. They were removed for subsequent flight tests.

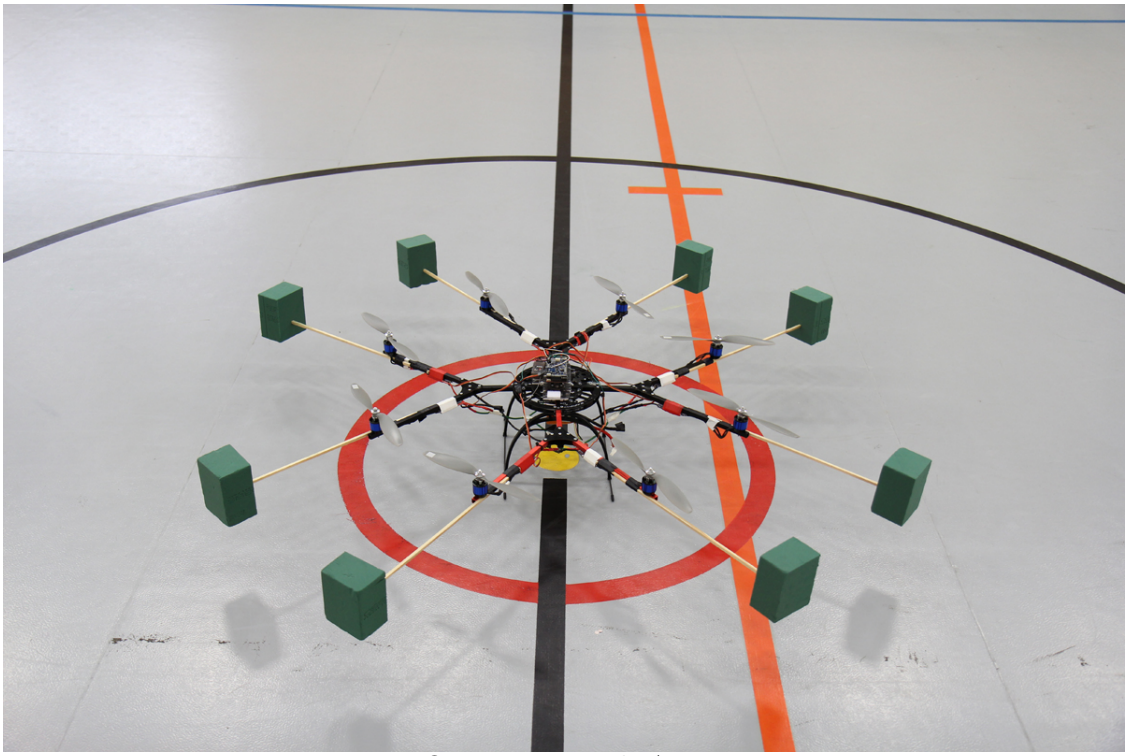

Figure 7.1: Octorotor With Arm Extensions

The IMU measurements from the indoor flight tests showed inaccurate yaw angle measurements. This effect was attributed to the interference of the steel structure. To avoid this the testing was moved outdoors where the magnetometer interference was avoided but other challenges (such as gust disturbances) were introduced. The results are shown in Section 7.5.

7.3.3 XBee Modules

A known issue is that the XBee modules can lock up ('brick') if data is sent between them before they are fully powered. This involves tedious resetting and pairing of the devices. This was made more difficult with the introduction of Windows 7 where the inbuilt security settings make it harder to perform this task. Overall they proved useful to transmit and receive telemetry during the tests.

7.4 Lessons Learnt

7.4.1 Choice of Hardware

Overall the hardware choice proved to be successful. The frame proved to be resilient to impacts and allowed for various vehicle configurations. The controller was sufficient to implement a modified code to control the octorotor, implement control allocation with a pseudo inverse method, and allowed access to sensor data for plotting. It was also possible to change the control allocation matrix to reflect the failed effectors. The batteries were replaced every year as lighter, quicker charging, and higher capacity versions were released. The rotor blades were purchased in bulk so as to reduce variation in production standard and were replaced if damaged. Extra ESCs and motors were purchased so as to replace broken ones as necessary. The extra protection offered by the arm extensions was useful not only to avoid collisions between the rotors and obstacles but also to provide stabilisation if a hard landing was carried out in which the flexible landing legs would deflect to absorb some of the impact and the rigid vehicle disc would wobble. This prevented striking the floor with the rotors. A suggestion is made to implement protective hardware as used on the QBall X-4 where the vehicle is totally enclosed in a protective cage (Figure 7.2 from Ireland and Anderson [2012]). This not only allows for more adventurous flight testing due to reduced risk of damage to the vehicle and its surroundings, but also allows the vehicle to roll along the floor before takeoff. The hardware also survived being taken to Japan in 2012 and performing flight demonstrations in extreme cold conditions before being disassembled for the return trip to the UK.

Figure 7.2: QBall-X4 Showing Protective Cage [Ireland and Anderson, 2012]

7.4.2 Controller

The choice of controller was largely driven by the requirement to be able to implement control allocation as well as to be able to extract sensor data. The open source nature of the Arducopter project, along with the help available in the Arducopter community made this a reality. Being able to tune controller gains 'on the fly' by using the XBee modules meant that initial flight testing could achieve a number of gain variations without having to dismantle the vehicle and risk damage when transporting to the laboratory.

7.4.3 Communications Method

The XBee modules performed adequately for the task of sending and receiving the telemetry data. Pairing of the devices proved frustrating initially but eventually was solved by waiting for the autopilot to initialise before applying power to the on-board module. There were no problems in using the Spektrum DSM2 modulation and the frequency band of 2.4GHz meant that there was no interference between the radio transmitter/receiver and the XBee transmitter/receiver.

7.5 Results

7.5.1 Hover

An arrow was put on the floor of the flight test area so that each flight could be initialised with the vehicle at the same initial attitude. During the test the vehicle was brought under control to a level hover at an altitude of approximately 1.5m. This ensured that the vehicle was outside of ground effect, yet it was easy enough to distinguish the body attitude without reference to the live IMU data. Once in the correct position and pose, a manual data flag was inserted into the data stream so that manoeuvre points could be identified after the flight. The data for the plots were sampled at 6Hz and is not filtered.

The Euler angles for the first flight are shown in Figure 7.3. The Euler angles are plotted rather than the quaternions since it is easier to visualise these angles. The noise in the signals come from a number of sources including the vibrations carried through the vehicles structure due to slight imballances in the propellers and flexure of the autopilot mount due to this excitation.

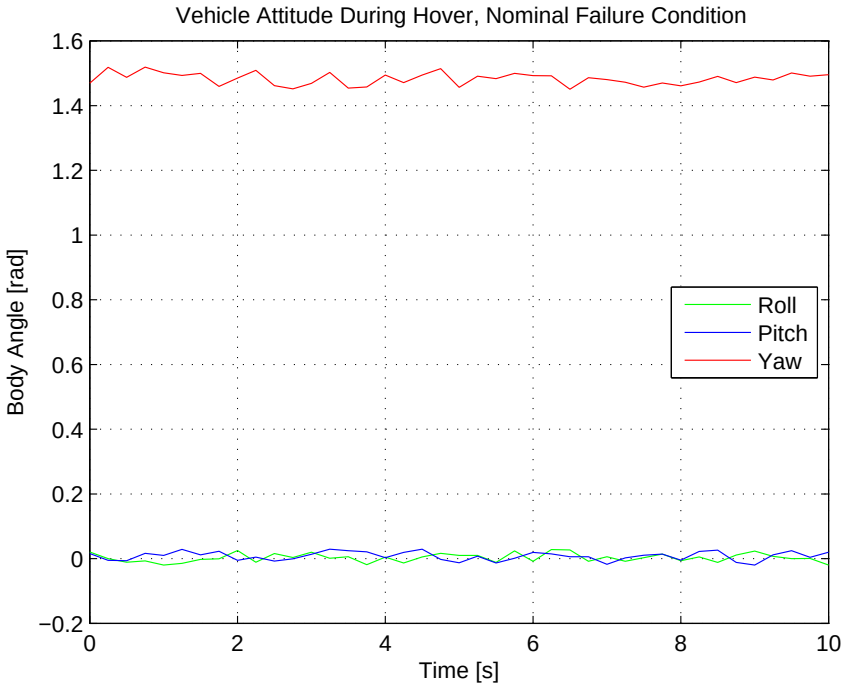

Figure 7.3: Nominal Hover Performance

The roll and pitch angles are below 0.1 rads for the duration of the flight and so the vehicle did not deviate far from the initial position. The yaw angle begins at close to $\frac{\pi}{2}$ which corresponds to pointing East. This attitude was maintained for the duration of the flight with only small deviations meaning that the vehicle did not translate far from its original position. Overall the vehicle is shown to be controllable for the level hover which is the position that is most desirable for conducting surveillance

work. This orientation means that the camera position does not move and a stable image can be obtained.

Figure 7.4 shows the Euler angles for a hover manoeuvre but with the vehicle utilising only 7 of the effectors. The vehicle performance is similar to the nominal case shown in Figure 7.3, and this is achieved by changing the control allocation matrix and using an invarient controller. This was accomplished by setting the control allocation a-priori. This was necessary since there was no autonomous online effector health monitoring system.

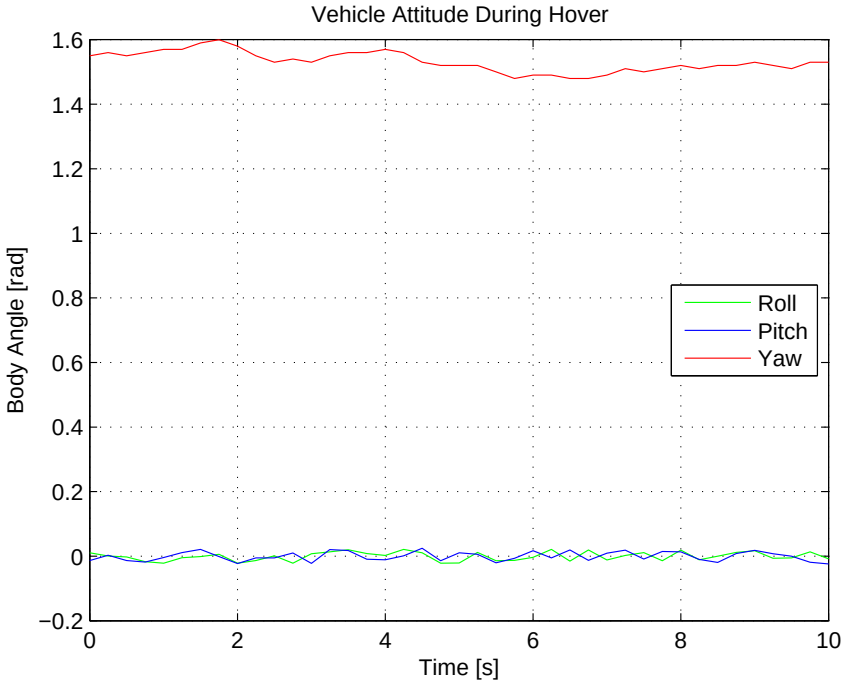

Figure 7.4: Euler Angles for Octorotor with 7 Effectors

Overall there are no substantial differences in the flight performances between the fully functioning octorotor and the vehicle with the effector failures. The Euler angles for the hover flights of the vehicle with fewer than 8 effectors are shown in Figures 7.4 to 7.9 and closely mirror the nominal results in Figure 7.3. The vehicle is able to maintain a level hover with the failures that are shown to be controllable as outlined in Table 6.1.

A general point to note is that the yaw angle contains a very low frequency oscillation about the desired value which is not seen with the roll and pitch values. This is because it was harder to visually detect a small movement in yaw and the yaw angle was controlled with reference to a magnetometer reading. This had a slight delay and discrete values in 1 degree increments, and so the small yaw variation is to be expected.

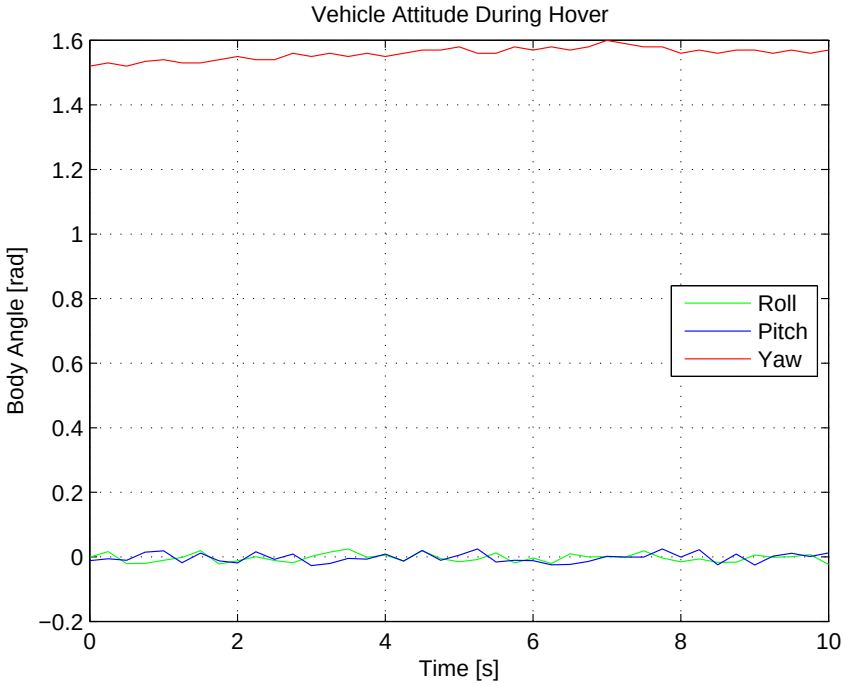

Figure 7.5: Euler Angles for Octorotor with 2 Consecutive Effector Failures

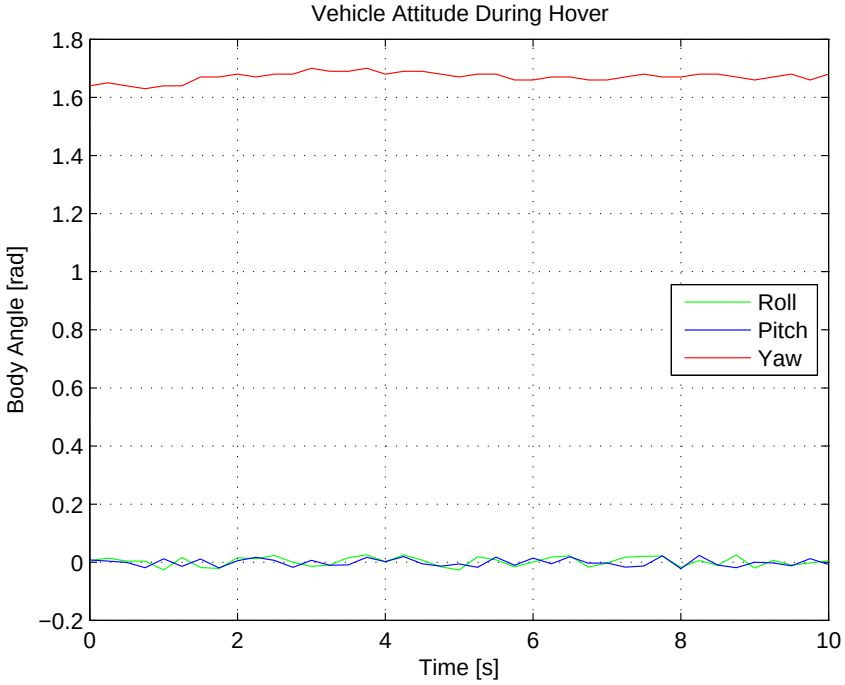

Figure 7.6: Euler Angles for Octorotor with 2 Non-Consecutive Effector Failures

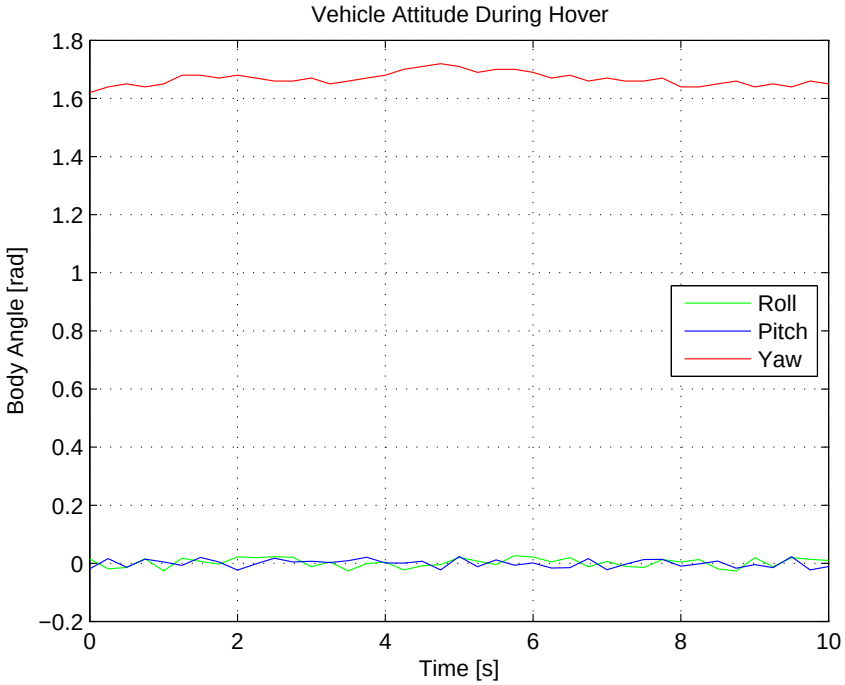

Figure 7.7: Euler Angles for Octorotor with 3 Effector Failures, 2 Consecutive

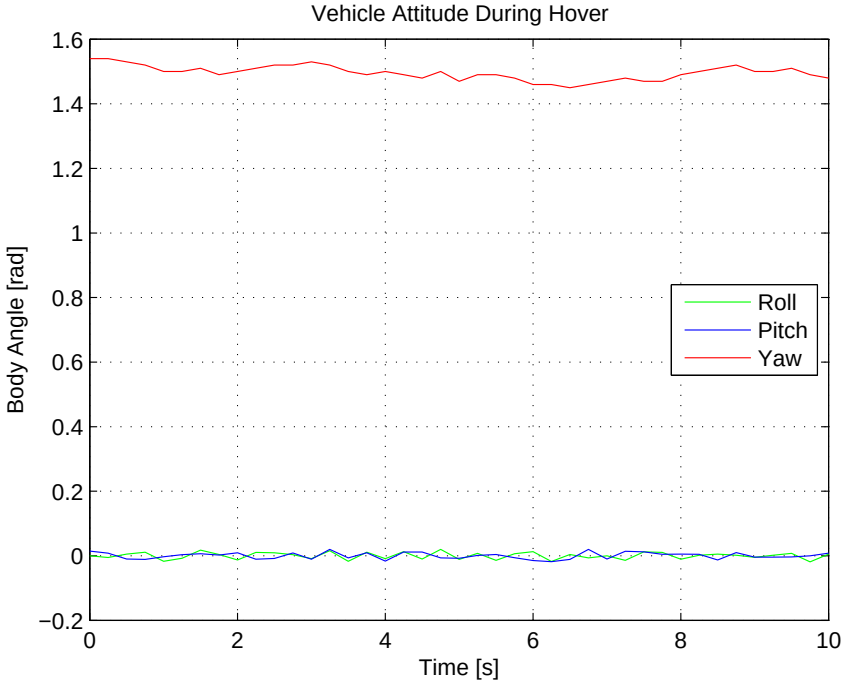

Figure 7.8: Euler Angles for Octorotor with 3 Non-Consecutive Effector Failures

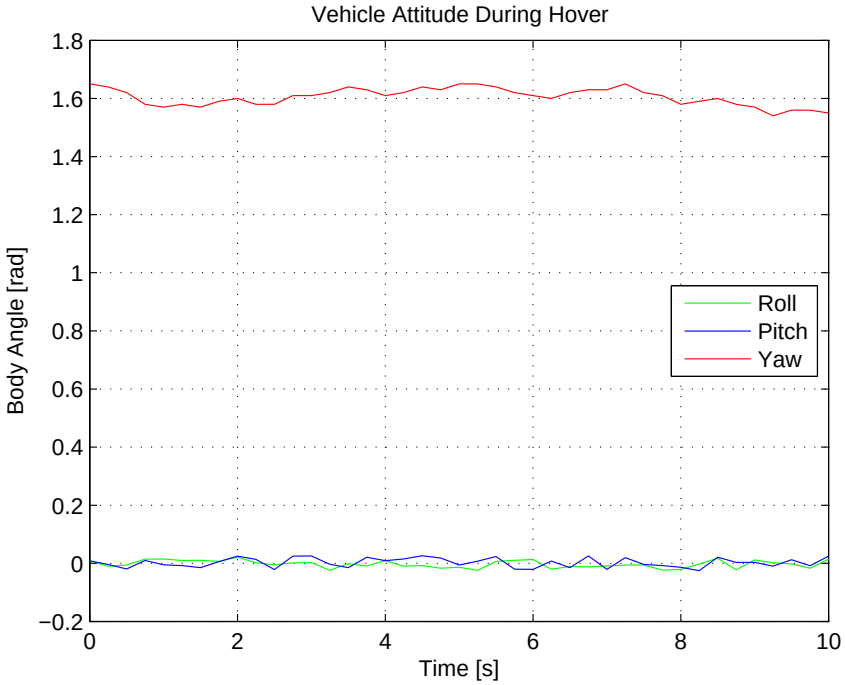

Figure 7.9: Euler Angles for Octorotor with 4 Effector Failures

7.5.2 Yaw Manoeuvre

The next manoeuvre considered was a change in yaw angle. The vehicle was initialised in the level hover pointing East, and the yaw angle demand was set to $\frac{\pi}{4}$, i.e. a yaw of 45° counter-clockwise. Figure 7.10 shows the simulation result. Figures 7.11 to 7.17 show the vehicle response. The performance of the vehicle remains invariant to the hardware failures and is comparable to the simulation.

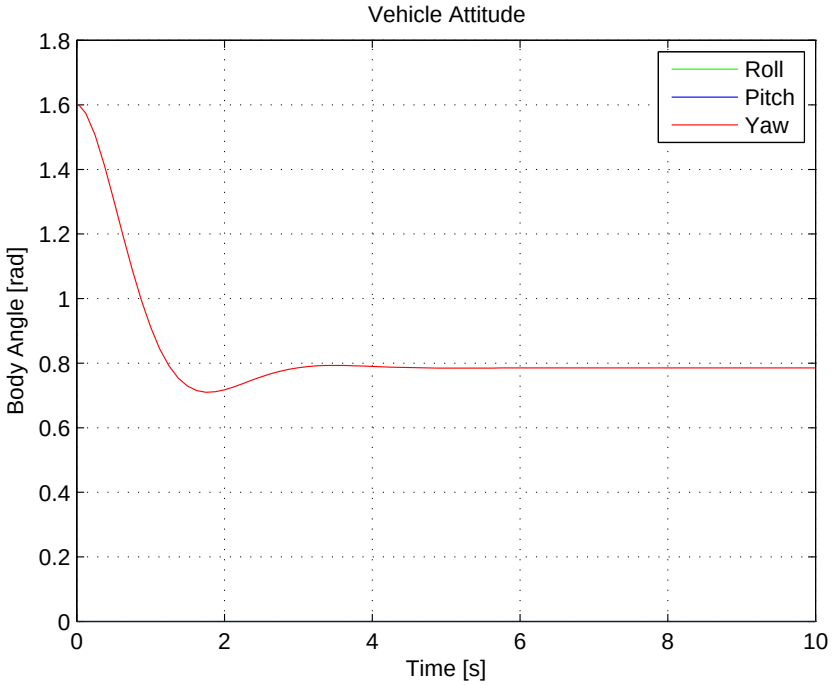

Figure 7.10: Simulation Result for Yaw Angle Manoeuvre

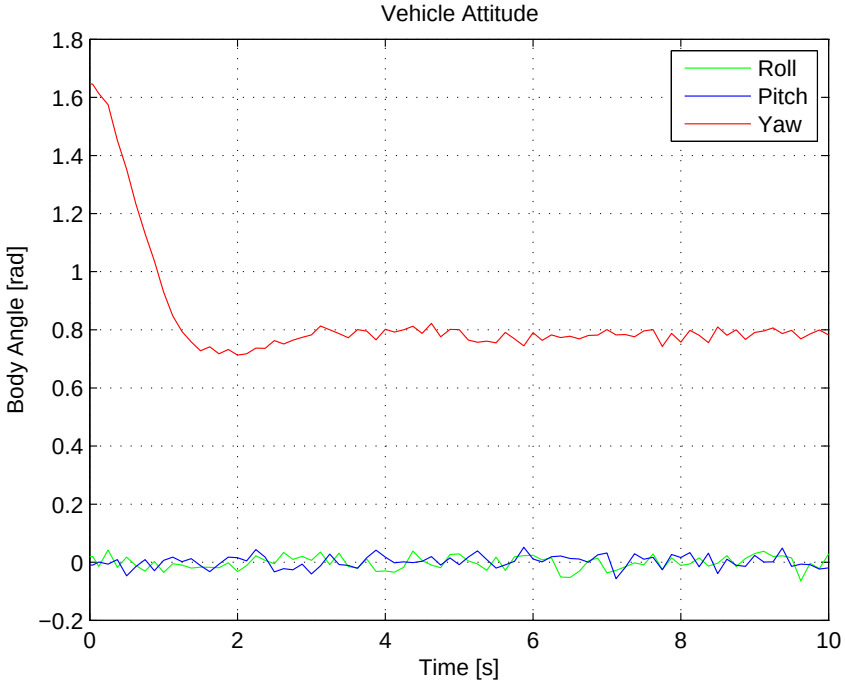

Figure 7.11: Nominal Yaw Angle Manoeuvre

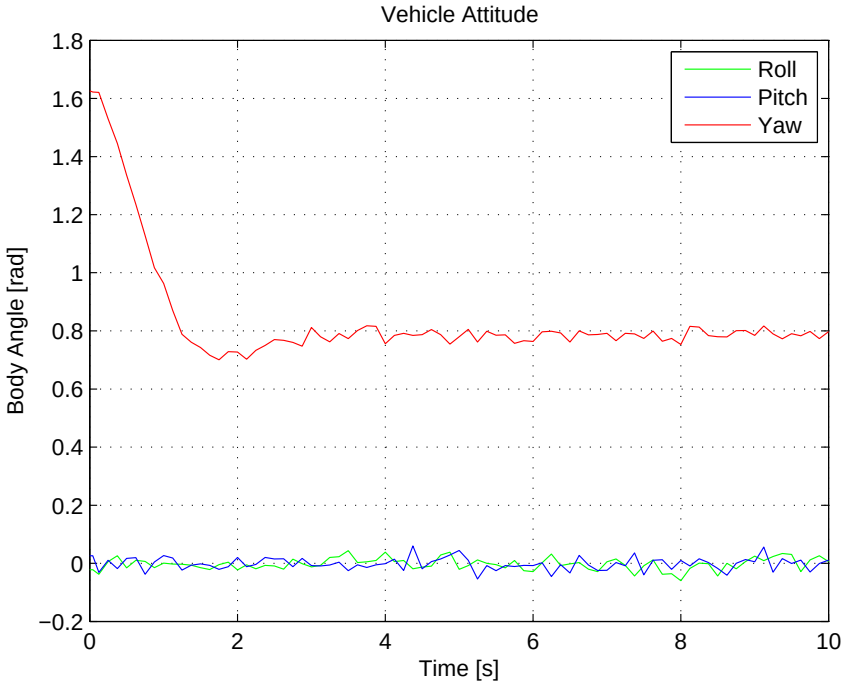

Figure 7.12: Octorotor with 7 Effectors Yaw Angle Manoeuvre

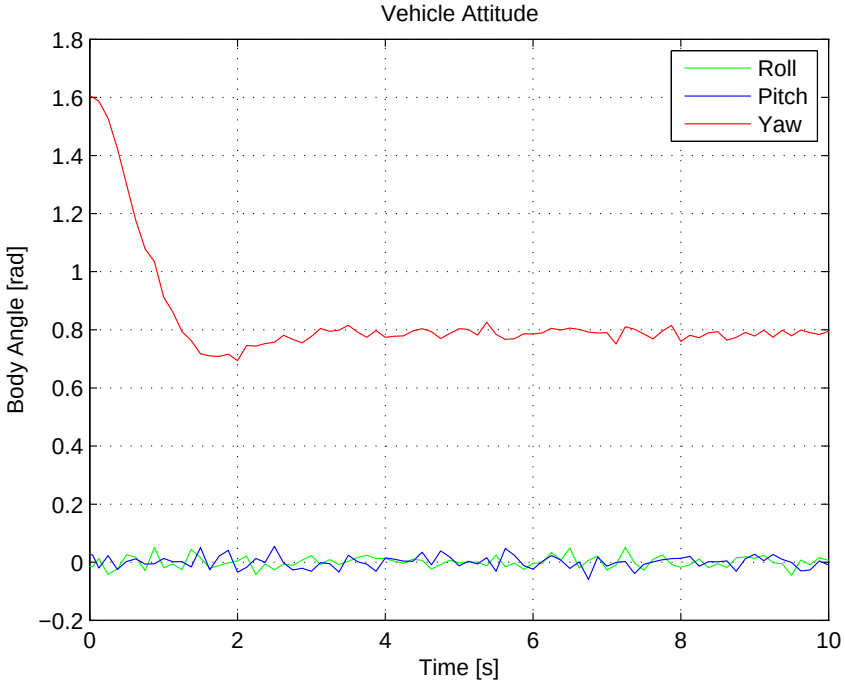

Figure 7.13: Octorotor with 2 Non-Consecutive Effector Failures Yaw Angle Manoeuvre

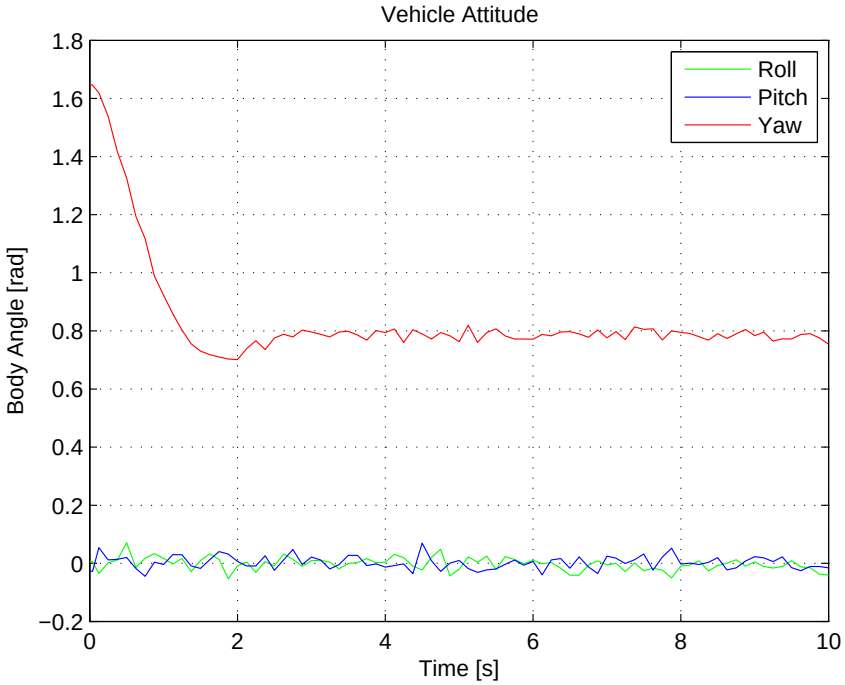

Figure 7.14: Octorotor with 2 Consecutive Effector Failures Yaw Angle Manoeuvre

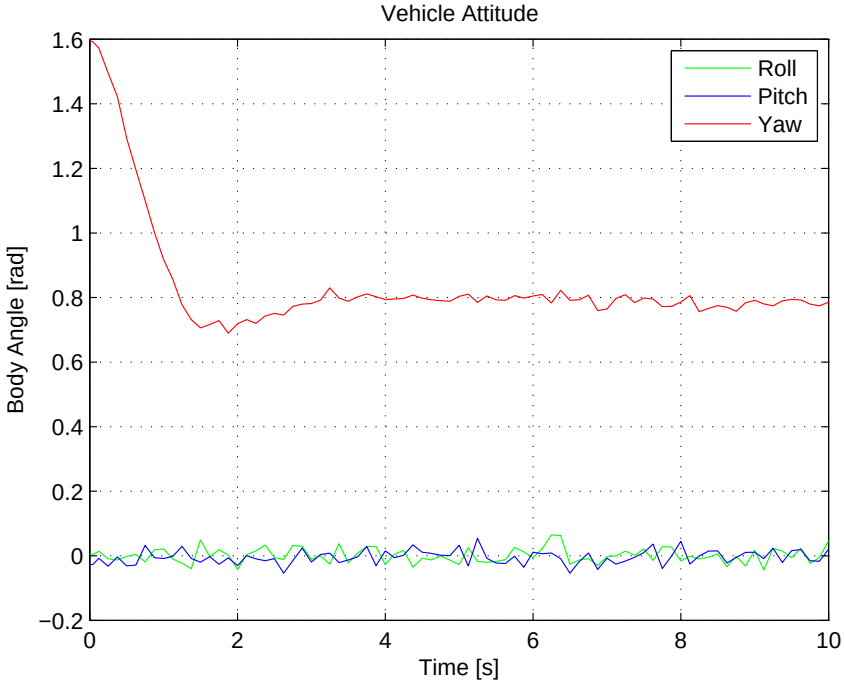

Figure 7.15: Octorotor with 3 Effector Failures, 2 Consecutive Yaw Angle Manoeuvre

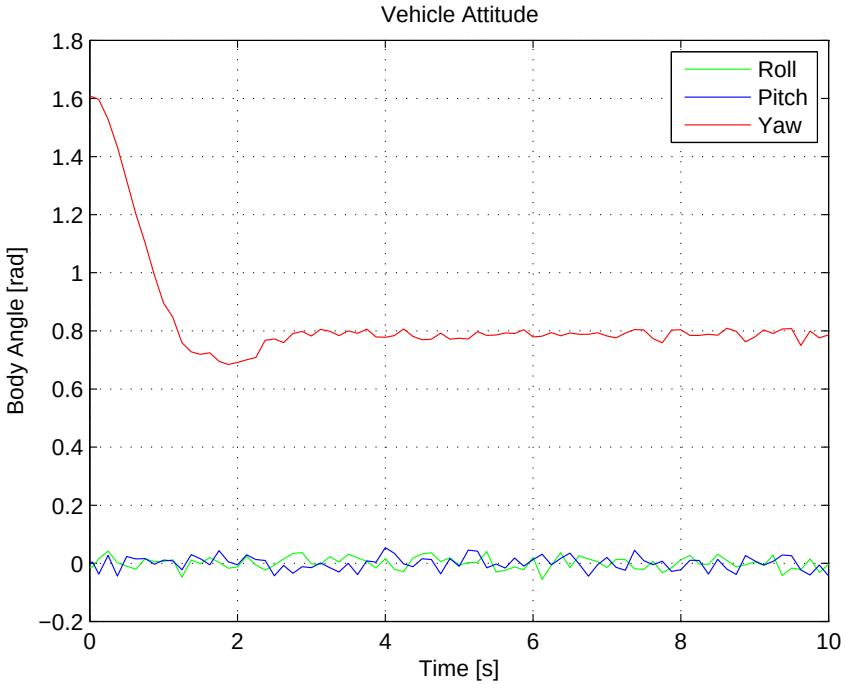

Figure 7.16: Octorotor with 3 Non-Consecutive Effector Failures Yaw Angle Manoeuvre

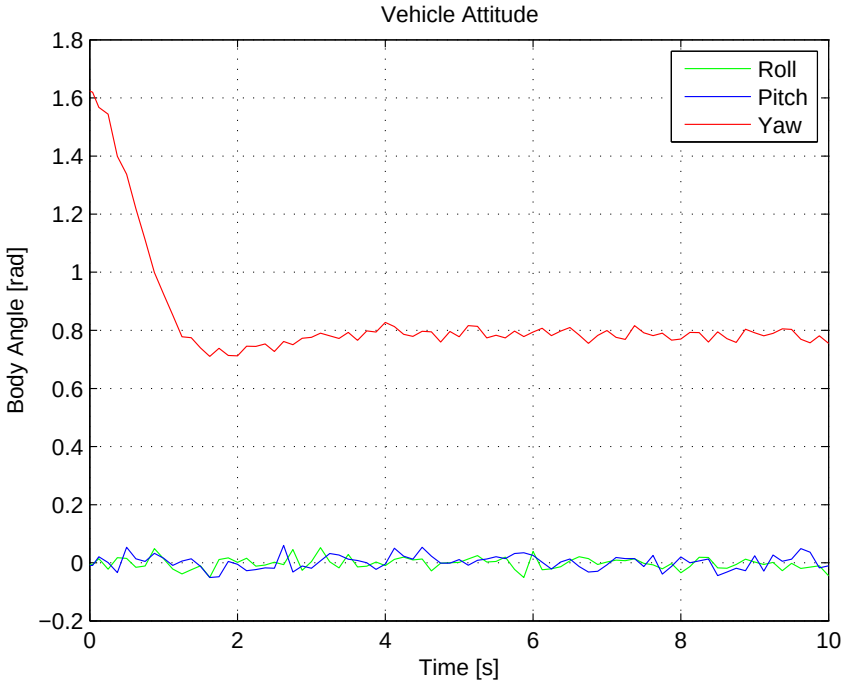

Figure 7.17: Octorotor with 4 Effector Failures Yaw Angle Manoeuvre

7.5.3 Small Change in x_d

During this flight the vehicle follows a small step demand in x_d. This is performed by pitching forwards to rotate the thrust vector so that the vehicle accelerates, then pitching backwards to stop the motion at the desired position. This flight is comparable to Mission 5 in Section 5.7. Figure 7.18 shows the simulation result. This manoeuvre is performed purely by pitching and the manoeuvre is complete in approximately 4 seconds. The results for the octorotor with various effector failures are shown in Figure 7.19 to 7.25.

The performance of the vehicle subject to failures remains invariant to the nominal case. The vehicle pitches forwards to increase the forward velocity, then pitches backwards to slow this translation and hovers at the set position.

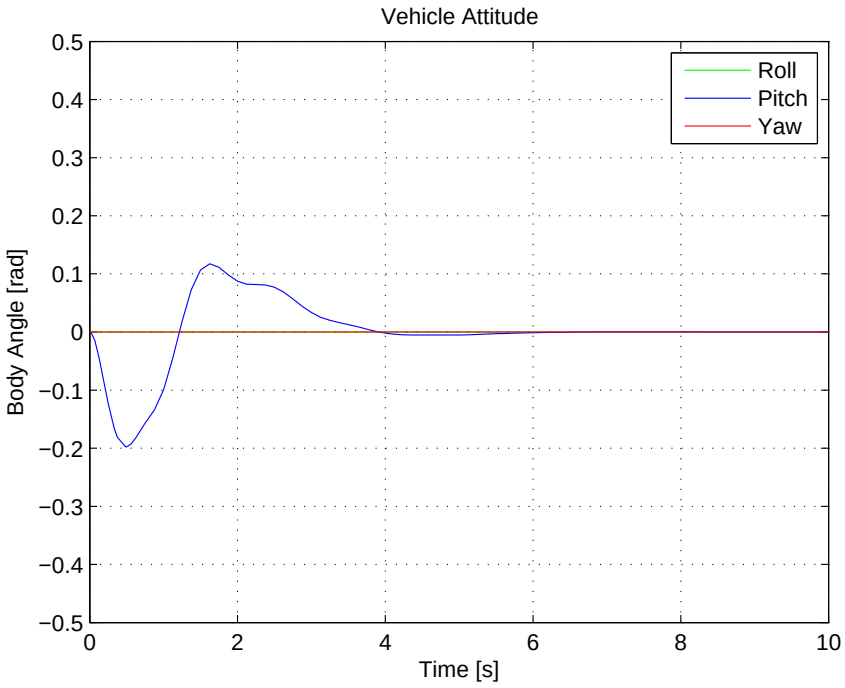

Figure 7.18: Simulation Result for Small Position Change

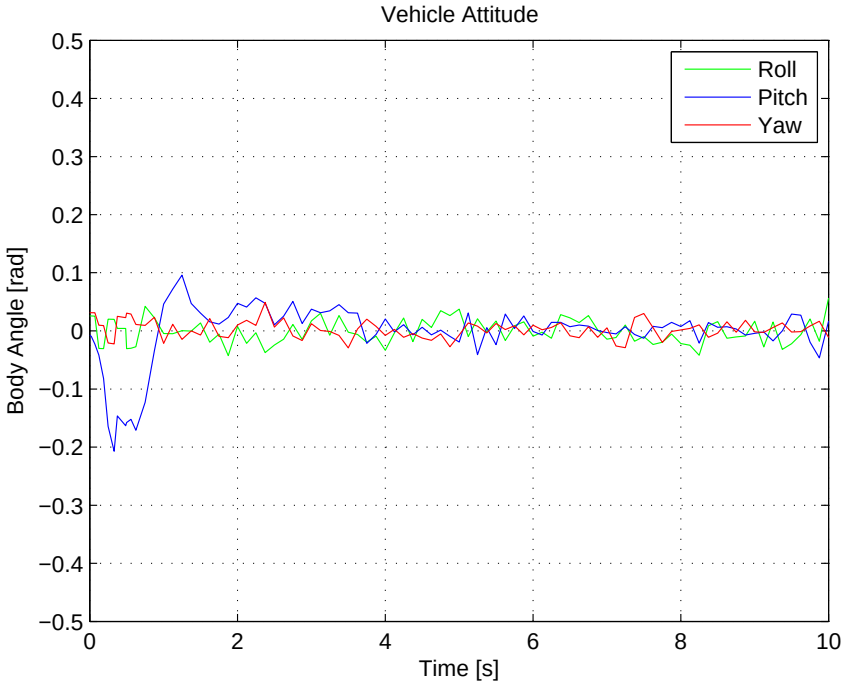

Figure 7.19: Nominal Small Position Change

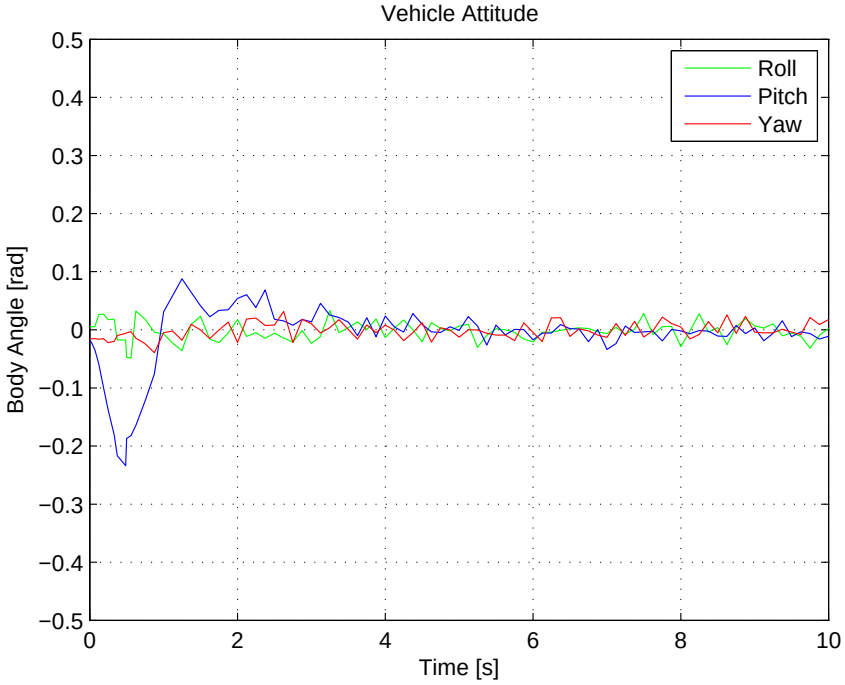

Figure 7.20: Octorotor with 7 Effectors Small Position Change

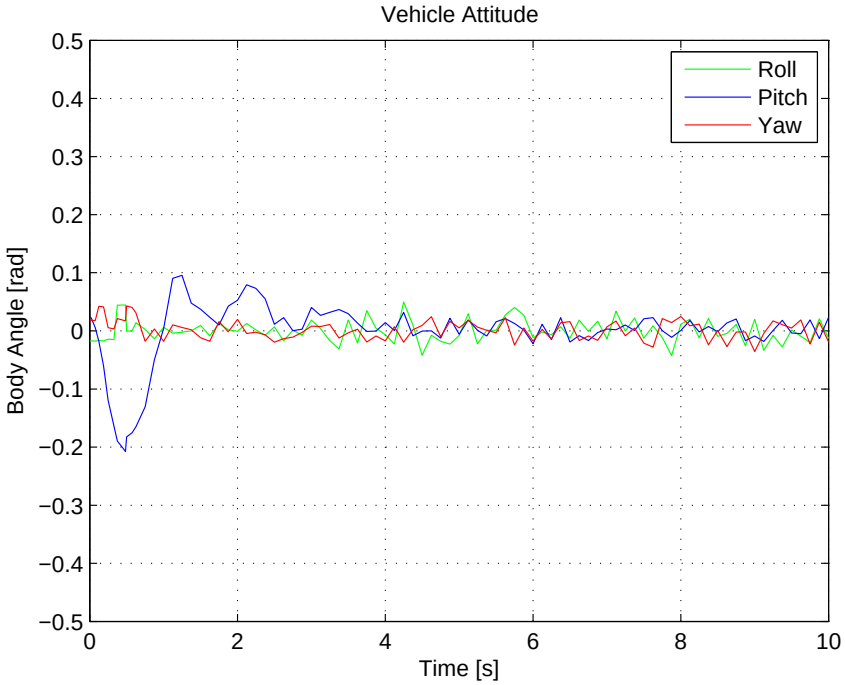

Figure 7.21: Octorotor with 2 Non-Consecutive Effector Failures Small Position Change

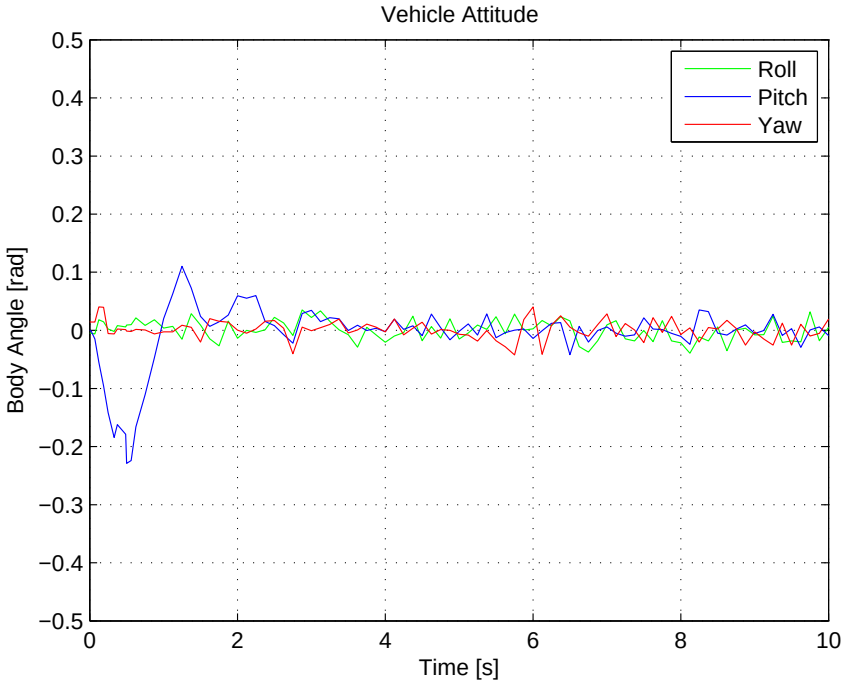

Figure 7.22: Octorotor with 2 Consecutive Effector Failures Small Position Change

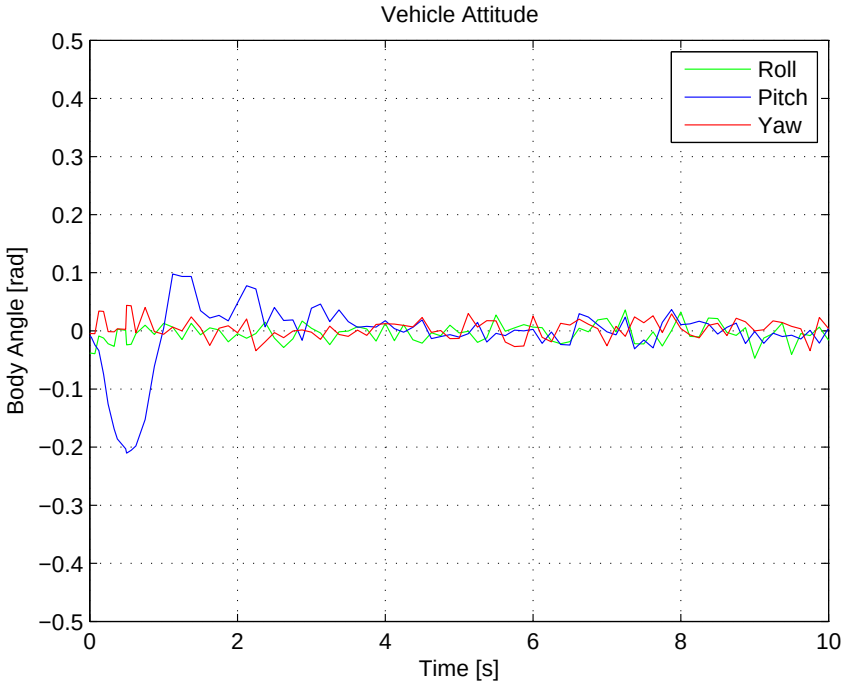

Figure 7.23: Octorotor with 3 Effector Failures, 2 Consecutive Small Position Change

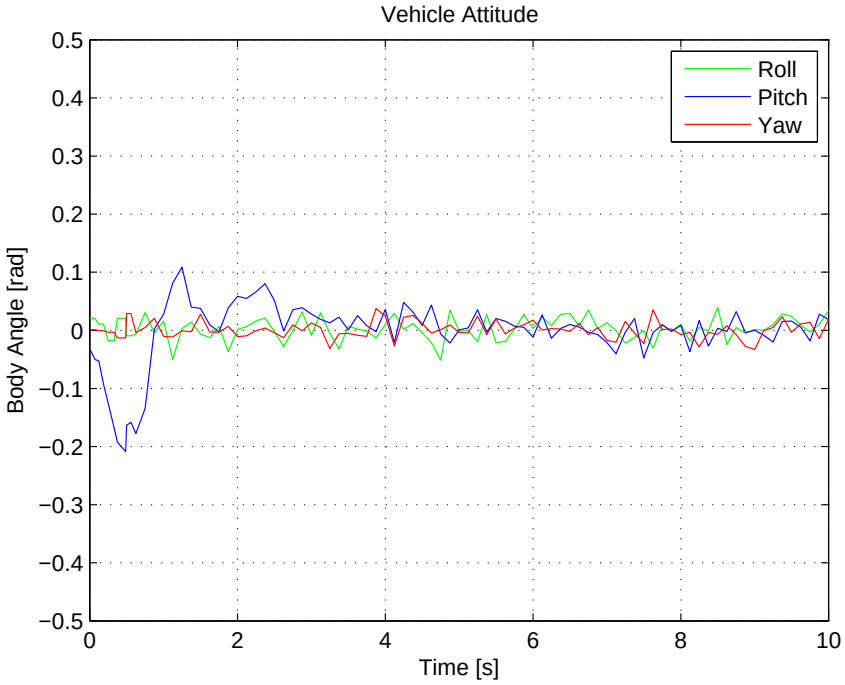

Figure 7.24: Octorotor with 3 Non-Consecutive Effector Failures Small Position Change

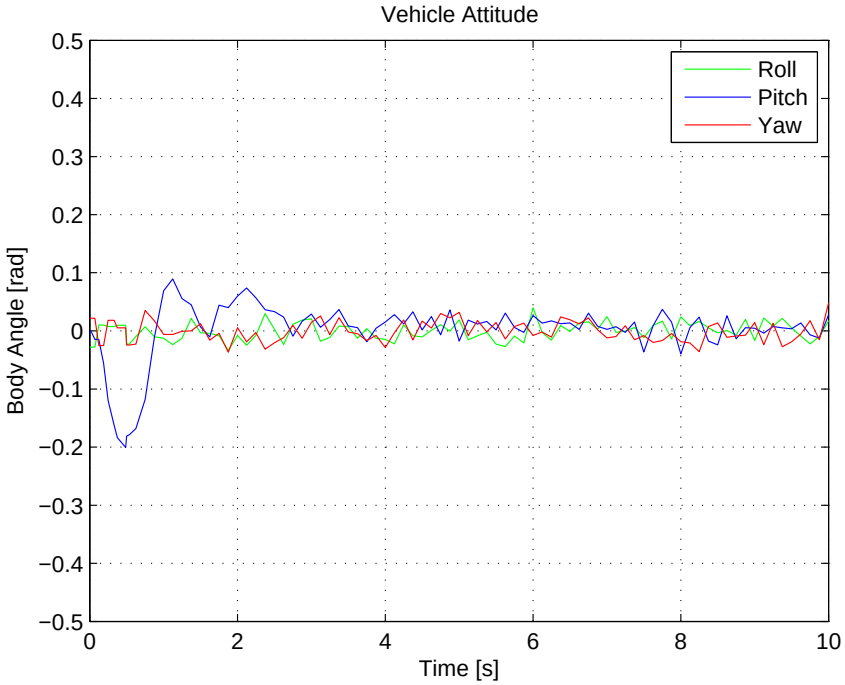

Figure 7.25: Octorotor with 4 Effector Failures Small Position Change

7.5.4 Large Change in x_d

This flight demonstrates how the vehicle is capable of tracking a large position error and is analogous with Mission 6 in Section 5.8. The simulation result is shown in Figure 7.26. Note how the value of $\alpha_{\max}$ restricts the pitch angle and results a slightly sluggish position response. However, this is a suitable tradeoff to maintain controllability during a delay in detecting an effector failure. Additionally, such a large step demand should not be generated during regular flight operations and would be the result of a software glitch or a loss of GPS signal.

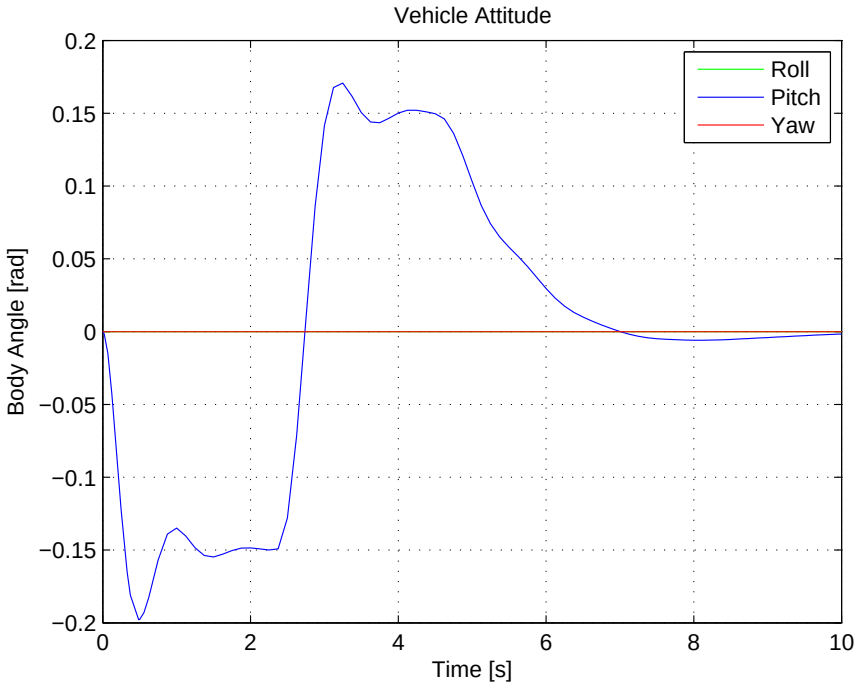

Figure 7.26: Simulation Result for Large Position Change

This manoeuvre is completed in under 8 seconds. The pitch angle oscillates but the vehicle remains controlled. Figures 7.27 to 7.33 show the results for the various effector failure scenarios. The results for the test vehicle are similar to the simulation results.

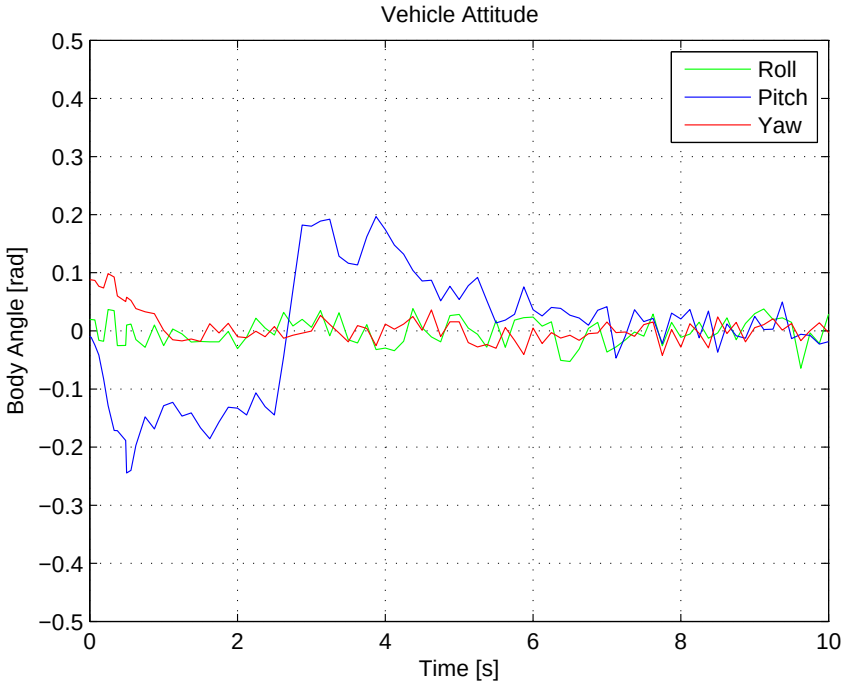

Figure 7.27: Nominal Large Position Change

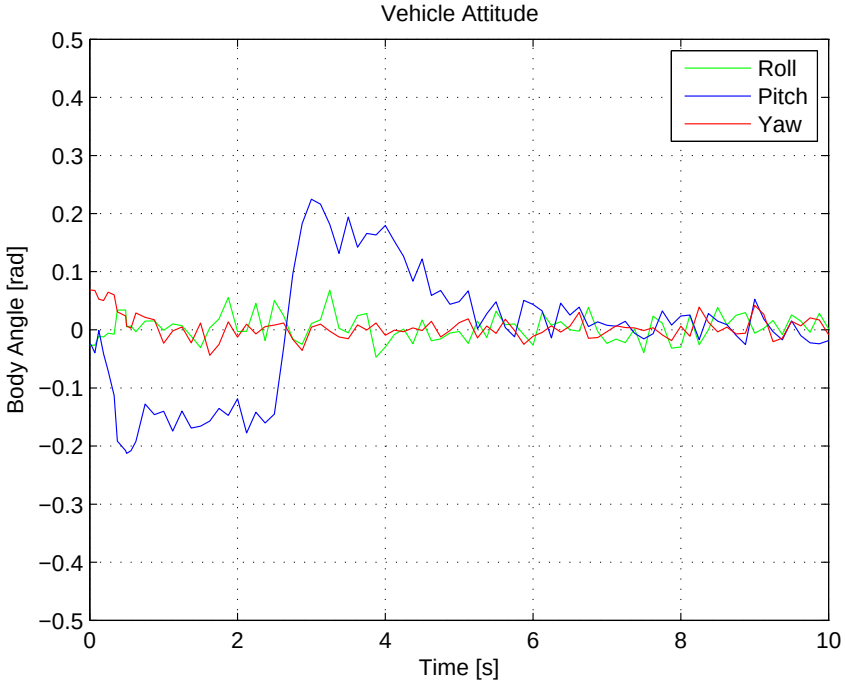

Figure 7.28: Octorotor with 7 Effectors Large Position Change

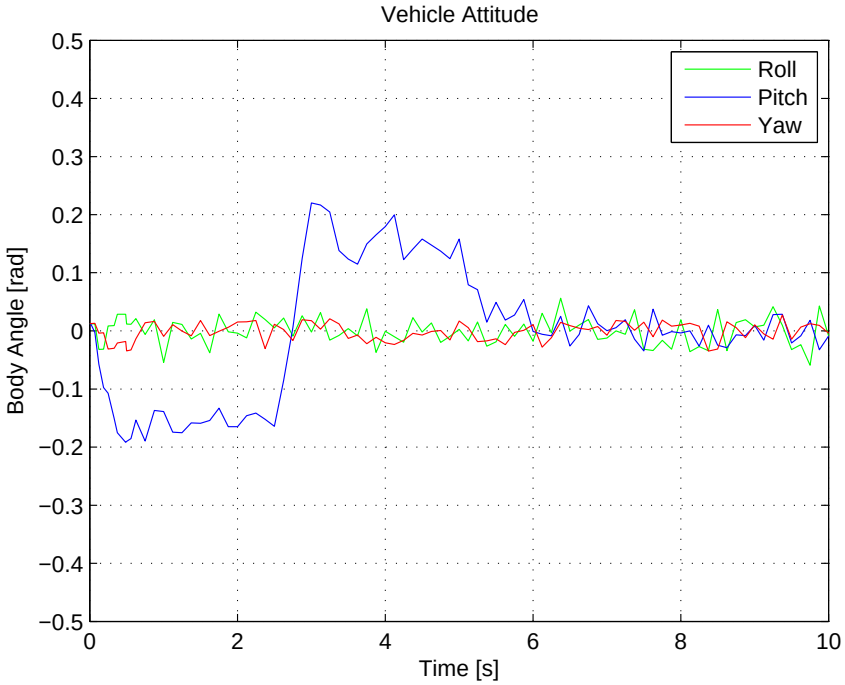

Figure 7.29: Octorotor with 2 Non-Consecutive Effector Failures Large Position Change

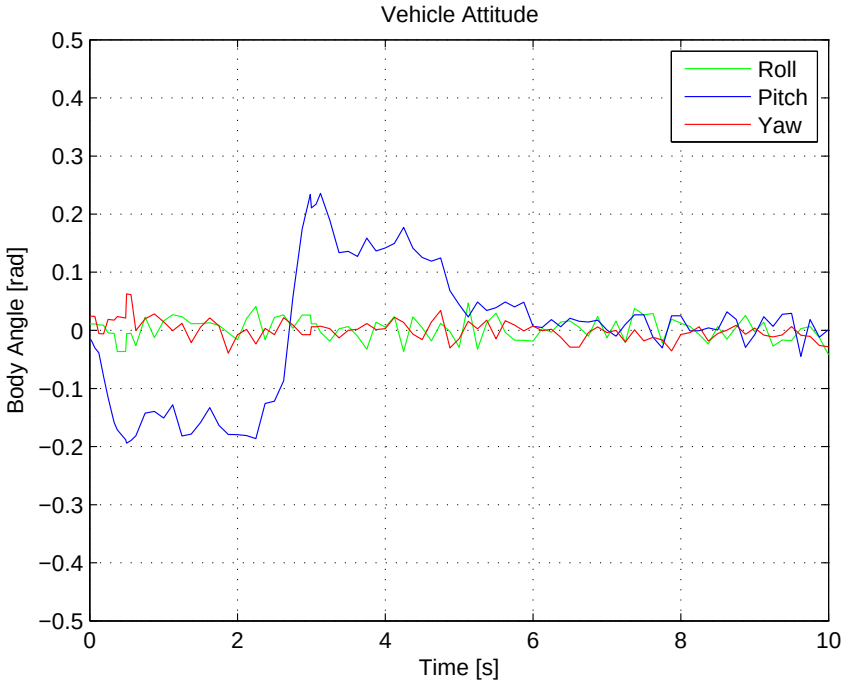

Figure 7.30: Octorotor with 2 Consecutive Effector Failures Large Position Change

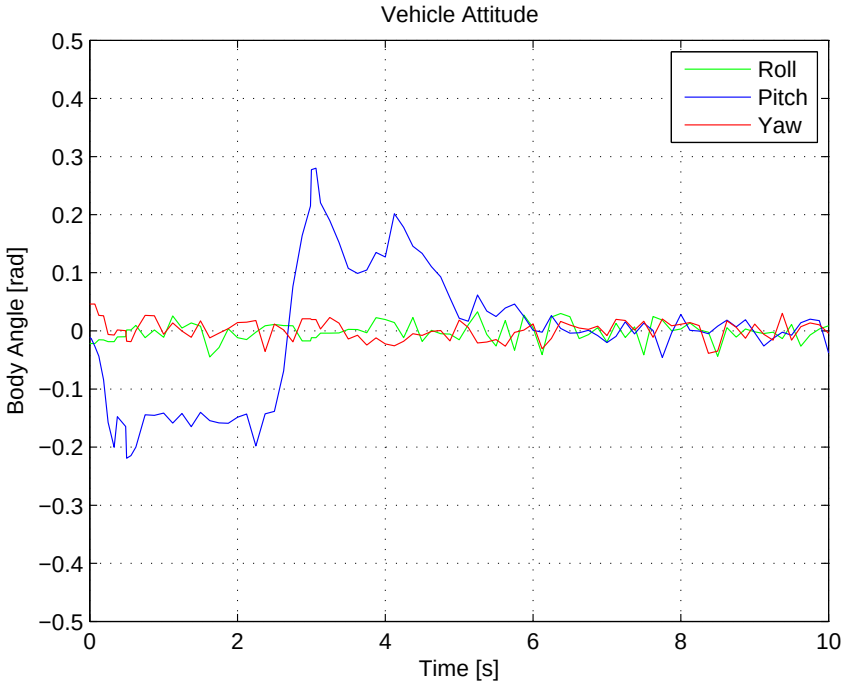

Figure 7.31: Octorotor with 3 Effector Failures, 2 Consecutive Large Position Change

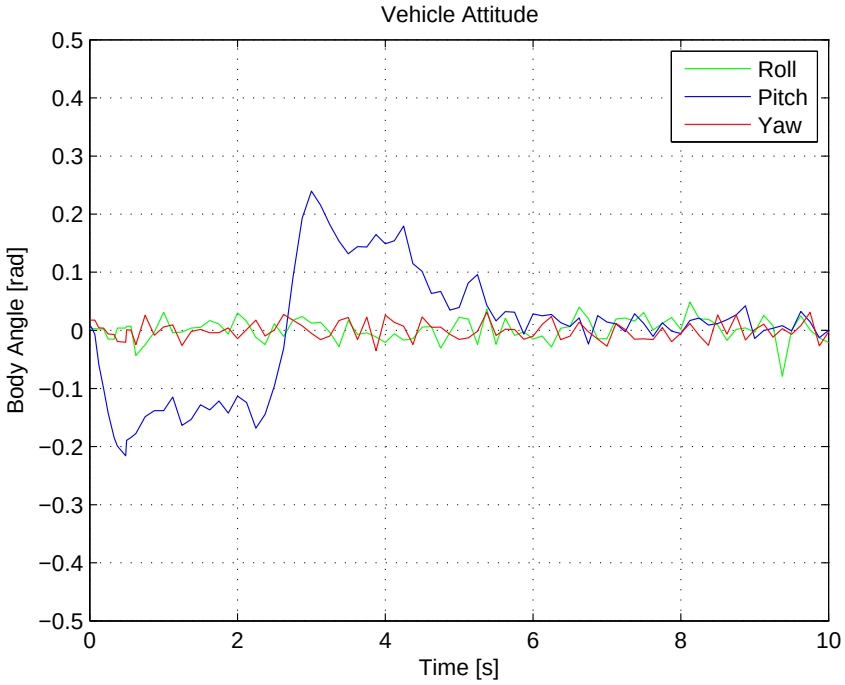

Figure 7.32: Octorotor with 3 Non-Consecutive Effector Failures Large Position Change

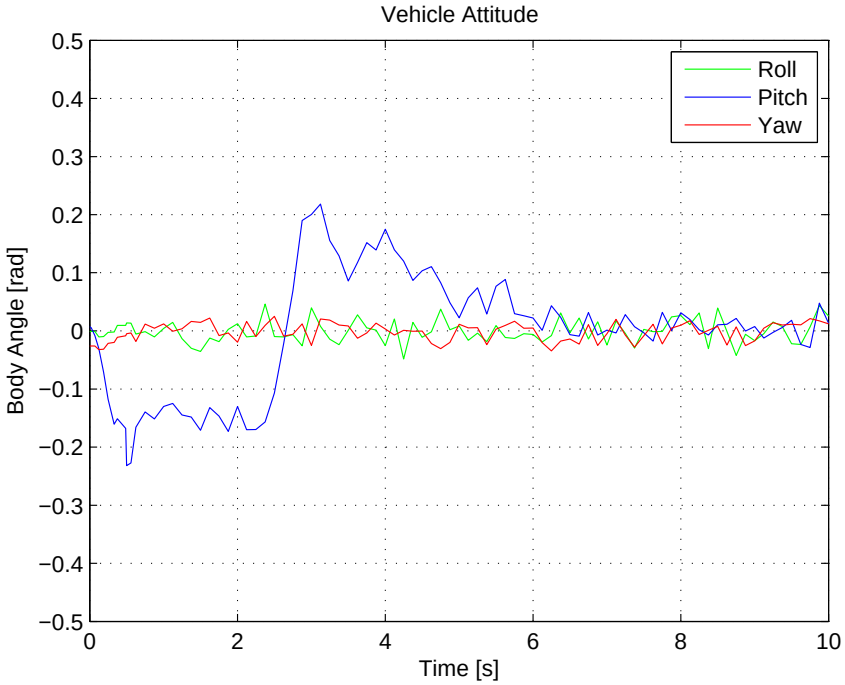

Figure 7.33: Octorotor with 4 Effector Failures Large Position Change

7.6 Conclusion

The flight test results closely mirror the simulation results and the effector failures do not adversely affect the vehicle performance. However, there is a noise signal which is present in the simulation results which is not represented in the simulation data. This noise does not adversly affect the vehicle performance.

The following are contributing factors to the differences between the simulations and the test vehicle data and arise because the assumptions from Section 2.4 are not all valid:.

- the structure is not rigid and shows flexure,
- the propellers are not fully rigid, especially under large load such as a large control input and with a large payload,
- the vehicle inertia matrix is not diagonal and symmetrical since the battery is a significant additional mass and is cuboid in shape,
- there is slight motor lag, and
- vibrations are generated by the effectors.

This Chapter has described the hardware choice for the flight test vehicle. It contains flight test results for the vehicle in the nominal effector health state (all effectors functional) and contains flight test data for the controllable failure scenarios. The flight test performance for both nominal and failure vehicle is similar to the simulation results

Chapter 8

Conclusion

8.1 Achievements and Contribution

- The quaternion attitude representation is used to provide for global attitude control of the octorotor.
- An attainable force set allows for constrained control allocation where the thrust vector is not rotated as it might be using other methods.
- The fault hiding technique can be applied to an octorotor in order to provide for fault tolerance extending to failures of a number of the effectors. The controller remains invariant throughout and nominal performance can be maintained for the post-failure vehicle.
- Flight tests have been performed and show that the controller is suitable for position control. The results for the post-failure vehicle are comparable to the nominal performance and similar to the simulation results

8.2 Octorotor

The octorotor was selected as the flight test vehicle and the dynamic model and control effectiveness matrix was derived in Section 2. The model utilises the quaternion attitude representation to avoid gimbal lock. The effector constraints are implemented in the controller meaning that the control allocation is the constrained control allocation.

The physical layout of the vehicle allows for yaw independent position control and the octorotor remains controllable for a number of combinations of effector failures. The payoff is that the octorotor must be physically larger than a corresponding vehicle with fewer effectors such as a quadrotor. This is due to propeller clearance as a design driver – aerodynamic interactions between effectors reduces the overall efficiency of

the generation of thrust. It is possible that a vehicle with fewer effectors than the octorotor, but more than the quadrotor (such as a hexarotor) will provide for some degree of failure tolerance (for example, failure of one effector) whilst optimising payload capability and satisfying size constraints. Indeed, hexarotor vehicles are increasingly being used for commercial filming work and were used during the Winter Olympics in 2014 to capture video during snowboarding events [oly]. A cost analysis was performed showing that the octorotor has lower effective costs to increase the system reliability than a vehicle with a larger amount of hardware redundancy.

There is a large number of potential vehicle designs including star shaped, 'H', 'V', and staggered, and it is intractable to perform analysis for each one. Implementing movable mounts for the effectors introduces additional degrees of freedom and potentially increases the failure tolerance.However this introduces another point of failure into the system and a suitable analysis must be performed to determine the suitability of this scheme.

A number of technical challenges were overcome to assemble a suitable test vehicle which was controlled by a pilot using a conventional radio transmitter. The initial flight tests are promising and show that the vehicle can be controlled in a hover, can track a yaw change demand, and the inertial position is changed easily. The response of the post-failure vehicle is similar to the nominal vehicle as the effector constraints are not exceeded and effector saturation does not occur.

8.3 Controller

The controller outputs are the virtual controls and these can be constrained by the saturation function σ_M. This time-dependant constraint can become difficult to determine when the number of effectors is high and so can be removed (made arbitrarily large) provided that the effector values are measurable. The controller is failure invariant and provided no effectors are saturated the post-failure performance is the same as the nominal performance. Furthermore, the vehicle inertia is not accounted for in the controller and so it can be directly transferred to a different airframe or remain in use after releasing/collecting a payload. Of course, the gains will need to be suitably changed to provide acceptable performance, but this means that it can be implemented on a time varying plant model such as an aircraft where the mass changes throughout the flight due to fuel burn.

8.4 Quaternion Attitude Representation

The quaternion attitude representation is used to avoid gimbal lock which can occur during high-attitude aerobatic manoeuvres or as the vehicle tumbles after an effector failure. The control law provides almost global asymptotic stability. The double covering of SO(3) means that two quaternions can be used to describe the same

physical orientation of the vehicle. This can lead to unwinding where the vehicle rotates away from the desired position and follows a large rotation angle where there is a shorter one. This undesirable behaviour is removed by using a non-continuous control strategy and ensuring that the sign of q_0 is constant between updates in a discrete time controller.

8.5 Control Allocation

Constrained control allocation is performed using the redistributed pseudo inverse method whereby saturated effectors are set to their saturation values and are removed from subsequent iterations of the control allocation. It has been shown that this method is not guaranteed to be successful and when this occurs (i.e. effectors are set to their saturation limits) the thrust vector can be unintentionally rotated.

If the control demand itself is constrained then unconstrained control allocation can be used and the allocation will always be successful. If the motor speed demands are known then it is possible to ensure that they are not exceeded. This is achieved by analysing the demanded effector values and ensuring that none exceed the saturation limit. If the limit is exceeded then the virtual control is scaled so that the effector demands sit on the saturation limit. This is a novel implementation of a force set and it is easier to implement with a controller of limited processing capacity and a large number of effectors. The performance of this scheme may be lower than the RPI method, but the allocation is always successful and will allow for manoeuvring even when the virtual control demands are large.

A point to remember is that the failed effector on a p-rotor vehicle does not contribute any significant additional forces or moments since its thrust output is zero and it can practically be removed from post-failure control allocation. The design of the brushless DC motor is such that it can not fail to maximum thrust and maintain this. In contrast, a 'hard-over', 'stuck' or 'floating' effector on a vehicle with aerodynamic surfaces (such as an aircraft canard or submarine fin) may contribute parasitic forces and moments which must be countered by the remaining effectors.

8.6 Attitude Control

The method used for attitude stabilisation is shown in Section 4.5 where the desired quaternion is $q_d = [\pm 1 \ 0 \ 0 \ 0]^T$. The sign of $q_{0,d}$ is determined by the shortest rotational path. Heuristic weighting can be implemented to derive $q_{0,d}$ using an additional derivative term to ensure that the rotation is performed with minimal energy. An example of this is where the vehicle has an initial yaw angle close to π and an angular rate about z_b as shown in Section 5.6. Tthe value of $q_{0,d}$ is set to reflect the minimum rotation angle which means that for the above situation where the angular rate is positive (ψ increases with time) the controller attempts to stop

the rotation by applying a negative yaw control. When the angular rate is low this solution is satisfactory. When the angular rate is high there is insufficient control authority to quickly stop the rotation and the yaw angle passes above π. The sign of $q_{0,d}$ changes to reflect the shorter rotation angle and a subsequent positive yaw control is demanded. The total rotational distance in this scenario is $2\pi - \psi$. Since the direction of the yaw control reverses throughout the manoeuvre the total energy is higher than if the initial control is positive and the larger rotational distance is considered. The heuristic method suggested by Schlanbusch et al. [2010] is one such solution.

8.7 Fault Hiding

The fault hiding method allows for one controller to be applied for all failure scenarios as well as allowing direct transfer of controller between different airframes giving identical nominal performance. The advantage of separating the control allocation from the controller also means that a failure in one subsystem does not necessitate retuning the controller for the whole plant. Rather, the control demands are allocated among the functioning effectors and nominal performance is achieved.

8.8 Failure Detection

The work done in this thesis assumes that a suitable fault detection system is in place which is sensitive to effector failures but does not produce false alarms. In practice this system is complex to integrate, but the most likely way of implementing it is to use a combination of motors with position sensors and Hall Effect sensors.

The position sensors of the motor are important in order to measure the rotational speed. Combining this with the Hall Effect sensor allows the load to be measured. For a normal motor with no faults a certain rotational speed will result in a specific load. If the rotational speed is high with a low load this may indicate that the rotor has detached from the motor spindle. If the motor speed goes to zero then it indicates a likely failure in the motor unit. Using both of the sensors allows for diagnostics to be sent via telemetry where the health of the motor can be judged separately from the health of the rotor – something which may not be possible using a Hall Effect sensor by itself. The speed sensor also enables the control allocation to be successful so that the saturation limit of the effector can be calculated for different environmental conditions and different motor-rotor combinations.

8.9 Future Work

The future work is split into two areas; optimisation of the vehicle design to allow for failure tolerance whilst reducing hardware costs, and validation of the controller and fault hiding scheme through integration on a flight test vehicle.

8.9.1 Vehicle Optimisation

There is a diverse range of vehicle designs which can all accomplish the goal of providing a failure tolerant platform for sensitive payloads where a hardware failure cannot cause a loss of control of the vehicle. The added benefits of yaw angle invariance or the possibility of inverted hover and highly agile manoeuvre capabilities should be considered in future research.

The order of rotational sense of the motors is to be a topic for future investigation. It was seen through the Kalman controllability analysis that if the motors are in co-rotating pairs, the vehicle is not controllable if two effectors fail in the same body quadrant. If the motors alternate rotational sense then the vehicle does not retain yaw invariance after a single failure and the performance in one axis direction is not the same as performance in the perpendicular axis.

Variable pitch rotor blades have been investigated [Cutler and How, 2012] and allow for increased controller bandwidth and controllability when a single effector is inoperative. This can be combined with a vehicle setup as suggested by Driessens and Pounds [2013] where the central rotor provides the majority of the lift thrust and the rotors around the vehicle (manoeuvre effectors) are used to provide body attitude control. In such a case, if the central rotor was replaced with a coaxial rotor pair the position control can theoretically be achieved by implementing only one variable pitch manoeuvre effector on the vehicle body. This scheme means that the vehicle is no longer yaw independent as the vehicle can only accelerate in the axis parallel to the manoeuvre effector, and this axis may be rotated by changing the vehicle yaw angle. However, the efficiency gained by implementing a large main rotor could offset this operational disadvantage.

8.9.2 Validation

- GPS data is needed in order to implement increased fidelity position control.
- A faster flight control processor is needed which is capable of performing control allocation ‘on the fly’. At present the control effectiveness matrix is initialised when the vehicle is powered up, and remains constant throughout the flight.
  - This will enable controlled shut-downs of effectors during flight where there is sufficient altitude to act as a ‘safety net’ whilst the controls are

reallocated to different effectors.

- A fault detection system will be implemented in order to provide autonomous failure tolerance without pilot intervention.

References

https://store.3drobotics.com/products/apm-3dr-x8-rtf. Accessed 04/14.

http://www.aerovelo.com/. Accessed 04/14.

CAA Article 166 ANO 2009. http://www.caa.co.uk/default.aspx?catid=1995&pageid=16012. Accessed 01/15.

http://www.theatlantic.com/technology/archive/2014/02/the-future-of-sports-photography-drones/283896/. Accessed 02/14.

Quanser - Qball-X4. http://www.quanser.com/products/qball. Accessed 04/14.

Turnigy motor. http://hobbyking.com/hobbyking/store/__39036__Turnigy_Multistar_2213_980Kv_14Pole_Multi_Rotor_Outrunner.html. Accessed 01/15.

V. G. Adîr, A. M. Stoica, A. Marks, and J. F. Whidborne. Modelling, stabilization and single motor failure recovery of a 4Y octorotor. In Proc. 13th IASTED International Conference on Intelligent Systems and Control (ISC 2011), pages 82–87, Cambridge, U.K., July 2011. doi: 10.2316/P.2011.744-070.

A. Akhtar, S.L. Waslander, and C. Nielsen. Fault tolerant path following for a quadrotor. In Decision and Control (CDC), 2013 IEEE 52nd Annual Conference on, pages 847–852, Dec 2013. doi: 10.1109/CDC.2013.6759988.

H. Alwi and C. Edwards. LPV sliding mode fault tolerant control of an octorotor using fixed control allocation. In Control and Fault-Tolerant Systems (SysTol), 2013 Conference on, pages 772–777, Oct 2013a. doi: 10.1109/SysTol.2013.6693887.

H. Alwi and C. Edwards. Fault tolerant control of an octorotor using LPV based sliding mode control allocation. In 2013 American Control Conference, pages 6505–6510, June 2013b.

G. Antonelli and S. Chiaverini. Singularity-free regulation of underwater vehicle-manipulator systems. In American Control Conference, 1998. Proceedings of the 1998, volume 1, pages 399–403 vol.1, Jun 1998. doi: 10.1109/ACC.1998.694699.

O. Araar and N. Aouf. Full linear control of a quadrotor UAV, LQ vs H∞. In Control (CONTROL), 2014 UKACC International Conference on, pages 133–138, July 2014. doi: 10.1109/CONTROL.2014.6915128.

Arducopter. `https://code.google.com/p/arducopter/`. Accessed 06/14.

Ardupilot. `http://code.google.com/p/ardupilot-mega/wiki/Hardware`, a. Accessed 02/14.

Ardupilot. `http://code.google.com/p/ardupilot-mega/wiki/IMUHardware`, b. Accessed 02/14.

Ardupirates. `https://code.google.com/p/ardupirates/`. Accessed 06/14.

Atmel. `http://www.atmel.com/devices/atmega2560.aspx`. Accessed 02/14.

A.H. Bajodah. Inertia-independent generalized dynamic inversion feedback control of spacecraft attitude maneuvers. In Recent Advances in Space Technologies (RAST), 2011 5th International Conference on, pages 903–908, June 2011. doi: 10.1109/RAST.2011.5966974.

L. Besnard, Y. B. Shtessel, and B. Landrum. Quadrotor vehicle control via sliding mode controller driven by sliding mode disturbance observer. Journal of the Franklin Institute, 349(2):658 – 684, 2012. ISSN 0016-0032. doi: http://dx.doi.org/10.1016/j.jfranklin.2011.06.031. Advances in Guidance and Control of Aerospace Vehicles using Sliding Mode Control and Observation Techniques.

S. Bhat and D.S. Bernstein. A topological obstruction to continuous global stabilization of rotational motion and the unwinding phenomenon. Systems & Control Letters, 39(1):63–70, 2000.

M. Bodson. Evaluation of optimization methods for control allocation. Journal of Guidance, Control, and Dynamics, 25:703–711, July-August 2002.

M. A. Bolender and D. B. Doman. Nonlinear control allocation using piecewise linear functions. Journal of Guidance, Control, and Dynamics, 27:1017–1027, 2004.

M. A. Bolender and D. B. Doman. Nonlinear control allocation using piecewise linear functions: A linear programming approach. Journal of Guidance, Control, and Dynamics, 28(3):558–562, 2005.

K.A. Bordignon. Constrained Control Allocation for Systems with Redundant Control Effectors. PhD thesis, Virginia Polytechnic Institute, VA, 1996.

J.D. Boskovic, Sai-Ming Li, and R.K. Mehra. Globally stable adaptive tracking control design for spacecraft under input saturation. In Decision and Control, 1999. Proceedings of the 38th IEEE Conference on, volume 2, pages 1952–1957 vol.2, 1999. doi: 10.1109/CDC.1999.830922.

S. Bouabdallah and R. Siegwart. Backstepping and sliding-mode techniques applied to an indoor micro quadrotor. In Proceedings IEEE International Conference on Robotics and Automation (ICRA 2005), pages 2247 – 2252, April 2005. doi: 10.1109/ROBOT.2005.1570447.

S. Bouabdallah and R. Siegwart. Full control of a quadrotor. In Intelligent Robots and Systems, 2007. IROS 2007. IEEE/RSJ International Conference on, pages 153 –158, November 2007. doi: 10.1109/IROS.2007.4399042.

S. Bouabdallah, P. Murrieri, and R. Siegwart. Design and control of an indoor micro quadrotor. In Robotics and Automation, 2004. Proceedings. ICRA '04. 2004 IEEE International Conference on, volume 5, pages 4393 – 4398, May 2004a. doi: 10.1109/ROBOT.2004.1302409.

S. Bouabdallah, A. Noth, and R. Siegwart. PID vs LQ control techniques applied to an indoor micro quadrotor. In Proceedings IEEE/RSJ International Conference on Intelligent Robots and Systems (IROS 2004)., volume 3, pages 2451 – 2456, Sendai, Japan, September 2004b. doi: 10.1109/IROS.2004.1389776.

M. Bouchoucha, M. Tadjine, A. Tayebi, and P. Mullhaupt. Step by step robust nonlinear PI for attitude stabilisation of a four-rotor mini-aircraft. In Control and Automation, 2008 16th Mediterranean Conference on, pages 1276 –1283, June 2008a. doi: 10.1109/MED.2008.4602258.

M. Bouchoucha, M. Tadjine, A. Tayebi, and P. Mullhaupt. Backstepping based nonlinear PI for attitude stabilisation of a quadrotor: From theory to experiment. In Intelligent Robots and Systems, 2008. IROS 2008. IEEE/RSJ International Conference on, page 4183, September 2008b. doi: 10.1109/IROS.2008.4651238.

S. Bouhired, M. Bouchoucha, and M. Tadjine. Quaternion-based global attitude tracking controller for a quadrotor uav. In Systems and Control (ICSC), 2013 3rd International Conference on, pages 933–938, Oct 2013. doi: 10.1109/ICoSC.2013.6750969.

T. Bresciani. Modelling, identification and control of a quadrotor helicopter. PhD thesis, 2008.

F. Caccavale, C. Natale, B. Siciliano, and L. Villani. Six-dof impedance control based on angle/axis representations. Robotics and Automation, IEEE Transactions on, 15(2):289–300, Apr 1999. ISSN 1042-296X. doi: 10.1109/70.760350.

E. Cetinsoy. Design and flight tests of a holonomic quadrotor UAV with sub-rotor control surfaces. In Mechatronics and Automation (ICMA), 2013 IEEE International Conference on, pages 1197–1202, Aug 2013. doi: 10.1109/ICMA.2013.6618084.

G.B. Chatterji and Minjea Tahk. A quaternion formulation for boost phase attitude estimation, guidance and control of exoatmospheric interceptors. In American Control Conference, 1989, pages 1561–1566, June 1989.

N.A. Chaturvedi, A.K. Sanyal, and N.H. McClamroch. Rigid-body attitude control. IEEE Control Systems Magazine, 31(3):30–51, June 2011. ISSN 1066-033X. doi: 10.1109/MCS.2011.940459.

M. Cutler and J. P. How. Actuator constrained trajectory generation and control for variable-pitch quadrotors. In AIAA Guidance, Navigation, and Control Conference (GNC), 2012.

P. de Lamberterie, T. Perez, and A. Donaire. A low-complexity flight controller for unmanned aircraft systems with constrained control allocation. In Australian Control Conference (AUCC), 2011, pages 284–289, Nov 2011.

E. de Vries and K. Subbarao. Backstepping based nested multi-loop control laws for a quadrotor. In Control Automation Robotics Vision (ICARCV), 2010 11th International Conference on, pages 1911–1916, Dec 2010. doi: 10.1109/ICARCV.2010.5707890.

C. Diao, B. Xian, X. Gu, B. Zhao, and J. Guo. Nonlinear control for an underactuated quadrotor unmanned aerial vehicle with parametric uncertainties. In Control Conference (CCC), 2012 31st Chinese, pages 998–1003, July 2012.

J. Diebel. Representing attitude: Euler angles, unit quaternions, and rotation vectors. Stanford University, 2006.

S. Driessens and P.E.I. Pounds. Towards a more efficient quadrotor configuration. In Intelligent Robots and Systems (IROS), 2013 IEEE/RSJ International Conference on, pages 1386–1392, Nov 2013. doi: 10.1109/IROS.2013.6696530.

W. C. Durham. Attainable moments for the constrained control allocation problem. J. Guid. Control Dyn., 17:1371–1373, 1994.

W.C. Durham. Constrained control allocation. Journal of Guidance, Control, and Dynamics, 16(4):717–725, 1993.

M. Elfeky, M. Elshafei, A.-W.A. Saif, and M.F. Al-Malki. Quadrotor helicopter with tilting rotors: Modeling and simulation. In Computer and Information Technology (WCCIT), 2013 World Congress on, pages 1–5, June 2013. doi: 10.1109/WCCIT.2013.6618768.

D. Enns. Control allocation approaches. In Proc AIAA Guid., Nav. and Control Conf., pages 98–108, Boston, MA, 1998.

Z. Fang, Z. Zhi, L. Jun, and W. Jian. Feedback linearization and continuous sliding mode control for a quadrotor UAV. In Control Conference, 2008. CCC 2008. 27th Chinese, pages 349–353, July 2008. doi: 10.1109/CHICC.2008.4605334.

Zheng Fang and W. Gao. Adaptive integral backstepping control of a micro-quadrotor. In Intelligent Control and Information Processing (ICICIP), 2011 2nd International Conference on, volume 2, pages 910–915, July 2011. doi: 10.1109/ICICIP.2011.6008382.

P. Ferrell, B. Smith, B. Stark, and YangQuan Chen. Dynamic flight modeling of a multi-mode flying wing quadrotor aircraft. In Unmanned Aircraft Systems (ICUAS), 2013 International Conference on, pages 398–404, May 2013. doi: 10.1109/ICUAS.2013.6564714.

O.-E. Fjellstad and T.I. Fossen. Singularity-free tracking of unmanned underwater vehicles in 6 DOF. In Decision and Control, 1994., Proceedings of the 33rd IEEE Conference on, volume 2, pages 1128–1133 vol.2, Dec 1994. doi: 10.1109/CDC.1994.411068.

T.I. Fossen and T.A. Johansen. A survey of control allocation methods for ships and underwater vehicles. In 14th Mediterranean Conference on Control and Automation, pages 1–6, Ancona, Italy, 2006.

D. Fragopoulos and M. Innocenti. Stability considerations in quaternion attitude control using discontinuous lyapunov functions. Control Theory and Applications, IEE Proceedings -, 151(3):253–258, May 2004. ISSN 1350-2379. doi: 10.1049/ip-cta:20040311(410)151.

A. Freddi, A. Lanzon, and S. Longhi. A feedback linearization approach to fault tolerance in quadrotor vehicles. In Proceedings of the 18th IFAC World Congress, pages 5413 – 5418, Milano, Italy, September 2011.

E. Fresk and G. Nikolakopoulos. Full quaternion based attitude control for a quadrotor. In Control Conference (ECC), 2013 European, pages 3864–3869, July 2013.

W. Gai and H. Wang. Closed-loop dynamic control allocation for aircraft with multiple actuators. Chinese Journal of Aeronautics, 26(3):676 – 686, 2013. ISSN 1000-9361. doi: http://dx.doi.org/10.1016/j.cja.2013.04.031.

I. González, S. Salazar, and R. Lozano. Chattering-free sliding mode altitude control for a quad-rotor aircraft: Real-time application. Journal of Intelligent & Robotic Systems, 73(1-4):137–155, 2014. ISSN 0921-0296. doi: 10.1007/s10846-013-9913-8.

J. A. Guerrero, R. Lozano, G. Romero, D. Lara-Alabazares, and K. C. Wong. Robust control design based on sliding mode control for hover flight of a mini tail-sitter unmanned aerial vehicle. In Industrial Electronics, 2009. IECON '09. 35th Annual Conference of IEEE, pages 2342–2347, Nov 2009. doi: 10.1109/IECON.2009.5415267.

J. F. Guerrero-Castellanos, A. Hably, N. Marchand, and S. Lesecq. Bounded attitude stabilization: Application on four-rotor helicopter. In Robotics and Automation, 2007 IEEE International Conference on, pages 730–735, April 2007. doi: 10.1109/ROBOT.2007.363073.

O. Harkegard. Backstepping and Control Allocation with Application to Flight Control. PhD thesis, Linkoping University, Linkoping, Sweden, 2003.

F. Hoffmann, N. Goddemeier, and T. Bertram. Attitude estimation and control of a quadrocopter. In Intelligent Robots and Systems (IROS), 2010 IEEE/RSJ International Conference on, pages 1072 –1077, October 2010. doi: 10.1109/IROS.2010.5649111.

G. Hu, S. Gupta, N. Fitz-Coy, and W.E. Dixon. Lyapunov-based visual servo tracking control via a quaternion formulation. In Decision and Control, 2006 45th IEEE Conference on, pages 3861–3866, Dec 2006. doi: 10.1109/CDC.2006.377301.

H. Huang, G.M. Hoffmann, S.L. Waslander, and C.J. Tomlin. Aerodynamics and control of autonomous quadrotor helicopters in aggressive maneuvering. In Robotics and Automation, 2009. ICRA '09. IEEE International Conference on, pages 3277 –3282, May 2009. doi: 10.1109/ROBOT.2009.5152561.

M. Huang, B. Xian, C. Diao, K. Yang, and Y. Feng. Adaptive tracking control of underactuated quadrotor unmanned aerial vehicles via backstepping. In American Control Conference (ACC), 2010, pages 2076 –2081, July 2010.

M. Ireland and D. Anderson. Development of navigation algorithms for nap-of-the-earth UAV flight in a constrained urban environment. September 2012. URL `http://eprints.gla.ac.uk/68501/`.

T.A. Johansen. Optimizing nonlinear control allocation. In Decision and Control, 2004. CDC. 43rd IEEE Conference on, volume 4, pages 3435–3440. IEEE, 2004.

T.A. Johansen and T.I. Fossen. Control allocation - a survey. Automatica, 49(5): 1087 – 1103, 2013. ISSN 0005-1098. doi: 10.1016/j.automatica.2013.01.035.

S.M. Joshi, A.G. Kelkar, and J.T.-Y. Wen. Robust attitude stabilization of spacecraft using nonlinear quaternion feedback. Automatic Control, IEEE Transactions on, 40(10):1800–1803, Oct 1995. ISSN 0018-9286. doi: 10.1109/9.467669.

J. Kim, I. Yang, and D. Lee. Accommodation of actuator faults using control allocation with modified daisy chaining. In Control, Automation and Systems (ICCAS), 2011 11th International Conference on, pages 717–720, 2011.

W. C. A. Kishore, S. Dasgupta, G. Ray, and S. Sen. Control allocation for an over-actuated satellite launch vehicle. Aerospace Science and Technology, 28(1):56 – 71, 2013. ISSN 1270-9638. doi: http://dx.doi.org/10.1016/j.ast.2012.10.004.

A. Lanzon, A. Freddi, and S. Longhi. Flight control of a quadrotor vehicle subsequent to a rotor failure. Journal of Guidance, Control, and Dynamics, 37:580–591, 2014.

T. Lee. Robust adaptive attitude tracking on SO(3) with an application to a quadrotor UAV. Control Systems Technology, IEEE Transactions on, 21(5):1924–1930, Sept 2013. ISSN 1063-6536. doi: 10.1109/TCST.2012.2209887.

J Gordon Leishman. The Breguet-Richet quad-rotor helicopter of 1907. Vertiflite, 47(3):58–60, 2002.

Guang-Xing Li, Jun Zhou, and Feng-Qi Zhou. Variable structure control for flexible spacecraft. In Control Conference, 2006. CCC 2006. Chinese, pages 943–946, Aug 2006. doi: 10.1109/CHICC.2006.280813.

J. Lunze and J. H. Richter. Reconfigurable fault-tolerant control: A tutorial introduction. Eur. J. Control, 14(5):359–386, 2008.

S. Lupashin, A. Schollig, M. Sherback, and R. D'Andrea. A simple learning strategy for high-speed quadrocopter multi-flips. In Robotics and Automation (ICRA), 2010 IEEE International Conference on, pages 1642–1648, May 2010. doi: 10.1109/ROBOT.2010.5509452.

Jianjun Ma, Wenqiang Li, Zhiqiang Zheng, and Dewen Hu. Robust reconfigurable flight control based on control reallocation for a tailless aircraft. In Systems and Control in Aerospace and Astronautics, 2008. ISSCAA 2008. 2nd International Symposium on, pages 1–6, Dec 2008. doi: 10.1109/ISSCAA.2008.4776304.

Y. Ma, B. Jiang, G. Tao, and Y. Cheng. Actuator failure compensation and attitude control for rigid satellite by adaptive control using quaternion feedback. Journal of the Franklin Institute, 351(1):296 – 314, 2014. ISSN 0016-0032. doi: http://dx.doi.org/10.1016/j.jfranklin.2013.08.028.

J. Maciejowski. Discussion on: "reconfigurable fault-tolerant control : A tutorial introduction". European Journal of Control, 14(5):387 – 389, 2008. ISSN 0947-3580. doi: http://dx.doi.org/10.1016/S0947-3580(08)70784-2. URL `http://www.sciencedirect.com/science/article/pii/S0947358008707842`.

T. Madani and A. Benallegue. Backstepping sliding mode control applied to a miniature quadrotor flying robot. In IEEE Industrial Electronics, IECON 2006 - 32nd Annual Conference on, pages 700 –705, November 2006a. doi: 10.1109/IECON.2006.347236.

T. Madani and A. Benallegue. Backstepping control for a quadrotor helicopter. In Intelligent Robots and Systems, 2006 IEEE/RSJ International Conference on, pages 3255 –3260, October 2006b. doi: 10.1109/IROS.2006.282433.

J.L. Marins, X. Yun, E.R. Bachmann, R.B. Mcghee, and M.J. Zyda. An extended kalman filter for quaternion-based orientation estimation using MARG sensors. In Intelligent Robots and Systems, 2001. Proceedings. 2001 IEEE/RSJ International Conference on, volume 4, pages 2003–2011 vol.4, 2001. doi: 10.1109/IROS.2001.976367.

A. Marks, J. F. Whidborne, and I. Yamamoto. Fault tolerant control of a VTOL octorotor UAV using control allocation. In UKACC International Conference on Control 2012, Cardiff, U.K., September 2012.

C.G. Mayhew, R.G. Sanfelice, and A.R. Teel. Quaternion-based hybrid control for robust global attitude tracking. Automatic Control, IEEE Transactions on, 56 (11):2555–2566, Nov 2011. ISSN 0018-9286. doi: 10.1109/TAC.2011.2108490.

D. Mellinger and V. Kumar. Minimum snap trajectory generation and control for quadrotors. In Robotics and Automation (ICRA), 2011 IEEE International Conference on, pages 2520–2525, May 2011. doi: 10.1109/ICRA.2011.5980409.

A.-R. Merheb, H. Noura, and F. Bateman. Passive fault tolerant control of quadrotor UAV using regular and cascaded sliding mode control. In Control and

Fault-Tolerant Systems (SysTol), 2013 Conference on, pages 330–335, Oct 2013. doi: 10.1109/SysTol.2013.6693910.

N. Metni and T. Hamel. A UAV for bridge inspection: Visual servoing control law with orientation limits. Automation in construction, 17(1):3–10, 2007.

A.A. Mian and Wang Daobo. Nonlinear flight control strategy for an underactuated quadrotor aerial robot. In IEEE International Conference on Networking, Sensing and Control (ICNSC 2008), pages 938 –942, April 2008. doi: 10.1109/ICNSC.2008.4525351.

B. Michini, J. Redding, N.K. Ure, M. Cutler, and J.P. How. Design and flight testing of an autonomous variable-pitch quadrotor. In 2011 IEEE International Conference on Robotics and Automation (ICRA), pages 2978 –2979, Shanghai, China, May 2011. doi: 10.1109/ICRA.2011.5980561.

Mikrokopter. `http://www.mikrokopter.de/en/products/kits`. Accessed 02/14.

M. W. Oppenheimer, D. B. Doman, and M. A. Bolender. Control allocation for over-actuated systems. In Proc. 14th Mediterranean Conference on Control and Automation (MED 06.), Ancona, Italy, June 2006. doi: 10.1109/MED.2006.328750. Paper no. FEA4-3.

C. Papachristos, K. Alexis, G. Nikolakopoulos, and A. Tzes. Model predictive attitude control of an unmanned tilt-rotor aircraft. In Industrial Electronics (ISIE), 2011 IEEE International Symposium on, pages 922–927, June 2011. doi: 10.1109/ISIE.2011.5984282.

G.V. Raffo, M.G. Ortega, and F.R. Rubio. Backstepping/nonlinear H∞; control for path tracking of a quadrotor unmanned aerial vehicle. In American Control Conference, 2008, pages 3356–3361, June 2008. doi: 10.1109/ACC.2008.4587010.

G.B. Raharja, Kim Gyou Beom, and Yoon Kwangjoon. Design and implementation of coaxial quadrotor for an autonomous outdoor flight. In Ubiquitous Robots and Ambient Intelligence (URAI), 2011 8th International Conference on, pages 61–63, Nov 2011. doi: 10.1109/URAI.2011.6145933.

H. Ramirez-Rodriguez, V. Parra-Vega, A. Sanchez, and O. Garcia. Integral sliding mode backstepping control of quadrotors for robust position tracking. In Unmanned Aircraft Systems (ICUAS), 2013 International Conference on, pages 423–432, May 2013. doi: 10.1109/ICUAS.2013.6564717.

M. Ranjbaran and K. Khorasani. Fault recovery of an under-actuated quadrotor aerial vehicle. In 49th IEEE Conference on Decision and Control (CDC), pages 4385 –4392, December 2010. doi: 10.1109/CDC.2010.5718140.

H. Romero, S. Salazar, A. Sanchez, and R. Lozano. A new UAV configuration having eight rotors: Dynamical model and real-time control. In Decision and Control, 2007 46th IEEE Conference on, pages 6418–6423, Dec 2007. doi: 10.1109/CDC.2007.4434776.

H. Romero, S. Salazar, and R. Lozano. Real-time stabilization of an eight-rotor UAV using optical flow. Robotics, IEEE Transactions on, 25(4):809 –817, August 2009. ISSN 1552-3098. doi: 10.1109/TRO.2009.2018972.

D. Rotondo, F. Nejjari, A. Torren, and V. Puig. Fault tolerant control design for polytopic uncertain LPV systems: Application to a quadrotor. In Control and Fault-Tolerant Systems (SysTol), 2013 Conference on, pages 643–648, 2013. doi: 10.1109/SysTol.2013.6693899.

K. Runcharoon and V. Srichatrapimuk. Sliding mode control of quadrotor. In Technological Advances in Electrical, Electronics and Computer Engineering (TAEECE), 2013 International Conference on, pages 552–557, May 2013. doi: 10.1109/TAEECE.2013.6557334.

M. Ryll, H.H. Bulthoff, and P.R. Giordano. Modeling and control of a quadrotor UAV with tilting propellers. In Robotics and Automation (ICRA), 2012 IEEE International Conference on, pages 4606–4613, May 2012. doi: 10.1109/ICRA.2012.6225129.

I. Sadeghzadeh, A. Mehta, A. Chamseddine, and Youmin Zhang. Active fault tolerant control of a quadrotor UAV based on gainscheduled PID control. In Electrical Computer Engineering (CCECE), 2012 25th IEEE Canadian Conference on, pages 1–4, April 2012. doi: 10.1109/CCECE.2012.6335037.

S. Salazar-Cruz and R. Lozano. Stabilization and nonlinear control for a novel trirotor mini-aircraft. In Robotics and Automation, 2005. ICRA 2005. Proceedings of the 2005 IEEE International Conference on, pages 2612–2617, April 2005. doi: 10.1109/ROBOT.2005.1570507.

A.L. Salih, M. Moghavvemi, H.A.F. Mohamed, and K.S. Gaeid. Modelling and PID controller design for a quadrotor unmanned air vehicle. In Automation Quality and Testing Robotics (AQTR), 2010 IEEE International Conference on, volume 1, pages 1 –5, May 2010. doi: 10.1109/AQTR.2010.5520914.

R. Schlanbusch, R. Kristiansen, and P.J. Nicklasson. Considerations choosing the optimal equilibrium point on the rotational sphere. In American Control Conference (ACC), 2010, pages 6169–6174, June 2010.

F. Senkul and E. Altug. Modeling and control of a novel tilt - roll rotor quadrotor UAV. In Unmanned Aircraft Systems (ICUAS), 2013 International Conference on, pages 1071–1076, May 2013. doi: 10.1109/ICUAS.2013.6564796.

F. Sharifi, M. Mirzaei, B.W. Gordon, and Youmin Zhang. Fault tolerant control of a quadrotor UAV using sliding mode control. In 2010 Conference on Control and Fault-Tolerant Systems (SysTol), pages 239 –244, October 2010. doi: 10.1109/SYSTOL.2010.5675979.

X. Shi, Y. Wei, J. Ning, and M. Fu. Constrained control allocation using cascading generalized inverse for dynamic positioning of ships. In Mechatronics and

Automation (ICMA), 2011 International Conference on, pages 1636 –1640, August 2011. doi: 10.1109/ICMA.2011.5985959.

P. Sinha, P. Esden-Tempski, C.A. Forrette, J.K. Gibboney, and G.M. Horn. Versatile, modular, extensible VTOL aerial platform with autonomous flight mode transitions. In Aerospace Conference, 2012 IEEE, pages 1–17, March 2012. doi: 10.1109/AERO.2012.6187313.

Y.D. Song and W.C. Cai. New intermediate quaternion based control of spacecraft: Part 1-almost global attitude tracking. International Journal of Innovative Computing, Information and Control, 8(10):7307–7319, 2012.

Spektrum. `https://www.spektrumrc.com/Products/Default.aspx?ProdID=SPMAR8000`, a. Accessed 04/14.

Spektrum. `http://www.spektrumrc.com/Products/Default.aspx?ProdId=SPM8800`, b. Accessed 04/14.

J. Spjtvold and T.A. Johansen. Fault tolerant control allocation for a thruster-controlled floating platform using parametric programming. In Decision and Control, 2009 held jointly with the 2009 28th Chinese Control Conference. CDC/CCC 2009. Proceedings of the 48th IEEE Conference on, pages 3311 –3317, December 2009. doi: 10.1109/CDC.2009.5400701.

E. Stingu and F. Lewis. Design and implementation of a structured flight controller for a 6 DOF quadrotor using quaternions. In Control and Automation, 2009. MED '09. 17th Mediterranean Conference on, pages 1233 –1238, June 2009. doi: 10.1109/MED.2009.5164715.

L. Tan, L. Lu, and G. Jin. Attitude stabilization control of a quadrotor helicopter using integral backstepping. In Automatic Control and Artificial Intelligence (ACAI 2012), International Conference on, pages 573–577, March 2012. doi: 10.1049/cp.2012.1044.

A. Tayebi and S. McGilvray. Attitude stabilization of a four-rotor aerial robot. In 43rd IEEE Conference on Decision and Control (CDC), volume 2, pages 1216 – 1221, December 2004. doi: 10.1109/CDC.2004.1430207.

A. Tayebi and S. McGilvray. Attitude stabilization of a VTOL quadrotor aircraft. IEEE Transactions on Control Systems Technology, 14(3):562 – 571, May 2006. ISSN 1063-6536. doi: 10.1109/TCST.2006.872519.

R. Voyles and Guangying Jiang. Hexrotor uav platform enabling dextrous interaction with structures 2014; preliminary work. In Safety, Security, and Rescue Robotics (SSRR), 2012 IEEE International Symposium on, pages 1–7, Nov 2012. doi: 10.1109/SSRR.2012.6523891.

S.L. Waslander, G.M. Hoffmann, Jung Soon Jang, and C.J. Tomlin. Multi-agent quadrotor testbed control design: integral sliding mode vs. reinforcement learning. In Proceedings 2005 IEEE/RSJ International Conference on Intelligent Robots

and Systems (IROS 2005), pages 3712 – 3717, Edmonton, Canada, August 2005. doi: 10.1109/IROS.2005.1545025.

J.T. Wen and Kenneth Kreutz. Globally stable control laws for the attitude maneuver problem: tracking control and adaptive control. In Decision and Control, 1988., Proceedings of the 27th IEEE Conference on, pages 69–74 vol.1, Dec 1988. doi: 10.1109/CDC.1988.194271.

B. Wie and P.M. Barba. Quaternion feedback for spacecraft large angle maneuvers. Journal of Guidance, Control, and Dynamics, 8(3):360–365, 1985.

Draganflyer X4-P. Draganflyer x4-p four rotor uav helicopter aerial video platform. `http://www.draganfly.com/uav-helicopter/draganflyer-x4p/index.php`. Accessed 04.14.

XBee. `http://www.digi.com/products/wireless-wired-embedded-solutions/zigbee-rf-modules/point-multipoint-rfmodules/xbee-pro-900`. Accessed 02/14.

R. Xu and U. Ozguner. Sliding mode control of a quadrotor helicopter. In Decision and Control, 2006 45th IEEE Conference on, pages 4957 –4962, December 2006. doi: 10.1109/CDC.2006.377588.

Y. Yali, C. Jiang, and H. Wu. Backstepping control of each channel for a quadrotor aerial robot. In International Conference on Computer, Mechatronics, Control and Electronic Engineering (CMCE), volume 3, pages 403 –407, August 2010. doi: 10.1109/CMCE.2010.5610299.

I. Yamamoto, Rui Zhu, J.F. Whidborne, and A. Marks. Research and design on a control system for a disk-type flying robot with multiple rotors. In Control (CONTROL), 2014 UKACC International Conference on, pages 337–342, July 2014. doi: 10.1109/CONTROL.2014.6915163.

Y. Yang. Spacecraft attitude determination and control: Quaternion based method. Annual Reviews in Control, 36(2):198 – 219, 2012. ISSN 1367-5788. doi: http://dx.doi.org/10.1016/j.arcontrol.2012.09.003.

Y.C. Yang, K.S. Yang, C.Y. Chen, L.J. Mu, Y.M. Chiu, C.M. Yu, and W.C. Yang. Robust trajectory control for an autonomous underwater vehicle. In OCEANS - Bergen, 2013 MTS/IEEE, pages 1–9, June 2013. doi: 10.1109/OCEANS-Bergen.2013.6607946.

F.K. Yeh, H.H. Chien, and L.C. Fu. A midcourse guidance law for missiles with thrust vector control. In American Control Conference, 2001. Proceedings of the 2001, volume 3, pages 2357–2362 vol.3, 2001. doi: 10.1109/ACC.2001.946104.

F.K. Yeh, K.Y. Cheng, and L.C. Fu. Variable structure-based nonlinear missile guidance/autopilot design with highly maneuverable actuators. Control Systems Technology, IEEE Transactions on, 12(6):944–949, Nov 2004. ISSN 1063-6536. doi: 10.1109/TCST.2004.833622.

B. Yu, Y. Zhang, I. Minchala, and Y. Qu. Fault-tolerant control with linear quadratic and model predictive control techniques against actuator faults in a quadrotor uav. In Control and Fault-Tolerant Systems (SysTol), 2013 Conference on, pages 661–666, Oct 2013. doi: 10.1109/SysTol.2013.6693925.

J.S. Yuan. Closed-loop manipulator control using quaternion feedback. Robotics and Automation, IEEE Journal of, 4(4):434–440, Aug 1988. ISSN 0882-4967. doi: 10.1109/56.809.

R. Zhang, Q. Quan, and K.-Y. Cai. Attitude control of a quadrotor aircraft subject to a class of time-varying disturbances. Control Theory Applications, IET, 5(9): 1140–1146, June 2011. ISSN 1751-8644. doi: 10.1049/iet-cta.2010.0273.

Youmin Zhang, V.S. Suresh, Bin Jiang, and D. Theilliol. Reconfigurable control allocation against aircraft control effector failures. In Control Applications, 2007. CCA 2007. IEEE International Conference on, pages 1197–1202, Oct 2007. doi: 10.1109/CCA.2007.4389398.

Appendix A

Arduino Code

A.1 Octorotor

The code used for the octorotor is based on the Arducopter [Arducopter] and Ardupirates [Ardupirates] open source Arduino code. It calls a number of Arduino libraries which are freely available on the internet. With the change from APM1 to APM2 hardware the original Arducopter project page is no longer supported and the individual code libraries are now encompassed into a user-friendly installer. However, this means that it is harder to edit the individual files without having to change a number of other libraries which call the setup functions.

A.1.1 Initialisation

```
// -*- tab-width: 4; Mode: C++; c-basic-offset: 4; indent-tabs-mode: t -*-

/// @file       AP_MotorsOcta.h
/// @brief      Motor control class for Octorotor

#ifndef AP_MOTORSOCTA
#define AP_MOTORSOCTA

#include <FastSerial.h>
#include <AP_Common.h>
#include <AP_Math.h>            // ArduPilot Mega Vector/Matrix math Library
#include <RC_Channel.h>         // RC Channel Library
#include <APM_RC.h>             // ArduPilot Mega RC Library
#include <AP_MotorsMatrix.h>    // Parent Motors Matrix library

/// @class      AP_MotorsOcta
class AP_MotorsOcta : public AP_MotorsMatrix {
public:

    /// Constructor
    AP_MotorsOcta( uint8_t APM_version, APM_RC_Class* rc_out,
```

```
    RC_Channel* rc_roll, RC_Channel* rc_pitch, RC_Channel* rc_throttle,
    RC_Channel* rc_yaw, uint16_t speed_hz = AP_MOTORS_SPEED_DEFAULT) :
    AP_MotorsMatrix(APM_version, rc_out, rc_roll, rc_pitch, rc_throttle,
    rc_yaw, speed_hz) {
    };

    // setup_motors - configures the motors for a quad
    virtual void        setup_motors();

protected:

};

#endif  // AP_MOTORSOCTA
```

A.1.2 Control Allocation

The control allocation is achieved by specifying the number of effectors and their position around the vehicle. The position of the motors is described in a similar way as in Section 2.6 except that the angle is that subtended by the vehicle arm and the y_b axis positive counter-clockwise.

```
/*
 *       AP_MotorsOcta.cpp - ArduCopter motors library
 *       Code by Aryeh Marks. Cranfield Univeristy
 *
 *           Code is for the fully functioning octorotor
 *
 *       This library is free software; you can redistribute it and/or
 *   modify it under the terms of the GNU Lesser General Public
 *   License as published by the Free Software Foundation; either
 *   version 2.1 of the License, or (at your option) any later version.
 */

#include "AP_MotorsOcta.h"

// setup_motors - configures the motors for an octa
void AP_MotorsOcta::setup_motors()
{
    // call parent
    AP_MotorsMatrix::setup_motors();

    // hard coded config for supported frames
   {
        // X frame set-up - fully functional vehicle
        add_motor(AP_MOTORS_MOT_1,    22.5, AP_MOTORS_MATRIX_MOTOR_CW,
AP_MOTORS_MOT_2, 1);
        add_motor(AP_MOTORS_MOT_2, -157.5, AP_MOTORS_MATRIX_MOTOR_CW,
AP_MOTORS_MOT_1, 5);
        add_motor(AP_MOTORS_MOT_3,    67.5, AP_MOTORS_MATRIX_MOTOR_CCW,
AP_MOTORS_MOT_6, 2);
        add_motor(AP_MOTORS_MOT_4,   157.5, AP_MOTORS_MATRIX_MOTOR_CCW,
AP_MOTORS_MOT_5, 4);
        add_motor(AP_MOTORS_MOT_5,   -22.5, AP_MOTORS_MATRIX_MOTOR_CCW,
AP_MOTORS_MOT_4, 8);
        add_motor(AP_MOTORS_MOT_6, -112.5, AP_MOTORS_MATRIX_MOTOR_CCW,
AP_MOTORS_MOT_3, 6);
        add_motor(AP_MOTORS_MOT_7,   -67.5, AP_MOTORS_MATRIX_MOTOR_CW,
AP_MOTORS_MOT_8, 7);
        add_motor(AP_MOTORS_MOT_8,   112.5, AP_MOTORS_MATRIX_MOTOR_CW,
AP_MOTORS_MOT_7, 3);
    }
}
```

A.2 Failure in Effector 7

A.2.1 Initialisation

The vehicle is initialised so that the control allocation is for 7 effectors.

```
// -*- tab-width: 4; Mode: C++; c-basic-offset: 4; indent-tabs-mode: t -*-

/// @file       AP_MotorsSepta.h
/// @brief      Motor control class for Septarotor
                - octorotor with failure in effector 7

#ifndef AP_MOTORSSEPTA
#define AP_MOTORSSEPTA

#include <FastSerial.h>
#include <AP_Common.h>
#include <AP_Math.h>          // ArduPilot Mega Vector/Matrix math Library
#include <RC_Channel.h>       // RC Channel Library
#include <APM_RC.h>           // ArduPilot Mega RC Library
#include <AP_MotorsMatrix.h>    // Parent Motors Matrix library

/// @class      AP_MotorsOcta
class AP_MotorsSepta : public AP_MotorsMatrix {
public:

    /// Constructor
    AP_MotorsSepta( uint8_t APM_version, APM_RC_Class* rc_out,
    RC_Channel* rc_roll, RC_Channel* rc_pitch, RC_Channel* rc_throttle,
    RC_Channel* rc_yaw, uint16_t speed_hz = AP_MOTORS_SPEED_DEFAULT)
    : AP_MotorsMatrix(APM_version, rc_out, rc_roll, rc_pitch, rc_throttle,
    rc_yaw, speed_hz) {
    };

    // setup_motors - configures the motors for a septa rotor
        - engine failure in effector 7
    virtual void        setup_motors();

protected:

};

#endif  // AP_MOTORSEPTA
```

A.2.2 Control Allocation

```
/*
 *       AP_MotorsOcta.cpp - ArduCopter motors library
 *       Code by Aryeh Marks. Cranfield Univeristy
 *
 *           Code is for a failure in effector 7
 *
 *       This library is free software; you can redistribute it and/or
 *   modify it under the terms of the GNU Lesser General Public
 *   License as published by the Free Software Foundation; either
 *   version 2.1 of the License, or (at your option) any later version.
 */

#include "AP_MotorsSepta.h"

// setup_motors - configures the motors for a octa
void AP_MotorsSepta::setup_motors()
{
    // call parent
    AP_MotorsMatrix::setup_motors();

    // hard coded config for supported frames
   {
        // X frame set-up - failure in effector 7
        add_motor(AP_MOTORS_MOT_1,   22.5, AP_MOTORS_MATRIX_MOTOR_CW,
AP_MOTORS_MOT_2, 1);
        add_motor(AP_MOTORS_MOT_2, -157.5, AP_MOTORS_MATRIX_MOTOR_CW,
AP_MOTORS_MOT_1, 5);
        add_motor(AP_MOTORS_MOT_3,   67.5, AP_MOTORS_MATRIX_MOTOR_CCW,
AP_MOTORS_MOT_6, 2);
        add_motor(AP_MOTORS_MOT_4,  157.5, AP_MOTORS_MATRIX_MOTOR_CCW,
AP_MOTORS_MOT_5, 4);
        add_motor(AP_MOTORS_MOT_5,  -22.5, AP_MOTORS_MATRIX_MOTOR_CCW,
AP_MOTORS_MOT_4, 8);
        add_motor(AP_MOTORS_MOT_6, -112.5, AP_MOTORS_MATRIX_MOTOR_CCW,
AP_MOTORS_MOT_3, 6);
        add_motor(AP_MOTORS_MOT_7,  -67.5, AP_MOTORS_MATRIX_MOTOR_CW,
AP_MOTORS_MOT_8, 7);
       // add_motor(AP_MOTORS_MOT_8,  112.5, AP_MOTORS_MATRIX_MOTOR_CW,
AP_MOTORS_MOT_7, 3);
    }
}
```

A failure in an effector is initialised by commenting out the representative line in the control allocation code as shown in the code above where '//' is inserted before the last line.

A.3 Frame Setup

The vehicle frame setup is defined using the control allocation matrix. The following two codes show a 'plus' and a 'cross' shaped quadrotor.

```
/*
 *       AP_MotorsQuad.cpp - ArduCopter motors library
 *       Code by Aryeh Marks. Cranfield University
 *
 *       All code should be treated as experimental and is used for research
 *   purposes only. Do not use if you are concerned about losing equipment
 *   on your vehicle. No responsibility is taken for application of the code.
 *
 *       This library is free software; you can redistribute it and/or
 *   modify it under the terms of the GNU Lesser General Public
 *   License as published by the Free Software Foundation; either
 *   version 2.1 of the License, or (at your option) any later version.
 */

#include "AP_MotorsQuad.h"

// setup_motors - configures the motors for a quad
void AP_MotorsQuad::setup_motors()
{
    // call parent
    AP_MotorsMatrix::setup_motors();

    // hard coded config for supported frames
    if( _frame_orientation == AP_MOTORS_PLUS_FRAME ) {
        // plus frame set-up
        add_motor(AP_MOTORS_MOT_1,   90, AP_MOTORS_MATRIX_MOTOR_CCW,
AP_MOTORS_MOT_2,  2);
        add_motor(AP_MOTORS_MOT_2,  -90, AP_MOTORS_MATRIX_MOTOR_CCW,
AP_MOTORS_MOT_1,  4);
        add_motor(AP_MOTORS_MOT_3,    0, AP_MOTORS_MATRIX_MOTOR_CW,
AP_MOTORS_MOT_4,  1);
        add_motor(AP_MOTORS_MOT_4,  180, AP_MOTORS_MATRIX_MOTOR_CW,
AP_MOTORS_MOT_3,  3);
    }else{
        // Cross frame set-up
        add_motor(AP_MOTORS_MOT_1,   45, AP_MOTORS_MATRIX_MOTOR_CCW,
AP_MOTORS_MOT_2,  1);
        add_motor(AP_MOTORS_MOT_2, -135, AP_MOTORS_MATRIX_MOTOR_CCW,
AP_MOTORS_MOT_1,  3);
        add_motor(AP_MOTORS_MOT_3,  -45, AP_MOTORS_MATRIX_MOTOR_CW,
AP_MOTORS_MOT_4,  4);
        add_motor(AP_MOTORS_MOT_4,  135, AP_MOTORS_MATRIX_MOTOR_CW,
AP_MOTORS_MOT_3,  2);
    }
}
```

Appendix B

Systems Diagram

This section provides systems level diagrams for the hardware architecture and for the power distribution. Solid lines denote physical (wired) connections, dashed lines represent non-physical connections such as bluetooth or radio.

B.1 Hardware Architecture

Pilot inputs are sent through the transmitter/receiver pair and receives telemetry data sent over bluetooth from the XBee module onboard the vehicle. This is paired with a XBee bluetooth receiver module which is connected to a laptop over USB. It is possible to send commands over the XBee connection and this is how the position commands are sent when GPS data is available. The transmitter is only able to send data and cannot receive from the vehicle.

If an onboard camera is attached it is powered from its own battery and the images and video are saved to an internal hard drive. These data are downloaded after the flight.

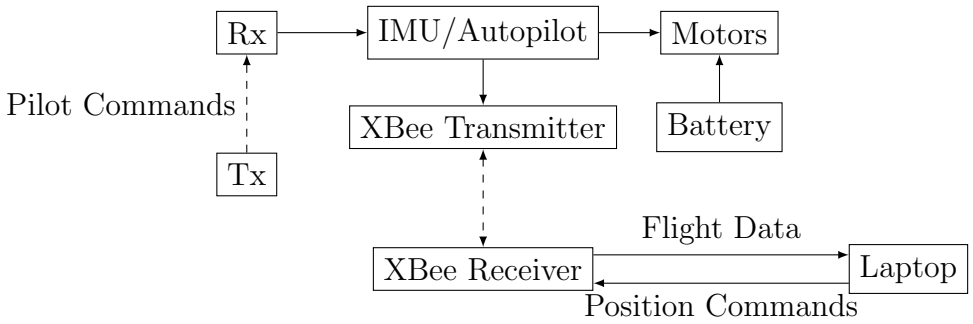

Figure B.1: System Diagram

B.2 Power Distribution

The brushless DC motors are provided with a nominal 11.1 volts from the LiPo battery through the power distribution board. They provide a regulated 5 volt power supply and this is fed back to the IMU/autopilot. The radio receiver and XBee transmitter are powered from a 5 volt output on the autopilot board. The laptop has its own power supply and the XBee receiver is powered over its USB laptop connection.

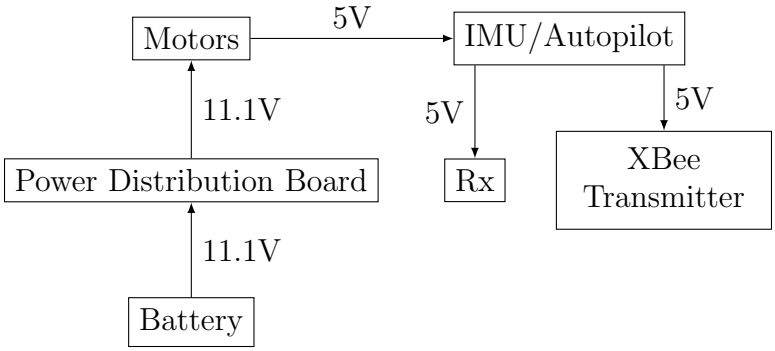

Figure B.2: Power Distribution

Appendix C

Additional Photographs

This section contains additional photographs of the vehicle. Figure C.1 is from the front of the vehicle, aligned in the 'cross' configuration. The rotors are removed from the motors to avoid potential damage.

C.1 Octorotor

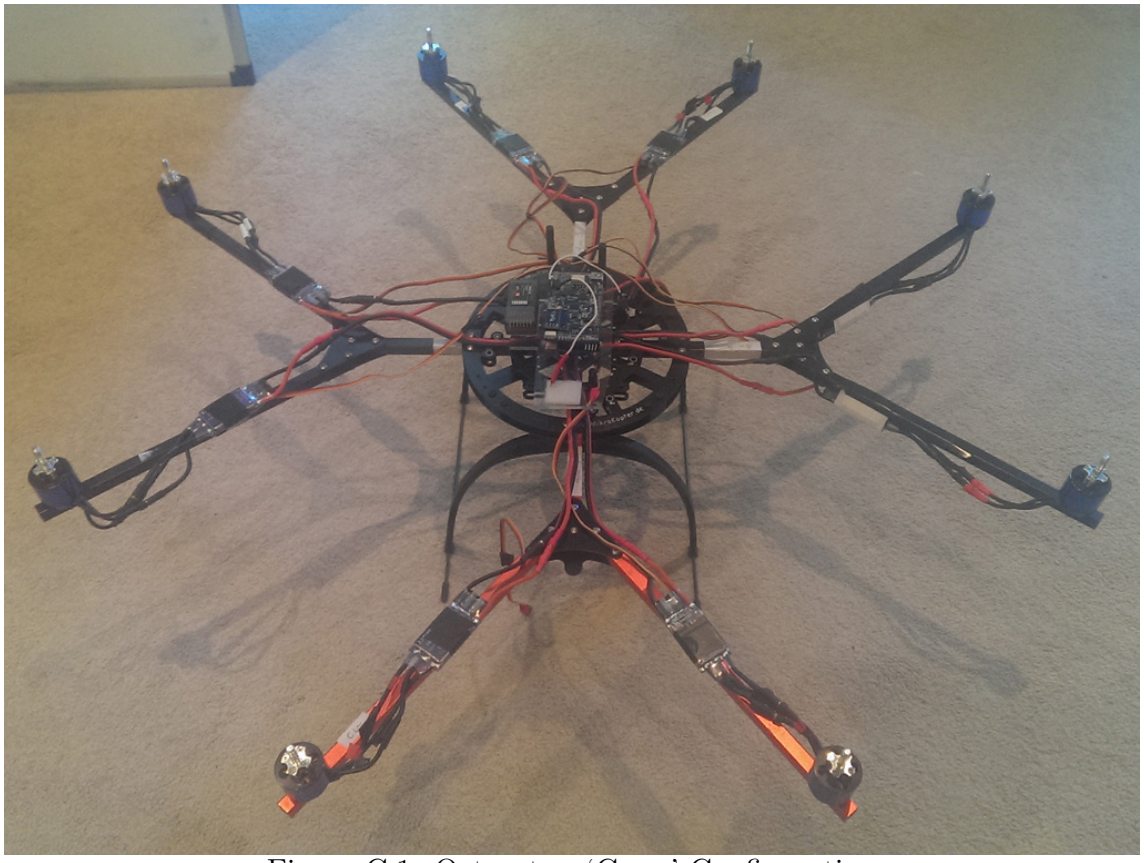

Figure C.1: Octorotor, 'Cross' Configuration

Figure C.2 is taken from the rear of the vehicle and shows an 'aligned' configuration.

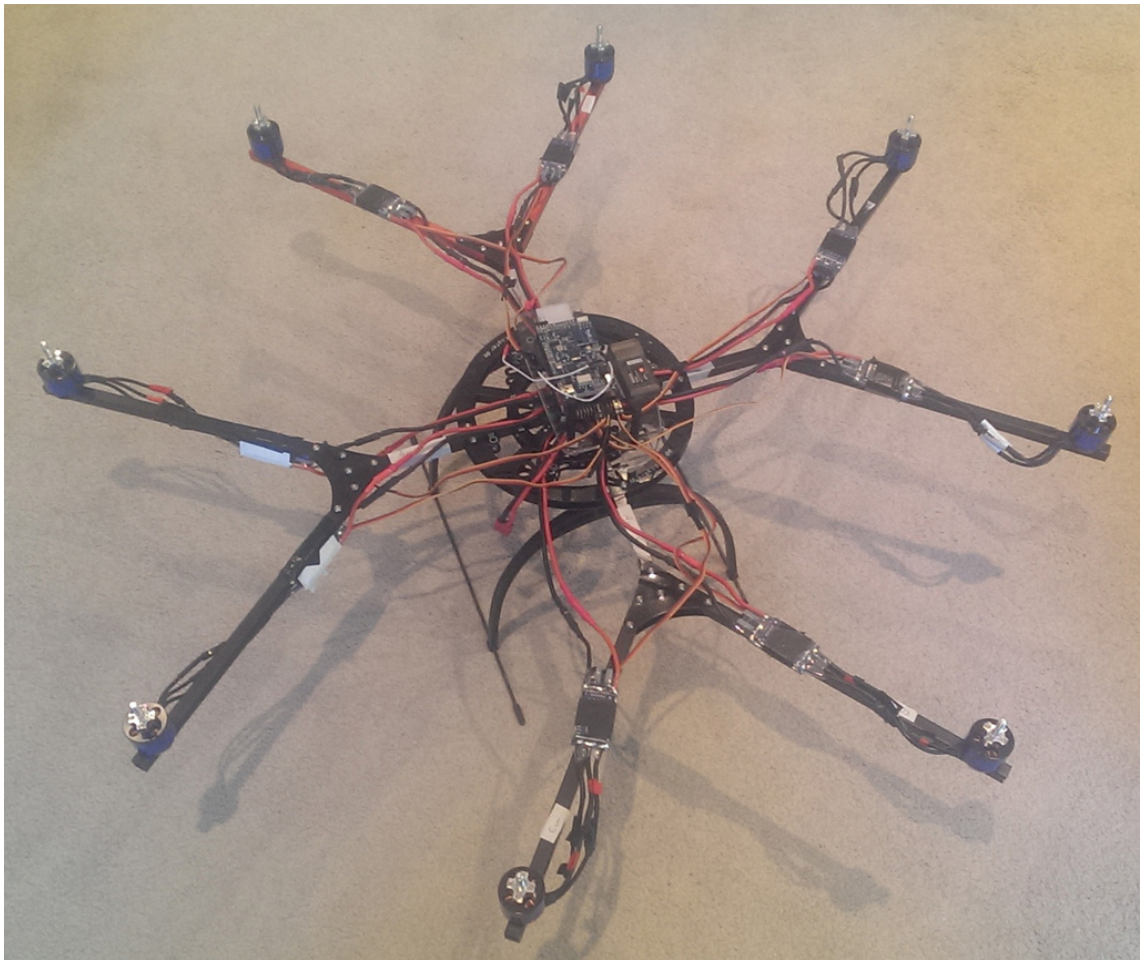

Figure C.2: Octorotor 'Aligned' Configuration

The Velcro battery attachment is shown in Figure C.3 which shows the underside of the vehicle body. The battery has a Velcro strip and this is shown in Figure C.4.

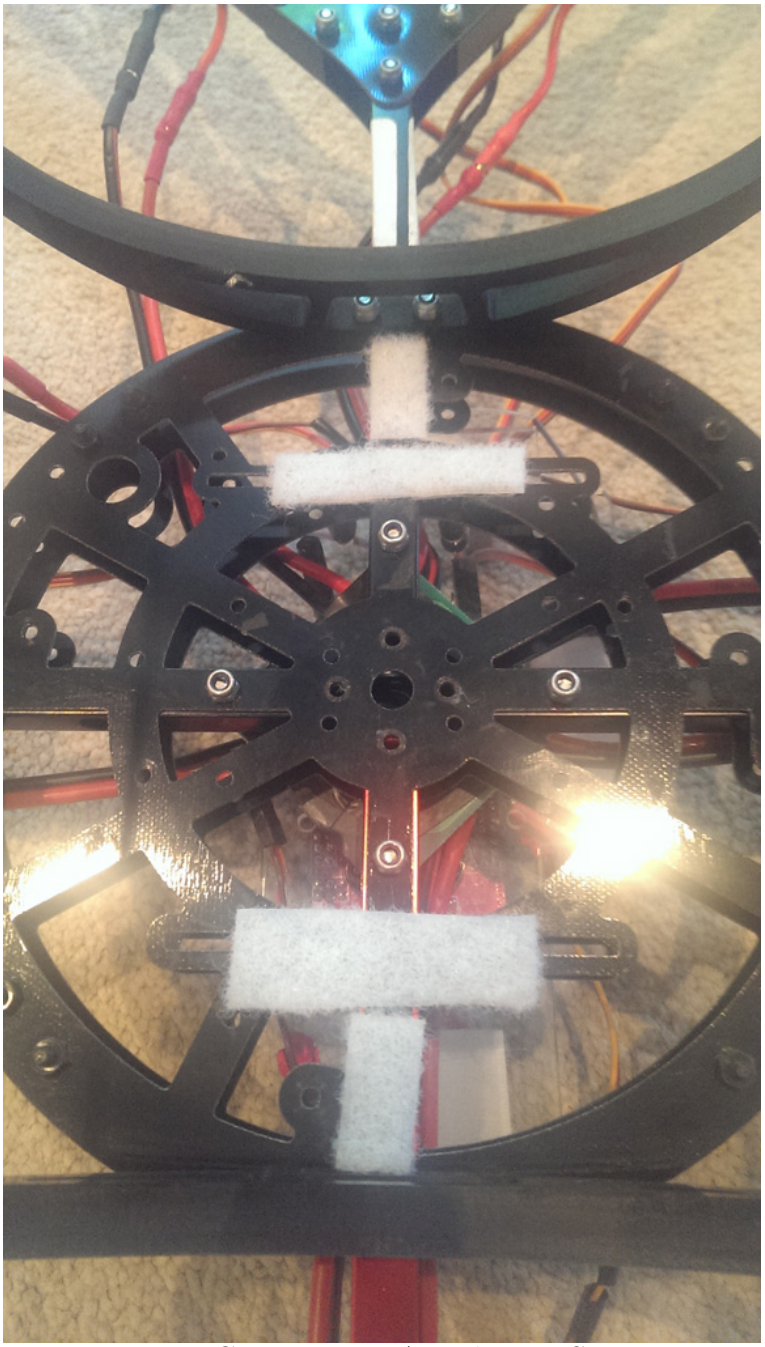

Figure C.3: Battery Attachment Strips

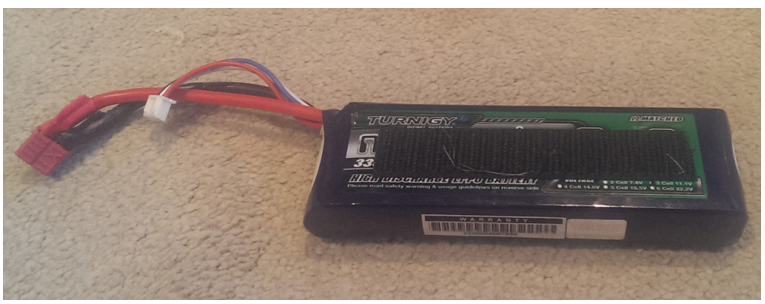

Figure C.4: Battey Velcro Strip

The ground clearance is shown in Figure C.5. This space is to allow the legs to flex to reduce impact forces after a heavy landing. There is also the opportunity to attach a camera to the battery, shown in Figure C.6.

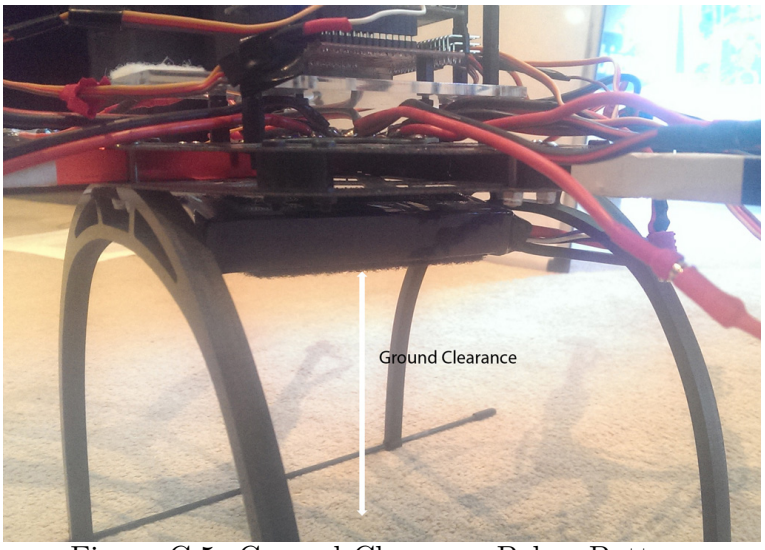

Figure C.5: Ground Clearance Below Battery

Figure C.6: Camera Attached to Battery

Figure C.7: Camera

C.2 Telemetry

The following photograph was taken during a presentation in Kumamoto Prefecture, Japan. It shows the flight planning software screen which contains an artificial horizon, primary flight instruments, and a GPS position plotter. The data is sent to the laptop over bluetooth and provides for real-time telemetry monitoring.

Figure C.8: Flight Control Software